

ABSTRACT

Aggregation of Cu, Zn Superoxide Dismutase in Amyotrophic Lateral Sclerosis: Kinetic, Mechanistic, and Therapeutic Approaches

Alireza Abdolvahabi, Ph.D.

Advisor: Bryan F. Shaw, Ph.D.

Investigating *in vitro* kinetics of protein aggregation using high-throughput microplate-based assays provides open venues for obtaining valuable information regarding mechanism(s) of pathogenesis of protein aggregates in neurodegenerative diseases, and facilitates development of effective therapies. In this dissertation, I use high-throughput microplate-based assays for studying the real-time kinetics of wild type and ALS-variant Cu, Zn superoxide dismutase (SOD1) aggregation in the context of amyotrophic lateral sclerosis (ALS). ALS is a neurodegenerative disease that is hallmarked with selective death of motor neurons, which leads to muscle paralysis, and eventually death. Mutations in *SOD1* gene are believed to underlie ~ 3 % of cases of ALS via triggering the misfolding and aggregation of SOD1 protein. These SOD1 aggregates render toxicity in motor neurons via interfering with and disrupting normal functions of cells such as cytoplasmic and axonal transport or membrane integrity.

In this dissertation, I first show that aspirin (the quintessential acylating pharmacopoeia) can inhibit the amyloidogenesis of wild-type (WT) and ALS-variant apo-SOD1 by increasing the intrinsic net negative charge of the polypeptide, via acetylation of multiple lysines. In the third chapter, I measure rates of fibrillar and amorphous SOD1 aggregation at high iteration and show that rates of oligomerization were intrinsically irreproducible and populated continuous probability distributions. In the fourth chapter, I used Kaplan-Meier estimators to quantify the probability of apo-SOD1 fibrillization (*in vitro*) from $\sim 10^3$ replicate amyloid assays of WT SOD1 and nine ALS variants, and showed that the probability of apo-SOD1 fibrillization is non-uniformly altered by different mutations. I found a linear correlation between the Hazard ratios of SOD1 fibrillization and those of patient survival in SOD1-linked ALS.

The fifth chapter answers a very fundamental question: “how do gyrating beads accelerate amyloid fibrillization?” I found that increasing the mass in beads from non-polymeric materials (e.g., steel) increases the nucleation rate of SOD1 fibrillization, whereas hydrophobicity and surface adhesion affected rate of SOD1 fibrillization in the case of polymeric beads.

In chapter six, I study the mechanism behind Hofmeister series in proteins. Chapter seven includes a project dedicated to early detection of leukocoria in children with retinoblastoma, during recreational photography.

Aggregation of Cu, Zn Superoxide Dismutase in Amyotrophic
Lateral Sclerosis: Kinetic, Mechanistic, and Therapeutic
Approaches

by

Alireza Abdolvahabi, B.Sc., M.Sc.

A Dissertation

Approved by the Department of Chemistry and Biochemistry

Patrick J. Farmer, Ph.D., Chairperson

Submitted to the Graduate Faculty of
Baylor University in Partial Fulfillment of the
Requirements for the Degree
of
Doctor of Philosophy

Approved by the Dissertation Committee

Bryan F. Shaw, Ph.D., Chairperson

Mary Lynn Trawick, Ph.D.

Sung Joon Kim, Ph.D.

Kevin L. Shuford, Ph.D.

Bessie Kebaara, Ph.D.

Accepted by the Graduate School

December 2017

J. Larry Lyon, Ph.D., Dean

Page bearing signatures is kept on file in the Graduate School.

Copyright © 2017 by Alireza Abdolvahabi

All rights reserved

TABLE OF CONTENTS

LIST OF FIGURES	x
LIST OF TABLES.....	xvi
LIST OF SCHEMES	xix
ACKNOWLEDGMENTS	xx
CHAPTER ONE.....	1
Mechanism of protein aggregation in neurodegenerative diseases: the case of Cu, Zn superoxide dismutase aggregation in amyotrophic lateral sclerosis ...	1
Introduction	1
Protein misfolding and aggregation in neurodegenerative diseases.....	1
SOD1 and ALS.....	4
The Underrated Biophysical Factor Involved in Protein Aggregation: Protein Net Electrostatic Charge.....	7
Statement of Contribution.....	9
CHAPTER TWO	11
Arresting amyloid with Coulomb’s law: acetylation of ALS-linked SOD1 by aspirin impedes the nucleation, propagation and thermostability of fibrils	11
Abstract.....	11

Introduction	12
Materials and Methods	15
Results and Discussion	20
“Drugging Z”	43
Acknowledgments	45
 CHAPTER THREE.....	 46
Stochastic formation of fibrillar and amorphous SOD1 oligomers linked to amyotrophic lateral sclerosis	46
Abstract.....	46
Introduction.....	47
Results and Discussion	49
Conclusion	71
Materials and Methods	72
Acknowledgments	74
 CHAPTER FOUR.....	 75
Kaplan–Meier Meets Chemical Kinetics: Intrinsic Rate of SOD1 Amyloidogenesis Decreased by Subset of ALS Mutations and Cannot Fully Explain Age of Disease Onset.....	75
Abstract.....	75
Introduction.....	76
Results and Discussion	79
Conclusion	96
Materials and Methods	99

Acknowledgments	103
CHAPTER FIVE.....	104
How do gyrating beads accelerate amyloid fibrillization?	104
Abstract	104
Introduction	105
Materials and Methods	108
Results and Discussion	111
Conclusion	134
Acknowledgments	135
CHAPTER SIX.....	136
Metal-ion-specific screening of charge effects in protein amide H/D exchange and the Hofmeister series.....	136
Abstract	136
Introduction	137
Materials and Methods	140
Results and Discussion	141
Conclusion	157
Acknowledgments	158

CHAPTER SEVEN.....	159
Colorimetric and longitudinal analysis of leukocoria in recreational photographs of children with retinoblastoma	159
Abstract.....	159
Introduction.....	160
Methods	163
Results and Discussion	168
Conclusion	194
Acknowledgments	196
CHAPTER EIGHT.....	197
Supporting Information	197
Arresting Amyloid with Coulomb’s Law: Acetylation of ALS-Linked SOD1 by Aspirin Impedes Aggregation	197
Stochastic formation of fibrillar and amorphous SOD1 oligomers linked to amyotrophic lateral sclerosis.....	229
Kaplan–Meier Meets Chemical Kinetics: Intrinsic Rate of SOD1 Amyloidogenesis Decreased by Subset of ALS Mutations and Cannot Fully Explain Age of Disease Onset.....	243
How do gyrating beads accelerate amyloid fibrillization?	248
Metal-ion-specific screening of charge effects in protein amide H/D exchange and the Hofmeister series.....	252
REFERENCES.....	261

LIST OF FIGURES

Figure 1.1 Schematic representation of mechanism of fibrillization of an amyloidogenic protein.....	2
Figure 1.2 Mechanism of toxicity of protein fibrils.	4
Figure 1.3 (A) Crystal structure of human SOD1 dimer (PDB ID: 2C9V). Copper and zinc atoms are shown with orange and violet spheres, respectively. (B) Structure of human SOD1 active site.	6
Figure 2.1 Chemically boosting the net charge (Z) of SOD1	16
Figure 2.2 Acetylation of multiple lysines in WT and ALS-variant apo-SOD1 by aspirin	23
Figure 2.3 Fibrillization of unacetylated (top) and acetylated (bottom) apo-SOD1 (0 mM NaCl) as measured by thioflavin-T fluorescence in a 96-well microplate	26
Figure 2.4 Effect of lysine acetylation on the rate of fibrillization of WT and ALS-variant apo-SOD1 in 0 mM NaCl	27
Figure 2.5 Effect of lysine acetylation on the rate of fibrillization of WT and ALS-variant apo-SOD1 in 100 mM NaCl.....	35
Figure 2.6 Effect of peracetylation of lysine in fibrillar WT and ALS-variant apo-SOD1 on fibril thermostability (i.e., acetylation after fibrillization)	42
Figure 3.1 In vitro fibrillization of apo-SOD1 in microplate-based ThT fluorescence assays.....	53
Figure 3.2 Increasing the degree of disulfide reduction from 30 % to 90 % does not eliminate the stochasticity of apo-SOD1 fibrillization in microplate-based ThT fluorescence assays.....	54
Figure 3.3 Alteration of experimental conditions (SOD1 concentration, gyration rate, and temperature) to mimic possible well-to-well variations in reaction conditions during microplate-based ThT assays of apo-SOD1 fibrillization..	57

Figure 3.4 Stochastic fibrillization of apo-SOD1 in microplate ThT assays is not an artifact of surface features in a microplate well (or bead), and is not caused by dust contamination from laboratory environment	58
Figure 3.5 Projection plot of maximal ThT fluorescence, lag time, and propagation rate constant of apo-SOD1 fibrillization derived from all 1132 ThT assays of WT and mutant proteins collected under all reaction conditions in this chapter.....	59
Figure 3.6 Comparison of oligomer morphology from replicate wells containing identical solutions of apo-SOD1	61
Figure 3.7 Distinct populations (microplate wells) of SOD1 stochastically diverge between exponential amorphous aggregation and sigmoidal amorphous/fibrillar aggregation according to DLS, TEM, and ANS fluorescence	65
Figure 3.8 Formation of small oligomers and amorphous species of apo-SOD1 is non-uniformly accelerated by ALS mutation	68
Figure 3.9 Noise (variability) associated with SOD1 oligomer nucleation is increased by ALS mutations	69
Figure 4.1 Biophysical characterization of apo-SOD1 proteins	82
Figure 4.2 Stochastic fibrillization of WT and ALS variant apo-SOD1	84
Figure 4.3 Kaplan-Meier analysis of stochastic <i>in vitro</i> apo-SOD1 fibrillization and comparison with clinical phenotypes	87
Figure 4.4 ALS-linked mutations in SOD1 do not uniformly accelerate fibril nucleation (at pH 7.4, 37 °C) but do uniformly accelerate fibril elongation (with the exception of H46R apo-SOD1).....	89
Figure 4.5 Fluorescence intensity of immature ThT-positive apo-SOD1 oligomers correlates with patient survivability and aggregation propensity in cultured cells.....	94
Figure 5.1 Chemistry and surface features of beads used in amyloid assays	113
Figure 5.2 Replicate ThT fluorescence amyloid assays for D90A apo-SOD1 in the absence and presence of beads with varying chemical and physical properties. The range in variation of lag time ($\Delta\tau$) is indicated with numbers above each arrow	114

Figure 5.3 Kinetics of fibrillization of apo-SOD1 vary with bead type	115
Figure 5.4 (A) Correlation between lag time of D90A apo-SOD1 fibrillization and bead mass. Blue dashed line indicates the best fit to the linear portion of the plot (non-polymeric beads). (B) Moderate linear correlation between rate of propagation of D90A SOD1 oligomers and bead mass. PP: Polypropylene; Del: Delrin; Acr: acrylic; Tor: Torlon; SiN: Silicon nitride ceramic; Al ₂ O ₃ : Alumina ceramic	118
Figure 5.5 Residual angular momentum of heavier beads cannot explain why mass of bead affects amyloid formation	121
Figure 5.6 Contact mechanics between beads and microplate surface can explain kinetics of amyloid nucleation and propagation	125
Figure 5.7 Surface adhesion and hydrophobicity can explain kinetic variation among polymeric beads, but not non-polymeric (ceramic, metallic, glass) beads ...	128
Figure 5.8 Heavier beads promote shorter SOD1 fibrils	129
Figure 5.9 Effect of scratching the surface of beads on rate and morphology of fibrillization	131
Figure 6.1 (A) Electrospray-ionization mass spectrum and capillary electropherogram of Lys-acetyl “protein charge ladder” of myoglobin (Mb) prepared by the acetylation of surface Lys- ϵ -NH ₃ ⁺ with acetic anhydride	142
Figure 6.2 Amide H/D exchange of the Mb-Lys-Ac(N) charge ladder at pH _{read} 7.4 without salt, i.e., I < 0.1 M	144
Figure 6.3 Amide H/D exchange of a Mb-Lys-Ac(N) charge ladder in the presence of 1 M metal chloride salts (Na ⁺ , K ⁺ , Li ⁺ , Mg ²⁺ , and Ca ²⁺)	150
Figure 6.4 (A) Traces of each exponential fit of the plot of $\partial H_{\text{uex}}/\partial N$ versus time for the Mb-Ac(N) charge ladder in the presence of each metal chloride (1 M). (B) Plot of shielding decay constant (ϕ) for each cation as a function of the cation’s charge density. (C) Plot of shielding decay constant (ϕ) for each cation as a function of its free energy of hydration.....	155
Figure 7.1 (A) The reflection of visible light by an intraocular Rb tumor can cause the pupil to appear white during photography; an increase in the size of a tumor will generally increase the number of photographic angles that will produce leukocoria during recreational photography. (B) An example of a leukocoric picture from a set of 7377 pictures of a patient with bilateral Rb. Images of Patient Zero were donated by his parents	169

Figure 7.2 (A) Longitudinal frequency of photography of “Patient Zero” by parents over a three year period (i.e., from birth to 3 years old; 7377 photographs). (B) The majority of leukocoric pictures (~ 80 %) were collected with this compact 7.1 megapixel Canon PowerShot SD750 camera. (C) Digital picture of Patient Zero (i.e., child on left, exhibiting leukocoria in left eye) and a healthy playmate (i.e., child on right, exhibiting a red reflex in both eyes). (D) Example of a digital picture of Patient Zero; right eye exhibited leukocoria, and the left eye exhibited a red reflex. Photographs in C&D were taken with Canon Power Shot SD750. Permission to include images of the healthy control child was granted by both parents.....	171
Figure 7.3 Examples of cropped leukocoric and non-leukocoric pupils from a set of 7377 pictures of Patient Zero and control children, photographed alongside patient	173
Figure 7.4 Comparison of frequency of leukocoria with age of Patient Zero and timeline of treatment	174
Figure 7.5 Quantification of Saturation and Value of right and left leukocoric pupils of Patient Zero, and 19 healthy control children	176
Figure 7.6 Quantification of Hue and Value of right and left leukocoric pupils of Patient Zero	178
Figure 7.7 A comparison of clinical images of the left retina of Patient Zero collected with fundus photography and leukocoria in left pupil	183
Figure 7.8 Longitudinal plot of HSV quantities of leukocoria in Patient Zero and treatment timeline listed at right	184
Figure 7.9 Examples of “pseudo-leukocoria” (bilateral or unilateral) in a healthy adult without any known eye disease.....	189
Figure 7.10 Sectioning the Saturation-Value plane of HSV color space into a useful scale for classifying pupillary reflexes in recreational photographs, and plot showing the average Hue of cropped pupils from panel	192
Figure 8.1 Sigmoidal curve used to fit fibrillization kinetics of apo-SOD1 protein variants as measured by an increase in thioflavin-T (ThT) fluorescence at 485 nm.....	207
Figure 8.2 Aspirin acetylates lysine residues in WT and ALS-variant apo-SOD1.....	208
Figure 8.3 Three dimensional structure and amino acid sequence of human SOD1	209

Figure 8.4 High concentration of aspirin can acetylate serine and threonine residues in A4V apo-SOD1.....	210
Figure 8.5 Relative concentration of each acetyl derivative in solutions of D90A and A4V apo-SOD1 that were acetylated with aspirin before fibrillization	210
Figure 8.6 Fibrillization of unacetylated and acetylated WT apo-SOD1 as measured by thioflavin-T fluorescence in a 96-well microplate in 0 mM NaCl.....	211
Figure 8.7 Fibrillization of unacetylated and acetylated WT apo-SOD1 as measured by thioflavin-T fluorescence in a 96-well microplate in 100 mM NaCl.....	212
Figure 8.8 Fibrillization of unacetylated and acetylated D90A apo-SOD1 as measured by thioflavin-T fluorescence in a 96-well microplate in 0 mM NaCl	213
Figure 8.9 Fibrillization of unacetylated and acetylated D90A apo-SOD1 as measured by thioflavin-T fluorescence in a 96-well microplate in 100 mM NaCl	214
Figure 8.10 Fibrillization of unacetylated and acetylated A4V apo-SOD1 as measured by thioflavin-T fluorescence in a 96-well microplate in 0 mM NaCl.....	215
Figure 8.11 Fibrillization of unacetylated and acetylated A4V apo-SOD1 as measured by thioflavin-T fluorescence in a 96-well microplate in 100 mM NaCl	216
Figure 8.12 Statistical comparison of mean lag time and mean inverse propagation constant (from Table 2.1) for fibrillization of unacetylated and acetylated apo-SOD1 proteins in 0 mM NaCl	217
Figure 8.13 Statistical comparison of mean lag time and mean inverse propagation constant (from Table 2.1) for fibrillization of unacetylated and acetylated apo-SOD1 proteins in 100 mM NaCl	218
Figure 8.14 Differential scanning calorimetry and H/D exchange of unacetylated and acetylated apo-SOD1 proteins	219
Figure 8.15 Effect of lysine acetylation in native apo-SOD1 on thermostability of resulting amyloid fibrils (i.e., acetylation before fibrillization)	220
Figure 8.16 Characterization of state of oligomerization of WT and ALS-linked apo-SOD1 after thermal defibrillization of amyloid fibrils of apo-SOD1	221

Figure 8.17 MS/MS spectra of tryptic SOD1 peptides from WT apo-SOD1 fibrils that were acetylated with aspirin after fibrillization	222
Figure 8.18 (A) Chemical anatomy of a prototype “charge boosting” drug that contains a “head” that either binds to a native protein or partitions to an amyloid-like oligomer, and an acylating “tail” that modifies nearby lysine residues. (B) The “head” does not become covalently attached to the protein, and can be displaced over time to allow for the binding and reaction of additional “charge boosters”	223
Figure 8.19 Differential scanning (DSC) thermograms and size-exclusion chromatograms of (a) apo-SOD1 ^{30%2SH} and (b) apo-SOD1 ^{90%2SH} after incubation in 10 and 100 mM TCEP for 6 hr, respectively	233
Figure 8.20 Sigmoidal fits of ThT fluorescence of replicate assays of A4V and D90A apo-SOD1 ^{30%2SH}	234
Figure 8.21 Sigmoidal fits of ThT fluorescence of replicate assays of A4V and D90A apo-SOD1 ^{90%2SH}	235
Figure 8.22 Average rate of nucleation and propagation of D90A apo-SOD1 ^{30%2SH} decreases linearly with increasing gyration speed	236
Figure 8.23 Fit traces of all replicates of ThT aggregation assays for A4V apo-SOD1 ^{90%2SH} in 100 mM TCEP at (a) T = 20 °C, (b) 25 °C, and (c) 30 °C (n _{total} = 102). Insets show the histograms of lag time and inverse propagation rate in each temperature. (d) Temperature-dependent range of lag time ($\Delta\tau$), i.e., the difference between maximum and minimum lag times (outlier replicates) in a single kinetic assay of A4V apo-SOD1 ^{90%2SH} . Histograms in (a-c) were fit with a 3-parameter log-normal function (Equation 8.8a).....	236
Figure 8.24 Noise plots of (a) D90A apo-SOD1 ^{30%2SH} during ThT assays at different shaking speeds, (b) ThT assays of A4V apo-SOD1 ^{90%2SH} at different temperatures, and (c) ThT assays of D90A apo-SOD1 ^{30%2SH} at different monomer concentrations	237
Figure 8.25 Plots of ANS fluorescence for (a) E100K, and (b) D90A apo-SOD1 ^{90%2SH} (n _{total} = 44).....	238
Figure 8.26 Selected replicate aggregation assays (as measured by DLS) for WT and three ALS-variant apo-SOD1 ^{90%2SH} proteins show a high degree of stochasticity among different replicates.....	239

Figure 8.27 Histogram of age of disease onset for ALS patients with L144F <i>SOD1</i> mutation (n = 30) shows a log-normal distribution (fit with a 3-parameter log-normal function, Equation 8.8a).....	240
Figure 8.28 (a) DSC thermograms of fully disulfide oxidized (black) and partially reduced (red) WT apo-SOD1. (b) Size exclusion chromatogram of partially reduced WT apo-SOD1	244
Figure 8.29 Correlation between mean lag times of apo-SOD1 fibrillization and Hazard ratios of apo-SOD1 fibrillization	244
Figure 8.30 Correlations between mean lag time and propagation rate of <i>in vitro</i> apo-SOD1 fibrillization and clinical phenotypes of ALS patients	245
Figure 8.31 Correlation plots of thermostability of ALS variants of apo-SOD1, fibrillization rates, and clinical phenotypes.....	246
Figure 8.32 Rate of ALS mutant apo-SOD1 fibrillization remains equal to or slower than WT apo-SOD1 fibrillization under different experimental conditions .	247
Figure 8.33 Histograms of lag time of D90A apo-SOD1 aggregation in the presence of different bead types.....	248
Figure 8.34 Transmission electron micrographs of D90A apo-SOD1 aggregates in the presence of different beads	249
Figure 8.35 Correlation plots of bead surface roughness vs. (A) lag time, and (B) propagation rate of apo-SOD1 aggregation.....	250
Figure 8.36 Amide H/D exchange of Mb-Lys-Ac(N) charge ladder measured at different pH with mass spectrometry	255
Figure 8.37 Amide H/D exchange for all 19 rungs of the Mb charge ladder in the (A) absence and (B) presence of 1 M NaCl; pD = 7.8.....	256
Figure 8.38 UV-Vis spectra of Mb-Ac(0) and Mb-Ac(~16)	257
Figure 8.39 (A) Differential scanning calorimetry of unacetylated and acetylated (i.e., Ac(~16)) Mb in the presence of 0 M, 200 mM, and 1 M CaCl ₂ . (B) Plot of T _m values of unacetylated and acetylated Mb as a function of CaCl ₂ concentration	258

Figure 8.40 (A) Amide H/D exchange of Mb-Lys-Ac(N) charge ladder at diminishing concentrations of $MgCl_2$. Error bars represent standard deviation from three separate measurements. (B) Partial derivatives of plots in part (A); error bars represent the standard deviation of three separate runs. (C) Plots of partial derivative as a function of time; in each panel, solid line represents partial derivative of Mb-Lys-Ac(N) charge ladder in 0 mM Mg^{2+} shown for reference 259

Figure 8.41 (A) Amide H/D exchange of Mb-Lys-Ac(N) charge ladder at diminishing concentrations of Ca^{2+} . Error bars represent standard deviation from three separate measurements. (B) Partial derivatives of plots in part (A); error bars represent the standard deviation of three separate runs. (C) Plots of partial derivative as a function of time; solid line in each panel represents partial derivative of Mb-Lys-Ac(N) charge ladder in 0 mM Ca^{2+} shown as reference 260

LIST OF TABLES

Table 2.1 Rate of nucleation and propagation of amyloid fibrils of WT and ALS-variant apo-SOD1 as a function of lysine acetylation, Ac(N)	28
Table 4.1 Thermostability and metal content of apo-SOD1 proteins	81
Table 4.2 Kinetic parameters of <i>in vitro</i> apo-SOD1 fibrillization (10 mM TCEP, 37 °C, pH 7.4) and corresponding patient Hazard ratios	88
Table 5.1 Physical and chemical properties of beads used in this chapter	117
Table 6.1 Electrostatic HDX screening constants for cations in the Hofmeister series.	146
Table 7.1 Mean HSV Quantities of Leukocoria in “Patient Zero” and Control Pupils Over 3 Years	179
Table 7.2 HSV Properties of Leukocoric Pupils in “Patient Zero” During Three Periods of Treatment	185
Table 7.3 Mean Colorimetric Properties Calculated From Images Containing Leukocoric and Healthy Control Pupils and Cropped by Two Different Researchers	187
Table 8.1 Results of tandem mass spectrometry of trypsin and pepsin digests of WT and ALS-variant apo-SOD1 at varying degrees of acetylation	224
Table 8.2 Average kinetic parameters of ThT aggregation assays for acetylated and unacetylated WT SOD1, in 0 mM and 100 mM NaCl	225
Table 8.3 Average kinetic parameters of ThT aggregation assays for acetylated and unacetylated D90A apo-SOD1, in 0 mM and 100 mM NaCl	226
Table 8.4 Average kinetic parameters of ThT aggregation assays for acetylated and unacetylated A4V SOD1, in 0 mM and 100 mM NaCl	227
Table 8.5 Thermostability of native and amyloid WT and ALS-variant apo-SOD1 as a function of lysine acetylation.....	228
Table 8.6 Metal content of WT and ALS-variant apo-SOD1 proteins before initiating the aggregation assay measured with ICP-MS	240

Table 8.7 Kinetic parameters of fibrillization of WT and ALS-variant apo-SOD1 ^{30%2SH} and apo-SOD1 ^{90%2SH} in 150 mM NaCl	241
Table 8.8 Kinetic parameters of aggregation of WT and ALS-variant apo-SOD1 ^{90%2SH} in 150 mM NaCl measured with ANS fluorescence	242
Table 8.9 Physicomechanical properties of all studied beads in chapter 5	251

LIST OF SCHEMES

Scheme 6.1 Mechanism of base catalyzed amide H/D exchange	138
---	-----

ACKNOWLEDGMENTS

To my love and my best friend, my wife Sanaz: because I owe it all to you!

To my advisor, Prof. Bryan Shaw; the most genius, most hard working, and the kindest person I have ever met in my life. Bryan, you taught me how to think, how to be a keeper, and most importantly, how to be a good scientist. I will always miss our interesting and long-lasting chats. I will never forget those long, brainstorming walks around the campus. I will miss your screams of joy whenever a significant moment was reached. It was a blessing to be your student.

I am grateful to my mother, father, and my sister, who have provided me through moral and emotional support in my life. I am also grateful to my other family members and friends who have supported me along the way.

With a special mention to all my friends and colleagues; Keats, Corbin, Devon, Lindsay, Aleks, Collin, Aaron, Jennifer, Nick, Richard (Dr. Mowery), and Mark. I hope I have not missed anyone. It was fantastic to have the opportunity to work with you! What a nice and cracking place to work!

I am also grateful to all the faculty members and staff of Department of Chemistry and Biochemistry, specially Prof. Sung Joon Kim, Prof. Mary Lynn Trawick, Prof. Charles Garner, Prof. Kevin Shuford, and Prof. Patrick Farmer.

Thanks for all your encouragement!

CHAPTER ONE

Mechanism of Protein Aggregation in Neurodegenerative Diseases: The Case of Cu, Zn Superoxide Dismutase Aggregation in Amyotrophic Lateral Sclerosis

Introduction

Protein Misfolding and Aggregation in Neurodegenerative Diseases:

Neurodegeneration is defined as the progressive and gradual dysfunctioning of nervous system, which ultimately leads to death of neurons. The reasons underlying neurodegeneration are not fully understood, but generally involve genetic and environmental (sporadic) factors.¹⁻² There are different classes of neurodegenerative diseases that target both central nervous system (CNS) and peripheral nervous system (PNS) such as Alzheimer's disease, amyotrophic lateral sclerosis (ALS or Lou Gehrig's disease), Parkinson's disease, and multiple sclerosis (MS). Together, these diseases affect tens of thousands of people worldwide every year, and the medical costs associated with them are extremely high. For example, by 2017, ~ 5 million Americans suffer from Alzheimer's disease; 1 million from Parkinson's disease; 400,000 from multiple sclerosis (MS); 30,000 from amyotrophic lateral sclerosis (ALS or Lou Gehrig's disease), and 30,000 from Huntington's disease.³

Many neurodegenerative diseases are classified as protheopathies, where the misfolding and subsequent aggregation of a protein leads to neuron death and neurodegeneration, which is historically known as the amyloid hypothesis.⁴ Prominent examples include the aggregation of amyloid beta protein ($A\beta_{1-40}$ and $A\beta_{1-42}$) and tau

protein in Alzheimer’s disease,⁵ aggregation of SOD1 in ALS,⁶⁻⁷ and aggregation of α -synuclein in Parkinson’s disease.⁸ Despite being different in biophysical and biochemical properties, almost all amyloidogenic proteins share two major aspects: (i) the mechanism of their aggregation *in vitro* and *in vivo*, and (ii) the structure of their final aggregates. The mechanism of aggregation of amyloidogenic proteins has been extensively studied both *in vitro* and *in vivo*. It involves three major steps including nucleation, elongation or propagation, and termination (Figure 1.1).

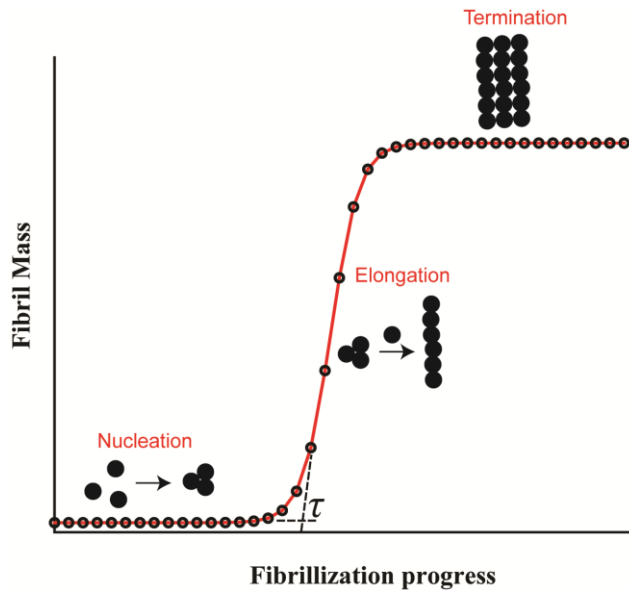


Figure 1.1 Schematic representation of mechanism of fibrillization of an amyloidogenic protein. The time required for the formation of “critical nucleus” is known as fibrillization lag time (τ). Each black circle illustrates monomeric protein.

The nucleation step (also known as “primary nucleation”⁹) involves the formation of a “critical nucleus” that comprises of certain number of misfolded, monomeric polypeptide units.¹⁰ The exact size or morphology of “critical nucleus” has not been determined for any protein, and might be as small as dimeric protein. The elongation

(propagation) involves the formation of oligomeric protofibrils upon the addition of monomeric polypeptides to critical nucleus. It has recently been shown that the major mechanism in elongation of protein oligomers/protofibrils is the continuous and dynamic fragmentation of oligomers into smaller species that can seed the oligomerization of free monomeric polypeptides.⁹ This process is known as “secondary nucleation”, and is believed to be the predominant mechanism underlying the formation of toxic oligomers, rather than “primary nucleation” events.⁹ The termination step is accompanied with the formation of mature, micrometer-sized protein fibrils that reach the thermodynamic equilibrium and would not elongate (plateau of sigmoid in Figure 1.1).

The final, mature fibrils share a common class of structures amongst all amyloidogenic proteins.¹¹ When studied with X-ray crystallography, these fibrils show a cross- β diffraction pattern (i.e., β -strands) with two characteristic reflections: 4.7 Å, along the main axis of fibril (i.e., inter-strand hydrogen bonding), and another reflection at ~ 11 Å, perpendicular to the fibril axis (i.e., inter-sheet hydrogen bonding).¹²

The β -sheets that form the main scaffold of amyloid fibrils are connected through the interaction of their hydrophobic amino acid residues. These structural motifs are known as “steric zippers”, and were first characterized by David S. Eisenberg’s group.¹³ So far, eight distinct classes of steric zippers have been discovered via studying the X-ray crystal structure of different small amyloidogenic proteins,¹³⁻¹⁴ including fibrillizing segments of SOD1.¹⁵⁻¹⁶

In addition to fibrillar aggregates, other morphologies of protein aggregates have been found both *in vitro* and *in vivo*.¹⁷⁻¹⁸ These morphologies include amorphous aggregates, and crystal-like or glass-like aggregates.¹⁸⁻¹⁹

The toxicity of protein fibrils in neurodegeneration is attributed to two major factors: (i) insoluble, large fibrils can destroy regular functions inside a cell such as axonal transport,²⁰ or via rupturing cell membranes;²¹ and (ii) through prion-like propagation of small, soluble oligomers/protofibrils into healthy cells (via exo- and endocytosis processes) and seeding the aggregation of folded proteins.²²⁻²³ Based on these mechanisms (Figure 1.2) and data obtained from cell viability studies,²⁴⁻²⁵ it is currently widely accepted that mature protein fibrils are the least toxic species, whereas small, soluble oligomers are the most toxic amyloid species. This notion has revolutionized the drug design strategies, so that most of these strategies are focused on targeting small oligomers instead of mature protein fibrils.²⁵

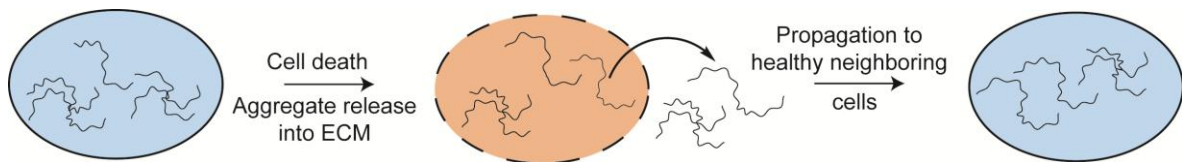


Figure 1.2 Mechanism of toxicity of protein fibrils. Cell death is a result of either interruption of function of different cell organelles or disruption of cell membrane. ECM: extracellular matrix.

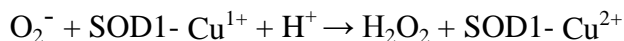
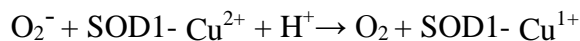
SOD1 and ALS

Amyotrophic lateral sclerosis (ALS; or Lou Gehrig's disease) is a progressive and fatal neurodegenerative disease caused by the selective death of motor neurons. ALS affects as many as 30,000 people in the United States, with 5,000 new cases diagnosed each year (that is 15 new cases every day). Estimates suggest that ALS is responsible for as many as five of every 100,000 deaths in people aged 20 or older. The annual cost of

ALS in the United States is ~ 64,000 dollars per-patient, and the total national cost is 256-433 million dollars. Aggregation of several proteins have been linked to ALS, including SOD1, FUS, TDP-43, OPTN, UBQLN2 and the translational product of intronic repeats in the gene C9ORF72.⁶ Mutations in the genes encoding these proteins comprise ~ 10 % of the cases of ALS (i.e., familial ALS or fALS). Approximately 90 % of ALS cases are non-genetic (i.e., sporadic ALS or sALS), where aggregation of wild-type protein (for some unknown reason) leads to neurodegeneration and ALS symptoms.⁶

In this dissertation, I have focused on studying and investigating the detailed mechanism(s) of WT and mutant SOD1 aggregation in both fALS and sALS. I chose to work on SOD1, because it is one of the most well characterized proteins in biochemistry, and a plethora of biophysical and biochemical information is available for this protein. Human SOD1 is a 32-kDa homodimeric protein that is present in the cytoplasm of almost all living cells. Each subunit consists of (i) eight β -strands, which form two anti-parallel β -barrel sheets, and (ii) one disulfide bond between Cys57 and Cys146 residues (Figure 1.3A).²⁶ Each subunit (i.e., monomer) also binds one copper ion (through copper chaperone for SOD1, CCS protein) and one zinc ion (the pathway through which zinc binds SOD1 is unknown) that coordinate to a negatively charged histidine residue (H63; Figure 1.3B).²⁶

The SOD1 enzyme catalyzes the disproportionation (dismutation) of superoxide anion, a dangerous reactive oxygen species (ROS), to oxygen and hydrogen peroxide. The dismutation reaction is catalyzed via redox cycling of copper between Cu^{2+} and Cu^{1+} states, as shown below:²⁷



The catalytic activity of SOD1 is one of the highest in biochemistry with an apparent $k_{\text{cat}}/k_{\text{M}} \approx 7 \times 10^9 \text{ M}^{-1}\text{s}^{-1}$,²⁷ which passes the diffusion rate limit. One important step in SOD1 mechanism of O_2^- dismutation is the breakage of Cu-His63 bond and protonation of H63 residue. The real source of this added proton is not yet understood, and may be either the solvent or other neighboring residues. Zinc ions do not have any catalytic role in SOD1 enzymatic activity, and zinc coordination has been shown to be crucial for SOD1 dimer stability.²⁸

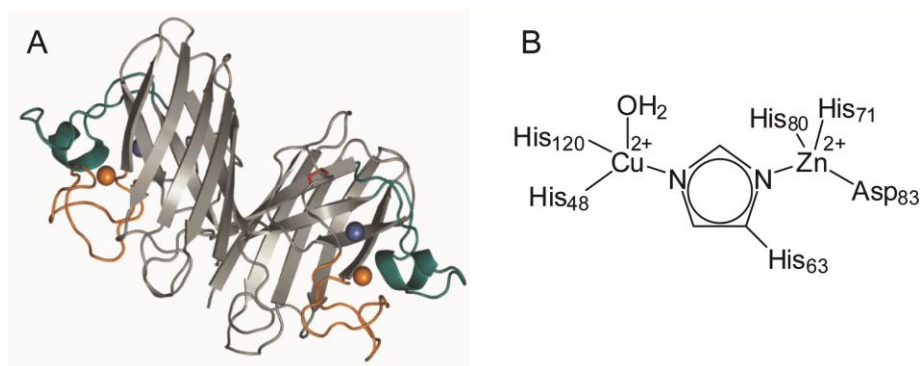


Figure 1.3 (A) Crystal structure of human SOD1 dimer (PDB ID: 2C9V).²⁷ Copper and zinc atoms are shown with orange and violet spheres, respectively. (B) Structure of human SOD1 active site.

The first report on the connection between misfolding and aggregation of mutant SOD1 proteins in familial cases of ALS was published in 1993.⁷ Since the first report, ~ 160 SOD1 mutations have been discovered to cause familial cases of ALS (<http://alsod.iop.kcl.ac.uk/>).²⁹ These mutations are spread throughout SOD1's structure

and have various effects on biophysical properties of SOD1. For example, some mutations decrease the stability of SOD1's tertiary structure such as A4V;³⁰ some mutations compromise the binding of SOD1 to Cu and Zn i.e., H46Q.³⁰ Most interestingly, there are mutations that do not alter any of the above-mentioned properties of SOD1 (i.e., show similar stability or metal affinity compared to WT SOD1 protein), but decrease the net electrostatic charge of SOD1 by one or two units. These mutations ("cryptic mutations") involve D90A, E100K, and D101N.³¹

It is well-established that mutations in SOD1 cause ALS through a "gain of toxic function" mechanism, that is the formation of amyloid fibrils of SOD1 that are toxic to healthy cells.³² This mechanism, which is proposed as opposed to the "loss of function" mechanism (which states that SOD1-linked ALS is caused mainly by lack of SOD1 enzymatic activity³³) is proposed based on the experimental findings that *sod*-knockout transgenic mice do not develop ALS symptoms, whereas overexpression of human SOD1 in transgenic mice result in ALS symptoms, including muscle weakness and hind limbs paralysis after several months.³⁴ Based on these findings, drug design strategies have almost entirely focused on battling SOD1 aggregates to inhibit their formation, or somehow, decrease their toxicity.

The Underrated Biophysical Factor Involved in Protein Aggregation: Protein Net Electrostatic Charge

Abnormalities in several biochemical and biophysical properties of a protein can lead to a higher propensity of aggregation. These properties include low structural stability,³⁵ high affinity to adopt β -sheet conformations and form hydrogen bonds,³⁶ low energy of folding,³⁷ and low net electrostatic charge.^{36,38-39} Among these

properties, net charge (Z) of a protein has been greatly overlooked, mostly because there are very few methods to accurately measure the net charge of a protein. The role of protein net charge in its propensity to aggregate becomes clear when considering that, in general, proteins possess a relatively small net charge. Using theoretical calculations of net charge of $\sim 15,000$ discrete polypeptides in Protein Data Bank (PDB), Felder et al. have shown that the net charge of most of proteins lies between -10 to +10, with a median of -3.⁴⁰ This study reveals that proteins, in general, are teetering on the brink of neutrality (i.e., $Z = 0$), which is equivalent to maximization of the propensity for precipitation (i.e., aggregation). Accordingly, strategies that aim to manipulate the net electrostatic charge of an amyloidogenic protein to inhibit its aggregation into amyloid do not seem to be far-fetched.

Targeting net electrostatic charge of SOD1 (a negatively charged protein with a net negative charge of $Z = -6.05$ per monomeric protein⁴¹) as a Druggable target to battle protein aggregation, a hypothesis that I will expand on and discuss in Chapter 2 of this dissertation, is a promising strategy because: (i) increasing net charge of SOD1 would push the protein away from neutrality and by definition would decrease its probability of aggregation; and (ii) increasing the net charge of SOD1 (either native or oligomeric) would increase its electrostatic repulsion with anionic cell membranes.⁴² Specifically, the latter strategy is very promising when considering that the prion-like, cell-to-cell propagation of SOD1 oligomers (Figure 1.2) has been recently shown to be a crucial pathway for SOD1 toxicity in ALS.⁴³⁻⁴⁴ This prion-like propagation occurs mainly through the interaction of SOD1 oligomers/fibrils with cellular membranes, via endocytosis, exocytosis, or pinocytosis processes.⁴⁴ Thus, inhibiting SOD1

oligomers/fibrils from interacting with cellular membranes via increasing electrostatic repulsion between SOD1 and cell membranes would hinder entrance of SOD1 oligomers into healthy cells, and thus inhibit its prion-like, toxic activity.

Statement of Contribution

I am more than grateful that I have been able to contribute to the publication of nine peer-reviewed publications under the supervision of Prof. Bryan F. Shaw, in seven of which I contributed as the first author. These comprise the chapters two through seven of this dissertation, and are as follows: (1) Arresting amyloid with Coulomb's law: acetylation of ALS-linked SOD1 by aspirin impedes aggregation; (2) Stochastic formation of fibrillar and amorphous superoxide dismutase oligomers linked to amyotrophic lateral sclerosis; (3) Kaplan–Meier meets chemical kinetics: intrinsic rate of SOD1 amyloidogenesis decreased by subset of ALS mutations and cannot fully explain age of disease onset; (4) How do gyrating beads accelerate amyloid fibrillization?; (5) Metal ion-specific screening of charge effects in protein amide H/D exchange follows the Hofmeister series; and (6) Colorimetric and longitudinal analysis of leukocoria in recreational photographs of children with retinoblastoma.

Dr. Yunhua Shi, Dr. Nicholas Rhodes, Dr. Nathan Cook, and Prof. Angel Martí contributed in performing experiments, data analysis, and writing of manuscript for the publication “Arresting amyloid with Coulomb's law: acetylation of ALS-linked SOD1 by aspirin impedes aggregation”. Dr. Yunhua Shi, Ms. Alexandra Chuprin, and Ms. Sanaz Rasouli contributed in conducting

experiments and analysis of data in the publication “Stochastic Formation of Fibrillar and Amorphous Superoxide Dismutase Oligomers Linked to Amyotrophic Lateral Sclerosis”. Ms. Sanaz Rasouli, Dr. Yunhua Shi, Mr. Corbin Croom, Mr. Amir Aliyan, and Prof. Angel Martí contributed in performing experiments, data analysis, and writing of manuscript “Kaplan–Meier Meets Chemical Kinetics: Intrinsic Rate of SOD1 Amyloidogenesis Decreased by Subset of ALS Mutations and Cannot Fully Explain Age of Disease Onset”. Dr. Yunhua Shi, Ms. Sanaz Rasouli, and Mr. Corbin Croom contributed in conducting experiments and analysis of data in the publication “How Do Gyration Beads Accelerate Amyloid Fibrillization?”. Ms. Jennifer Gober, Dr. Richard Mowery, and Dr. Yunhua Shi contributed in performing experiments, data analysis, and writing of manuscript for the publication “Metal Ion-Specific Screening of Charge Effects in Protein Amide H/D Exchange Follows the Hofmeister Series”. And finally, Mr. Brandon Taylor, Ms. Rebecca Holden, Ms. Elizabeth Shaw, Dr. Alex Kentsis, Dr. Carlos Rodriguez-Galindo, and Dr. Shizuo Mukai contributed in writing of “Colorimetric and Longitudinal Analysis of Leukocoria in Recreational Photographs of Children with Retinoblastoma”.

CHAPTER TWO

Arresting Amyloid with Coulomb's Law: Acetylation of ALS-Linked SOD1 by Aspirin Impedes the Nucleation, Propagation and Thermostability of Fibrils.

This chapter is published as:

Abdolvahabi A, Shi Y, Rhodes NR, Cook NP, Martí AA, Shaw BF (2015) Arresting amyloid with Coulomb's law: acetylation of ALS-linked SOD1 by aspirin impedes the nucleation, propagation and thermostability of fibrils. *Biophys. J.* **108**, 1199-1212.⁴⁵

Abstract

Although the magnitude of a protein's net charge (Z) can control its rate of self-assembly into amyloid, and its interactions with cellular membranes, the net charge of a protein is not viewed as a "druggable" parameter. In the study presented in this chapter, I have demonstrated that aspirin (the quintessential acylating pharmacoon) can inhibit the amyloidogenesis of SOD1 by increasing the intrinsic net negative charge of the polypeptide, i.e., by acetylation (neutralization) of multiple lysines. The protective effects of acetylation were diminished (but not abolished) in 100 mM NaCl and were statistically significant: a total of 432 thioflavin-T amyloid assays were performed for all proteins studied. The acetylation of as few as 3 lysines by aspirin in A4V apo-SOD1—a variant that causes familial amyotrophic lateral sclerosis (ALS)—delayed amyloid nucleation by 38 % and slowed amyloid propagation by two-fold. Lysines in WT and ALS-variant apo-SOD1 could also be peracetylated with aspirin after fibrillization, resulting in "supercharged" fibrils, with an increase in formal net charge of ~ 2 million units. Peracetylated SOD1 amyloid defibrillized at temperatures below unacetylated fibrils, and below the melting temperature of native $\text{Cu}_2, \text{Zn}_2\text{-SOD1}$ (e.g., fibril $T_m = 84.49$ °C for

acetylated D90A apo-SOD1 fibrils). Targeting the net charge of native or misfolded proteins with small molecules—analogueous to how an enzyme's K_m or V_{max} are medicinally targeted—holds promise as a new strategy in the design of therapies for diseases linked to protein self-assembly.

Introduction

Coulombic forces drive the intermolecular repulsion and attraction of protein molecules at distances up to 10 Å in physiological buffer and possibly longer if the interaction occurs across the hydrophobic interior of a protein or lipid bilayers.⁴⁶⁻⁴⁷ Although these far-reaching forces scale with each protein's magnitude of net positive or net negative charge (Z), the net charge of a protein has never been scrutinized as a medicinal target that can be permuted with a small molecule. Instead, small molecule drugs that target proteins are designed to affect other classical parameters such as K_m , V_{max} , K_d , and ΔG^\ddagger_{fold} , by the introduction of hydrophobic, dipolar, or H-bonding interactions.⁴⁸⁻⁵⁰ Developing drugs that can increase the magnitude of net charge of a protein—for example, making an anionic protein more anionic—and thereby control intermolecular interactions *electrostatically*, might be effective in combating diseases that are linked to protein self-assembly, such as amyotrophic lateral sclerosis (ALS).⁵¹ ALS, a currently untreatable and a fatal neurodegenerative disease is characterized by the selective, progressive death of motor neurons. More than 150 different mutations in the gene encoding SOD1 cause familial ALS by a gain of function mechanism.⁵¹ What this function might be is still unclear but one leading hypothesis suggests that SOD1 mutations cause ALS by accelerating the rate of self-assembly of SOD1 into oligomers

that are, for some unknown reason, toxic to motor neurons⁵¹ The self-assembly of wild-type (WT) SOD1 is also suspected to cause certain cases of sporadic (non-familial) ALS.⁵¹ The exact stoichiometry, morphology, and structure of neurotoxic SOD1 oligomers (assuming that such oligomers do cause ALS) have not been determined, although several studies point to amyloid-like SOD1 oligomers as toxic species.²⁵

In this chapter, I describe a first order proof of this “charge boosting” principle by demonstrating that lysine residues in WT and ALS-linked SOD1 can be acetylated with an aryl ester drug (acetylsalicylic acid; aspirin), both before and after the fibrillization of SOD1 into amyloid (Figure 2.1). I find that the nonspecific acetylation of as few as three lysines (out of 11) in a subunit of A4V apo-SOD1—a reaction that increases the magnitude of net negative charge of SOD1 (pI = 5.9)—delayed the nucleation of amyloid fibrillization by up to 5 hr and decreased the rate of fibril propagation by two-fold (Table 2.1). This diminished rate of nucleation is similar to, and the rate of propagation is slower than that of unacetylated WT apo-SOD1.

I chose acetylsalicylic acid in this proof of concept study because it acetylates lysine residues in multiple proteins *in vivo*⁵²⁻⁵³ (in addition to acetylating serine in its primary target, cyclooxygenase-1; COX1).⁵³ Aspirin was recently found to acetylate lysine and serine in 120 different proteins in cultured cells,⁵⁴ but its reaction with SOD1 has never been reported, either *in vivo* or *in vitro*. Aspirin also exhibits therapeutic effects in several diseases,⁵³ and has mysteriously beneficial effects in ALS-SOD1 transgenic mouse models.⁵⁵ The acetylation of lysine is a post-translational modification that is involved in controlling multiple cellular processes such as: cell signaling, nucleic acid binding, gene expression, protein-protein interactions, and enzymatic activity.⁵⁶

The “charge boosting” hypothesis was inspired, and is supported by: (i) the inverse correlation between the magnitude of a protein’s net charge and its rate of self-assembly into amyloid and non-amyloid aggregates⁵⁷⁻⁵⁸ (including the historical observation that proteins precipitate rapidly at their isoelectric point^{39,59}); (ii) the naturally small net charge of proteins (~ 80 % are predicted to have net charges between +10 and -10, with median $Z = -3$);⁴⁰ (iii) the observation that lysine acetylation can prevent protein precipitation by increasing net negative charge;^{31,60} (iv) observations that the permeability of a protein across glycated, anionic cellular membranes—a process that might be requisite for the cell-to-cell, prion-like propagation of aggregated SOD1⁴⁴—can be abolished by inverting the protein’s sign of net charge from positive to negative;⁴² and (v) the occurrence of “cryptic” ALS mutations in *sod1* (e.g., D90A, D101N, E100K, and N139K) that do not appear to alter the structure, stability, enzymatic activity, or metal binding properties of the SOD1 native state, but do neutralize its net negative charge.^{30,61} While these “cryptic” substitutions might promote aggregation by altering local patterns of net charge, their scattering across SOD1’s surface suggests that neutralizing the negative surface potential at multiple loci is sufficient to trigger ALS, or equally and alternately, that neutralizing the net negative charge of SOD1 is sufficient for pathogenesis.⁴¹

The use of a small molecule to increase the net charge of a folded protein is complicated by the absence of experimentally determined values of net charge for nearly all folded proteins. I estimate that the net charge of < 0.1 % of proteins in the Protein Data Bank have been measured, at $pI \neq pH$.^{41,62} Recently, my colleagues and I used “protein charge ladders” and capillary electrophoresis (CE) to show that the measured net

charge (denoted Z_{CE}) of WT and ALS-variant SOD1 can deviate (in sign and magnitude) from predicted values (denoted Z_{seq}) at certain metal stoichiometries and subcellular pH.⁶² At pH 7.4, the net charge of WT Cu_2, Zn_2 -SOD1 was $Z_{CE} = -7.37$ charge units per dimer ($Z_{seq} = -8.2$); the net charge of apo-SOD1 was $Z_{CE} = -12.13$ units per dimer ($Z_{seq} = -13.0$). At pH 5.0 (i.e., the pH of the lysosome, one of SOD1's subcellular loci⁶³), the net charge of WT Cu_2, Zn_2 -SOD1 was only $Z_{CE} = -3.7$ units per dimer, which is opposite in sign and 8 units more negative than the predicted value of $Z_{seq} = +4.0$.⁶² The net charge of WT apo-SOD1 could not be determined at pH 5, presumably because SOD1 approached $Z = 0$ and precipitated during CE.⁶² Nevertheless, the acetylation of a single lysine in a subunit of WT SOD1 is expected to increase its magnitude of net negative charge by ~ 15-50 % (per subunit), depending upon its state of metalation and subcellular locus (Figure 2.1A). The effects of lysine acetylation on certain ALS-variant SOD1 proteins (e.g., D90A, G93R, E100K) will be even larger, as these proteins teeter on the edge of electrostatic neutrality at physiological pH.⁴¹

Materials and Methods

Purification of WT and ALS-Variant Apo-SOD1:

Detailed descriptions of all experimental procedures can be found in chapter 8 of this dissertation. Briefly, human WT, D90A, and A4V SOD1 proteins were recombinantly expressed in *Saccharomyces cerevisiae*, purified, demetallated, and characterized as previously described.⁶² The absence of metals was confirmed after demetallation (and again after acetylation) with inductively coupled plasma mass spectrometry (ICP-MS), as previously described.⁶²

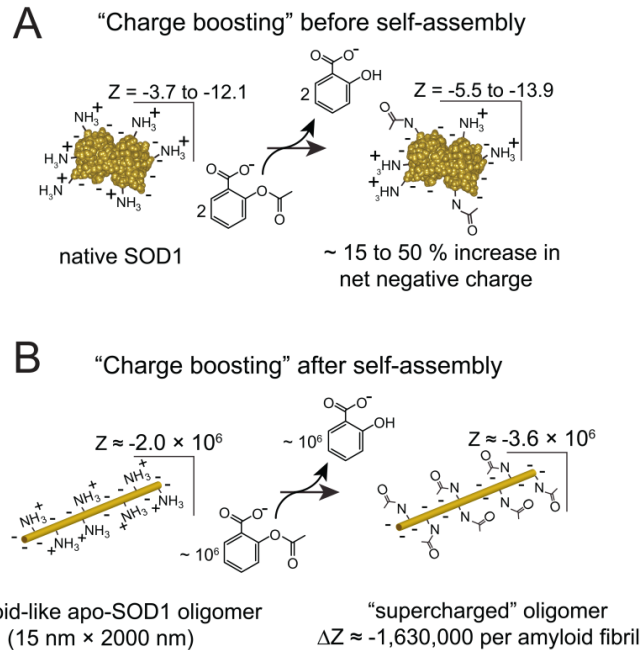


Figure 2.1 Chemically boosting the net charge (Z) of SOD1. The accumulation of acetyl modifications on native or oligomeric SOD1 by repeated doses of an acylating agent is plausible when considering the long lifetime of native SOD1 in motor neurons,⁶⁴ and the generally long lifetime of amyloid oligomers *in vivo*.⁶⁵⁻⁶⁶ (A) The net charge of dimeric WT SOD1 has been measured to vary from ~ -3.7 to ~ -12.1 , depending upon the metalation state and subcellular pH.⁶² Acetylation of lysine residues in native SOD1 will increase the magnitude of net negative charge by between 15 and 50 %, depending upon subcellular pH and metalation state. (B) Peracetylation of lysine residues in an amyloid fibril of SOD1 ($d = 15$ nm, $l = 2$ μ m) with aspirin is expected to increase the magnitude of net negative charge by $\sim 10^6$ formal units.

Acetylation of WT and ALS-Variant Apo-SOD1 with Aspirin:

Crystalline acetylsalicylic acid was purchased from Sigma-Aldrich® (purity > 99.0 %) and used for the acetylation of lysine residues in WT and ALS-variant apo-SOD1 (see Chapter 8 for additional details). All solutions and buffers were made with ultrapure metal-free water with a measured resistance of 18.2 M Ω /cm (dispensed through a Millipore MilliQ® system). All containers used for making buffers or other solutions were rinsed with 5 mM EDTA and ultrapure metal-free water prior to use. Peracetylated

apo-SOD1 fibrils were also prepared by adding crystalline acetylsalicylic acid to aqueous solutions of unacetylated amyloid fibrils of apo-SOD1. Reaction byproducts (acetic acid and salicylic acid) and unreacted aspirin were removed by centrifugation and the discarding of supernatant. An identical aliquot of unmodified fibrils was set aside and not reacted with aspirin and functioned as a negative control. The buffer in which fibrils were suspended was changed to 10 mM potassium phosphate, 5 mM EDTA, pH 7.4 (for thermal stability assays) via centrifugation, and removal of supernatant followed by addition of fresh buffer. After acetylation, all apo-SOD1 proteins were analyzed with ICP-MS to confirm the absence of metal ions.

Biophysical Characterization and Mass Spectrometric Analysis of Native and Fibrillar Apo-SOD1 Proteins:

Analysis of acetylated and unacetylated apo-SOD1 proteins with capillary electrophoresis, differential scanning calorimetry, transmission electron microscopy, mass spectrometry, and tandem mass spectrometry (MS/MS) was performed as previously described.^{64,67} MS/MS analysis was performed to characterize the types of acetyl-regioisomers that likely formed upon non-specific acetylation with aspirin. The effect of lysine acetylation on the structure of SOD1 proteins was also analyzed with amide H/D exchange and mass spectrometry, as previously described (see chapter 8 for additional details). Measuring H/D exchange with mass spectrometry allowed each acetyl derivative to be analyzed simultaneously under identical pH, and temperature, thus eliminating the sample-to-sample experimental variation that often occurs during H/D exchange-MS. To determine the identity of acetylated residues on fibrillar apo-SOD1,

LC-MS and MS/MS analysis was performed after fibril dissociation to monomeric SOD1. Fibrils were dissociated by incubation in 6.5 M guanidinium hydrochloride (Gdm-HCl), 20 mM dithiothreitol (DTT) at 50 °C for one hour. This thermo-chemical defibrillization protocol has been previously shown to be adequate for dissociating amyloid fibrils of apo-SOD1.⁶⁸

Fluorescent Kinetic Assays for Apo-SOD1 Proteins:

Thioflavin-T (ThT) fluorescence assays for apo-SOD1 fibrillization were performed in a sealed 96-well microplate as previously described.⁶⁴ To acquire statistically meaningful lag times and propagation rates, I performed 18 replicates of ThT assays for each of the three apo-SOD1 proteins and their four sets of acetylated derivatives, in the absence and presence of 100 mM NaCl, amassing a total of 432 separate assays. For any set of acetylated proteins, each of the 18 replicates was performed simultaneously in the same 96-well plate, on solutions of SOD1 taken from the same stock of acetylated or unacetylated SOD1. Prior to aggregation assays, solutions were filtered with a syringe filter (0.2 µm hydrophilic polypropylene, Acrodisc® Pall co., Port Washington, NY, USA) to remove any type of high molecular weight oligomers of apo-SOD1 (or other colloids) that might seed or catalyze fibrillization. The concentration and purity of apo-SOD1 was confirmed with reducing SDS-PAGE immediately prior to the initiation of each aggregation assay and at the completion of the assay. The volume of each well was also measured at the end of the assay (with a micropipette) to ensure that evaporation did not occur during the aggregation assay.

Thermal Stability Assays for Supercharged Fibrillar Apo-SOD1 Proteins:

The thermal stability of the unacetylated and acetylated apo-SOD1 fibrils was determined with a thermal defibrillization assay that was adapted from a previous study by Shamma et al.⁶⁹ Fibril homogenate from both acetylated and unacetylated fibrils of apo-SOD1 (in 10 mM potassium phosphate, 5 mM EDTA, pH 7.4) were aliquoted into ten different tubes that were each heated to a specific temperature between 40 °C to 130 °C. The temperature was raised at an average rate of 0.5-1.0 °C/min (similar to a typical heating rate during differential scanning calorimetry). To reach temperatures up to 100 °C, solutions were heated using a PCR machine (Mastercycler®, Eppendorf®, Hamburg, Germany). For temperatures above 100 °C, a heat block was used (VWR®, Radnor, PA, USA). To avoid solvent evaporation during heating above 100 °C, I used a pressurized external lid that was designed to cover the sample vials (that reached pressures of approximately 350 kPa). At each temperature, a tube of protein solution was cooled and centrifuged at $17,000 \times g$ (4 °C) for 30 minutes and the supernatants were analyzed with UV-Vis spectrophotometry (240-300 nm).

Thus, the thermal defibrillization of the fibrils was detected by the retention of soluble, non-sedimentable SOD1 in the supernatant. The same 4-parameter sigmoidal function that was fitted to the ThT fibrillization data (Equation 8.1) was fitted to the data points from the thermal defibrillization assays using SigmaPlot™, version 11.0 (Systat Software Inc., Chicago, IL, USA); see Figure 8.1.

The inflection point of the sigmoid, x_0 , was reported as the melting temperature (T_m) of the amyloid fibrils. The relative molecular weights of non-sedimentable species that might be left over from the thermal defibrillization assays—i.e., melted fibrils, which

still might exist as low molecular weight oligomers—were determined with size-exclusion liquid chromatography (SE-LC) and native PAGE. See chapter 8 for additional details.

Estimating the Net Charge of Fibrillar Apo-SOD1:

The magnitude by which peracetylation affected the net charge of apo-SOD1 fibrils was estimated by approximating the number of SOD1 chains in an average-sized SOD1 fibril, and assuming that each lysine acetylation increased the net negative charge of the polypeptide by 0.9 units (instead of 1.0 unit), because of charge regulation.⁴⁷ The number of SOD1 subunits in each fibril was approximated by estimating the molecular volume of misfolded SOD1 as described in chapter 8 of this dissertation (Supporting Information), based upon a spherical approximation.⁷⁰

Results and Discussion

Acetylation of Lysine in Dimeric WT and ALS-Variant Apo-SOD1 with Acetylsalicylic Acid:

Mass spectrometry and capillary electrophoresis showed that the reaction of 25-150 mM aspirin with native WT or ALS-variant apo-SOD1 resulted in chemical arrays of apo-SOD1 proteins with varying degrees of acetylation per monomer (denoted “Ac(~N)”, Figure 2.2 and Figure 8.2). These concentrations are considerably higher than peak concentrations of intact (unhydrolyzed) acetylsalicylic acid in human plasma, which reach 30-150 μ M (depending upon dosage); concentrations of salicylic acid reach as high as 2.5 mM.⁵³ The degree of acetylation for each mixture is expressed as the mean number of acetyl modifications in each mixture (per monomer), as measured by mass

spectrometry and capillary electrophoresis (Figure 2.2 and Figure 8.2). The mean number of acetylated lysines was determined from a Gaussian distribution of the MS charge ladders. Each acetylation is associated with a +42 Da increase in mass, Figure 2.2A-C. At 25 mM aspirin, approximately 1 lysine (mean) was acetylated in each WT apo-SOD1 monomer; 2 lysines per monomer in D90A; and 3 lysines per monomer in A4V apo-SOD1 (MS/MS sequencing is discussed below). At 150 mM aspirin, the mean acetylation observed for WT apo-SOD1 was 6 lysines per monomer; 5 lysines per monomer for D90A; and 9 lysines per monomer for A4V apo-SOD1 (Figure 2.2 and Table 8.1).

Each of these acetylated arrays (“charge ladders”) of WT and D90A apo-SOD1 were partially resolvable with capillary electrophoresis, wherein each acetylation increased the electrophoretic mobility, i.e., increased the net negative charge of SOD1 (Figure 8.2A-B). The capillary electropherogram of A4V apo-SOD1 exhibited poor resolution (Figure 8.2C), possibly due to its well-known dimer instability and dynamic structure.⁷¹ Proteolysis and MS/MS confirmed that each modification occurred on lysine; no other acetylated residues were detected in WT, D90A, or A4V apo-SOD1, with the following exception: in A4V apo-SOD1, I did detect (via MS/MS analysis) a small amount of acetylation on Thr-88 and Ser-105, but only at [aspirin] = 150 mM (Figure 8.4). I was not able to add sufficient aspirin to peracetylate any of the three SOD1 proteins because each protein began to precipitate after the addition of > 150 mM aspirin.

The acetylation of 9 lysines in WT and D90A apo-SOD1 was apparently nonspecific according to MS/MS (Table 8.1). For example, at least 9 out of 11 lysines were acetylated in WT or D90A apo-SOD1 regardless of the mean acetylation. Lys-3 and Lys-91, however, were not acetylated in WT and D90A apo-SOD1 at any concentration

of aspirin, except 150 mM aspirin, wherein Lys-91 was found to be acetylated in WT apo-SOD1 (Table 8.1). In contrast, the acetylation of all 11 lysines in A4V apo-SOD1 by aspirin was nonspecific. For example, a solution of A4V apo-SOD1 with a mean number of 3 acetylations per monomer was found with MS/MS to contain acetyl modifications on all 11 lysines (Table 8.1). See Chapter 8 for additional discussion of the MS/MS data. Thus, each “rung” in the charge ladder consisted of a mixture of regioisomers. If I assume that all 11 lysines in a monomeric SOD1 protein are equally reactive (which is unlikely, considering that each lysine likely has its own specific pK_a), then the maximum number of *statistically* possible regioisomers (r) can be expressed by $r = 11!/[N!(11-N)!]$, where N is the number of acetylated lysines for that particular rung. For example, $r = 11$ for Ac(1); $r = 55$ for Ac(2), and $r = 165$ for Ac(3). The actual number of regioisomers that exist in solution is likely to be lower than the statistically possible maximum because of the disparate reactivity of each lysine (i.e., the unique solvent accessibility or pK_a of each lysine), especially in the case of WT and D90A apo-SOD1 where Lys-3 and Lys-91 appear to be less reactive than the other 9 lysines (Figure 8.3 and Table 8.1).

The concentration of each rung could be approximated from its mass spectrum. For example, the A4V apo-SOD1-Ac(~3) protein consisted of: 3.6 % Ac(0), 10.9 % Ac(1), 19.5 % Ac(2), 22.6 % Ac(3), 16.8 % Ac(4), 16.7 % Ac(5), and 9.9 % Ac(6) (Figure 8.2C, red spectrum, and Figure 8.5C).

Aspirin Inhibits Amyloidogenesis of WT and ALS-Variant Apo-SOD1 by Acetylation of Lysine.

The rates of amyloid formation for WT, A4V, and D90A apo-SOD1 (acetylated and unacetylated forms) were measured under reducing conditions (10 mM TCEP) with a

thioflavin-T (ThT) fluorescence assay,⁷² in replicates of $n = 18$ for each derivative of each protein. The longitudinal plots of ThT fluorescence from each experiment exhibited a sigmoidal increase in fluorescence at 485 nm. A set of 18 of these raw, unnormalized sigmoids are shown, as an example, for WT-Ac(0) and WT-Ac(~6) (Figure 2.3). All other sets of sigmoidal plots for all three proteins (at different degrees of acetylation, with and without 100 mM NaCl) are presented in Figures 8.6 to 8.11. To increase visual clarity, each set of 18 replicate plots of ThT fluorescence were also averaged (combined) into a single sigmoid for each set of acetyl derivatives and are shown for all three SOD1 proteins in Figure 2.4A-C (0 mM NaCl) and Figure 2.5A-C (100 mM NaCl).

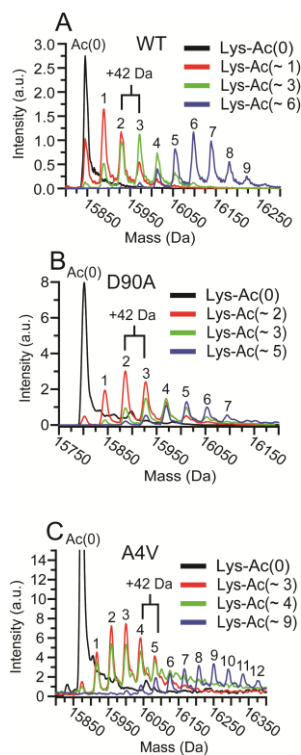


Figure 2.2 Acetylation of multiple lysines in WT and ALS-variant apo-SOD1 by aspirin. Electrospray ionization mass spectra of soluble (A) WT, (B) D90A, and (C) A4V apo-SOD1 after reaction with different concentrations of aspirin (in aqueous buffer). The mean number of acetylated lysines are denoted as “Lys-Ac(~N)”, and are listed per apo-SOD1 monomer.

The high number of replicate assays (i.e., a total of 432 amyloid assays) was necessary to acquire statistically significant fibrillization rates because the fibrillization of apo-SOD1 in the microplate-based ThT assay is apparently stochastic (as previously observed for unacetylated SOD1⁶⁴). By stochastic, I do not mean entirely random, but rather non-deterministic, i.e., that the measured rates of amyloid formation in each well will fall within some type of mathematical distribution (e.g., Gaussian or Lorentzian) wherein the mean or maximum of the distribution is the best expression of the “rate” of the process. Whether or not the nucleation of amyloid can occur through a stochastic mechanism is apparently controversial. Stochastic nucleation is nevertheless observed in other self-assembled systems, at all scales of size and complexity, from the crystallization of water,⁷³ to the cAMP-induced aggregation of social amoeba.⁷⁴ The nucleation of amyloid fibrils has been observed (and described) to be stochastic for proteins including $A\beta_{1-40}$, β_2 -microglobulin, and insulin.⁷⁵⁻⁷⁹ Even in reports that describe amyloid nucleation as a non-stochastic, deterministic process, these studies still report large, unexplained variations in lag times of replicate measurements (e.g., the lag time of nucleation of $A\beta_{1-42}$ varied by ~ 7 hr (i.e., between 17 to 24 hr) in replicate measurements made by Hellstrand and coworkers⁸⁰).

The rate of nucleation of amyloid fibrils is expressed as the lag time and the propagation of fibrils (elongation) is expressed as the inverse rate constant of propagation ($1/k$, i.e., the steepness of the sigmoid), as previously described (Table 2.1).⁶⁴ See Figure 8.1 for a graphical illustration of this parameterization. The lag time and inverse propagation constants in Table 2.1 are average values calculated from 18 individual fits of the 18 replicate amyloid assays. An unpaired Student’s t-test was used to verify the

statistical significance of any measured differences in the lag time and propagation rate for acetylated and unacetylated proteins (at a 95 % confidence interval). P-values are shown in Figures 8.11 and 8.12. Additional mathematical parameters from the sigmoidal fits of fluorescence data (i.e., a , x_0 , b , and x_0-2b from Equation 8.1, and R^2 values for fits) are also listed in Tables 8.2, 8.3, and 8.4.

I also experimented with calculating parameters such as lag time by first averaging all longitudinal fluorescence data into a single sigmoid and then performing a single non-linear regression analysis of the average sigmoid (wherein each point in the sigmoid contains its own error). This method produced similar average values of lag time compared to the above method, but with error values that were, in my opinion, unrealistically small (e.g., 10-fold smaller). For example, the average lag time for WT Ac(0) (0 mM NaCl) was calculated to be $t = 13.9 \pm 1.1$ hr when each sigmoid (data set) was analyzed individually with non-linear regression analysis (Table 2.1), compared to $t = 14.7 \pm 0.1$ hr when individual sigmoidal plots were averaged into a single sigmoid and analyzed with a single non-linear regression analysis. Thus, I chose to report lag times (in Table 2.1) as averages of 18 separate non-linear regression analyses for each derivative of each protein.

Many of the longitudinal plots of ThT fluorescence show a decrease in fluorescence after fibrillization is complete (Figures 8.6 to 8.11). This artifactual decrease has been previously observed⁶⁴ and was not included in sigmoidal fitting or the calculation of lag time and propagation rate. This decrease in fluorescence is likely caused by the adhesion of aggregated protein to the side of the polystyrene wells of the microplate, as inferred from visual inspection of each well at the end of the assay.

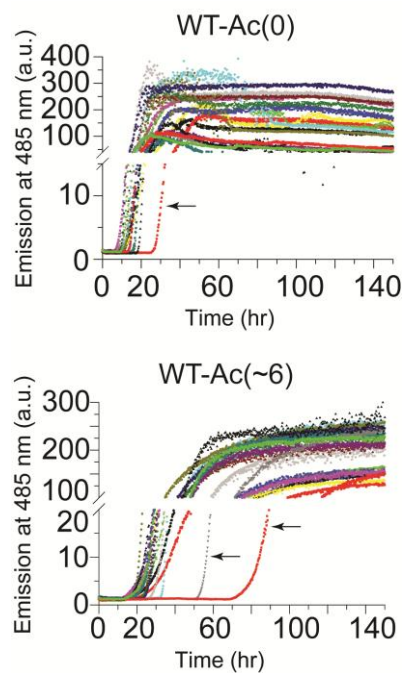


Figure 2.3 Fibrillization of unacetylated (top) and acetylated (bottom) apo-SOD1 (0 mM NaCl) as measured by thioflavin-T fluorescence in a 96-well microplate. Eighteen plots of thioflavin-T fluorescence from 18 replicate amyloid assays of WT apo-SOD1-Ac(0) (top) and WT apo-SOD1-Ac(~6) (bottom) carried out simultaneously in the same 96-well microplate. Each of the 18 aliquots were taken from the same stock solution of acetylated or non-acetylated SOD1 and analyzed simultaneously in the same 96-well microplate in order to eliminate variations in solution conditions and minimize random error. Black arrows identify the outlier sigmoids in the data set. The raw plots of ThT fluorescence for other acetyl derivatives of WT apo-SOD1 (and D90A and A4V) can be found in Figures 8.6 to 8.11. The mean number of acetylated lysines (Ac(~N)) is listed per apo-SOD1 monomer.

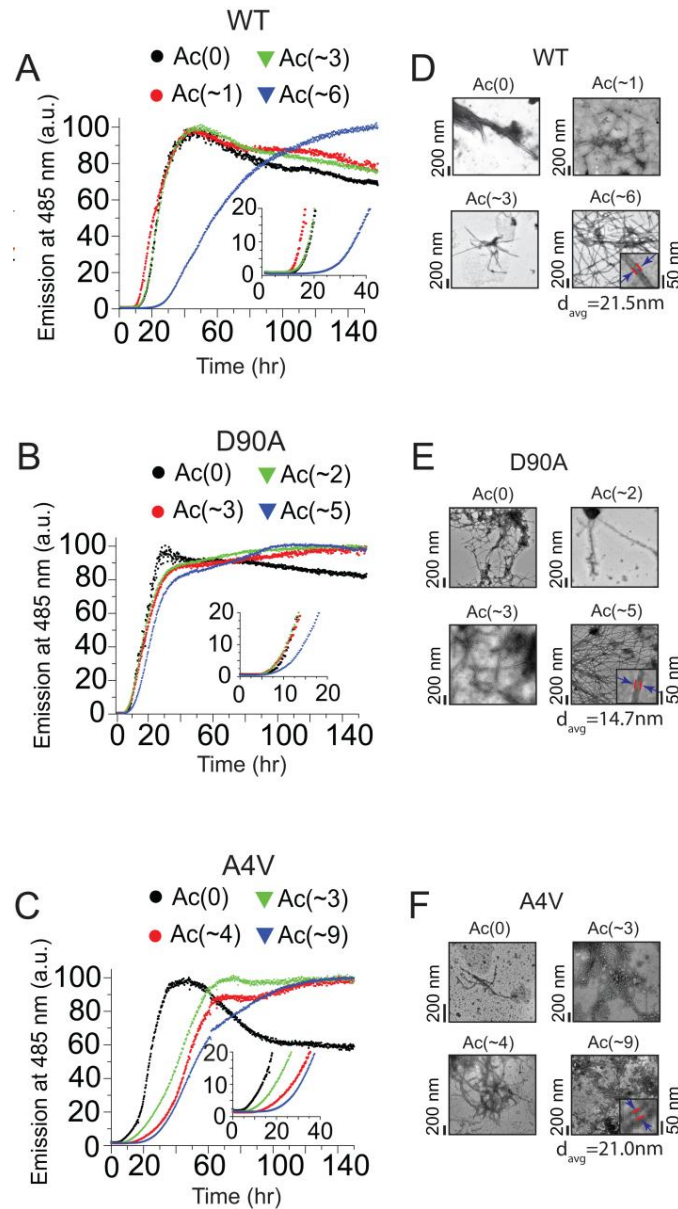


Figure 2.4 Effect of lysine acetylation on the rate of fibrillization of WT and ALS-variant apo-SOD1 in 0 mM NaCl. Thioflavin-T fluorescence assays of unacetylated and acetylated (A) WT, (B) D90A, and (C) A4V apo-SOD1 proteins (pH 7.4, 37 °C). Each curve is an average of normalized fluorescence measurements from 18 separate replicate experiments (of the sort shown in Figure 2.3). Transmission electron micrographs of fibrillar forms of acetylated (D) WT, (E) D90A, and (F) A4V apo-SOD1 after the ThT assay. The mean number of acetylated lysines is denoted as Lys-Ac(~N), per apo-SOD1 monomer. P-values for all kinetic analyses extracted from ThT fluorescence assays are listed in Table 2.1 and Figure 8.12.

Table 2.1 Rate of nucleation (τ) and propagation (k) of amyloid fibrils of WT and ALS-variant apo-SOD1 as a function of lysine acetylation, Ac(N).

SOD1 ^a	Ac (~N) ^b	0 mM NaCl (n = 18)			100 mM NaCl (n = 18)		
		τ (hr) ($\Delta\tau$) ^c	1/k (hr) ^c ($\Delta(1/k)$) ^d	P-value ^e	τ (hr) ($\Delta\tau$) ^d	1/k (hr) ^b ($\Delta(1/k)$) ^d	P-value ^e
WT	0	13.9 ± 1.1	1.1 ± 0.1		15.4 ± 1.1	1.8 ± 0.1	
	1	15.0 ± 1.2 (1.1 ± 1.6)	2.2 ± 0.2 (1.1 ± 0.2)	0.48	17.6 ± 1.6 (2.2 ± 1.9)	2.7 ± 0.2 (0.9 ± 0.2)	0.27
	3	16.5 ± 0.7 (2.6 ± 1.3)	2.6 ± 0.1 (1.5 ± 0.1)	0.06	16.9 ± 0.8 (1.5 ± 1.4)	2.4 ± 0.1 (0.6 ± 0.1)	0.28
	6	24.9 ± 1.3 (11.0 ± 1.7)	3.3 ± 0.3 (2.2 ± 0.3)	< 0.001	25.5 ± 0.9 (10.1 ± 1.4)	3.2 ± 0.3 (1.4 ± 0.3)	< 0.001
D90A	0	11.9 ± 1.0	2.1 ± 0.2		9.3 ± 0.9	1.5 ± 0.2	
	2	11.1 ± 1.1 (-0.8 ± 2.1)	3.3 ± 0.3 (1.2 ± 0.5)	0.57	14.0 ± 1.1 (4.7 ± 1.4)	2.1 ± 0.2 (0.6 ± 0.2)	0.002
	3	9.8 ± 1.1 (-2.1 ± 2.1)	3.4 ± 0.2 (1.3 ± 0.4)	0.15	14.1 ± 1.1 (4.8 ± 1.4)	2.2 ± 0.2 (0.7 ± 0.2)	0.002
	5	12.4 ± 1.2 (0.5 ± 1.6)	3.8 ± 0.2 (1.7 ± 0.2)	0.76	15.2 ± 1.4 (5.9 ± 1.7)	2.6 ± 0.2 (1.1 ± 0.2)	0.001
A4V	0	13.8 ± 1.7	2.2 ± 0.2		12.7 ± 1.3	2.2 ± 0.3	
	3	20.1 ± 2.1 (6.3 ± 2.7)	4.1 ± 0.4 (1.9 ± 0.4)	0.02	17.5 ± 1.3 (4.8 ± 1.3)	4.8 ± 0.3 (2.6 ± 0.3)	0.01
	4	11.5 ± 0.7 (-2.3 ± 1.8)	3.2 ± 0.3 (1.0 ± 0.4)	0.21	15.6 ± 2.2 (2.9 ± 2.5)	4.6 ± 0.5 (2.4 ± 0.6)	0.26
	9	28.3 ± 1.7 (14.5 ± 1.7)	4.9 ± 0.3 (2.7 ± 0.4)	< 0.001	17.1 ± 1.2 (4.4 ± 1.3)	4.7 ± 0.4 (2.5 ± 0.5)	0.02

^aAll acetylated and unacetylated SOD1 proteins were in the metal free state with $< 0.06 \pm 0.02$ Zn²⁺ and $< 0.03 \pm 0.01$ Cu²⁺ bound per SOD1 dimer. ^bMean number of acetylated residues, per apo-SOD1 monomer, as inferred from CE and MS. ^cRate of propagation expressed as inverse propagation constant (1/k). ^d $\Delta\tau$ and $\Delta(1/k)$ values are expressed relative to Ac(0) for each protein. All values and errors are listed as mean \pm SEM from 18 replicate ThT assays for each sample; the R² values of all fits were > 0.98 . ^eThis table only lists p-values comparing the lag time of acetylated proteins with unacetylated protein.

The elongation (propagation) of amyloid fibrils of acetylated WT, A4V, and D90A apo-SOD1 was consistently slower (i.e., 1/k was consistently larger) than the unacetylated protein, both in the presence and absence of 100 mM NaCl (Table 2.1, Figures 2.4 and 2.5). In general, the rate of elongation of amyloid fibrils of maximally

acetylated apo-SOD1 proteins was slower than minimally acetylated forms (with the exception of A4V, wherein Ac(~3) and Ac(~9) elongated at similar rates). Acetylation of each apo-SOD1 protein also increased the lag time of amyloid formation, but with some acetyl derivatives, these effects were less uniform and not statistically significant (Table 2.1), e.g., with D90A in 0 mM NaCl (Table 2.1 and Figure 8.12C). Nevertheless, acetylation inhibited the formation of amyloid by either increasing the lag time or slowing fibril propagation, and in most cases by both increasing lag time and slowing propagation (Table 2.1, Figures 8.11 and 8.12).

When comparing the effects of acetylation on the average value of lag time and fibril propagation, it is important to remember that the set of 18 replicate sigmoidal plots of ThT fluorescence for each protein in Figure 2.3 and Figures 8.6 to 8.11 includes, in some cases, outlier sigmoids. I did not use a Dixon's Q-test to exclude outlier sigmoids with outlying lag times and/or propagation rates. Although such outliers (e.g., the far right sigmoids in Figure 2.3) can skew averages, these outliers cannot be excluded because I have no reason to suspect that experimental errors occurred in the collection of these data. I do not suspect that the presence of outlier sigmoids is caused by differences in "solution conditions" because assays were carried out on identical solutions that were simply aliquoted into different wells of the sealed microplate. The presence of a heterogeneous distribution of acetyl derivatives or regioisomers in any particular solution cannot explain why different aliquots of the same solution exhibit outlier kinetics because even the unacetylated SOD1 protein—which is chemically monodisperse/homogenous—exhibited outlier kinetics. For example, wells that contained unacetylated WT SOD1-Ac(0) (in 0 mM NaCl) exhibited lag times from ~ 6 hr to 28 hr, within the same

microplate and experiment (Figure 2.3). Thus, it is necessary to not only compare average values of lag time and propagation, but to also compare probabilities (p-values) of similarity among different data sets (Table 2.1).

I do not know why I observe the nucleation and aggregation of SOD1 to be effectively stochastic, that is, why identical, aliquoted solutions of SOD1, analyzed at the same time in the same sealed microplate, with the same instrument, occur at different rates. The nucleation of amyloid SOD1 might be best described by *non-classical* nucleation theory, wherein the ΔH and ΔS of the various nuclei that might form are different than the ΔH and ΔS of the final bulk assembly.^{64,81-82} A zeroth order approximation (using the Arrhenius equation) would suggest that variations in the ΔE_a of amyloid nuclei or the collision frequency of SOD1 proteins give rise to the non-deterministic rates. Variations in ΔE_a might be caused by a random element within the apo-SOD1 protein, such as one or both of its two intrinsically disordered metal binding loops, which could result in heterogeneous nuclei, that form and elongate with different values of ΔE_a (and thus whose relative concentrations vary from well to well). I also note that the self-assembly that I observe is likely to involve heterogeneous nucleation wherein ions, or surfaces of the apparatus (i.e., the Teflon® bead or polystyrene microplate) contribute to the observed rate of aggregation.

A variation in the collision frequency of reactants, from well to well, might be caused by variations in the trajectory or velocity of the Teflon® in each well. Variations in the mass of the machined Teflon® bead (purchased from McMaster-Carr®) is an unlikely source of variation, as these beads only vary in mass from 36.1 to 35.9 mg, according to my measurements. Variation in the temperature of each well is an unlikely

source of the kinetic variation as the plate is temperature-controlled. The presence of a dust particle or pre-formed aggregate in some of the wells is also an unlikely explanation as I filtered each solution immediately prior to aggregation assay. Variations in volume (SOD1 concentration) cannot explain variations in rates of fibrillization because all replicate solutions are aliquoted from the same stock and the volume of each well was measured at the end of an assay to ensure no evaporation through the sealed lid. Varying degrees and types of nano-, micro-, or macro-scopic surface imperfections (e.g., scratches) on the surface of the bead or the well cannot yet be ruled out. Identifying the source of the stochastic nature of SOD1 amyloidogenesis must be the subject of a future study.

The protective effect of acetylation against amyloid formation was generally more pronounced in the absence of 100 mM NaCl (Table 2.1 and Figure 8.12) than in the presence of salt (Table 2.1 and Figure 8.12). This sensitivity to NaCl suggests that lysine acetylation inhibited the nucleation and propagation of amyloid by an electrostatic mechanism (at least in part). Acetylation had the largest inhibitory effect on the nucleation and propagation of A4V and WT apo-SOD1 fibrils, and the smallest effect on the self-assembly of D90A apo-SOD1 (regardless of NaCl concentration). For example, in the absence of 100 mM NaCl, the acetylation of ~ 3 lysines per monomer in A4V and WT apo-SOD1 resulted in a ~ 2-fold increase in the inverse propagation constant for both proteins (i.e., a lower rate of propagation), $p < 0.0001$ *** (Figure 8.12). The lag time of A4V-Ac(~3) fibrillization was also increased by 6.3 ± 2.7 hr, $p = 0.0243$ * compared to A4V-Ac(0) (Table 2.1). Moreover, A4V-Ac(~3) exhibited a lower lag time of fibrillization than the unacetylated WT apo-SOD1 protein. The rate of aggregation for

WT apo-SOD1 is not necessarily a perfect benchmark for non-toxicity, because the WT SOD1 is causally linked to sporadic ALS⁸³ (but might require chemical modification prior to aggregation⁶⁴). Nevertheless, the slower aggregation of acetylated mutant SOD1 compared to WT SOD1 suggests that small increases in the magnitude of a mutant protein's net negative charge, afforded by lysine acetylation, might impart a therapeutic effect in ALS (or other diseases linked to protein self-assembly).

In the absence of 100 mM NaCl, the maximally acetylated forms of WT and A4V (i.e., Ac > ~5) exhibited increases in lag time of 11.0 ± 1.7 hr and 14.5 ± 1.7 hr, respectively, compared to their unacetylated forms (Table 2.1, Figure 2.4, and Figure 8.12, $p < 0.0001$ ***). Maximal acetylation of WT and A4V apo-SOD1 also increased the inverse propagation constant by 2.2 ± 0.3 hr (WT) and 2.7 ± 0.4 hr (A4V), which corresponded to a 2.5-fold decrease in k (Table 2.1, Figure 2.4, and Figure 8.12, $p < 0.0001$ ***). In the absence of 100 mM NaCl, the lag time of minimally acetylated D90A apo-SOD1, i.e., Ac(~2), did not differ significantly from unacetylated D90A apo-SOD1 (Table 2.1, Figure 2.4, and Figure 8.12, $p > 0.05$), but the inverse propagation constant increased by approximately 2-fold (Table 2.1, Figure 2.4, and Figure 8.12, $p = 0.0007$ ***).

In 0 mM NaCl, A4V-Ac(~3) had a greater lag time of aggregation than A4V-Ac(~4) by 8.6 ± 2.3 hr (but had similar rates of propagation) (Table 2.1 and Figure 8.12). This slower aggregation, despite slightly lower acetylation, might arise from difficulties in expressing mean acetylation. For example, the Gaussian fitting of the MS spectrum of A4V-Ac(~4) resulted in a mean acetylation of 3.8 Ac. Inspection of the MS spectrum, however, demonstrated that the most abundant peak is that of Ac(2) (Figure 2.2C). This difference might explain why A4V-Ac(~4) was found to aggregate faster than A4V-

Ac(~3) in 0 mM NaCl (albeit, the rates of A4V-Ac(~4) and A4V-Ac(~3) are statistically similar in 100 mM NaCl, Figure 2.5C and Figure 8.13F). It is unlikely that the different rates of fibrillization that I observed among WT and ALS mutant SOD1, and their acetyl derivatives, are caused by Cu^{2+} or Zn^{2+} contamination. All SOD1 proteins were demetallated and contained $< 0.06 \pm 0.02 \text{ Zn}^{2+}$ and $< 0.03 \pm 0.01 \text{ Cu}^{2+}$ per SOD1 dimer after acetylation (according to ICP-MS). After acetylation and analysis with ICP-MS, protein solutions were stored frozen until the initiation of the aggregation assay. Each aggregation assay was also carried out in the presence of 5 mM EDTA (to prevent metal contamination from reagents used during the assay). Moreover, all solutions and buffers were made with ultrapure metal-free water with a measured resistance of 18.2 M Ω /cm (dispensed through a Millipore MilliQ® system). All containers used for making buffers or other solutions were rinsed with 5 mM EDTA and pure water prior to use.

The addition of 100 mM NaCl at pH 7.4 increased the overall rate of aggregation of each apo-SOD1 protein (regardless of its degree of acetylation), which has been reported previously for other proteins⁸⁴ (Figure 2.5A-C and Figure 8.13). Although the presence of 100 mM NaCl generally diminished—but did not abolish—the magnitude by which acetylation slowed the rate of fibril initiation and propagation, the D90A apo-SOD1 protein was one exception (Table 2.1). For example, the acetylation of five lysine residues had a negligible effect on the lag time of D90A fibrillization, in 0 mM NaCl, whereas the acetylation of five lysines increased the lag time by $5.9 \pm 1.7 \text{ hr}$ in the presence of 100 mM NaCl (Table 2.1, Figure 2.5A-C and Figure 8.13, $p = 0.0022^{**}$). Thus, acetylation had a greater effect on inhibiting the fibrillization of D90A apo-SOD1 in 100 mM NaCl than in 0 mM NaCl. Notably, in the presence of 100 mM NaCl, the

acetylation of A4V apo-SOD1 also slowed its fibrillization to a value below that of unacetylated WT apo-SOD1 (Figure 8.13). The inability of Na^+ and Cl^- to *completely* screen the electrostatic repulsions between negatively charged SOD1 proteins—i.e., to completely abolish the protective effects of acetylation against aggregation—is not surprising and strengthens the potential utility of the “charge boosting” strategy. Free cations and anions do not screen all types of intermolecular electrostatic interactions involving proteins,⁴⁷ especially for example, when: (i) the interaction occurs through the low dielectric interior of a protein; (ii) the interaction depends thermodynamically on desolvation of charged groups, or (iii) the electrostatic interaction occurs over a distance that is smaller than the Debye screening length (i.e., ~ 1 nm at $I = 0.1$ M).⁴⁷ All three of these criteria might exist within an initiating or elongating amyloid fibril.

To ensure that the inhibitory effects of acetylation on the aggregation of apo-SOD1 were not due to differences (or errors) in protein concentration, and that solutions did not contain soluble SOD1 at the end of the fluorescence assay, I quantified the amount of non-sedimentable apo-SOD1 proteins in solution at the start of the aggregation assay and at the completion of the assay. The concentration of all apo-SOD1 proteins, as measured by UV-Vis spectrophotometry, only varied by ± 2 μM prior to the start of the assay (Figure 2.5D-F; lower panels). SDS-PAGE also demonstrated that all proteins were initially present at similar concentration and purity at the start of the assay (Figure 2.5D-F, gels on left). The absence of SOD1 protein in the supernatant of solutions after completion of the aggregation assay (and centrifugation) demonstrated that all acetylated and unacetylated apo-SOD1 proteins underwent aggregation into a high molecular weight, sedimentable species (Figure 2.5D-F, gels on right).

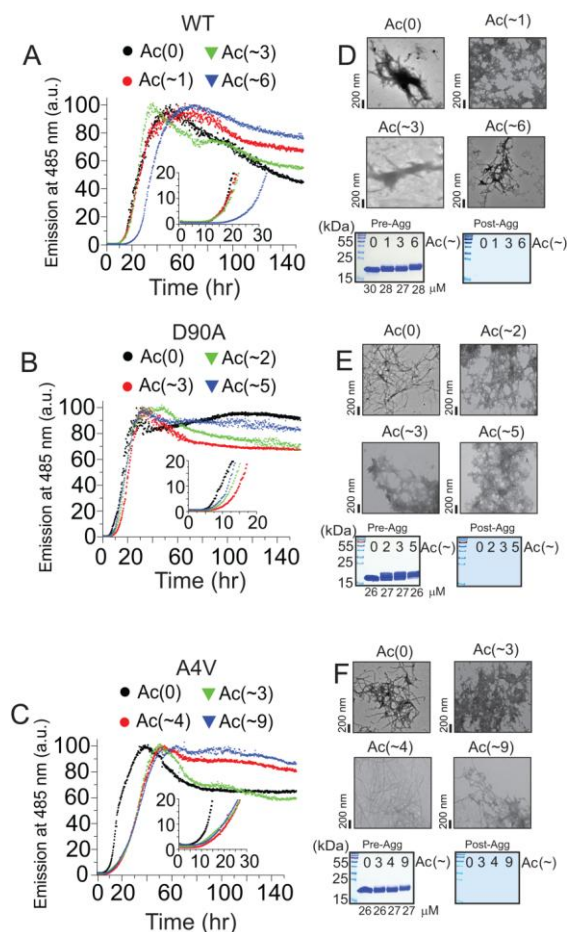


Figure 2.5 Effect of lysine acetylation on the rate of fibrillization of WT and ALS-variant apo-SOD1 in 100 mM NaCl. Thioflavin-T fluorescence assays of unacetylated and acetylated (A) WT, (B) D90A, and (C) A4V apo-SOD1 proteins (pH 7.4, 37 °C). Each curve is an average of data (normalized) from 18 separate replicate experiments. The mean number of acetylated lysines is denoted as Lys-Ac(~N), per apo-SOD1 monomer. (D-F; upper panels) Transmission electron micrographs of fibrillar forms of acetylated WT, D90A, and A4V apo-SOD1 after the ThT assay in 100 mM NaCl. (D-F; lower panels) SDS-PAGE of samples before (left) and after (right) ThT aggregation assay in 100 mM NaCl. The gels on the right in each panel are from supernatants of samples after aggregation and centrifugation. P-values for all kinetic analyses extracted from ThT fluorescence assays are listed in Table 2.1 and Figure 8.13.

I note that the acetylation of lysine residues in apo-SOD1 decreased its electrophoretic mobility during reducing SDS-PAGE, most likely because of a decrease in bound SDS (as demonstrated by a recent study into the long-standing mystery of

abnormal protein migration during SDS-PAGE⁶⁷). Transmission electron microscopy demonstrated that the high molecular weight aggregates of unacetylated and acetylated apo-SOD1 were fibrillar in nature (Figure 2.4D-F and Figure 2.5D-F; upper panels). The typical diameter of unacetylated and acetylated fibrils was ~ 15-20 nm, similar to previous studies.⁸⁵

Effect of Lysine Acetylation on The Thermostability and Structure of The Native State of Apo-SOD1:

The acetylation of lysine in a folded protein does not necessarily lower its melting transition temperature (T_m).⁶⁰ To determine if the acetylation of lysine diminished the rate of aggregation of WT and ALS-variant apo-SOD1 by increasing apo-SOD1 thermostability, in addition to by increasing net charge, I analyzed acetylated apo-SOD1 with differential scanning calorimetry, prior to fibrillization (Figure 8.14 and Table 8.5). The acetylation of lysine in WT and ALS-variant apo-SOD1 did not increase the thermostability of the native apo-protein, and therefore did not inhibit fibrillization by increasing the T_m of the native protein (Table 8.5). The acetylation of ~ 6 lysines (per monomer) in WT apo-SOD1, for example, lowered its T_m by $\Delta T_m = -6.1$ °C (Figure 8.14A). These DSC data show that chemical modifications to a protein can inhibit self-assembly even if the modification diminishes T_m of the native state.

The acetylation of lysine in SOD1 by aspirin did not disrupt the structure of the protein by a magnitude that resulted in an increased rate of amide H/D exchange. Instead, the acetylation of lysine in SOD1 proteins slightly *diminished* the rate of global amide H/D exchange by < 1 H per acetyl modification (Figure 8.14D-F). This result is consistent with previous reports showing that semi-random lysine acetylation slows the

rate of amide H/D exchange in proteins (e.g., myoglobin, carbonic anhydrase, and SOD1) despite also diminishing thermostability.^{41,60,62,86-87} The acetylation of lysine has been hypothesized to slow amide H/D exchange by a purely electrostatic mechanism, i.e., by not altering H-bonding or solvent accessibility, but rather by lowering the local concentration of the hydroxide catalyst of H/D exchange and/or the activation energy of the divalent anionic intermediate (R—N:[−]—R₁).⁸⁷ In the case of A4V, the acetylated and unacetylated apo-protein exchanged most of its amide hydrogens after only 5 min, which is consistent with previous reports of its low thermostability.

Acetylation of Lysine in Soluble Apo-SOD1 Diminishes The Thermostability of Resulting Amyloid Fibrils:

The cytotoxicity of an amyloid oligomer is thought to be caused, in part, by its high thermostability, which inhibits proteolysis by intracellular and extracellular proteases.⁸⁸ One important caveat is, however, that the breakage of amyloid fibrils has been shown to increase cytotoxicity by seeding amyloidogenesis and/or increasing membrane permeability of oligomers.²⁵ In the case of SOD1 this latter hypothesis has not yet been rigorously (quantitatively) tested. The thermostability and material properties of amyloid-like oligomers comprised of WT and mutant SOD1 are unmeasured. In fact, I could find only one study that analyzed the thermostability of amyloid fibrils of any protein with DSC. This study showed that $T_m = 83$ °C for amyloid fibrils of the N47A mutant of alpha-spectrin SH3 domain, compared to $T_m = 49$ °C for the protein's native state.⁸⁹ Nevertheless, it is reasonable to hypothesize that an amyloid oligomer could be made less toxic by “supercharging” the fibril, assuming that supercharging destabilized the fibril to a level that rendered it a substrate for intra- or extra-cellular proteases, and

diminished its permeability (electrostatically) across anionic cellular membranes. This type of successive “supercharging” after fibrillization, by repeated doses of an acylating agent, might represent a practical medicinal approach because the long half-life of amyloid-like oligomers would permit accumulation of chemical modifications.⁶⁶

The method that I used to determine the thermostability of acetylated and unacetylated apo-SOD1 fibrils was modified from Shamma and coworkers⁶⁹ and is illustrated in Figure 8.15A. I chose to measure the stability of fibrils using thermal defibrillization, instead of chemical defibrillization, because the interaction of chemical denaturants (such as guanidinium hydrochloride, sodium dodecyl sulfate, or urea) can be dependent upon the net charge and hydrophobicity of proteins, both of which are altered by acetylation of Lys-NH₃⁺ to Lys-NHCOCH₃.⁹⁰⁻⁹¹ I assume that the low pressure generated in this thermal defibrillization assay (~ 350 kPa) had a negligible effect on the thermostability of fibrils because it is 1000-fold lower than minimal values reported to induce protein aggregation (i.e., ~ 400 MPa).⁹² The T_m of SOD1 amyloid fibrils composed of unacetylated apo-SOD1 were: 99.42 ± 0.89 °C for WT, 104.69 ± 0.24 °C for D90A, and 99.85 ± 0.48 °C for A4V (Figure 8.15B-D and Table 8.5). Maximal acetylation of lysine residues in apo-SOD1 with aspirin, prior to fibrillization, decreased the T_m of resulting fibrils by between ~ 3 and 7 °C (Table 8.5): ΔT_m = -3.15 ± 1.1 °C for WT-Ac(0) and WT-Ac(~6) amyloid; ΔT_m = -7.07 ± 0.64 °C for D90A-Ac(0) and D90A-Ac(~5) amyloid; and ΔT_m = -4.78 ± 0.58 °C for A4V-Ac(0) and A4V-Ac(~9) amyloid SOD1. These differences in the T_m values of unacetylated and acetylated fibrils were statistically significant for all three proteins, with p-values uniformly < 0.0001^{***}. In general, successive acetylation of native SOD1 diminished the T_m of resulting fibrils,

however, the differences in the T_m of fibrils from proteins that differed in mean acetylation by $< \sim 3$ lysines were often statistically indistinguishable (Table 8.5). This result might be caused by similarities (overlap) in the distribution of acetylated lysines among different samples. For example, the T_m of fibrillar D90A SOD1-Ac(~ 3) = 96.02 ± 0.97 °C whereas the T_m of fibrillar D90A SOD1-Ac(~ 5) = 97.62 ± 0.60 °C (Table 8.5). Although these two sets of proteins have different mean numbers of acetylated lysines, these two sets have ~ 70 % overlap in the distribution of acetylated species (Figure 8.5A-B) and this similar degree of acetylation might account for the statistically similar values of T_m .

To ensure that the total concentration of apo-SOD1 protein did not change during the course of heating (via solvent evaporation) I performed reducing SDS-PAGE on solutions before and after thermal defibrillization. I observed no significant difference in apo-SOD1 concentration before and after heating (Figure 8.15E), indicating that protein concentration did not change via solvent evaporation during thermal defibrillization.

Although the turbidity of each fibrillar solution was abolished at the end of each thermal scan, it is possible that fibrils of apo-SOD1 melted incompletely into small oligomeric forms that did not sediment or scatter light, but are nonetheless still in an amyloid state. To assay for such small oligomers, I performed size-exclusion liquid chromatography (SE-LC) and native PAGE on solutions at the end of thermal defibrillization experiment (Figure 8.16A-C). The supernatant solutions of melted fibrils from all three apo-SOD1 proteins contained SOD1 species that were < 50 kDa, according to SE-LC calibration curve (Figure 8.16B). All three apo-SOD1 proteins did, however, migrate slower than the dimeric form of soluble WT apo-SOD1 during native PAGE

(Figure 8.16C), which might be caused by improper refolding after cooling the thermally defibrillized and denatured polypeptides. I also filtered the supernatants of melted fibrils with a 0.2 μm filter and performed SE-LC, native PAGE, and TEM and found no significant difference in the chromatography, electrophoresis, or microscopy of non-filtered and filtered samples, which suggested that oligomers that are $> 0.2 \mu\text{m}$ in diameter were not present after thermal defibrillization (Figure 8.16A, C, and D). Fibrillar species were not detected by TEM in these heated samples, even after examining $\sim 3.5 \text{ mm}^2$ of the grid surface in three separate replicate analyses (Figure 8.16D). Thus, the assay I used to measure the T_m of fibrillar apo-SOD1 appears to be a valid method for determining the stability of the large SOD1 fibrils depicted in TEM images of Figure 2.4D-F and Figure 2.5D-F. In conclusion, the predominant amyloid framework of fibrillar apo-SOD1 is not as thermostable as I expected and does not represent a thermodynamic “black hole” for SOD1. For example, the T_m of unacetylated WT apo-SOD1 fibrils is only a few degrees higher than the T_m of the properly folded and fully metalated WT Cu_2 , Zn_2 -SOD1 protein.⁹³ Moreover, the fibrils formed in this study did not appear to involve extensive intermolecular disulfide crosslinks,⁹⁴ i.e., the thermal defibrillization assay did not include any reducing agent and fibrils nevertheless dissociated to species with molecular weights $\leq 50 \text{ kDa}$ (Figure 8.16).

Lysine, Serine, and Threonine Residues in Amyloid Apo-SOD1 Are Reactive with Aspirin:

I also wanted to determine if lysine residues in amyloid apo-SOD1 could be acetylated with aspirin *after* fibrillization of unacetylated apo-SOD1, and the degree to which these modifications affect fibril thermostability. To determine the reactivity of

fibrils, I prepared amyloid fibrils of WT and ALS-variant apo-SOD1 from each unacetylated protein and reacted the amyloid fibrils with aspirin in aqueous buffer. The number of acetylated lysines in fibrillized apo-SOD1 polypeptides was determined by thermo-chemically dissociating fibrils and analyzing the dissociated polypeptides with ESI-MS (Figure 2.6A-C). Fibrils were gently dissociated by heating at 50 °C, in 6.5 M guanidinium hydrochloride (Gdm-HCl), 20 mM dithiothreitol (DTT), pH 8. This protocol has been proven to dissociate fibrils of SOD1 into monomeric polypeptides.⁶⁸

The mass spectra of apo-SOD1 polypeptide chains from thermo-chemically dissociated fibrils demonstrated that each of the 11 lysine residues in apo-SOD1 amyloid fibrils could be acetylated by aspirin (Figure 2.6A-C, right panels). Thus, unlike the native soluble protein, I was able to acetylate all 11 lysine residues in fibrillar apo-SOD1; the formation of amyloid by SOD1 does not cause its lysines to be protected from chemical modification. Mass spectrometry also showed that a significant population of SOD1 proteins contained additional acetyl modifications (up to 7 additional acetyl groups) on residues other than lysine (Figure 2.6A-C, right panels). I was able to identify acetyl modifications on each lysine with MS-MS analysis (Figure 8.17A), and also detected acetyl groups on Ser-134, Ser-142, Thr-135, and Thr-137 (Figure 8.17B). I hypothesize that these types of Ser and Thr modifications were not detected (and were presumably not present) in acetylated native WT and D90A apo-SOD1 because: (i) native forms of these proteins precipitated before a sufficient excess of aspirin could be added to acetylate Ser and Thr (this impediment did not occur when acetylating amyloid fibrils) and/or (ii) fibrillization protected ester groups on Ser and Thr from hydrolysis.

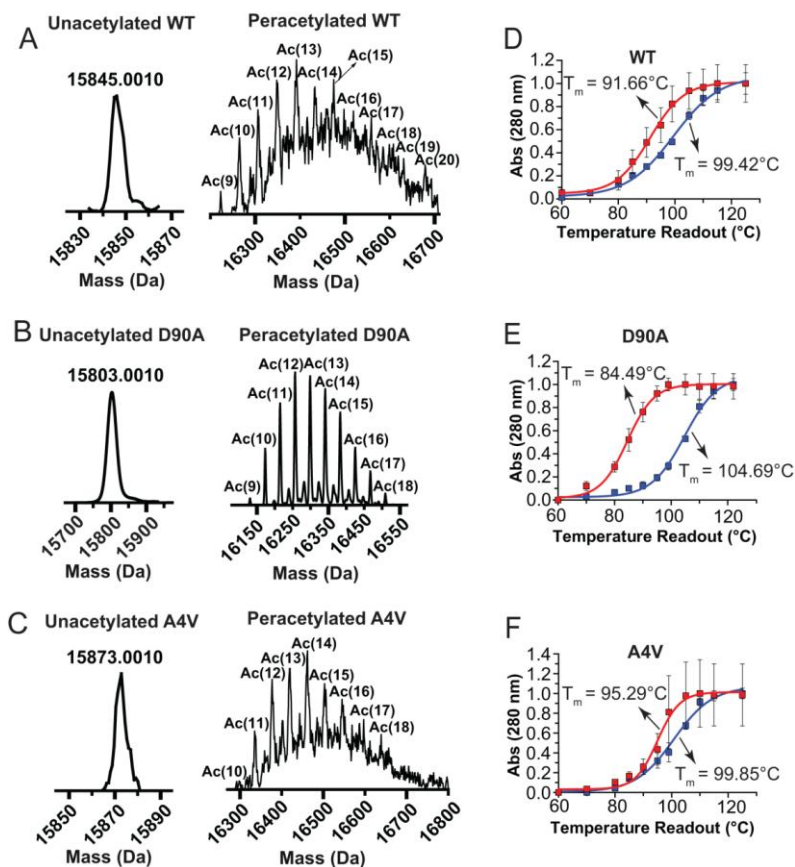


Figure 2.6 Effect of peracetylation of lysine in fibrillar WT and ALS-variant apo-SOD1 on fibril thermostability (i.e., acetylation after fibrillization). (A-C) Mass spectra of unacetylated and peracetylated WT and ALS-variant apo-SOD1 thermochemically dissociated from amyloid fibrils (acetylation was performed after fibrillization). (D-F) Thermal stability curves of unacetylated (—■—) and peracetylated (—■—) WT, D90A, and A4V apo-SOD1 amyloid fibrils.

Peracetylation of Lysine in Amyloid (After Fibrillization) Increases Formal Net Charge by Millions of Units and Lowers Fibril Thermostability:

Thermostability assays for peracetylated amyloid fibrils of WT, D90A, and A4V apo-SOD1 (that were peracetylated after fibrillization) are shown in Figure 2.6D-F; fibril T_m values are listed in Table S5. Peracetylation lowered the T_m of D90A fibrils by three to four-fold more than A4V or WT fibrils. Peracetylation lowered fibril T_m by $\Delta T_m = -7.76 \pm 1.18^\circ\text{C}$ for WT fibrils; $\Delta T_m = -20.2 \pm 0.48^\circ\text{C}$ for D90A fibrils; and $\Delta T_m = -4.56 \pm$

0.69 °C for A4V fibrils (Figure 2.6D-F and Table 8.5). I point out that the T_m of peracetylated fibrils of D90A ($T_m = 84.49 \pm 0.42$ °C), A4V ($T_m = 95.29 \pm 0.50$ °C) and WT SOD1 ($T_m = 91.66 \pm 0.78$ °C) are near or below the reported T_m for the WT holo-SOD1 enzyme (Cu₂, Zn₂-SOD1) in its native state ($T_m \sim 90-95$ °C).⁹³ These low T_m values for supercharged fibrils raise the possibility that unstable, acetylated fibrils might have sufficient instability for proteolysis by intracellular or extracellular proteases.⁹⁵ I also point out that any SOD1 oligomers or polypeptides that would dissociate from these unstable fibrils would be less prone to seed aggregation (than unacetylated polypeptides), because of their supercharged state.

The most straightforward explanation for why peracetylation diminished the thermostability of amyloid SOD1 is that peracetylation strengthened the repulsive Coulombic forces between similarly charged—now supercharged—SOD1 polypeptides. The peracetylation of an amyloid fibril with dimensions of 15 nm by 2 μm (composed of $\sim 1.9 \times 10^5$ SOD1 polypeptide chains) will increase the net negative charge of the fibril by $\sim 1.6 \times 10^6$ units of formal charge at pH 7.4. See Chapter 8 for details of this calculation.

“Drugging Z”:

The results of study presented in this chapter do not suggest that an acylating agent such as aspirin—which nonspecifically acetylates SOD1—can function as a “charge boosting” drug in the treatment of ALS. Instead, future work will be required to design and synthesize compounds that selectively boost the net charge of SOD1 (or its oligomers). I envision the general chemical anatomy of a selective “charge booster” to consist of a “head” for molecular recognition of the target protein or protein oligomer

(Figure 8.18), and a reactive acylating “tail” that acylates nearby lysine residues. One advantage to designing small reactive molecules that increase the net charge of a target protein, as opposed to designing conventional ligands that non-covalently stabilize the structure of the native or oligomeric protein, is that the former might be much easier to accomplish (medicinally). The acetylation of lysines in WT or mutant apo-SOD1 by aspirin inhibited the nucleation and propagation of amyloid fibrils, even though the acetylation was nonspecific. This result suggests that increasing the net surface potential of different surface loci—perhaps acetylating *any* surface lysine on a small anionic protein such as SOD1—will inhibit aggregation. This large number of chemical targets in a single protein is in stark contrast to the chemical constraints that typify conventional medicinal chemistry. It is also important to remember that this study demonstrated the basic tenet of the “charge boosting” strategy by using the least potent (electrostatically speaking) type of chemistry, i.e., $\Delta Z = -1$ per modification.

The interactions between highly charged proteins and cellular membranes were not examined in this study. Nevertheless, it is reasonable to hypothesize that a hyper-anionic, acetylated SOD1 protein (oligomeric or native) will resist electrostatic interactions with inner and outer cellular membranes (which are generally anionic because of sialylated and sulfated glycans⁹⁶) more than unacetylated SOD1 proteins.

For example, it has been shown that “supercharged” green fluorescent proteins (GFP) with magnitudes of negative charge reaching $Z = -30$ are resistant to association with outer cellular membranes, while “supercharged” proteins with $Z = +36$ permeate the same cellular membranes.⁴²

Increasing the electrostatic repulsion between cellular membranes and SOD1 proteins might diminish the cell-to-cell propagation of oligomeric SOD1^{44,97} and halt the progressive death of motor neurons in ALS.

Acknowledgement:

Financial support for this research was provided to B.F.S. by the Department of Defense (W81XWH-11-1-0790), the National Science Foundation (CAREER CHE: 1352122), and the Welch Foundation (AA-1854).

CHAPTER THREE

Stochastic Formation of Fibrillar and Amorphous Superoxide Dismutase Oligomers Linked to Amyotrophic Lateral Sclerosis.

This chapter is published as:

Abdolvahabi A, Shi Y, Chuprin A, Rasouli S, Shaw BF (2016) Stochastic formation of fibrillar and amorphous superoxide dismutase oligomers linked to amyotrophic lateral sclerosis. *ACS Chem. Neurosci.* **7**, 799-810.⁹⁸

Abstract

Recent reports suggest that the nucleation and propagation of oligomeric SOD1 is effectively stochastic *in vivo* and *in vitro*. This perplexing kinetic variability—observed for other proteins and frequently attributed to experimental error—plagues attempts to discern how *SOD1* mutations and post-translational modifications linked to amyotrophic lateral sclerosis (ALS) affect SOD1 aggregation. In this chapter, I used microplate fluorescence spectroscopy and dynamic light scattering to measure rates of fibrillar and amorphous SOD1 aggregation at high iteration ($n_{\text{total}} = 1.2 \times 10^3$). Rates of oligomerization were intrinsically irreproducible and populated continuous probability distributions. Modifying reaction conditions to mimic random and systematic experimental error could not account for kinetic outliers in standard assays, suggesting that stochasticity is not an experimental artifact, rather an intrinsic property of SOD1 oligomerization (presumably caused by competing pathways of oligomerization). Moreover, mean rates of fibrillar and amorphous nucleation were not uniformly increased by mutations that cause ALS, however, mutations did increase kinetic noise (variation) associated with nucleation and propagation. The stochastic aggregation of SOD1

provides a plausible statistical framework to rationalize how a pathogenic mutation can increase the probability of oligomer nucleation within a single cell, without increasing the mean rate of nucleation across an entire population of cells.

Introduction

The prion-like aggregation of wild-type (WT) and mutant SOD1 in neuronal cells, followed by propagation to neighboring neurons, is linked to a fraction of familial and sporadic amyotrophic lateral sclerosis (ALS) cases.^{18,43-44,68,83,99} It remains unclear whether *SOD1* mutations induce cytotoxicity by accelerating the intrinsic rate of SOD1 oligomerization, or by a separate mechanism, e.g., by increasing the cytotoxicity of an SOD1 oligomer, irrespective of its rate of formation. This question remains unanswered, in part, because it remains unknown whether the stochastic aggregation of SOD1—observed *in vitro* and *in vivo*¹⁰⁰⁻¹⁰¹—is a thermodynamic property of SOD1 self-assembly, or an experimental artifact generated by random or systematic error. This lack of clarity has made it technically challenging to precisely quantify how ALS-linked mutations in *SOD1* affect the actual rate (or mean rate) of nucleation and propagation of oligomeric SOD1.

Statistical analysis of amyloid nucleation and elongation rates for several proteins suggests that amyloidogenesis is intrinsically stochastic,^{75,78,100} that is, measured rates span a continuous probability distribution that cannot be explained by experimental error.^{73,79,102-104} Other studies invoke deterministic models,⁸⁰ but report replicate rates that span a distribution of inexplicable breadth.⁸⁰ Models of stochastic nucleation are generally invoked to explain the irreproducible rates of self-assembly of systems across

all size scales, from the crystallization of H₂O⁷³ and the aggregation of proteins⁷⁸ and mRNA,¹⁰⁵ to gene expression¹⁰⁶ and the mesoscale aggregation of social amoeba.¹⁰⁷ The intrinsic irreproducibility associated with measuring rates of these processes can be circumvented by collecting high numbers of replicate measurements (on the order of n = 10²) and calculating statistically significant rates and population comparisons.⁷³ In the case of amyloid self-assembly, the reproducibility of kinetic assays can be increased by the addition of “seed” oligomers,^{78,108} but this type of seeding presumably bypasses the stochastic steps of primary nucleation.

Two of previous investigations by our group into the fibrillization of apo-SOD1 uncovered a high degree of irreproducibility, when using thioflavin-T fluorescence assays to measure “unseeded” amyloid fibril nucleation and propagation.^{45,64} For example, the lag time of WT apo-SOD1 fibrillization varied by up to 68 % and propagation rates up to 50 % in *replicate* measurements that were made simultaneously in a 96-well plate, on sample aliquots from the same, filtered stock solution of pure apo-SOD1.^{45,64} Other investigations into apo-SOD1 oligomerization have not reported this apparent stochasticity,^{68,109-111} with the exception of a recent report by Lang and co-workers.¹⁰⁰ Although these previous studies suggest that the fibrillization of apo-SOD1 is stochastic, there have been no investigations into whether sample-to-sample variations in reaction conditions and/or competing pathways of non-fibrillar aggregation are a source of this apparent stochasticity.

Resolving why SOD1 aggregation is apparently stochastic during *in vitro* assays is relevant to understanding its aggregation *in vivo*. For example, the aggregation of ALS-mutant SOD1 in transgenic mouse models of ALS appears to follow the same sigmoidal,

stochastic nucleation kinetics observed *in vitro* with the types of assays used in this chapter (microplate-based, thioflavin-T fluorescence assays that employ mechanical agitation).^{100,112-115}

Results and Discussion

Apo-SOD1 fibrillization is effectively stochastic:

Thioflavin-T (ThT) fluorescence was used to measure the “unseeded” rate of nucleation and propagation of amyloid fibrils for WT and three biophysically diverse ALS-variant apo-SOD1 proteins, including A4V (which is intrinsically disordered in the disulfide-reduced apo state) and two “cryptic” variants, D90A and E100K (which have subtle effects on the structure and conformational stability of apo-SOD1).³¹ Microplate assays utilized mechanical agitation (i.e., a gyrating Teflon bead) to accelerate aggregation (possibly inducing fragmentation of elongating fibrils⁹). A total of 1132 ThT assays were made for all four proteins at a variety of experimental conditions.

Rates of aggregation were measured at two degrees of disulfide reduction, i.e., 30 % reduced (denoted as apo-SOD1^{30%2SH}, Figure 3.1) and ~ 90 % reduced (denoted as apo-SOD1^{90%2SH}, Figure 3.2) achieved by incubating apo-SOD1 in 10 mM or 100 mM TCEP, respectively, for 6 hr prior to assay. The semi-reduced state (i.e., apo-SOD1^{30%2SH}) was chosen to mimic the gradual reduction of apo-SOD1 proteins that will occur intracellularly upon loss of metal ions,¹¹⁶ whereas the more fully reduced state (i.e., apo-SOD1^{90%2SH}) was utilized to mimic the self-assembly of nascent protein immediately after translation.⁶⁸ The degree of disulfide reduction was determined with differential scanning calorimetry (DSC) and size-exclusion chromatography (SE-HPLC), per the effect of disulfide reduction on the monomerization of apo-SOD1 and lowering of its

melting transition temperature (Figure 8.19).^{30,117} Analysis of each apo-SOD1 protein with ICP-MS, DSC, and SE-HPLC confirmed that each set of proteins were demetallated ($< 0.04 \text{ Zn}^{2+}$ and $< 0.02 \text{ Cu}^{2+}$ per monomer, Table 8.6), properly folded (or disordered in the case of disulfide reduced A4V), and pure before each ThT assay (Figure 8.19 and Table 8.6). In this chapter, I only examined the aggregation rates of metal free SOD1, without the influence of metal ions on aggregation. Although the removal of metal ions typically increases the rate of SOD1 aggregation, recent studies have shown that the aberrant binding of zinc to SOD1 can trigger amorphous aggregation.¹¹⁸

A variation in lag time of more than 15 hr, and a variation in inverse propagation rate constant of several hours, was observed among replicate measurements for all ThT assays of apo-SOD1^{30%2SH} proteins at 37 °C, pH 7.4 (Figure 3.1a and Figure 8.20). This kinetic variability occurred even though replicate measurements were performed on aliquots from the same, filtered stock solution, and analyzed simultaneously in 96-well plates. This magnitude of kinetic variation has been observed in the fibrillization of several other proteins including β_2 microglobulin, $A\beta_{(1-42)}$ amyloid peptide, sickle hemoglobin, and insulin.^{75-79,103} Non-classical stochastic nucleation models best describe the variations in nucleation and elongation of SOD1 amyloid fibrils.^{82,102,119-120} Discarding any kinetic outliers based upon statistical tests (e.g., Dixon's Q test) is inappropriate because there is no reason to suspect, *ab initio*, that outliers were caused by error⁴⁵ (this point is investigated in detail below). Evaporation from sealed wells, for example, cannot account for these variations: measurement of volume of wells exhibiting outlier aggregation kinetics (with a micropipette at the end of each assay) revealed that volumes varied by $< \pm 3.5 \%$ from the mean volume of wells. I hypothesize that

variations in the rate of nucleation are caused by: (i) variations in the activation energy (E_a) of amyloid nuclei that formed in different wells, and/or (ii) off-amyloid pathways of aggregation that compete with amyloid formation and diminish the concentration of unassembled SOD1, e.g., formation of amorphous aggregates.¹⁹ For example, the early formation of amorphous aggregates (possibly also stochastic) would not be detected in the ThT assay, but would lower the concentration of free apo-SOD1 available to fibrillize which could explain ThT plots that exhibited increased lag time of fibrillization, decreased elongation rates, and decreased maximal ThT fluorescence (Figure 3.1a and Figure 8.20).

Histograms of fibril propagation (expressed as $1/k$) generally exhibited a log-normal behavior (Equations 8.8a and 8.8b), where lag time generally exhibited a bimodal Lorentzian distribution (Equation 8.9) with $R^2_{\text{average}} > 0.7$. Measuring apo-SOD1 fibrillization at such high iteration allowed me to conclude—with statistical significance—that ALS mutations do not uniformly decrease the mean lag time of apo-SOD1 fibrillization, at least at 30 % reduction (Figure 3.1b-c and Table 8.7). In fact, the A4V and D90A substitutions in apo-SOD1^{30%2SH} have statistically similar lag times of fibrillization as WT protein ($p > 0.05$). Moreover, A4V and D90A mutations did not uniformly accelerate the propagation (elongation rate) of apo-SOD1^{30%2SH} fibrillization under semi-reduced conditions (Figure 3.1b-c and Table 8.7).

The observed variation in lag time, propagation, and maximal ThT fluorescence was not caused by the presence of residual monomeric/dimeric SOD1 in each well (i.e., a lack of complete aggregation). For example, SDS-PAGE of protein supernatant at the end of the ThT assay confirmed that apo-SOD1 proteins were incorporated into a

sedimentable aggregate, with no residual monomer (Figure 3.1d). The morphology of apo-SOD1 aggregates generated during ThT assays was characterized with transmission electron microscopy (TEM), and found to be, generally, a mixture of fibrillar and amorphous species (Figure 3.1e).

Increasing the degree of disulfide reduction, from 30 % to 90 % did not improve the reproducibility of amyloid assays (Figure 3.2a and Figure 8.21). I point out that ALS mutations do not uniformly accelerate the nucleation and propagation (Figure 3.2b-c and Table 8.7) and morphology (Figure 3.2d) of apo-SOD1, even at 90 % reduction. This result is contrary to previous reports, that ALS mutations uniformly accelerate apo-SOD1 aggregation.^{100,110-111}

Well-to-Well Variation in Reaction Conditions Cannot Explain Observed Stochasticity of Apo-SOD1 Fibrillization.

In this chapter, I sought to determine if the observed stochasticity of SOD1 fibrillization, in particular, the presence of slowly aggregating wells, was an experimental artifact that was caused by well-to-well variations in: (i) the orbital velocity of each Teflon bead, (ii) the local temperature of each well (due to non-uniform heating or friction of the gyrating polystyrene microplate), (iii) variations in the mass or surface properties of one stirring bead, compared to the next, (iv) surface features (i.e., scratches) of one well compared to next, or (v) the presence of contaminants such as common dust particles. For example, I concede that it is possible that wells exhibiting outlier kinetics (“outlier wells”) in Figure 3.1, which aggregated with late lag times, were slow to fibrillize because Teflon beads were failing (for some reason) to orbit circularly in the well at the same mean velocity (rpm) as beads in other wells.

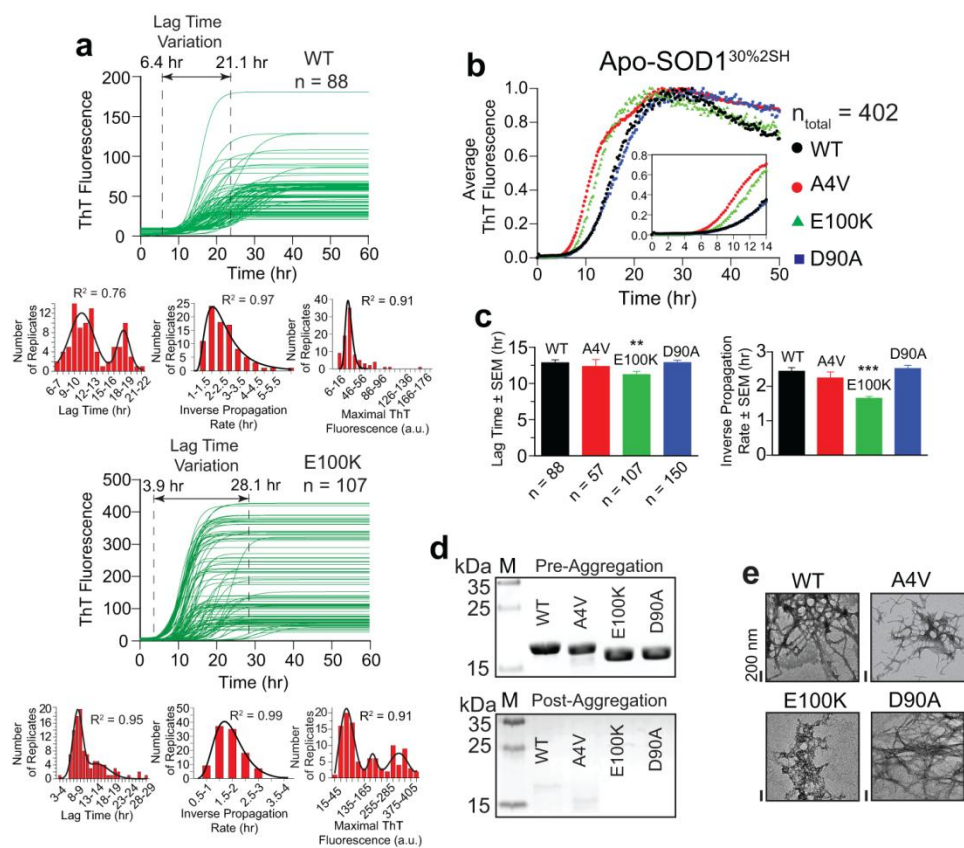


Figure 3.1. In vitro fibrillization of apo-SOD1 in microplate-based ThT fluorescence assays. (a) Sigmoidal fits of ThT fluorescence of replicate assays of WT and E100K apo-SOD1^{30%2SH} carried out in 96-well microplates with mechanical agitation (37 °C, pH 7.4, 150 mM NaCl, 10 mM TCEP, i.e., apo-SOD1^{30%2SH}). Histograms of iterate lag time, inverse propagation rate, and maximal ThT fluorescence are shown as insets below each plot, fit with either a 3-parameter log-normal distribution (Equation 8.8a) or a Lorentzian bimodal function (Equation 8.9). (b) Average and normalized plots of replicate ThT amyloid assays from (a). (c) Mean lag time and inverse propagation rate for all apo-SOD1^{30%2SH} proteins ($p < 0.0001$ ***; $p < 0.01$ **). (d) Upper gel: SDS-PAGE of WT and ALS-variant apo-SOD1^{30%2SH} solutions performed before ThT assay. Lower gel: SDS-PAGE of supernatant of same solutions after ThT aggregation assay and centrifugation. (e) TEM analysis of apo-SOD1^{30%2SH} fibril homogenates after the completion of aggregation assay.

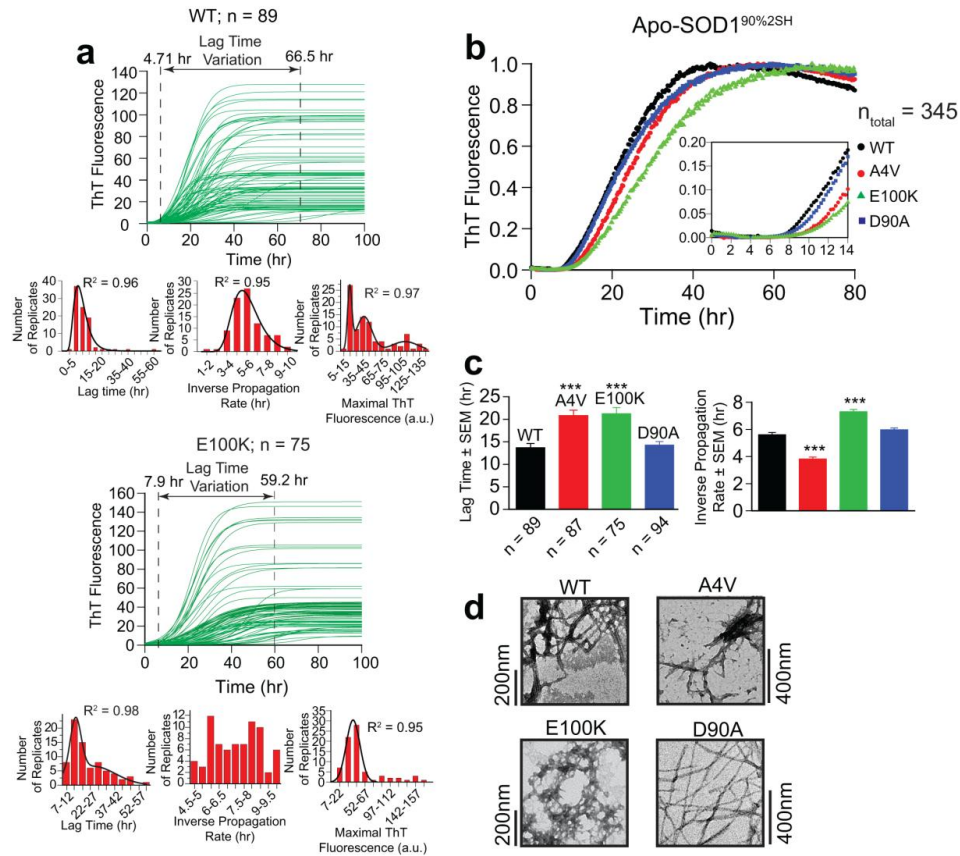


Figure 3.2 Increasing the degree of disulfide reduction from 30 % to 90 % does not eliminate the stochasticity of apo-SOD1 fibrillization in microplate-based ThT fluorescence assays. **(a)** Sigmoidal fits of ThT fluorescence of replicate assays of WT and E100K apo-SOD1^{90%2SH}. Histograms of lag time, inverse propagation rate, and maximal ThT fluorescence are shown as insets below each plot and are fit with either a 3-parameter log-normal distribution (Equation 8.8a) or bimodal Lorentzian function (Equation 8.9). **(b)** Average and normalized plots of ThT fluorescence for all apo-SOD1^{90%2SH} proteins. **(c)** Mean lag time and inverse propagation rate for apo-SOD1^{90%2SH} ($p < 0.0001$ ***). **(d)** TEM micrographs of apo-SOD1^{90%2SH} at the end of aggregation assay.

To test this hypothesis, I performed ThT assays on D90A apo-SOD1^{30%2SH} at 180 rpm and 600 rpm. I found that changing gyration speed by 3-fold did not alter mean lag time by a magnitude sufficient to account for outlier lag times at 360 rpm (Figure 3.3a). In fact, a linear correlation between lag time and shaking speed was found to be only 0.0041 hr/rpm (Figure 8.22), which is insufficient to explain 15 to 30 hr variation in lag

time among wells. The correlation in rpm and lag time translates to a correlation of shear force and gyration speed of 0.13 nN/rpm. Varying the temperature of the microplate from 15 °C to 45 °C—i.e., by a magnitude much larger than any expected well-to-well thermal variation in the temperature controlled fluorescence plate reader—slightly affected the variation in the lag time of fibrillization of A4V apo-SOD1 (Figure 3.3b). However, this temperature alteration (15-45 °C) resulted in $\Delta\tau_{\text{mean}} = 1.01 \text{ hr}/30 \text{ }^\circ\text{C}$, which is insufficient to account for > 15 hr variation in lag times observed at 37 °C (Figure 8.23). I chose to perform the temperature-specific experiments on A4V apo-SOD1^{90%SH} because this ALS-variant protein is intrinsically disordered and changes in temperature from 15 °C to 45 °C will not affect its degree of folding as much as ordered proteins.²⁶ Varying SOD1 concentrations revealed that the mean lag time of D90A apo-SOD1^{30%2SH} fibrillization increased with apo-SOD1 concentration by only $0.2 \text{ hr}\cdot\mu\text{M}^{-1}$, which is insufficient to explain the > 15 hr variation in lag time that I observed in replicate experiments of apo-SOD1 (the D90A apo-SOD1 protein was used for these experiments, per availability) (Figure 3.3c).

The effect of gyration speed (rpm), protein concentration, and temperature on the average noise (η) of each assay can be found in Figure 8.24. By “noise”, I refer to the coefficient of variation, that is calculated at each time point as $\eta = \sigma/I_{\text{avg}}$, where I_{avg} = mean intensity of fluorescence of all replicate measurements at a given time point, and σ = standard deviation of mean intensity. It is possible that some surface features of a specific well or bead (e.g., a scratch or lack thereof, or slight difference between the mass of different Teflon beads) could be the cause of outlier kinetics and apparent stochasticity. To test this hypothesis, I repeated aggregation assays in specific wells, and

reused the same Teflon bead (Figure 3.4a). For these experiments, a specific well and bead that resulted in outlier kinetics were washed with near-boiling SDS, followed by guanidinium hydrochloride, followed by incubation and washing with pepsin solutions to remove any adhered residual aggregates. Aggregation assays were then repeated in these identical wells (using the identical Teflon bead) under the exact same conditions, using apo-SOD1 proteins from the same “mother” stock. The initial rate of aggregation could not be uniformly replicated by repeating assays in the same microplate well, with the same bead (see dashed and solid traces, Figure 3.3a). I point out that small variations in the mass of different Teflon beads likely do not account for stochasticity observed in Figure 3.1a. The 3.18 mm diameter Teflon beads were found to vary in mass by only \pm 0.35 mg (from 36.20 mg to 36.90 mg). Anecdotal evidence suggests that the intrinsic irreproducibility of many amyloid assays is caused by the non-uniform presence of common dust particles that are inadvertently introduced in sample wells during laboratory preparation.

Dust could conceivably accelerate aggregation via surface catalysis,¹²¹⁻¹²² or decelerate aggregation (in the case of apo-SOD1) via Zn^{2+} contamination. Even though I filtered all solutions immediately before dispensing into each microplate, I tested this hypothesis (previously untested, to my knowledge) by deliberately contaminating wells with dust particles collected from bookshelves and windowsills of the Shaw laboratory (where all experiments were performed).

Approximately 1 μg of lab dust—presumably more than could ever be expected to contaminate a single well—was added to wells, and ThT assays were performed on D90A apo-SOD1^{30%2SH}.

Dust particles decreased the mean lag time of fibrillization by 7.2 ± 0.3 hr (Figure 3.4b), and decreased the inverse propagation rate constant from 2.52 ± 0.1 hr to 1.51 ± 0.1 hr.

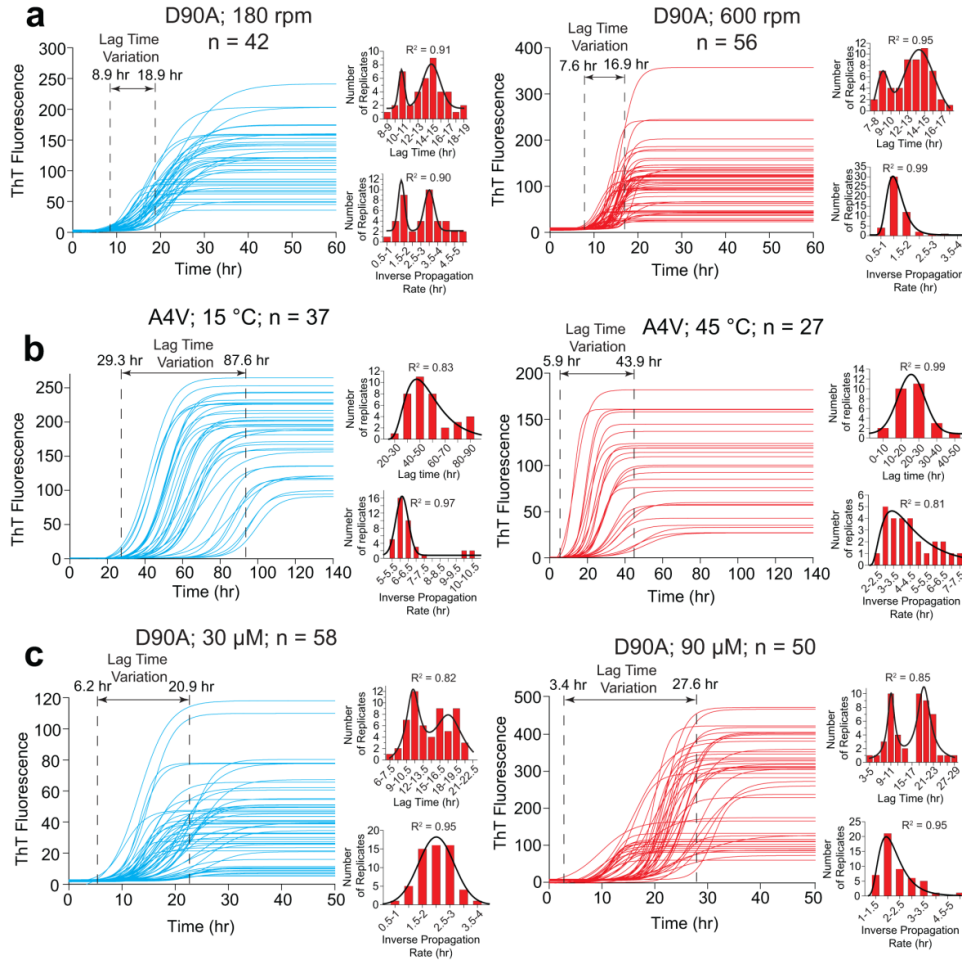


Figure 3.3 Alteration of experimental conditions (SOD1 concentration, gyration rate, and temperature) to mimic possible well-to-well variations in reaction conditions during microplate-based ThT assays of apo-SOD1 fibrillization. (a) ThT fluorescence assays of D90A apo-SOD1^{30%2SH} at different gyration speeds. (b) ThT fluorescence assays of A4V apo-SOD1^{90%2SH} at 15 °C and 45 °C. (c) ThT fluorescence assays at varying [D90A apo-SOD1^{30%2SH}]. Insets next to each plot represent the histograms of lag time and inverse propagation rate. Histograms were fit with either a 4-parameter log-normal function (Equation 8.8b) or a bimodal Lorentzian distribution function (Equation 8.9), except for the histograms of lag time at 45 °C and propagation rate at 30 μ M that showed normal distributions.

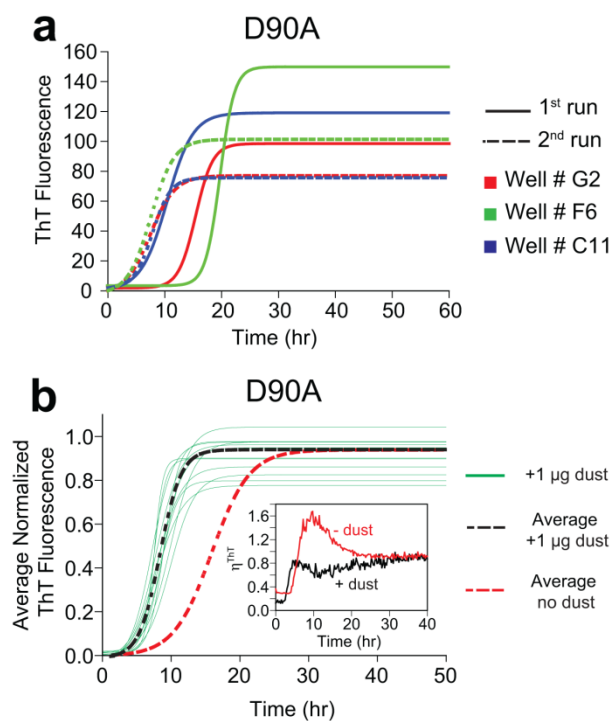


Figure 3.4 Stochastic fibrillization of apo-SOD1 in microplate ThT assays is not an artifact of surface features in a microplate well (or bead), and is not caused by dust contamination from laboratory environment. (a) Repetition of ThT assays in identical microplate wells (washed and reused), with identical Teflon beads (washed and reused) does not abolish kinetic variability. (b) Fibrillization of D90A apo-SOD1^{30%2SH} in the presence of ~ 1 μg of dust particles collected from our laboratory window sills (green traces and black dashed line, n = 12) and absence of dust particles (red dashed line), pH 7.4, 37 °C. Inset shows the plots of noise (η) associated with D90A apo-SOD1^{30%2SH} fibrillization in the presence and absence of room dust.

Moreover, dust contamination actually diminished the noise associated with lag time (inset in Figure 3.4b), as expected with a shorter lag time. Dust contamination cannot, therefore, account for the positive skewness of the probability distributions observed in Figure 3.1, i.e., slow, outlier kinetics with lag times of 30-60 hr.

I found a global correlation between the lag time and propagation rate of amyloid fibrillization for all four apo-SOD1 proteins analyzed in this chapter, under all reaction conditions, i.e., temperature, gyration rate, protein concentration, reductant concentration (Figure 3.5; black circles). This correlation—observed for other proteins,^{9,123} including

apo-SOD1¹⁰⁰—suggests that the product of lag time and propagation rate of apo-SOD1 fibrillization (α) is a constant value ($\alpha = \tau \times k = 2.5 \pm 0.2$), regardless of variations in experimental conditions (Figure 3.5). This value of α for SOD1 is smaller than α reported for other amyloidogenic polypeptides, e.g., $\alpha = 4.5$ for insulin, glucagon, and various toxic mutants of $A\beta_{1-40}$,¹²³ but seems to suggest that the fibrillization mechanism of apo-SOD1 is similar to these proteins.¹²³ The maximal ThT fluorescence intensity also generally decreased with increasing lag time or rate (Figure 3.5; blue triangles and green squares), however, this correlation was not as strong as the logarithmic correlation between τ and k . The projection plots of ThT fluorescence do reveal boundary regions of allowable ThT fluorescence per lag time and propagation rate of a fibril, and vice versa.

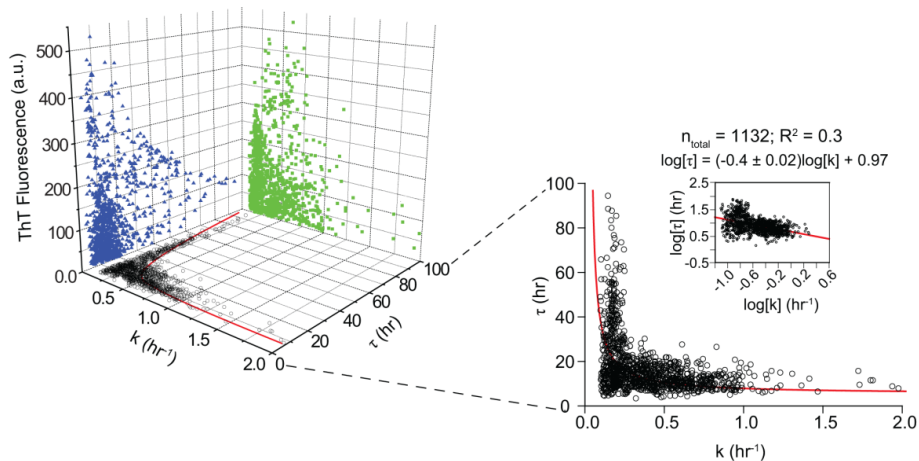


Figure 3.5 Projection plot of maximal ThT fluorescence, lag time, and propagation rate constant of apo-SOD1 fibrillization derived from all 1132 ThT assays of WT and mutant proteins collected under all reaction conditions in this chapter. Inset shows the projection of lag time vs. elongation rate (black circles). Solid red trace is characterized by an α value ($\alpha = \tau \times k$) of 2.5 ± 0.2 , and inset shows similar data in logarithmic scale.

Competition Between Amorphous and Fibrillar Aggregation Pathways Explains Variability of ThT Assays:

Dynamic light scattering and TEM were used to determine if wells that were slow to fibrillize during ThT assays contained monomeric SOD1 throughout the pre-lag phase (Figure 3.6). I do not suspect that such outlier wells were slow to fibrillize because they contained monomeric SOD1 that failed (for some reason) to aggregate, but rather because these wells rapidly formed a significant amount of amorphous aggregates before fibril nucleation, which lowered the concentration of free apo-SOD1 available to fibrillize. This mechanism would account for the trends of increased fibril lag time, decreased fibril propagation rate, and diminished maximal ThT fluorescence observed for outlier wells in Figures 3.1 and 3.2, and summarized in Figure 3.5.

To test this hypothesis, I briefly halted the ThT assays of A4V apo-SOD1^{90%2SH} aggregation after 10 hr, i.e., at a time point near the mean lag time, where several wells will and will not exhibit ThT fluorescence. Aliquots were quickly removed from 12 wells and the ThT assay was continued (each of these 12 wells eventually exhibited a sigmoidal increase in ThT fluorescence, of varying magnitude, with lag times between 12.8 hr and 58.3 hr, Figure 3.6a-c). The 10 hr-aliquots were immediately examined with DLS and TEM (Figure 3.6a-c). DLS showed the presence of an oligomer in all 12 wells of $R_H = 80$ nm (R_H : hydrodynamic radius). This oligomer was even present in wells that went on to fibrillize with a ~ 60 hr lag time, but exhibited zero baseline fluorescence at 10 hr (Figure 3.6c). Only wells that exhibited early lag times in ThT assays contained larger assemblies ($R_H = 8000$ nm) that are presumably fibrillar SOD1 (Figure 3.6a). Wells that exhibited zero fluorescence at 10 hr and lag times of ~ 60 hr did not contain (at 10 hr) monomeric SOD1 or oligomeric species with $R_H = 8000$ nm, but again contained only ThT-negative

assemblies with $R_H = 80$ nm (Figure 3.6c). TEM revealed predominantly amorphous species in these wells with zero fluorescence at 10 h, and lag times of ~ 60 hr. (Figure 3.6c). This result suggests that: (i) wells with late lag time do not contain monomeric SOD1 during the entire pre-lag phase; (ii) amyloidogenesis is in competition, in the microplate assay, with amorphous aggregation, and (iii) cooperativity between amorphous and fibrillar aggregation can explain (at least in part) why some wells form fibril nuclei early, propagate fibrils quickly, and exhibit high ThT fluorescence (Figure 3.6a), and why some wells fibrillize late, propagate slowly, and exhibit low ThT fluorescence, i.e., these wells form, instead, early amorphous aggregates during the ThT assay (Figure 3.6c).

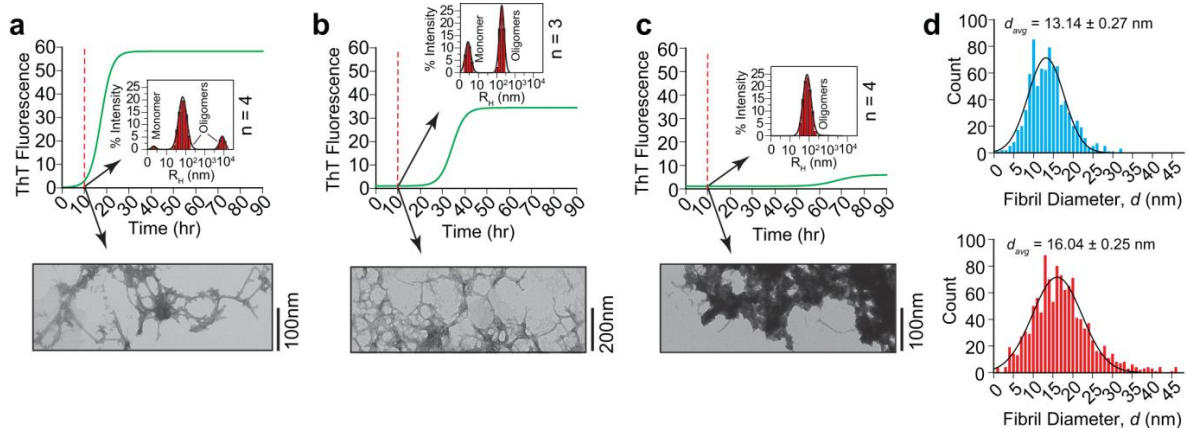


Figure 3.6 Comparison of oligomer morphology from replicate wells containing identical solutions of apo-SOD1. Plots of ThT fluorescence of A4V apo-SOD1^{90%2SH} are shown for (a) fast, (b) intermediate, and (c) slow outliers. Center insets show corresponding mean DLS regularization graphs at 10 hr; n = number of replicate DLS measurements on wells with similar lag times (± 2 hr); monomeric apo-SOD1 has a radius of 1.9 nm.¹²⁴ Insets below each plot are TEM micrographs of wells at 10 hr. (d) Fibril diameter measurements (from TEM micrographs) at the end of 168 hr assay. Upper histogram shows the measurements for fast outlier in panel (a) and lower histogram shows the measurements for slow outlier in panel (c).

Although the TEM analysis of wells that exhibited slow or fast aggregation showed differences in the abundance of fibrillar versus amorphous aggregates (Figure 3.6a,c), I note that the fibrils that were present in both types of wells generally had similar fibril diameter (Figure 3.6d). The average diameter of fibrils in wells that exhibited fibrillization lag times of ~ 10 hr was 13.14 ± 0.27 nm, whereas wells with lag time of ~ 60 hr contained fibrils with average diameter of 16.04 ± 0.25 nm (Figure 3.6d).

To measure the kinetics of amorphous aggregation and further confirm that amorphous aggregation occurs quickly in certain wells, and more slowly in others, I performed ANS fluorescence assays on all fully reduced apo-SOD1 proteins (apo-SOD1^{90%2SH}). Previous studies have utilized ANS to detect and study the formation kinetics of amorphous protein aggregates both *in vitro* and *in vivo*.^{19,125} ANS has been shown to specifically bind to amorphous aggregates, however, ANS has also been reported to bind to amyloid fibrils but fluoresces reportedly more weakly than ThT.¹²⁵ Thus, ANS fluorescence is a suitable probe for detecting total aggregate formation.

The most striking result of ANS assays was that the aggregation of SOD1 in individual wells exhibited divergent, two-state behavior (Figure 3.7a,d and Figure 8.25). For example, a minor fraction of wells (~ 22 %) exhibited exponential (fast) aggregation kinetics without a nucleation (lag) phase and with low maximal ANS fluorescence, whereas the majority of wells exhibited sigmoidal (slow) aggregation kinetics (Figure 3.7a,d and Figure 8.25). Wells that underwent exponential aggregation plots showed weaker ANS fluorescence than sigmoidal ones, and larger aggregates ($R_H \approx 420$ nm in exponential vs. $R_H \approx 160$ nm in sigmoidal, Figure 3.7d). I suspect that the weaker fluorescence in exponential wells compared to sigmoidal is due to light scattering, i.e., \sim

800 nm-wide non-fibrillar particles will scatter or reflect 444 nm and 485 nm light more than fibrillar particles with hydrodynamic diameters of ~ 320 nm. I analyzed these divergent wells with TEM to discern their morphology: wells with exponential kinetics contained amorphous aggregates without any traces of fibrillar structures (Figure 3.7d, red trace). Wells with sigmoidal kinetics contained both amorphous and fibrillar species (Figure 3.7d; black trace). This result suggests that discrete populations (wells) of SOD1 diverge stochastically between amorphous and fibrillar pathways. I hypothesize that isolated populations of SOD1 that exist *in vivo*—e.g., a population isolated by virtue of being in a particular cell—can undergo similar stochastic divergence along different pathways of aggregation.

The sigmoidal aggregation of apo-SOD1 as measured by ANS fluorescence was generally more reproducible than sigmoidal fibrillization measured by ThT (Figures 3.2 and 3.7). For each protein, the lag times associated with sigmoidal ANS-positive aggregation of apo-SOD1^{90%2SH} proteins were within error of the lag times associated with ThT-positive aggregation (Tables 8.7 and 8.8), with the exception of E100K apo-SOD1^{90%2SH} which exhibited the highest number of wells with exponential aggregation (Figure 8.25a). The propagation rate of sigmoidal aggregation was, however, markedly slower (by up to 20 hr) when measured by ANS fluorescence, compared to ThT (Figure 3.2b-c and Figure 3.7b-c), an effect that might be caused by the inhibitory effect of ANS on protein aggregation, compared to ThT.¹²⁶

I point out that none of the ALS mutations that I studied accelerated ANS-positive aggregate nucleation, compared to the WT protein (in the sigmoidal regime, Figure 3.7b-c). In fact, the A4V apo-SOD1^{90%2SH} protein exhibited a longer lag time (by 6.1 ± 2.6 hr)

compared to WT apo-SOD1^{90%2SH} in ANS assays (Figure 3.7b-c, Table 8.8). Moreover, ALS mutations did not uniformly accelerate propagation in ANS assays, e.g., E100K and D90A apo-SOD1^{90%2SH} aggregated with propagation rates within error of WT SOD1. The A4V mutation decreased the inverse rate of propagation of apo-SOD1^{90%2SH} by 6.5 ± 2.2 hr (Figure 3.7b-c, Table 8.8).

I also note that ALS mutations did not accelerate ANS-positive aggregation in the exponential regime (Table 8.8). For example, the rate of exponential aggregate formation of E100K and D90A apo-SOD1^{90%2SH} was lower than WT apo-SOD1^{90%2SH}, however, A4V showed statistically similar rates of exponential aggregation as WT apo-SOD1^{90%2SH} (Table 8.8).

Aggregation of Apo-SOD1 (Measured by DLS) Is Stochastic and Non-Uniformly Accelerated by ALS Mutations.

Because ThT fluorescence cannot detect non-amyloid (e.g., amorphous) or proto-fibrillar oligomers that might not bind ThT (both of which might be toxic species in ALS¹⁸) I also used DLS to measure the rate of formation of SOD1 aggregates, and to quantify the rate of disappearance of monomeric apo-SOD1. In these experiments, solutions of WT and ALS-variant apo-SOD1^{90%2SH} that were analyzed with DLS were treated identically to solutions in standard ThT assays (i.e., agitated in microplate wells, with Teflon beads, in the presence of ThT). DLS measurements were carried out on 33 wells for each ALS variant.

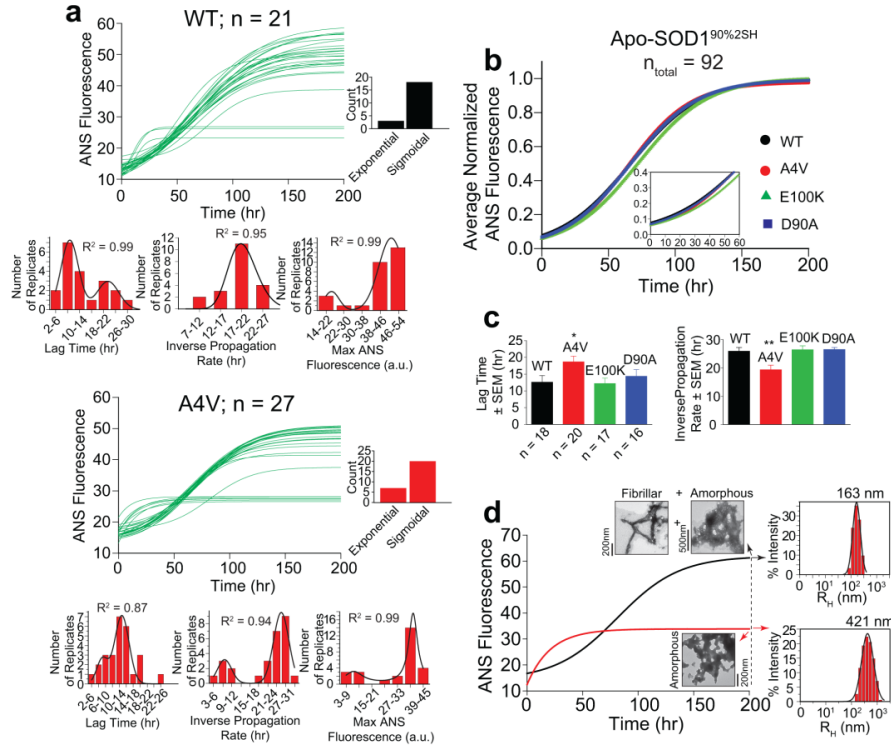


Figure 3.7 Distinct populations (microplate wells) of SOD1 stochastically diverge between exponential amorphous aggregation and sigmoidal amorphous/fibrillar aggregation according to DLS, TEM, and ANS fluorescence. (a) Plots of ANS fluorescence for WT and A4V apo-SOD1^{90%2SH} proteins ($n_{\text{total}} = 48$). Insets below each plot illustrate the histograms for lag time and inverse propagation rate. Inset next to each plot shows the comparison between the number of exponential and sigmoidal traces. **(b)** Average and normalized plots of ANS fluorescence for all apo-SOD1^{90%2SH} proteins (all data points included). Inset shows a magnification of lag phase. **(c)** Comparison plots of lag time and inverse propagation rate for all apo-SOD1^{90%2SH} proteins ($p < 0.05^*$; $p < 0.01^{**}$). **(d)** TEM micrographs and DLS regularization graphs of wells exhibiting exponential aggregating (red trace) and sigmoidal aggregating (black trace) at the end of the ANS fluorescence assay, i.e., ~ 200 hr (traces are for E100K apo-SOD1^{90%2SH}).

All apo-SOD1^{90%2SH} proteins exhibited, according to DLS, stochastic aggregation kinetics with a large range in individual lag times of > 10 hr, in agreement with their fibrillization kinetics (Figure 8.26 contains three representative kinetic plots for each mutant). The approximate lag times of aggregation, interpolated from plots of average radii (R_H) of all species, vs. time, were only 2 hr (Figure 3.8a), i.e., several hours earlier

than the mean lag time of fibrillization in complimentary ThT fluorescence assays (Figure 3.2). This result suggests that ThT-negative SOD1 oligomers form before mature fibrillar assemblies. The plots of R_H vs. time for D90A and WT apo-SOD1^{90%2SH} were superimposable (Figure 3.8a), suggesting identical rates of aggregation.

Extracting exact lag times from plots of R_H vs. time was not possible because mathematical fits of iterate plots only yielded $R^2 < 0.6$. To extract statistically meaningful (and comparable) kinetic values of aggregation, I plotted the decay of monomeric apo-SOD1^{90%2SH}, as measured by DLS (Figure 3.8b).

The decay of monomeric SOD1 was exponential (Figure 3.8b). The half-life of monomeric WT apo-SOD1^{90%2SH} was (according to DLS) statistically identical to the half-life of D90A ($p = 0.21$) and E100K ($p = 0.51$), but ~ 30 % faster than A4V apo-SOD1^{90%2SH} ($p = 0.02$) (Figure 3.8b). The decay of each monomer coincided with the appearance of at least one intermediate oligomer ($R_H = 10^2$ nm) and an equilibrium oligomer ($R_H = 10^3 - 10^4$ nm) (Figure 3.8c). In conclusion, ALS mutations do not uniformly accelerate the aggregation of apo-SOD1, as measured by DLS. These results are in contrast to a previous DLS analysis of apo-SOD1 aggregation by Vassal et al. that reported a uniform increase in the rates of aggregation of ALS-variant apo-SOD1, relative to WT apo-SOD1.¹¹⁰

In this previous study,¹¹⁰ aggregation rates were calculated from averages of 3-5 replicates for each mutant, which might be insufficient (in my opinion) to accurately express the rate of a process as stochastic as SOD1 aggregation.

Noise and Stochasticity in SOD1 Aggregation:

Why is the aggregation of SOD1 into amorphous or fibrillar aggregates stochastic? The most obvious explanation for stochasticity—if there is a singular explanation—is that values of E_a are similar for divergent aggregation pathways that branch from a common, peri-oligomeric state to mature amorphous and/or fibrillar oligomers. Such degeneracies in E_a , despite morphologically different end products (with presumably different equilibrium ΔG) are not far-fetched when considering that the proto-oligomers that precede fibrillization are generally amorphous¹²⁷ and might continue propagating amorphous aggregates as easily as fibrillar ones.

The fact that the nucleation of oligomers composed of ALS-variant SOD1 is “noisier” than that of WT SOD1 suggests that the nucleation of an individual population of ALS-variant SOD1 proteins will be less predictable and less reflective of mean nucleation rates. An ALS mutation can, for example, increase the rate of aggregation of a single population of SOD1 proteins—i.e., the discrete isolated population of SOD1 within a single cell (or here, microplate well)—without increasing the mean rate of aggregation of the entire population of cells or wells. This ability to accelerate aggregation by increasing noise can be seen in Figures 3.1a and 8.20: the fastest replicates of ALS-variant apo-SOD1^{30%2SH} have shorter lag times than the fastest replicates of the WT apo-SOD1^{30%2SH}. Conversely, the slowest wells to aggregate among all ALS-variant apo-SOD1^{30%2SH} data sets aggregated more slowly than the slowest replicates of WT apo-SOD1^{30%2SH}.

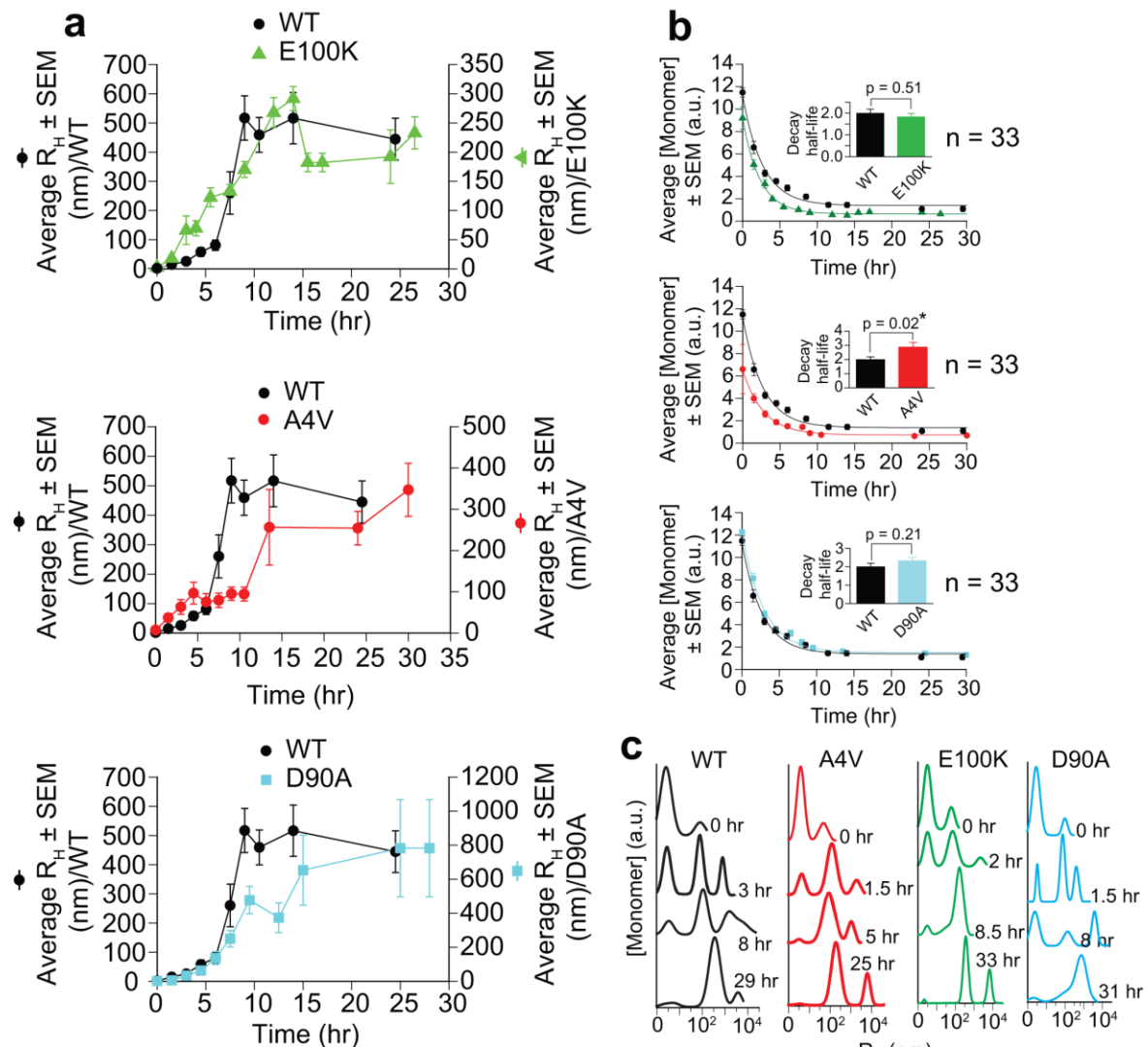


Figure 3.8 Formation of small oligomers and amorphous species of apo-SOD1 is non-uniformly accelerated by ALS mutation. (a) Dynamic light scattering (DLS) plots of aggregation of WT, E100K, A4V, and D90A apo-SOD1^{90%2SH}. Average R_H expresses the average hydrodynamic radius of all species in sample (including any monomeric SOD1), expressed as mean \pm SEM (n = 33). (b) SOD1 monomer decay plots of ALS-variant and WT apo-SOD1^{90%2SH} (derived from experiments in (a)). These plots were generated by the disappearance of monomeric SOD1 that appears at 1.9 nm. Insets show comparison of decay half-life for each protein (p < 0.05*), obtained by an exponential decay fit. (c) Representative DLS regularization graphs for all apo-SOD1^{90%2SH} proteins at different time points show the decay of monomer and formation of oligomers (from which plots in (b) are derived). Error bars express average \pm SEM (n = 33).

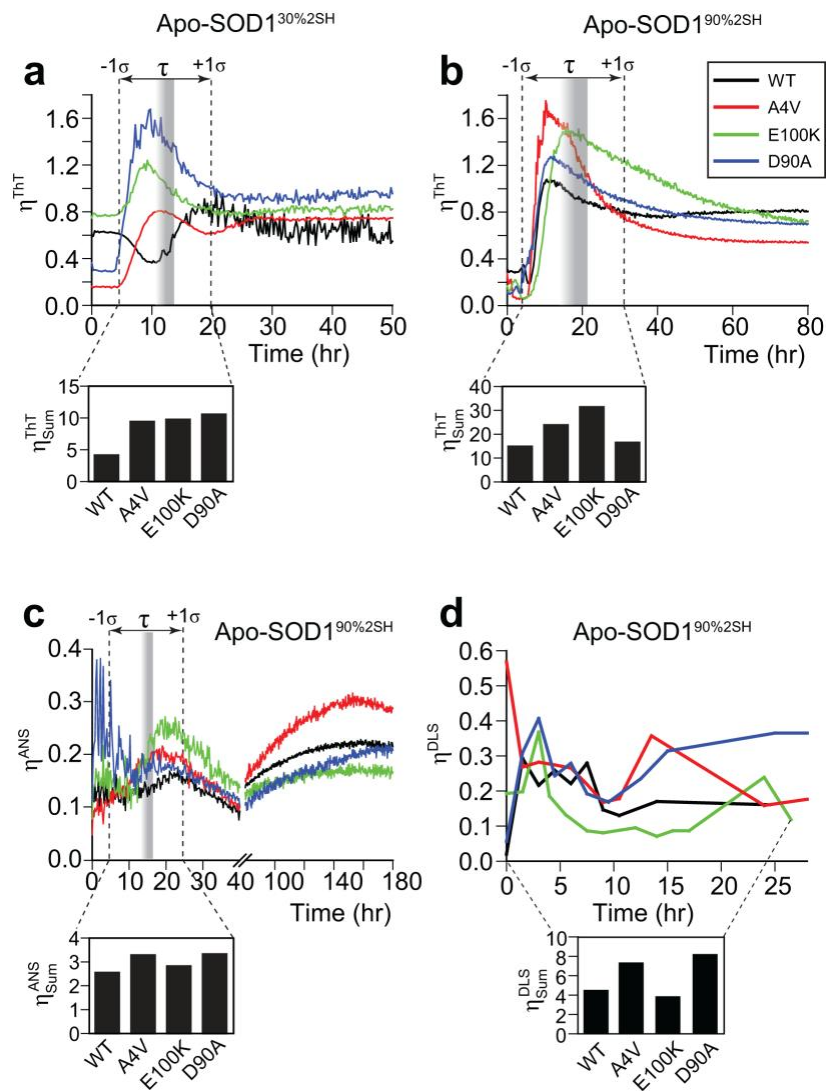


Figure 3.9 Noise (variability) associated with SOD1 oligomer nucleation is increased by ALS mutations. Kinetic plots of oligomer noise (η) associated with ThT fluorescence amyloid assays (**a-b**), ANS aggregate assays (**c**), and DLS non-amyloid aggregation assays (**d**) of WT and ALS-variant apo-SOD1 from Figures 3.1, 3.2, 3.7, and 3.8, respectively. The shaded bar in (**a-c**) represents the range of mean lag time (τ) for all proteins, and dashed lines indicate one standard deviation (σ) from mean lag time. Insets below panels (**a-c**) show plots of total noise (η_{Sum}) associated with the nucleation of oligomeric apo-SOD1. η_{Sum} was quantified via integration of noise plots over the time domain corresponding to $\tau \pm 1\sigma$. η_{Sum} for inset in panel (**d**) was calculated via integration of DLS noise plots over the entire experimental time period.

Implications of Oligomer Noise and Stochasticity in Prion-Like Aggregation:

The results of study presented in this chapter establish three implications for rationalizing *in vitro* SOD1 aggregation data with clinical phenotypes of ALS: (i) attempting to correlate *in vitro* lag times and propagation rates with *in vivo* data (e.g., age of disease onset, survival time after onset) will require mean values that are statistically significant (i.e., calculated from $\geq 10^2$ replicates), (ii) the “noise” of nucleation and propagation might be more important in pathogenesis than mean rates of nucleation and propagation, and (iii) the statistical distribution of iterate lag times and propagation rates (i.e., log normal distributions) might be useful in rationalizing variation in clinical phenotypes associated with a particular mutation. Regarding point (ii), the noise associated with aggregation can play a role in prion-like mechanisms of aggregation. It is reasonable to hypothesize that a mutation can accelerate the aggregation of SOD1 by increasing noise, without increasing mean rates of aggregation. In other words, pathogenesis might be triggered by rapid aggregation in a minor fraction of motor neurons (i.e., noise), wherein oligomeric SOD1 from these cells subsequently infects other cells.

Regarding point (iii), the distribution of onset age for 30 ALS patients with the L144F *SOD1* mutation (the only ALS-*SOD1* mutation I could find with individual ages of onset for a set of $n > 10$ patients) is log-normal ($R^2 = 0.99$, Figure 8.27). Log-normal distributions describe the underlying probability distribution for many stochastic biological phenomena e.g., the latency period of human diseases and variations in the age of onset of other neurodegenerative diseases linked to protein aggregation.¹²⁸

Conclusion:

The SOD1 apo protein proceeds down two divergent, kinetically similar pathways of aggregation—amyloid and amorphous aggregation—and these pathways are followed stochastically. Whichever pathway is initiated first will flourish (*in vitro*) while the other pathway will be diminished via removal of soluble SOD1 by the competing pathway. In other words, some wells will generate oligomers that are more fibrillar and less amorphous, while others will generate less fibrillar and more amorphous oligomers (both types of oligomers are observed *in vivo*^{18,100}). This conclusion not only explains the perplexing variability in ThT amyloid assays of SOD1,^{45,100} but suggests that an isolated population of SOD1—e.g., in an individual microplate well, or analogously in a single motor neuron—can stochastically diverge towards catastrophic oligomerization before populations of SOD1 in neighboring cells/wells.

ALS-linked mutations can also accelerate or decelerate the aggregation of individual populations of SOD1 (i.e., an individual well or cell) without altering mean rates of aggregation of the entire set of wells (or cells), via increasing the noise associated with oligomer nucleation and propagation. All ALS mutations studied in this chapter—including cryptic mutations that have minimal effects on the biophysical properties of SOD1—did not uniformly increase the mean rate of nucleation or propagation of fibrils, but did uniformly increase the noise level associated with fibrillization, that is, increased the probability that SOD1 will *sometimes* self-assemble at rates (and morphologies) that are far from mean values for the WT protein (Figure 3.8). The stochasticity associated with SOD1 oligomerization (*in vitro*), and the effects of ALS mutations on oligomer noise provides a quantitative mechanism for rationalizing the prion-like initiation of

misfolded SOD1 in one neuronal cell and propagation of the oligomer to other cells in the central nervous system. In particular, the stochastic nature of SOD1 aggregation provides a plausible molecular mechanism for McInnes' "one-hit" model of neurodegeneration in ALS.¹²⁹⁻¹³⁰ The "one-hit" model (analogous to Knudson's two-hit hypothesis for oncogenesis¹³¹) suggests that neurodegeneration initiates as a result of a random, catastrophic event inside one cell, followed by propagation to neighboring cells. The "one hit" model is based upon the exponential increase in probability of neuronal cell death with age, in contrast to the cumulative damage model that predicts linear increments in neuronal cell death. The results of the current study suggest that a fraction of individual populations of SOD1—i.e., a fraction of motor neurons—have the intrinsic propensity to undergo rapid, catastrophic self-assembly into neurotoxic oligomers (with rates and morphologies far from the mean) while populations in neighboring cells do not produce a similarly toxic mixture of oligomers, at a similarly rapid rate. The probability that this rare, catastrophic self-assembly might occur in a motor neuron might be increased by pathogenic mutations that increase the noise associated with oligomer nucleation.

Materials and Methods:

SOD1 purification, demetalation, and biophysical characterization:

WT and ALS-variant SOD1 proteins were recombinantly expressed in *S. cerevisiae*, purified and demetalated, as previously described.⁴⁵ The absence of metal ions was confirmed with inductively-coupled plasma mass spectrometry (ICP-MS). Protein purity, thermostability, and lack of tryptophan oxidation were confirmed with mass spectrometry and differential scanning calorimetry, as previously described.⁴⁵

Apo-SOD1^{30%2SH} (~ 30 % disulfide reduction) was prepared by incubating apo-SOD1^{S-S} in 10 mM TCEP (pH 7.4, 22 °C) with mild orbital shaking (90 rpm) for 6 hr prior to initiation of aggregation assay with Teflon bead and rapid shaking (360 rpm). Apo-SOD1^{90%2SH} (> 90 % disulfide reduction) was generated by incubating apo-SOD1^{S-S} in 100 mM TCEP (pH 7.4, 22 °C), with orbital shaking (90 rpm), for 6 hr. The degree of disulfide reduction was estimated with differential scanning calorimetry, based upon the T_m values for fully oxidized and fully reduced proteins. The degree of monomerization for WT and ALS-variant apo-SOD1 proteins was determined with size-exclusion chromatography using a Zorbax G250 column coupled to a photodiode array (PDA) detector, as previously described.⁴⁵ Differential scanning calorimetry was performed with a Microcal LLC VP-DSC at [SOD1] = 2 mg/mL (10 mM KPO₄, pH 7.4), as previously described.⁴⁵ Electrospray ionization mass spectrometry was performed on an LTQ LX/Orbitrap Discovery ESI-MS (Thermo Scientific), as previously described.⁴⁵

Thioflavin-T (ThT) and 1-anilino-8-naphthalene sulfonate (ANS) fluorescence aggregation assays:

High-throughput ThT and ANS aggregation assays were performed in a 96-well microplate, as previously described.⁴⁵ See chapter 8 for details on replicate assays that were performed on re-used Teflon beads and microplates.

Dynamic light scattering:

Dynamic light scattering (DLS) experiments were performed with a DynaPro Nanostar instrument (Wyatt Technology, Santa Barbara, CA). The following parameters were set for all measurements: peak radius low cutoff: 0.5 nm; peak radius high cutoff:

10^4 nm; correlation function low cutoff: 1.5 μ s; correlation function high cutoff: 6×10^4 μ s. For each DLS assay, a 10 μ L aliquot of each well was used and results were reported as the average of 10 consecutive autocorrelation functions (acquisition time = 5 s). Kinetic DLS assays were carried out on aliquots taken from wells of microplates. Protein solutions in microplates were prepared and treated identically as in ThT amyloid assays (i.e., filtered, shaken with rotary agitation using Fluoroskan plate reader and Teflon beads) and ThT was added.

Transmission electron microscopy (TEM):

Morphology of resultant aggregates of all apo-SOD1 proteins (fibrillar or amorphous) after ThT/ANS and DLS assays was determined with a JEOL 1230 High Contrast Transmission Electron Microscope operating at 80 kV, as described elsewhere.⁴⁵

Acknowledgement:

Financial support for this research was provided to BFS by the Department of Defense (W81XWH-11-1-0790), the National Science Foundation (CHE: 1352122), and the Welch Foundation (AA-1854). I would like to thank Dr. Bernd Zechmann (Center for Microscopy and Imaging, Baylor University, Waco, TX) for technical support during microscopy and image analysis.

CHAPTER FOUR

Kaplan–Meier Meets Chemical Kinetics: Intrinsic Rate of SOD1 Amyloidogenesis Decreased by Subset of ALS Mutations and Cannot Fully Explain Age of Disease Onset

This chapter is published as:

Abdolvahabi A, Shi Y, Croom CM, Rasouli S, Aliyan A, Martí AA, Shaw BF (2017)
Kaplan–Meier Meets Chemical Kinetics: Intrinsic Rate of SOD1 Amyloidogenesis Decreased by Subset of ALS Mutations and Cannot Fully Explain Age of Disease Onset. *ACS Chem. Neurosci.* **8**, 1378-1389.¹³²

Abstract

Over 150 mutations in *SOD1* cause amyotrophic lateral sclerosis (ALS), presumably by accelerating SOD1 amyloidogenesis. Like many nucleation processes, SOD1 fibrillization is stochastic (*in vitro*), which inhibits determination of aggregation rates (and obscures whether rates correlate with patient phenotypes). In this chapter, I diverged from classical chemical kinetics and used Kaplan-Meier estimators to quantify the probability of apo-SOD1 fibrillization (*in vitro*) from $\sim 10^3$ replicate amyloid assays of wild-type (WT) SOD1 and nine ALS variants. The probability of apo-SOD1 fibrillization (expressed as a Hazard ratio) is increased by certain ALS-linked *SOD1* mutations but is decreased or remains unchanged by other mutations. Despite this diversity, Hazard ratios of fibrillization correlated linearly with (and for three mutants, equaled) Hazard ratios of patient survival ($R^2 = 0.67$; Pearson's $r = 0.82$). No correlation exists between Hazard ratios of fibrillization and age of initial onset of ALS ($R^2 = 0.09$). Thus, Hazard ratios of fibrillization might explain rates of disease progression, but not onset. Classical kinetic metrics of fibrillization, i.e., mean lag time and propagation rate, did not correlate as strongly with phenotype (and ALS mutations did not uniformly

accelerate mean rate of nucleation or propagation). A strong correlation was found, however, between mean ThT fluorescence at lag time, and patient survival ($R^2 = 0.93$); oligomers of SOD1 with weaker fluorescence correlated with shorter survival. The study presented in this chapter suggests that *SOD1* mutations trigger ALS by altering a property of SOD1 or its oligomers other than the intrinsic rate of amyloid nucleation (e.g., oligomer stability; rates of intercellular propagation; affinity for membrane surfaces; maturation rate).

Introduction

Do *SOD1* mutations cause amyotrophic lateral sclerosis (ALS)⁷ by uniformly increasing the intrinsic rate of amyloidogenesis of SOD1?^{100,133} This simple question cannot be rigorously answered with current kinetic data. The intrinsic (*in vitro*) aggregation rates of only four out of > 150 different ALS variants of apo-SOD1 have been determined at pH 7,^{45,64,98,100} with the statistical significance required to measure rates of processes that are as stochastic.^{45,64,98,100}

Answering this question will help discern whether *SOD1* mutations trigger ALS by increasing intrinsic rates of nucleation or propagation of SOD1 oligomers or by another mechanism, such as increasing the intrinsic cytotoxicity of oligomers or impairing maturation processes critical to preventing oligomerization.¹³⁴ Quantifying intrinsic rates of SOD1 aggregation will help answer several other questions. For example, does SOD1 cause ALS by self-assembling into a neurotoxic, amyloid-like oligomer⁹⁹ or is fibrillization a primarily non-pathogenic side effect (similar to the amyloidosis of immunoglobulins in multiple myeloma)?¹³⁵ Can the intrinsic rate (or free

energy) of ALS-variant SOD1 amyloidogenesis explain (in part or whole) the wide variation in the age of onset or survival time of ALS patients with different *SOD1* mutations?^{111,136} Expecting a correlation (of some magnitude) between mutant SOD1 biophysics and patient phenotype is not unrealistic.¹³⁷⁻¹⁴⁰ Direct genotype-phenotype correlations exist in some monogenic diseases,¹⁴¹ e.g., Pompe disease¹⁴² and favism.¹⁴³

The importance of accurately quantifying the intrinsic (*in vitro*) rates of SOD1 fibrillization is buffeted by reports suggesting that SOD1 aggregation in transgenic ALS mice follows the same stochastic nucleation and propagation kinetics (or “simplistic test tube behavior”¹⁰⁰) as during *in vitro* experiments with recombinantly expressed SOD1.¹⁰⁰ Quantifying rates of SOD1 aggregation *in vitro* is difficult because SOD1 aggregation—both amorphous and fibrillar—is stochastic (in microplate assays that involve mechanical agitation and a significant air-water interface).^{45,64,100} For example, identical aliquots of E100K apo-SOD1 analyzed simultaneously in the same microplate can produce fibril lag times that vary from 7 to 50 hours.⁹⁸ Quantifying statistically significant rates of stochastic processes requires myriad replicate measurements (ideally, $n \geq 10^2$).⁷³

The stochasticity associated with SOD1 aggregation does not appear to be an artifact of random or systematic experimental error (although the importance of disruptions in the air-water-interface during mechanical agitation¹⁴⁴ have not been explored sufficiently for SOD1 to exclude interfacial effects as a partial source of stochasticity).⁹⁸ Processes of self-assembly that involve nucleation are commonly stochastic.^{73,107,145-146} The stochasticity associated with SOD1 nucleation might be caused by competing pathways of aggregation (i.e., amorphous versus fibrillar; branched fibrils versus unbranched) that have similar activation energies.⁹⁸ The stochastic elongation of

fibrils could be caused by random secondary nucleation⁹ (i.e., the random breaking of fibrils at myriad positions along a fibril axis). Previous kinetic measurements of apo-SOD1 aggregation that involved low (or variable) statistical power suggest that ALS mutations uniformly accelerate SOD1 aggregation *in vitro*,^{100,110-111} and that measured aggregation rates correlate with patient life-span.¹¹¹ Measurements in the two of these studies involved low numbers of replicate measurements for each variant protein (i.e., 2-10 replicate assays per protein).¹¹⁰⁻¹¹¹ A third study by Lang and co-workers measured fibrillization rates of four ALS-variants of SOD1 (at pH 6.3), and several other pseudo-ALS variants that also contain C6S, C111S, and F50E substitutions. Kinetic values in this study were reported as averages of between 6 and 198 replicates, which makes it difficult to assess the significance of rates for any given variant.¹⁰⁰ A recent study from our group examined rates of amorphous and fibrillar aggregation at reasonable statistical power (n > 50 per variant), but only examined three ALS-variants of SOD1.⁹⁸ I found that the D90A mutation affects the rate of apo-SOD1 fibrillization by a negligible amount.⁹⁸

The stochastic nature of SOD1 aggregation *in vitro* and observations *in vivo* that SOD1 oligomers form in a fraction of neural cells before prion-like transmission and propagation to neighboring cells,⁹⁹ caused me to question whether conventional metrics express aggregation kinetics in physiologically relevant terms. For example, does a probability-based metric more realistically reflect aggregation processes *in vivo*, compared to average rates of nucleation or elongation? In this chapter, I propose that the probability distribution of aggregation is a more realistic benchmark because pathogenesis might require initial aggregation of SOD1 in a small fraction of motor neurons, regardless of whether SOD1 aggregates *ab initio* in the vast majority of

cells.^{99,147} To this end, I used Kaplan-Meier estimators¹⁴⁸ to compute the probability of amyloid fibrillization among 825 identical (iterate) solutions of wild-type apo-SOD1 and nine different ALS-variants of apo-SOD1 using microtiter plates. Kaplan-Meier analysis is widely used¹⁴⁹ to quantify the probability of an “event” in test versus control subjects—typically the death of mice or humans¹⁵⁰⁻¹⁵²—but has not been used to monitor stochastic chemical reactions. In this chapter, Kaplan-Meier estimators were used to determine the risk that an isolated solution of purified ALS-variant apo-SOD1 (within a single microplate well) will aggregate into a thioflavin-T positive oligomer, relative to solutions of wild-type apo-SOD1 in other wells (both under reducing conditions).

Results and Discussion

ALS-variant SOD1 proteins examined in this chapter (Figure 4.1a) were chosen for their diverse clinical properties, their wide range in free energy of folding, and for their position as gross outliers in previous correlation plots of clinical and biophysical properties.¹⁵³ For example, the L38V missense mutation presents with a short survival time after disease onset (2.4 years), G37R with a long survival time (18 years); D90A is moderate (8 years);¹³⁶ E100K and D90A SOD1 are biophysically and chemically “cryptic” proteins with native structure, stability, metal affinity, and enzymatic activity similar to WT SOD1;¹⁵⁴ the H46R variant has impaired metal binding;²⁶ the A4V mutation severely destabilizes SOD1 and is the most common ALS-*SOD1* mutation in North America.³⁰ I measured fibrillization rates of SOD1 proteins in the metal-free (apo) state because: (i) I wished to determine if any uniform relationship exists between a fundamental biophysical property of ALS-variant SOD1 polypeptides—here, probability

of fibrillization for bare polypeptide—and clinical phenotype in patients. The apo state is the only state that all known ALS-variants of SOD1 can uniformly populate; (ii) demetallated SOD1 is the most prone to aggregate into amorphous and fibrillar species;^{94,155} (iii) active-site metal binding is not required for ALS pathogenesis;¹⁵⁶ and (iv) metal-free SOD1 is a primary constituent of aggregated SOD1 species that form *in vivo*.¹⁵⁷

Prior to initiating microtiter plate fibrillization assays, all recombinantly expressed and purified SOD1 proteins were demetallated and contained ≤ 0.08 equivalents of Zn^{2+} (per dimer) and ≤ 0.05 equivalents of Cu^{2+} (per dimer) according to ICP-MS (Table 4.1). SOD1 proteins were demetallated to levels that were between 97 % and 99 % free of copper and zinc for all proteins studied (i.e., the extent of demetallation only varied by 2 % across all mutants studied). Proteins with the highest levels of residual metal (e.g., WT SOD1) contained ~ 0.08 equivalents of Zn^{2+} per dimer and ~ 0.04 equivalents of Cu^{2+} per dimer (of a maximum of 4.0 theoretical equivalents), i.e., WT SOD1 was 97 % demetallated. Proteins with the lowest levels of Cu^{2+} and Zn^{2+} (e.g., H46R: 0.01 Zn^{2+} /dimer and 0.01 Cu^{2+} /dimer) were 99 % demetallated. Differential scanning calorimetry (DSC) and mass spectrometry confirmed that all proteins were properly folded and lacked any post-translational modifications (Figure 4.1b-c),

All amyloid assays were performed in 10 mM TCEP. I chose this level of reducing agent (instead of 100 mM levels used in some of my previous reports⁹⁸) because it more closely mimics intracellular redox potentials (intracellular glutathione can vary from 0.5 to 10 mM across subcellular loci¹⁵⁸). I chose TCEP, over DTT, because TCEP is ~ 10 -fold more stable to air oxidation than DTT.¹⁵⁹

Table 4.1 Thermostability and metal content of apo-SOD1 proteins.

SOD1 Variant	T _m (°C)	Zn ²⁺ (per dimer)	Cu ²⁺ (per dimer)
WT	53.54	0.08	0.04
A4V	41.61	0.03	0.01
G37R	45.51	0.04	0.04
L38V	42.70	0.02	0.02
H46R	53.48	0.01	0.01
D90A	49.70	0.07	0.03
G93R	42.80	0.05	0.02
E100K	49.18	0.08	0.05
E100G	43.51	0.02	0.04
I113T	42.36	0.02	0.01

Reduction of the disulfide bond in SOD1 has been shown to be critical in accelerating amyloid formation (more so than dissociation of Cu²⁺ or Zn²⁺).¹³⁴ All proteins were incubated in TCEP for 30 minutes prior to the initiation of the amyloid assay (i.e., prior to orbital gyration and fluorescence spectroscopy). I point out that after 30 min, only a fraction of proteins (e.g., ~ 5-10 % for WT apo-SOD1) are reduced, according to DSC and size-exclusion chromatography (Figure 8.28). This brief, incomplete reduction prior to the beginning of assays minimizes the formation of soluble oligomer seeds and allows sufficient time to pipette mixtures of SOD1, ThT, and TCEP into microplate wells, seal plate, and load into the fluorescence spectrophotometer. Complete reduction will occur, however, after the beginning of orbital gyration and fluorescence.¹³⁴ For example, previous studies have shown that SOD1 proteins require ~ 1.3 hr to be fully reduced in the presence of 5 mM DTT at 37 °C (with orbital gyration).¹³⁴ Thus, disulfide reduction kinetics (and how they might vary among mutant) is built into the assay design. The sets of individual longitudinal plots of ThT fluorescence for each replicate amyloid assay (Figure 4.2a) exhibited the characteristic broad range in lag time, steepness, and maximum fluorescence that have been previously

reported for the fibrillization of WT and ALS-variant apo-SOD1 in microtiter plate assays.^{45,64,98} Only one variant, H46R SOD1, did not show any ThT fluorescence during the course of assay (Figure 4.2a) and did not fibrillize according to TEM, but remained soluble according to SDS-PAGE (Figure 4.2c). The absence of fibrillization for H46R SOD1 has been recently reported by a separate research group (that studied the N-terminally unacetylated human protein expressed by *E. coli*).¹⁶⁰

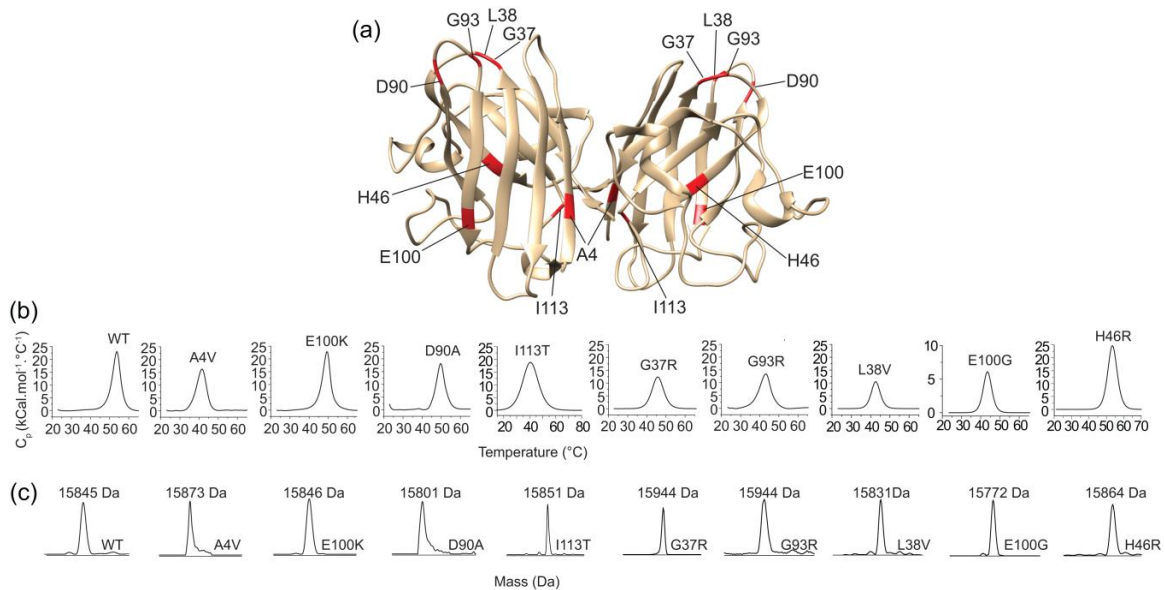


Figure 4.1 Biophysical characterization of apo-SOD1 proteins. (a) Ribbon structure of apo-SOD1 dimer (PDB: 2C9V). Location of amino acid substitutions highlighted in red. (b) Differential scanning thermograms, and (c) electrospray ionization mass spectra of WT and ALS-variant apo-SOD1 proteins.

All other ALS variants (and the WT protein) aggregated into fibrillar species (Figure 4.2b). The longitudinal traces with weak maximal fluorescence and late lag times have been previously shown to not be caused by a lack of protein aggregation, *per se*,^{19,98} but instead reflect the co-formation of different structural types of aggregates (some of

which are amorphous^{19,98}) that exhibit weaker ThT fluorescence. For example, analysis of protein solutions before each aggregation assay, and after centrifugation at the end of each assay demonstrated that SOD1 proteins aggregate into sedimentable species (except for H46R apo-SOD1, which remained mostly soluble), even in wells exhibiting weak maximal fluorescence (Figure 4.2c).

When analyzing replicate amyloid assays (from Figure 4.2a) with Kaplan-Meier analysis (Figure 4.3a), I defined an “event” as the occurrence of fibrillization in any well of the microtiter plate, as defined by reaching half of the maximum ThT fluorescence, i.e., the inflection point of the sigmoidal plots shown in Figure 4.2a (i.e., t_0 in Equation 4.1). In this chapter, the principal read-out of Kaplan-Meier analyses is a Hazard ratio of ALS-variant fibrillization. The Hazard ratio of fibrillization is the risk that an iterate solution of ALS-variant apo-SOD1 will fibrillize relative to the risk that an iterate solution of WT apo-SOD1 will fibrillize over that same time period. Hazard ratios of fibrillization were calculated using the log rank method (similar to methods used to calculate Hazard ratios of ALS patients¹³⁶). Hazard ratios > 1 indicate that the mutant SOD1 protein has a greater risk of fibrillization relative to WT SOD1; ratios = 1 demonstrate equal risk; ratios < 1 demonstrate less risk.

The sets of individual longitudinal plots of ThT fluorescence for each replicate amyloid assay (Figure 4.2a) exhibited the characteristic broad range in lag time, steepness, and maximum fluorescence that have been previously reported for the fibrillization of WT and ALS-variant apo-SOD1 in microtiter plate assays.^{45,64,98} Only one variant, H46R SOD1, did not show any ThT fluorescence during the course of assay (Figure 4.2a) and did not fibrillize according to TEM, but remained soluble according to

SDS-PAGE (Figure 4.2c). The absence of fibrillization for H46R SOD1 has been recently reported by a separate research group (that studied the N-terminally unacetylated human protein expressed by *E. coli*).¹⁶⁰

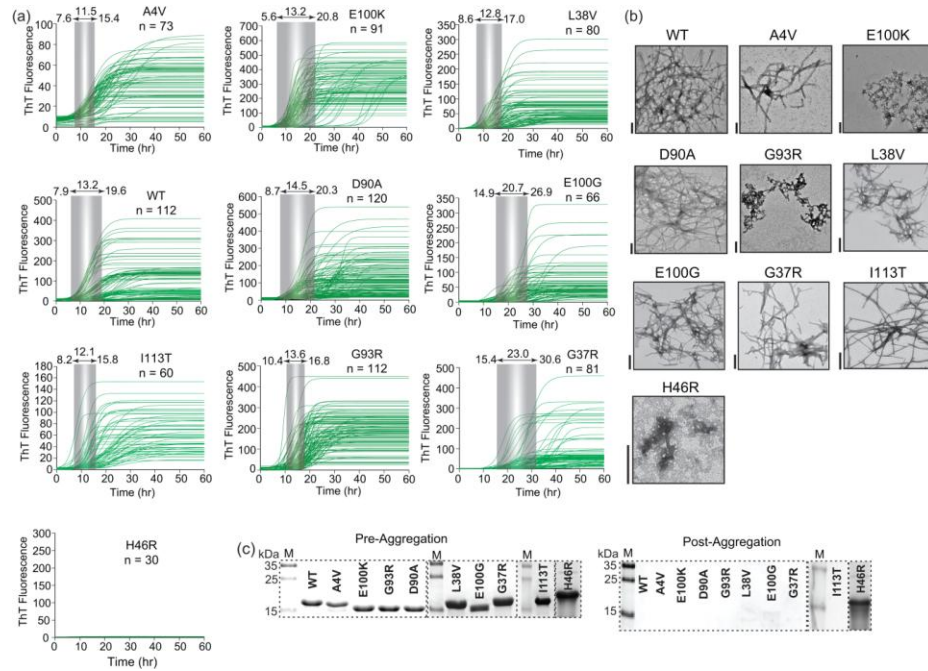


Figure 4.2 Stochastic fibrillization of WT and ALS variant apo-SOD1. (a) ThT fluorescence assays of fibrillization for WT and ALS-variant apo-SOD1 performed in microtiter plates (37 °C, pH 7.4, 10 mM TCEP). Each trace represents an iterate assay ($n_{\text{total}} = 825$; the number of assays for each variant depended upon availability). Shaded area in each plot illustrates the time range corresponding to the average lag time (τ) \pm one standard deviation (σ). The average lag time for each SOD1 variant is listed above double arrow. Note: H46R apo-SOD1 did not fibrillize. (b) Transmission electron micrographs of proteins after completion of assay. (c) SDS-PAGE of all apo-SOD1 proteins before and after the ThT aggregation assay. Scale bars = 200 nm.

The Hazard ratios of fibrillization calculated for each mutant protein from Kaplan-Meier analysis of amyloid assays in Figure 4.2a revealed multiple trends that do not emerge as clearly with classical metrics of fibrillization (Figure 4.3b). Several ALS variants exhibit a higher probability of fibrillization than WT SOD1, for example, A4V,

L38V, I113T and G93R have Hazard ratios > 1 (Figure 4.3b; Table 4.2). Other variants have lower probability, e.g., E100G, G37R, and H46R SOD1 have Hazard ratios < 1 . The Hazard ratio for H46R SOD1 was set to zero, because this SOD1 variant did not aggregate. For D90A SOD1, the risk of fibrillization equals that of the WT protein: Kaplan-Meier plots are statistically similar ($p = 0.76$; Table 4.2), perfectly superimposed (see black and red traces; Figure 4.3b), and the Hazard ratio for D90A is ~ 1 (Table 4.2). I point out that the G37R, D90A, and E100G variants of SOD1 have been classified previously as “WT-like”,^{93,161} that is, these proteins are isolated from biological systems with normal amounts of coordinated metal ions.⁹³

I compared Hazard ratios of fibrillization with survival Hazard ratios of 451 patients with SOD1-linked familial ALS and 269 patients with sporadic ALS (who presumably express wild-type SOD1). Hazard ratios of SOD1 fibrillization correlated linearly with Hazard ratios of survival for patients with SOD1-linked ALS (Figure 4.3c; $R^2 = 0.67$; Pearson's $r = 0.82^*$). In particular, for three mutations, Hazard ratios of fibrillization almost perfectly equaled Hazard ratios of patient survival (i.e., 1.60 vs. 1.40 for L38V; 0.07 vs. 0.00 for H46R; 0.69 vs. 0.70 for E100G; Table 4.2). Hazard ratios of survival reflect the ratio of probabilities that a patient with SOD1-linked familial ALS will succumb (after diagnosis) over a certain time period, relative to patients with sporadic ALS. Thus, Hazard ratios of survival express the rate of progression of SOD1-linked familial disease, relative to sporadic ALS: values > 1 indicate faster progression, relative to sporadic ALS; ratios $= 1$ and < 1 indicate equal or slower progression, respectively. The observation that ALS-SOD1 mutations do not uniformly increase the probability of fibrillization—that some mutations slow the rate of amyloidogenesis—is

consistent with clinical findings that these same mutations produce forms of SOD1-linked familial ALS that progress more slowly and present with longer survival times than typical sporadic ALS. Despite this apparent correlation, I caution that more mutants will need to be studied and more patient data collected before a general, definitive conclusion can be reached.

Hazard ratios of fibrillization also correlated moderately with mean survival time of ALS patients (post-diagnosis), where higher Hazard ratios of fibrillization corresponded to shorter patient lifespan after disease diagnosis ($R^2 = 0.71$; Pearson's $r = -0.84^*$). Unlike the link between Hazard ratios of SOD1 fibrillization and patient survival, Hazard ratios of SOD1 fibrillization did not correlate (positively or negatively) with the mean age of disease onset reported for each mutation ($R^2 = 0.09$; Pearson's $r = 0.29$). This lack of correlation suggests—but does not yet definitively prove—that the intrinsic rate at which apo-SOD1 fibrillizes is, by itself, not a singular dominant driving force in the initial onset of disease, but might be a driving force in disease progression.

In order to interpret Kaplan-Meier plots in explicit units of time, I also calculated the mean time to failure (i.e., the time at which 50 % of the wells aggregate) for each SOD1 variant. This value is calculated by fitting terrace plots in Figure 4.3 with a 4-parameter sigmoidal function (Equation 4.1). The mean time to failure for all SOD1 variants correlated fairly well with survival data from ALS patients (Figure 4.3d and Table 4.2).

Three classical metrics of aggregation (mean lag time; mean elongation/propagation rate; mean maximal ThT fluorescence) were also calculated for each SOD1 protein, from iterate amyloid assays in Figure 4.2a (Table 4.2). Mean lag

times of fibrillization for each variant showed a moderate correlation with Hazard ratios of fibrillization (Figure 8.29; $R^2 = 0.53$; Pearson's $r = -0.73^*$), as is typically observed in comparisons of mean rates of an “event” with Kaplan-Meier Hazard ratios of the same event. The rates of aggregation of some ALS variants, when expressed with classical metrics, qualitatively mirrored Hazard ratios of fibrillization. For example, consistent with Hazard ratios of fibrillization < 1 , G37R and E100G mutations increased mean lag times of fibrillization (by ~ 2 -fold) compared to WT apo-SOD1 ($p < 0.0001$). The two “cryptic” variants, E100K and D90A, showed statistically similar mean lag times to WT SOD1 (Figure 4.4a-b, Table 4.2); A4V decreased lag time by 1.91 ± 0.75 hr.

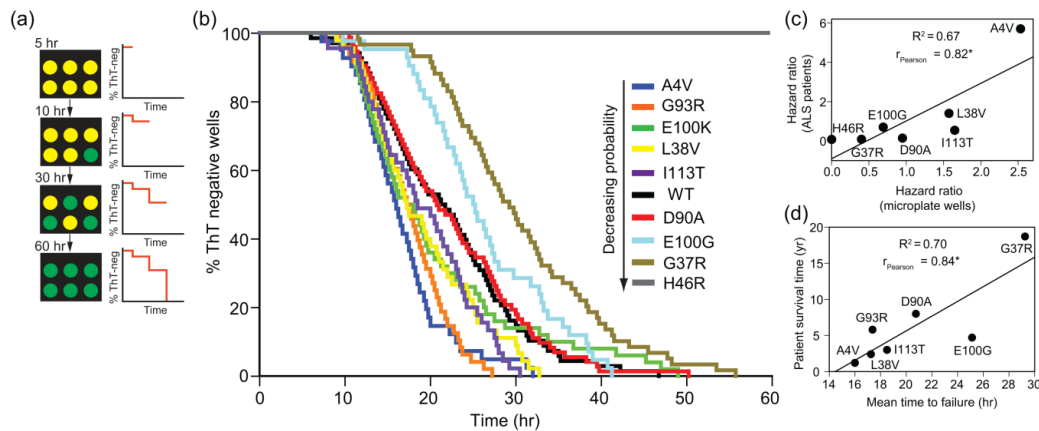


Figure 4.3 Kaplan-Meier analysis of stochastic *in vitro* apo-SOD1 fibrillization and comparison with clinical phenotypes. (a) Schematic illustration of Kaplan-Meier analysis of *in vitro* microtiter plate amyloid assays. Yellow and green circles illustrate the non-aggregated and aggregated wells, respectively; each “down step” in the Kaplan-Meier plot represents the aggregation of a specific well. (b) Kaplan-Meier plots for *in vitro* amyloid assays of all apo-SOD1 proteins studied. Each vertical line in each plot indicates the time when a microplate well reaches its inflection point during its sigmoidal increase in ThT fluorescence. (c) Linear correlation between clinical Hazard ratios (for ALS patients) and Hazard ratios of SOD1 fibrillization (slope = 1.92). Patient Hazard ratios were determined from 720 patients in a previous report.¹³⁶ Note: Hazard ratios are not available for G93R and E100K variants because of low patient number. (d) Linear correlation between patient survival time and mean time to failure for each SOD1 variant. Asterisk indicates statistical significance of Pearson’s coefficient (95 % confidence interval; * = $p < 0.05$).

Table 4.2 Kinetic parameters of *in vitro* apo-SOD1 fibrillization (10 mM TCEP, 37 °C, pH 7.4) and corresponding patient Hazard ratios. Data are shown as mean \pm standard error of the mean (SEM).

SOD1 ^a	Lag time, τ (hr)	Propagation rate, k (hr ⁻¹)	Maximal fluorescence f (a.u.)	HR (fibrillization) ^b	HR (ALS patients) ^c	Mean time to failure (hr)
WT	13.4 \pm 0.5 (n = 112)	0.20 \pm 0.01	88.5 \pm 9.6	1.00	1.00	21.50
A4V	11.5 \pm 0.5 (n = 73)	0.50 \pm 0.02	33.3 \pm 2.1	2.50 (p < 0.0001)	5.70	16.00
G37R	23.0 \pm 0.8 (n = 81)	0.35 \pm 0.01	86.0 \pm 10.2	0.40 (p < 0.0001)	0.08	29.25
L38V	12.8 \pm 0.5 (n = 80)	0.46 \pm 0.02	74.5 \pm 6.4	1.60 (p = 0.03)	1.40	17.25
H46R	N/A	N/A	\approx 0.00	0.00 ^d	0.075	N/A ^d
D90A	14.5 \pm 0.7 (n = 120)	0.41 \pm 0.02	114.6 \pm 7.9	0.95 (p = 0.76)	0.14	20.75
G93R	13.6 \pm 0.3 (n = 112)	0.57 \pm 0.03	221.2 \pm 23.9	2.58 (p < 0.0001)	N/A	17.38
E100K	13.2 \pm 0.8 (n = 91)	0.63 \pm 0.03	303.7 \pm 14.3	1.05 (p = 0.61)	N/A	17.63
E100G	20.7 \pm 0.8 (n = 66)	0.46 \pm 0.02	71.4 \pm 7.5	0.69 (p = 0.05)	0.70	25.13
I113T	12.0 \pm 0.5 (n = 60)	0.39 \pm 0.03	62.2 \pm 4.2	1.65 (p = 0.02)	0.54	18.50

^aAverage R² of sigmoidal fits for all replicate assays was 0.98.

^bP values are calculated from the statistical comparison between Kaplan-Meier plots of each mutant SOD1 and that of WT SOD1, using Log-Rank (Mantel-Cox) algorithm at 95 % confidence interval (p < 0.05).

^cData obtained from Wang et al.¹³⁶

^dH46R apo-SOD1 did not fibrillize during the 160 hr assay.

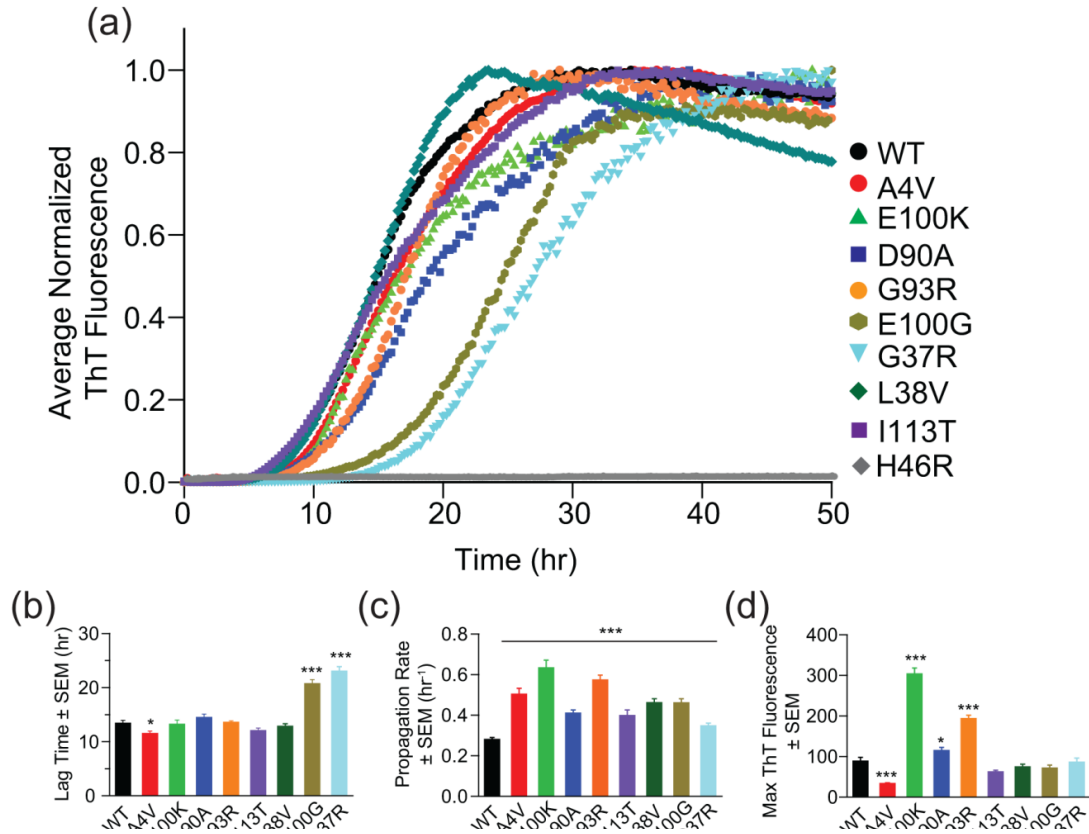


Figure 4.4 ALS-linked mutations in SOD1 do not uniformly accelerate fibril nucleation (at pH 7.4, 37 °C) but do uniformly accelerate fibril elongation (with the exception of H46R apo-SOD1). (a) Average and normalized plots of replicate ThT amyloid assays (comprised from traces in Figure 4.2) for all apo-SOD1 proteins. Comparison plots of average (b) lag time (τ), (c) propagation rate (k), and (d) maximal ThT fluorescence (f) for all apo-SOD1 proteins (* = $p < 0.01$; ** = $p < 0.001$; *** = $p < 0.0001$).

The most pronounced difference between classical metrics and Hazard ratios of fibrillization is that only a single ALS mutation, A4V, accelerated fibrillization of SOD1 according to classical metrics (i.e., only A4V decreased the mean lag time of fibrillization by a statistically significant amount (Figure 4.4b); whereas several mutations accelerated fibrillization according to Kaplan-Meier analysis. In addition, five mutations resulted in statistically insignificant changes in mean lag time (L38V, D90A, G93R, I113T, and E100K) and two increased lag time (G37R, E100G; Figure 4.4b). With the exception of

H46R (which did not fibrillize), all ALS mutations did uniformly increase the rate of apo-SOD1 fibril elongation/propagation (Figure 4.4c). Mean lag time and propagation rate did not correlate as strongly with clinical Hazard ratios compared to Hazard ratios of fibrillization (Figure 8.30). For example, mean lag times for each ALS variant showed weak correlations with Hazard ratios of survival ($R^2 < 0.23$; Figure 8.30). The mean lag time did correlate moderately with patient survival time ($R^2 = 0.46$; Figure 8.30). Mean lag time and mean propagation rate did not correlate with the average age of disease onset ($R^2 = 0.05, 0.06$; Pearson's $r = -0.07, -0.24$, respectively).

I also sought to determine if the thermostability of ALS variants of apo-SOD1 might correlate with any of the kinetic parameters of SOD1 aggregation or clinical phenotype of ALS patients. As shown in Figure 8.31, no strong correlation was found between the melting temperature (T_m) of ALS variants of SOD1 and *in vitro* kinetic parameters or clinical phenotype ($R^2 \leq 0.53$). These weak correlations suggest that protein stability cannot entirely explain the fibrillization rate or toxicity of different ALS variants of SOD1.

The lower risk (and rate) of fibrillization that I observed for certain ALS variants, compared to WT SOD1, contradicts previous *in vitro* studies which reported that ALS mutations uniformly accelerate the *in vitro* aggregation of apo-SOD1, relative to WT SOD1.^{100,110-111} I do not doubt the accuracy and validity of previous studies, but I do question their statistical significance because conclusions were based on between 2 and 10 replicate assays per ALS-variant protein in some studies¹¹⁰⁻¹¹¹ and between 6 and 198 replicate assays in others.¹⁰⁰

In addition to variations in statistical power, discrepancies with previous studies might also be caused by different assay conditions utilized by different research groups (e.g., pH 6.3 in a previous study¹⁰⁰ versus pH 7.4 in this chapter). I continued, however, to observe slower (or equal) rates of SOD1 fibrillization for certain ALS-variants (relative to WT; Figure 8.32) across a wide range of experimental conditions (e.g., solvent pH 5.5-7.4, gyration rate = 120-360 rpm; see chapter 8 for more details).

It is important to note that my aggregation assays involved both mechanical agitation (a Teflon stirring bead in each microplate) and a significant air-water interface (AWI). The air headspace in each well is approximately 75 μL (i.e., $\sim 75 \mu\text{L}$ of air between the protein solution and the polypropylene seal; the maximum capacity of a well is 360 μL and my solution volume is 200 μL ; bead volume = 85 μL). This AWI is disrupted by the Teflon bead during gyration of the microplate and the total surface area of the AWI is presumably increased during mixing, which might promote protein unfolding and fibrillization.^{144,162} A recent study has shown that this headspace can accelerate the rate and affect the stochasticity of fibrillization of α -synuclein.¹⁴⁴ In this previous study, removal of the AWI prevented fibrillization across the experimental time scale (thus, the effect of an AWI on the stochasticity of nucleation could not be determined). However, seeded fibrillization remained somewhat stochastic in the absence of an AWI, as demonstrated by 3-fold variations in ThT fluorescence.¹⁴⁴ The observed stochasticity of SOD1 fibrillization cannot be entirely attributed to the presence of an air-water interface (however, future studies will be needed to address how this interface affects stochasticity and the distributions of rates).

I presume that the type of nucleation that is occurring in my microplate-based assay is a mixture of heterogeneous nucleation (occurring at phase interfaces or surfaces) and homogenous nucleation (occurring entirely in solution). Microplates used in this study are made of polystyrene, with a polyethylene oxide coating (contact angle = 63°). The contact angle of the Teflon stirring bead is ~ 110°. There could be, therefore, four distinct groups of nuclei forming in different regions of the microplate system: 1) at the air-solvent interface, 2) at the hydrophobic microplate-solvent interface, 3) at the omniphobic Teflon bead-solvent interface, and 4) in solution, without assistance from surfaces. While I can assume that my assay involves a large degree of heterogeneous nucleation—especially at the air-water interface—I cannot abolish heterogeneous nucleation by performing the same assay without agitation. Phase interfaces with hydrophobic and omniphobic surfaces are ubiquitous in this system.

It should be remembered that the magnitude of shear force encountered by SOD1 proteins during *in vitro* microplate-based amyloid assays (via orbital gyration) are not entirely physiologically irrelevant, but are similar in magnitude to local shear forces generated within living cells. These forces are generated by motor proteins during cytoplasmic transport.¹⁶³ The shear stress generated in the cytoplasm of *C. elegans* embryonic cells is ~ 0.01 N/m²,¹⁶³ which is of the same order of magnitude of shear stress in my assays (~ 0.05 N/m²). These types of shear forces are relevant to SOD1, which undergoes slow component b axonal transport in motor neurons.¹⁶⁴⁻¹⁶⁵ Shear forces are also generated during physical trauma (e.g., diffuse axonal injury¹⁶⁶⁻¹⁶⁷), which is causally linked to protein aggregation and neurodegenerative disease. The ability of certain ALS-linked mutations to diminish the probability or mean rate of SOD1

fibrillization does not necessarily conflict with reports that these same mutations promote the formation of high molecular weight, detergent-insoluble or ThT-positive SOD1 species in transgenic ALS mice or cultured cells, relative to WT SOD1.¹⁶⁸⁻¹⁶⁹ First and foremost, the total abundance of aggregated SOD1 measured in mice will not necessarily correlate with rates of SOD1 aggregation measured during *in vitro* experiments. Animal experiments involve measurements of aggregation over weeks and months, i.e., equilibrium (thermodynamic) measurements, which reflect the ΔG (not the rate) of aggregation *in vivo*. Whereas microplate amyloid assays reflect rates (not ΔG 's) measured over the course of minutes and hours, i.e., non-equilibrium (kinetic) measurements. Moreover, the expression of a missense mutation such as D90A might increase the apparent accumulation of SOD1 fibrils in transgenic mice by promoting interactions of SOD1 with cellular or organellar membrane surfaces that, generally speaking, catalyze protein fibrillization¹⁷⁰ or are requisite (by definition) for cell-to-cell transmission.¹⁷¹ I was not entirely surprised that the D90A apo-SOD1 protein exhibited a Hazard ratio approximately equal to 1, and that D90A and WT apo-SOD1 exhibited statistically similar mean nucleation and propagation rates of fibrillization. Apart from a measured difference in net charge,¹⁵⁴ the metal binding properties, structure, and thermostability of D90A SOD1 are so similar to WT SOD1 that the mutation has been described as “cryptic”.³¹

Considering the apparent link between Hazard ratios of SOD1 fibrillization and patient survival, I sought to determine if the fluorescence intensity of ThT-positive SOD1 oligomers might offer clues about the structure of toxic oligomers in ALS, i.e., whether fluorescence correlated with a clinical phenotype. The values of fluorescence during

ThT-based amyloid assays for SOD1 (which do vary from mutant to mutant; Figure 4.2a and Figure 4.4d) have not been previously deciphered or interpreted because signal variation and low iteration in measurement made it difficult to obtain statistically significant results. The large number of replicate measurements collected in this study allowed me to calculate statistically significant values of mean fluorescence for immature (propagating) fibrillar oligomers (i.e., fluorescence intensity at the lag time) and for mature fibrillar oligomers (i.e., plateau fluorescence at the end of the assay).

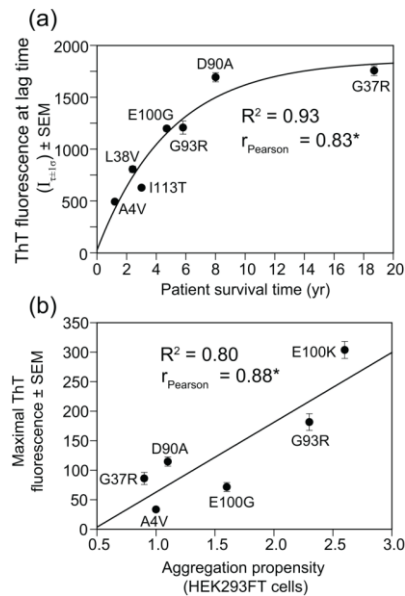


Figure 4.5 Fluorescence intensity of immature ThT-positive apo-SOD1 oligomers correlates with patient survivability and aggregation propensity in cultured cells. (a) Correlation between the average intensity of ThT fluorescence at the mean lag phase ($I_{\tau \pm 1\sigma}$) and patient survivability for all apo-SOD1 proteins. $I_{\tau \pm 1\sigma}$ was calculated via summing fluorescence intensities in the time range corresponding to the mean lag time and one standard deviation (i.e., $\tau \pm 1\sigma$, or the shaded areas in Figure 4.2a). The Pearson's r (0.83^*) was determined from a linear fit of data ($R^2 = 0.70$), suggesting that the exponential fit ($R^2 = 0.93$) is significant and more appropriate. **(b)** Plot of average maximal ThT fluorescence of ALS-variant apo-SOD1 from microplate assays and previously measured quantities of detergent resistant SOD1 oligomers from cultured HEK cells (measured by Borchelt and co-workers¹⁶⁸). Asterisks in both plots indicate statistical significance of correlations ($* = p < 0.05$).

A surprisingly strong (and non-linear) correlation was found between the mean fluorescence intensity of immature oligomers (i.e., fluorescence intensity at lag time, denoted as $I_{\tau \pm 1\sigma}$) and patient survival time (Figure 4.5a). Here, lower fluorescence correlates with shorter survivability ($R^2 = 0.93$; Pearson's $r = 0.83^*$). This result suggests that the ThT fluorescence of an immature oligomer is inversely correlated with its toxicity. I found no correlation between fluorescence of mature oligomers and onset or survival time in patients. The intensity of ThT fluorescence is not necessarily a reflection of the amount of fibrillar SOD1 that is present, but is rather an indicator of the gross morphology, atomic structure, charge, surface hydrophobicity, and dynamic stability of the aggregates that are present (the structural determinants that cause ThT fluorescence in amyloid fibrils are not clearly understood¹⁷²). The low fluorescence of immature fibrils ($I_{\tau \pm 1\sigma}$) formed by aggressive variants such as A4V SOD1, might appear to suggest that amyloid-like oligomers are non-toxic. This correlation could also suggest, however, that dynamic, non-classical amyloid oligomers with low ThT fluorescence might be more toxic species than their mature end products.

The 10-fold variation in mean ThT fluorescence exhibited by the set of ALS-variant proteins, relative to one another, is not unique to SOD1 and has been reported for variants of other amyloidogenic polypeptides. For example, two recently discovered missense mutations in amyloid-beta protein, i.e., E22K $A\beta_{1-42}$ and $\Delta E22A\beta_{1-39}$, fibrillize rapidly and are capable of seeding the aggregation of the WT $A\beta$ peptide, despite producing fibrils with very low ThT fluorescence *in vitro*¹⁷³ compared to that of WT protein.¹⁷⁴⁻¹⁷⁵ This significant difference in fluorescence intensity was attributed to structural differences between mutant and WT $A\beta$ peptides, such as “fibril matting”,

which causes the blockage of available binding sites for ThT¹⁷⁴⁻¹⁷⁵ relative to WT peptide (i.e., ~ 4.5-fold¹⁷⁵). The variations in ThT fluorescence intensity between different SOD1 variants might also be caused by differences in the secondary structure or dynamics of fibrils that hinder the free rotation of C2-C12 bond in ThT, resulting in a significant decrease in the quantum yield of fibril-bound ThT. Although I found no link between the fluorescence of mature SOD1 fibrils and patient survival, I did find that the intensity of fluorescence for mature SOD1 fibrils (i.e., the mean fluorescence at the end of each assay) correlated linearly with the quantity of detergent-insoluble SOD1 aggregates that Borchelt and co-workers¹⁶⁸ observed in cultured human embryonic kidney (HEK) cells (Figure 4.5b; $R^2 = 0.80$; Pearson's $r = 0.88^*$). This correlation suggests that the equilibrium ΔG of SOD1 fibrillization in microtiter plate amyloid assays scales with the ΔG of SOD1 aggregation in cultured cells.

Conclusion

The study presented in this chapter has described how Kaplan-Meier estimators can be used to quantify rates of stochastic protein aggregation and applied the method to SOD1-linked ALS. This study did not seek to determine the source or sources of stochasticity in SOD1 aggregation during microplate-based amyloid assays.¹⁰⁸ These new probability-based metrics (Hazard ratios) of protein fibrillization demonstrate that some ALS mutations accelerate the fibrillization of SOD1, while others decelerate fibrillization (or do not affect fibrillization rate). These probability-based metrics correlate better with clinical phenotypes than classical metrics, such as mean lag time and mean elongation rate. For two mutations in particular, the Hazard ratio of fibrillization almost perfectly

matched the Hazard ratio of patient survival (Table 4.2). Future studies—and the collection of additional patient data—will be required to determine if this correlation is a mere coincidence or a general link between genotype and phenotype. Regardless, this study suggests that Hazard ratios are more descriptive metrics of stochastic protein fibrillization than average values of lag time or elongation rate.

To the best of my knowledge, the study presented in this chapter represents the first report of this wide-ranging kinetic diversity in the intrinsic rates of SOD1 fibrillization. These results suggest—but do not yet prove beyond a doubt—that despite this diversity, the probabilities of fibrillization can partially explain the wide range in rate of disease progression for patients with SOD1-linked familial ALS (which itself can be faster or slower than sporadic ALS). The probability of apo-SOD1 fibrillization does not correlate with the age of disease onset (at least at pH 7.4). Surprisingly, several ALS-variant apo-SOD1 proteins (i.e., G37R, D90A, I113T, and E100G) aggregate at similar or slower rates than WT apo-SOD1, yet still trigger the onset of ALS (albeit, trigger a form of the disease that also progresses more slowly than in patients with sporadic ALS who generally express WT SOD1). Thus, fibrillization rates or probabilities that I measure with microplate assays are insufficient to explain the age of initial onset or pathogenesis. This lack of correlation might be partially explained by the large variability in age of ALS onset for patients with different SOD1 mutations. For example, the onset age can range by up to 60 years for patients with the A4V mutation, even with patients from the same family.¹³⁶ This study by no means suggests that intrinsic rates or probabilities of aggregation cannot explain disease onset. I cannot categorically conclude that ALS mutations such as G37R and D90A—mutations that do not accelerate intrinsic rates or

probabilities of fibrillization—cannot accelerate aggregation in biological systems (or in other types of *in vitro* assays). Myriad reports show that transgenic ALS-SOD1 mice and cultured cells expressing D90A and G37R SOD1 develop more insoluble aggregated SOD1 than similar systems expressing WT SOD1.¹⁷⁶⁻¹⁷⁸ The implications of the study presented in this chapter are purely chemical: intrinsic aggregation probabilities of metal-free mutant polypeptides, in phosphate buffer, during standard microplate-based amyloid assays, are not increased by ALS mutations and cannot explain disease onset. This null effect would not necessarily hold true in the presence of cellular or organellar membrane surfaces (which are generally anionic) that catalyze aggregation,¹⁷⁹ and whose interactions will depend upon surface hydrophobicity and net charge; and this null effect might not apply universally to all conceivable types of conditions used during *in vitro* assays for amyloid. For example, the D90A mutation, while it does not accelerate SOD1 fibrillization in dilute phosphate buffer, might promote interactions between SOD1 and anionic membrane surfaces (D90A has increased surface hydrophobicity¹⁷⁸ and decreased net negative charge¹⁵⁴). Lipid-protein interactions generally accelerate protein aggregation.¹⁸⁰ One limitation of this study is that it did not examine hetero-fibrillization, that is, the effects of the WT protein on the fibrillization rate of ALS-variant apo-SOD1. There are no statistically significant aggregation rates available for mixtures of ALS-variant and WT apo-SOD1 (despite the fact that most ALS-SOD1 mutations are heterozygous¹⁸¹). The co-expression of the WT protein is known to increase the toxicity of ALS-variant SOD1 in mice (or is required for disease onset in the case of A4V SOD1 mice¹⁸²⁻¹⁸³). Future studies are needed to address how fibrillization rates of ALS-variant SOD1 are impacted by the presence of lipid surfaces or interactions with WT SOD1.

Materials and Methods

SOD1 Purification and Demetallation:

All SOD1 variants were recombinantly expressed in *S. cerevisiae*, purified using ammonium sulfate precipitation followed by three sequential chromatographic separations: hydrophobic interaction chromatography, ion-exchange chromatography, and size-exclusion chromatography, as previously described.¹⁸⁴ Purified SOD1 proteins were demetallated via dialysis against: i) 0.1 M sodium acetate, 10 mM EDTA, pH 3.8; ii) 0.1 M sodium acetate, pH 3.8; and iii) 0.1 M sodium acetate, pH 5.5 during a 6 days period, as previously described.⁴⁵

Inductively-Coupled Plasma Mass Spectrometry (ICP-MS):

A 7900 ICP-MS instrument (Agilent Technologies, Santa Clara, CA) was used to determine the residual metal content of demetallated SOD1 proteins. SOD1 proteins were diluted in 2 % nitric acid solution to a final concentration of 60 μ M (per monomer) and injected into ICP-MS using an autosampler. Calibration curves for zinc and copper were constructed in the range of 0 to 100 ppb and used to calculate the amount of each metal in SOD1 samples.

Differential Scanning Calorimetry (DSC):

The thermostability and extent of disulfide reduction of WT and ALS-variant apo-SOD1 was assessed using a Microcal VP-DSC calorimeter (Malvern, UK). Protein samples were in 10 mM potassium phosphate buffer (pH 7.4) at [SOD1] = 60 μ M per monomer. Samples were heated from 20 °C to 80 °C at a scan rate of 1 °C/min.

Electrospray Ionization Mass Spectrometry (ESI-MS):

A nanoflow Synapt G2 high definition mass spectrometer (Waters, Milford, MA) was used to analyze the purity of apo-SOD1 proteins. Proteins were diluted with 0.1 % formic acid to a final concentration of 1 μM , desalted using a reversed-phase C-18 trapping column, and directly injected into the mass spectrometer. Mass spectra were deconvoluted using the MaxEnt1 module in Masslynx™ software.

Size-Exclusion Chromatography:

The extent of disulfide reduction/monomerization of WT apo-SOD1 in the presence of 10 mM TCEP was determined using a 25 cm Zorbax Bio Series G-250 size-exclusion column (Agilent Technologies, Santa Clara, CA, USA). The column properties are as follow: internal diameter = 4.6 mm; resolving range = 4-400 kDa; void volume = 1.4 mL. The running buffer (10 mM potassium phosphate, 5 mM EDTA, pH 7.4) contained 10 mM TCEP, and HPLC flow rate was set to be 0.2 mL/min (run time = 16 minutes). WT apo-SOD1 was detected at 280 nm using a photodiode array detector.

Thioflavin-T (ThT) Fluorescence Aggregation Assays:

Apo-SOD1 proteins were transferred to aggregation buffer (10 mM potassium phosphate, 5 mM EDTA, pH 7.4) via centrifugal filtration. Concentration of SOD1 proteins was determined with UV-vis spectrophotometry, using $\epsilon_{280\text{nm}} = 10800 \text{ M}^{-1}\text{cm}^{-1}$, per dimeric protein. The “mother” stock solution for each SOD1 protein ($[\text{SOD1}]_{\text{final}} = 60 \mu\text{M}$ monomer) was prepared by adding tris(2-carboxyethyl)phosphine (TCEP) to a final concentration of 10 mM followed by incubation at room temperature for 30 min. Immediately prior to starting the assay, 20 μM of freshly made ThT solution was added

to the protein/TCEP solution and mixed. Protein solutions were filtered with a 200 nm filter, prior to initiating the aggregation assay. Two hundred microliter aliquots of SOD1/TCEP/ThT solution were added to each well of a 96-well polystyrene microplate (only 60 wells were utilized per plate, because I avoided perimeter wells). Each well contained a 1/8" (3.13 mm) Teflon bead (McMaster-Carr®, Elmhurst, IL).

A Fluoroskan Ascent™ FL microplate fluorometer (Thermo Scientific™, Waltham, MA) was used to measure the kinetics of apo-SOD1 aggregation. The fluorometer instrument was pre-warmed for 30 min and the temperature of the plate housing was set to 37 °C. Excitation and emission filters were set at 444 nm and 485 nm, respectively. Microplates were gyrated at 360 rpm with a radius of gyration of 3 mm. Gyration occurred intermittently (gyration for 15 sec, followed by 15 sec pause). Fluorescence measurements were taken at 15 min interval over ~ 168 hr.

The following 4-parameter sigmoidal function was fit to each sigmoid:

$$f = f_0 + \frac{f_{\max} \frac{t-t_0}{b}}{1 + e^{\frac{t-t_0}{b}}} \quad (\text{Equation 4.1})$$

Where f is the ThT fluorescence intensity at time t ; f_0 and f_{\max} are the ThT fluorescence at $t = 0$ (beginning of the assay) and $t = t_{\text{plateau}}$ (the time that sigmoid reaches its plateau), respectively, t_0 is the time that sigmoid reaches its inflection point, and b is the slope of linearly increasing portion of sigmoidal plot. The lag time of aggregation was defined as $\tau = t_0 - 2b$, and the rate of fibril propagation was defined as $k = 1/b$. Kinetic parameters (mean lag time and propagation rate) were calculated for each iterate set of data and averaged for each protein, as previously described.⁴⁵

Transmission Electron Microscopy (TEM):

General morphologies of mature aggregates of apo-SOD1 proteins were determined using a JEOL JEM-1010 transmission electron microscope operating at 60 kV, equipped with a XR16 CCD camera. Homogenates of aggregate solutions were vigorously shaken, washed with Milli-Q pure water (18.2 M Ω /cm) to remove residual TCEP (that can create false positive signals via binding with uranyl ions). One droplet of aggregate solution was placed on a copper grid, incubated for 1 min, and dried out with a filter paper. One droplet of a 1 % solution of uranyl acetate (in water) was delivered to grid and allowed to dry for 1 min. Grids were then incubated at room temperature overnight inside a clean, dust-free chamber prior to imaging.

Kaplan-Meier Analysis of Apo-SOD1 Fibrillization:

Kaplan-Meier plots were created using Graphpad Prism software. In order to construct the Kaplan-Meier plots from kinetic data of each apo-SOD1 variant, I used values of t_0 (Equation 4.1) as the indication of an “aggregation event” in a particular well, meaning that a well is showing ThT fluorescence and therefore aggregation has occurred in that well at $t = t_0$. Each aggregation event was assigned the value “1”, and other time points that did not match with any t_0 value were left blank. The statistical significance between the Kaplan-Meier plots of each mutant compared to that of WT was determined using Log-Rank (Mantel-Cox) algorithm at 95 % confidence interval.

Hazard ratios were calculated with the Log-rank (Mantel-Cox) method using Graphpad Prism® software. The Hazard ratio for each ALS-variant apo-SOD1 protein was calculated relative to WT SOD1. In order to calculate the mean time to failure,

Kaplan-Meier plots were fit with a 4-parameter sigmoidal function (Equation 4.1), from which values of t_0 (i.e., inflection point) were extracted and assigned as mean time to failure.

Acknowledgements

Financial support for this research was provided to B.F.S by the Department of Defense (W81XWH-11-1-0790), the National Science Foundation (CHE: 1352122), and the Welch Foundation (AA-1854). AAM acknowledges the Welch Foundation grant (C-1743).

CHAPTER FIVE

How Do Gyration Beads Accelerate Amyloid Fibrillization?

This chapter is published as:

Abdolvahabi A, Shi Y, Rasouli S, Croom CM, Chuprin A, Shaw BF (2017) How do gyration beads accelerate amyloid fibrillization? *Biophys. J.* **112**, 250-264.¹⁸⁵

Abstract

The chemical and physical mechanisms by which gyration beads accelerate amyloid fibrillization in microtiter plate assays are unclear. Identifying these mechanisms will help optimize high-throughput screening assays for molecules and mutations that modulate aggregation and might explain why different research groups report different rates of aggregation for identical proteins. The study presented in this chapter investigates how the rate of SOD1 fibrillization is affected by 12 different beads with a wide range of hydrophobicity, mass, stiffness, and topology but identical diameter. All assays were performed on D90A apo-SOD1, which is a stable and wild-type-like variant of SOD1. The most significant and uniform correlation between any material property of each bead and that bead's effect on SOD1 fibrillization rate was with regards to bead mass. A linear correlation existed between bead mass and rate of fibril elongation ($R^2 = 0.7$): heavier beads produced faster rates and shorter fibrils. Nucleation rates (lag time) also correlated with bead mass, but only for non-polymeric beads (i.e., glass, ceramic, metallic). The effect of bead mass on fibrillization correlated ($R^2 = 0.96$) with variations in buoyant forces and contact forces (between bead and microplate well), and was not an artifact of residual momentum during intermittent gyration. Hydrophobic effects were observed, but

only for polymeric beads: lag times correlated negatively with contact angle of water and the degree of protein adhesion (surface adhesion and hydrophobic effects were negligible for non-polymeric beads). These results demonstrate that contact forces (alone) explain kinetic variation among non-polymeric beads, whereas surface hydrophobicity and contact forces explain kinetic variation among polymeric beads. This study also establishes conditions for high-throughput amyloid assays of SOD1 that enables the control over fibril morphologies and produce 8-fold faster lag times and 4-fold less stochasticity than previous studies.

Introduction

The ability to accurately and reproducibly measure rates of amyloidogenesis is critical for uncovering mechanisms by which pathogenic mutations and post-translational modifications affect protein fibrillization,¹⁸⁶⁻¹⁸⁸ and for discovering compounds that act upon amyloid-like oligomers.¹⁸⁹⁻¹⁹² Under quiescent conditions, that is without stirring, neurotoxic polypeptides such as α -synuclein and SOD1 self-assemble into amyloid fibrils at time scales ranging from days to months.^{108,110,155,193} To accelerate amyloidogenesis and reduce stochasticity,¹⁰⁸ solutions are gyrated in microtiter plates at > 100 rpm with millimeter-sized stirring beads placed in each sample well.^{98,108,194} Beads are typically composed of polytetrafluoroethylene (Teflon), however, borosilicate glass and polymethylmethacrylate (PMMA) have also been used.^{45,108,171,193-195} Establishing a few basic rules of thumb for how different bead types do or do not affect formation rates (and morphologies) of amyloid fibrils will help optimize assays; help discern the growing (and often inconsistent) list of reported rates of amyloid nucleation and elongation,^{155,195-197} and might uncover clues about the mechanical, chemical, and surface forces that drive

fibrillization. In general, the mechanical agitation of protein solutions by a gyrating bead is hypothesized to accelerate aggregation by exposing hydrophobic amino acid residues to the air-water interface^{193,198-200} and separately, by inducing the fragmentation of oligomers, which allows secondary nucleation and elongation^{193,201-202} (stirring also, of course, increases collision frequency and abolishes local gradients of reagents). A complete set of physical and chemical rules by which a gyrating bead affects the rate of amyloid formation—i.e., a set that includes hydrophobic, omniphobic and electrostatic effects, contact mechanics, shear force, mass—does not exist. For example, will a Teflon bead of 3.13 mm diameter (used in some studies of SOD1 fibrillization⁹⁸) accelerate fibrillization more or less than a Teflon bead of 2.4 mm diameter (used in other studies¹⁰⁰) and could these differences explain the disparity in reported rates? In microplate-based assays that commonly employ discontinuous gyration (e.g., gyration for 15 seconds, followed by a 15-second pause), will the momentum of a gyrating bead cause a heavier bead to continue orbiting the well longer than a bead of lower mass? Does this residual momentum produce significant differences in observed rates? Moreover, will a bead with smooth surface topology, for example borosilicate glass, stainless steel or silicon nitride ceramic (Figure 5.1), increase the reproducibility of measured aggregation rates, compared to more irregular surfaces (e.g., polypropylene; Figure 5.1)? And do micrometer-scale scratches or crevices on the surface of a bead significantly affect rates of fibrillization by providing nucleation sites (as they do with crystallization in glassware²⁰³)? Will a polyethylene bead accelerate aggregation by the same magnitude as its more commonly used fluorinated analog, Teflon (Figure 5.1)?^{194,204-206} Regarding hydrophobic effects: if hydrophobic effects between bead and protein are so dominant (as

reported for α -synuclein fibrillization¹⁹³), why do some research groups report identical rates of fibrillization in the presence of either glass or Teflon beads,¹⁹⁵ even though water contact angles for borosilicate glass and Teflon differ by $> 80^\circ$ (Table 5.1)? This chapter set out to answer a few of these questions.

Previous investigations into the kinetic effects of different beads have focused on the chemical properties of beads (primarily on hydrophobicity^{121,195,207}). These studies have demonstrated the importance of surface-induced changes in protein conformation²⁰⁷ and oligomer morphology,¹²¹ and induction of fibril fragmentation.¹⁹⁵ Very little is known, however, regarding how the basic physical properties of beads—mass and surface roughness for example—affect the aggregation rate of proteins. The momentum-based and friction forces that emerge from the mass, buoyancy, stiffness (defined as Young's modulus and Poisson's ratio), and sleekness (defined as friction coefficient) of the gyrating bead will alter the contact mechanics between bead and microplate well, and affect shear forces at the water-bead interface. These forces might impact, for example, rates of fibril fragmentation and secondary nucleation.¹⁹³

In this chapter, I studied the effect of 12 chemically and physically diverse spherical beads (of identical diameter) on the fibrillization of metal free (apo) SOD1 in 96-well microtiter plates. My original intent was to find assay conditions that increased the reproducibility and speed of amyloid assays for SOD1. The amyloidogenesis of SOD1 is slow and notoriously stochastic,^{45,64,98,100} and morphology of SOD1 aggregates are strongly dependent on reaction conditions.⁹⁸ The stochastic nature of SOD1 self-assembly is not a property that is unique to SOD1, or to any other protein or macromolecule. Stochastic self-assembly has been observed in all types of living and

non-living systems, from the crystallization of water,⁷³ to the aggregation of nucleic acids,¹⁰⁵ gene expression,¹⁰⁶ and the aggregation of the social amoeba *Dictyostelium discoideum*.¹⁰⁷ I succeeded in this effort: simply using stainless steel beads diminishes much of the stochasticity in fibril nucleation (but not elongation) and accelerates fibrillization. In the course of doing so, I discovered trends between various properties of gyrating beads and fibril lag time and propagation rate. These trends show, for example, that surface chemistry of the bead and protein-surface interactions can only partially explain why some beads accelerate protein fibrillization more than others. In addition to these effects, Newtonian forces (arising from the mass of the bead) significantly affect the kinetics and stochasticity of SOD1 fibrillization. I interpret these Newtonian effects in terms of shear and contact forces between bead and microplate well, which are greater for heavier beads and likely induce fibril fragmentation and secondary nucleation¹⁹⁵ at the bead-microplate and/or bead-solvent interface.

Materials and Methods

SOD1 Expression, Purification, and Demetalation:

Human SOD1 plasmid carrying the D90A mutation was expressed in *S. cerevisiae*. SOD1 was purified, and immediately demetalated, as previously described.⁶⁴ The demetalated state of SOD1 was confirmed to contain < 0.05 equivalents of Zn²⁺ or Cu²⁺ per dimer, using ICP-MS. Protein concentration was determined with UV-vis using an extinction coefficient of 10,800 M⁻¹·cm⁻¹ for human apo-SOD1, $\lambda_{\max} = 280$ nm.

Thioflavin-T Fluorescence Aggregation Assay:

Fibrillization of D90A apo-SOD1 was monitored and assayed using a microtiter plate-based thioflavin-T (ThT) aggregation assay, as previously described.⁹⁸ Briefly, pure D90A apo-SOD1 at a concentration of 30 μM (per dimer) in 10 mM phosphate/5 mM EDTA buffer (pH 7.4) was incubated with 10 mM TCEP (tris(2-carboxyethyl)phosphine) and 150 mM NaCl for 6 h, with gentle shaking at room temperature. The concentration of TCEP is 10 mM in my assays (~ 300 times higher than [SOD1]) to mimic intracellular conditions. This concentration of TCEP also prevents the random disulfide cross-linking of SOD1 oligomers. The 96-well microplate used to perform the ThT fluorescence aggregation assays was carefully sealed with a polypropylene film. I calculated that, throughout the 168 h assay, only 0.02 % of TCEP would be oxidized by oxygen, assuming that the rate of O_2 diffusion through the polypropylene seal at 37 $^\circ\text{C}$ is $\approx 4.3 \times 10^{-7}$ mg/hr. After 6 h, 20 μM of ThT was added to apo-SOD1 solution (filtered with a 200 μm syringe filter), and 200 μL aliquots of this “mother stock” were added to the wells of a 96-well black polystyrene microplate, which contained various types of beads (McMaster-Carr®, Elmhurst, IL, USA). Intensity of ThT fluorescence was recorded (for ~ 5 days with circular shaking at 360 rpm) using an Ascent 2.5 Fluorescence spectrophotometer (Thermo Scientific, Waltham, MA, USA). The excitation and emission filters were set to be 444 nm and 485 nm, respectively.

Electron Microscopy:

Surface topology of each bead (under different conditions) was visualized using a FEI™ Versa 3D focused ion beam scanning electron microscope (SEM). For regular SEM

imaging, beads were sputter coated with gold to a thickness of 20 nm. Morphology of apo-SOD1 fibrils after the termination of aggregation assays was determined with a JEOL JEM 1010 transmission electron microscope (JEOL Ltd., MA, USA). Sample preparation for TEM imaging was as follows: fibril homogenates from each well were centrifuged at $13000 \times g$ for 20 min, supernatants were separated, and fibril precipitates were washed 5 times with pure MilliQ water to remove any residual TCEP. Four microliters of fibril homogenates were then placed on a 200-mesh copper grid and dried after 1 min. By “fibril homogenates”, I simply mean a well-suspended solution of SOD1 fibrils that was prepared via vigorous shaking (without centrifugation). This “homogenization” ensured that a sufficient amount of fibrils was placed on the grid for TEM imaging. Four μL of 3 % uranyl acetate solution was placed on the grid for 1 min and dried using a clean filter paper. Samples were then incubated for ~ 1 h in a clean, dust-free container and imaged under ~ 80 kV.

Atomic Force Microscopy:

Beads were fixed on the AFM discs using a double-sided tape and imaged using a Dimension Icon AFM equipped with NanoScope V software (Bruker, Santa Barbara, CA). Tapping mode probes from MikroMarsh (NSC35/ALBS, 5.4 N/m) were used to acquire topography images. The cantilever oscillated at near the resonance frequency (150 KHz) to acquire the images. Images were processed using NanoScope Analysis software. Sample roughness was obtained via analyzing topography frames. Values for surface roughness in Table 5.1 are reported as root mean square average of roughness (R_q) calculated as:²⁰⁸

$$R_q = \sqrt{\frac{\sum_{i=1}^N (Z_i)^2}{N}} \quad (\text{Equation 5.1})$$

Where N is the number of equally differentiated points (*i*) along the measured surface, and Z_i is the difference between the height of each data point and the mean horizontal line.

Results and Discussion

Rates of Amyloid Formation Vary Seven-Fold with Bead Type:

In the current study, I examined the fibrillization of the ALS-linked D90A variant of apo-SOD1 because this protein was readily available in our laboratory and our group is familiar with its fibrillization kinetics in microplate assays.^{45,98} Thioflavin-T fluorescence aggregation assays were performed on D90A apo-SOD1 in 96-well microtiter plates, under reducing physiological conditions (10 mM TCEP, 150 mM NaCl, pH 7.4; the well-to-well variation in pH of SOD1 solutions was measured to be < 0.1 %). I measured rates of fibril nucleation and propagation (elongation) in the presence of the following beads (Figure 5.1): polytetrafluoroethylene (PTFE or Teflon), extracted acrylic, polypropylene, polyoxymethylene (Delrin), high density polyethylene (HDPE), and polyamide-imide (Torlon) (all of which are denoted in this chapter as “polymeric beads”); aluminum, titanium, alumina ceramic, silicon nitride ceramic, borosilicate glass, and stainless steel (denoted as “non-polymeric beads”). The nanoscopic and microscopic topologies of each bead type were visualized using atomic force microscopy (AFM) and scanning electron microscopy (SEM), prior to the start of assays. All polymeric beads possessed roughness on a micrometer scale according to AFM, except for extracted acrylic, which was

smoother on the micrometer scale but showed nanometer-scale roughness (Figure 5.1). Accordingly, SEM showed that polymeric beads have a higher degree of “waviness” than non-polymeric beads (“waviness” refers to surface irregularities at the micrometer scale, whereas “roughness” refers to irregularities at the nanometer scale²⁰⁹). Surface features on polymeric beads exhibited heights up to 10 μm , with the exception of extracted acrylic beads (Figure 5.1). Ceramic, glass, and metallic beads (i.e., non-polymeric beads), on the other hand, possess smoother microscopic surfaces with average depths < 400 nm (Figure 5.1).

Iterative ThT fluorescence aggregation assays were performed on D90A apo-SOD1 in replicates of ~ 40 assays per bead type. Individual (iterative) plots of ThT fluorescence are shown for all beads in Figure 5.2. I repeated amyloid assays at this high level of iteration because the fibrillization of apo-SOD1 is intrinsically stochastic and myriad replicates are needed to obtain statistically significant rates.⁹⁸

The longitudinal plots of ThT fluorescence are shown for each bead in Figure 5.3A. Plots in Figure 5.3A are averaged, normalized plots of all replicate experiments for each bead type. A few important trends are immediately observable: non-polymeric beads accelerated the aggregation of apo-SOD1 more than polymeric beads (Figure 5.3A).

As expected, the lag time and propagation (elongation) rate derived from each of the 445 iterative experiments (16 replicates were performed for “No bead” condition, which did not result in any ThT fluorescence) fell along a rational function, regardless of bead type (Figure 5.3B), i.e., $\alpha = \text{lag time } (\tau) \times \text{rate } (k)$, where $\alpha = 4.21$.

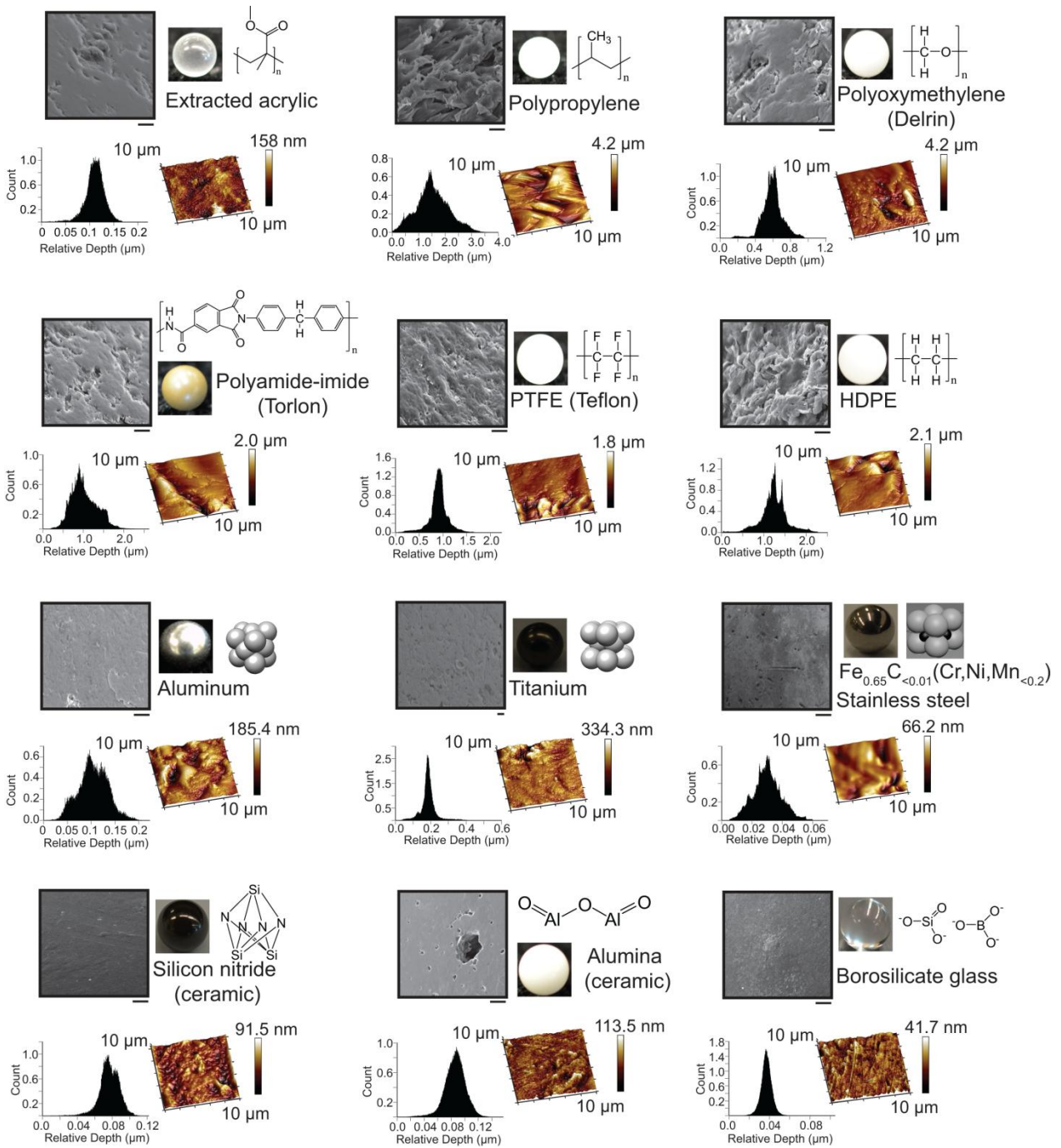


Figure 5.1 Chemistry and surface features of beads used in amyloid assays. Scanning electron micrographs of beads showing surface topology. Scale bars = 10 μm. Inset below each SEM image is the atomic force micrograph collected across a 10 μm × 10 μm scanned area (light color indicates shallower surfaces). Histograms in each panel show the relative surface depth, calculated from AFM imaging.

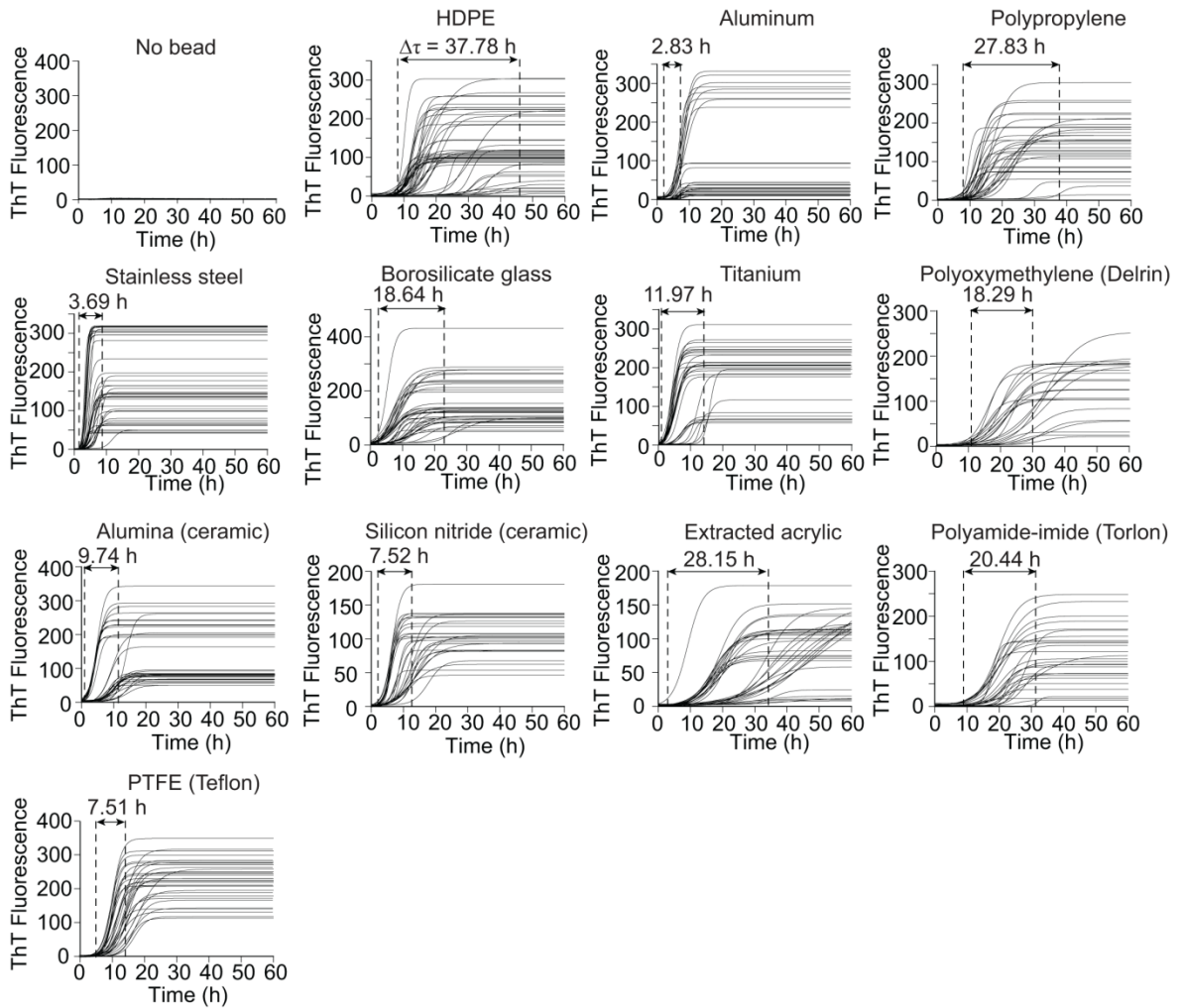


Figure 5.2 Replicate ThT fluorescence amyloid assays for D90A apo-SOD1 in the absence and presence of beads with varying chemical and physical properties. The range in variation of lag time ($\Delta\tau$) is indicated with numbers above each arrow.

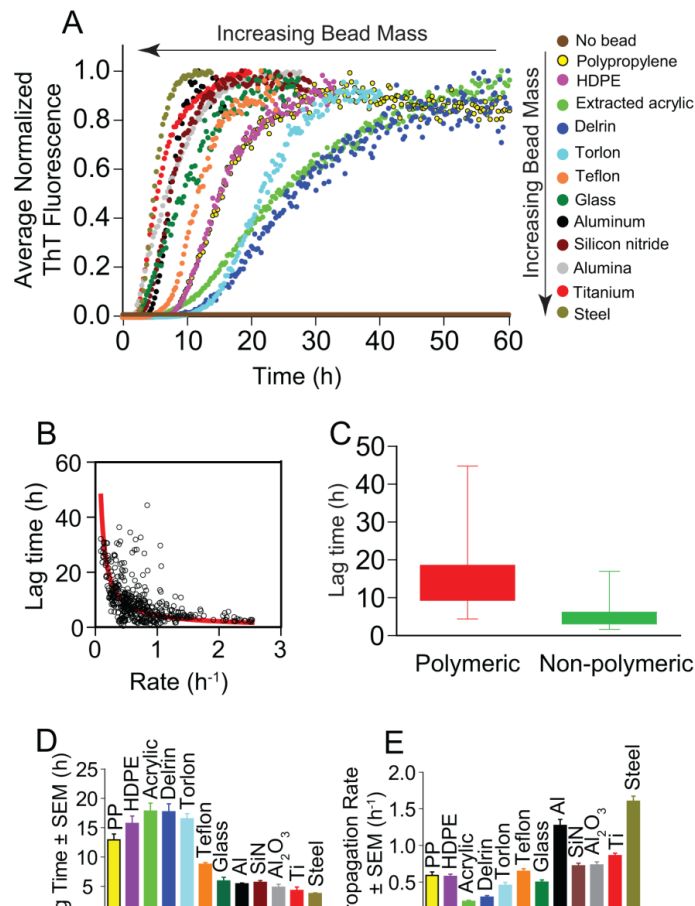


Figure 5.3 Kinetics of fibrillization of apo-SOD1 vary with bead type. (A) Average and normalized plots of ThT fluorescence for D90A apo-SOD1 aggregation (from Figure 5.2; $n_{\text{total}} = 461$). Assays were performed in the presence of 10 mM TCEP, pH 7.4 and physiological concentration of NaCl (150 mM). (B) The correlation plot between lag time and rate of fibril propagation (from all 461 assays). Red line shows the best fit to the data using rational function. (C) Box-and-whisker plot illustrates stochasticity in lag time for each type of bead. (D-E) Comparison plots of lag time and propagation rate of D90A apo-SOD1 aggregation in the presence of different bead types. For visual clarity, error bars in (D) and (E) are depicted as standard error of the mean (SEM), not standard deviation (SD), where $\text{SEM} = \text{SD}/\sqrt{n}$.

The α constant is similar to the value previously reported for the aggregation of other variants of apo-SOD1.^{98,100} The distribution of iterate lag times, for each bead type (Figure 8.33), suggests that apo-SOD1 aggregation was generally more stochastic in the

presence of polymeric beads compared to non-polymeric beads, as shown with a wider range in lag time (i.e., higher $\Delta\tau$; Figure 5.2, Figure 5.3C, and Figure 8.33). The most reproducible amyloid assays were obtained using stainless steel ($\Delta\tau = 3.69$ h) and aluminum beads ($\Delta\tau = 2.83$ h) (Figure 5.2). This diminished stochasticity is partially due to the accelerated fibrillization, which by definition narrows any distribution of rates, *ceteris paribus*, because negative values of time are not real.

It is also important to note that the maximal intensity of ThT fluorescence associated with SOD1 aggregation varied by up to 30 fold in the presence of different beads and among replicates of each bead (Figure 5.2). I attribute this difference in ThT fluorescence intensity to: 1) differences in the number of bound ThT molecules, and 2) differences in the fluorescence intensity (quantum yield) of fibril-bound ThT.²¹⁰ Differences in the structures, dynamics and morphologies of fibrils could cause the binding affinity and quantum yield to change. For example, interactions between fibrils, e.g., “fibril matting”¹⁷⁴ could lead to diminished ThT binding via diminished solvent accessibility, or disruptions of secondary structure. Differences in the secondary structure or dynamics of fibrils could also alter the degree to which the C2-C12 bond in ThT is prevented from rotating when bound to a fibril (the absence of rotation is thought to be the cause of ThT fluorescence upon amyloid binding).

The mass of beads I chose varied 10-fold, from polypropylene (15.6 ± 0.6 mg) to stainless steel (131.9 ± 0.1 mg). I hypothesized that the mass of each bead type might be one (of perhaps several) causes of the kinetic trend in Figure 5.2 and Figure 5.3.

Table 5.1 Physical and chemical properties of beads used in this study. The bead diameter is 3.13 mm.

Bead	Mass \pm SD (mg) ^a	Surface roughness; R _q (nm) ^b	Water contact angle (°) ^c	Lag time \pm SEM (h)	Propagation rate \pm SEM (h ⁻¹)
Polypropylene	15.6 \pm 0.6	615	99.0	12.9 \pm 1.0 (n = 35)	0.59 \pm 0.05
HDPE	15.7 \pm 0.2	312	99.1	15.7 \pm 1.3 (n = 52)	0.58 \pm 0.03
Extracted acrylic	20.8 \pm 1.1	19.5	75.0	17.8 \pm 1.4 (n = 35)	0.24 \pm 0.02
Polyoxymethylene (Delrin)	22.8 \pm 0.1	117	73.0	17.7 \pm 1.4 (n = 20)	0.29 \pm 0.02
Polyamide-imide (Torlon)	23.6 \pm 0.2	322	78.0	16.5 \pm 0.9 (n = 28)	0.46 \pm 0.04
PTFE (Teflon)	35.9 \pm 0.1	205	110.0	8.7 \pm 0.3 (n = 42)	0.65 \pm 0.04
Borosilicate glass	40.8 \pm 0.1	5.42	24.0	5.9 \pm 0.6 (n = 41)	0.49 \pm 0.03
Aluminum	46.9 \pm 0.3	30.9	89.2	5.4 \pm 0.1 (n = 32)	1.27 \pm 0.08
Silicon nitride (ceramic)	54.1 \pm 0.01	11.6	26.6	5.7 \pm 0.3 (n = 32)	0.72 \pm 0.04
Alumina (ceramic)	64.6 \pm 0.1	15.5	37.0	4.8 \pm 0.5 (n = 32)	0.73 \pm 0.04
Titanium	72.9 \pm 0.4	48.3	83.0	4.3 \pm 0.6 (n = 31)	0.86 \pm 0.03
Stainless steel	131.9 \pm 0.1	9.23	80.3	3.7 \pm 0.1 (n = 31)	1.60 \pm 0.07

^aMass of each bead was measured using a sensitive bench top scale in replicates of four and reported as mean \pm SD.

^bValues for surface roughness were calculated using atomic force microscopy.

^cValues for water contact angle were obtained from references.²¹¹⁻²²²

The lag time correlated exponentially (negatively) with increasing bead mass (Figure 5.4A; $R^2 = 0.91$). The rate of fibril propagation correlated linearly (positively) with bead mass (Figure 5.4B; $R^2 = 0.70$).

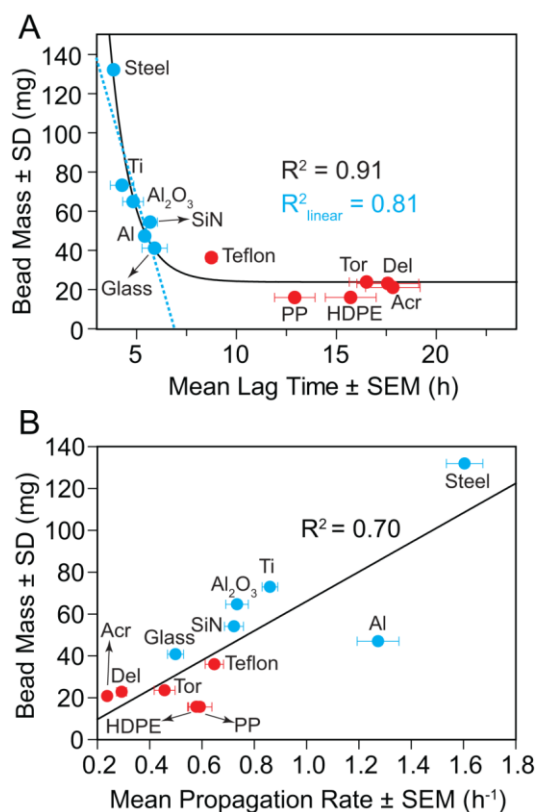


Figure 5.4 (A) Correlation between lag time of D90A apo-SOD1 fibrillization and bead mass. Blue dashed line indicates the best fit to the linear portion of the plot (non-polymeric beads). **(B)** Moderate linear correlation between rate of propagation of D90A SOD1 oligomers and bead mass. PP: Polypropylene; Del: Delrin; Acr: acrylic; Tor: Torlon; SiN: Silicon nitride ceramic; Al_2O_3 : Alumina ceramic.

There are a few possible reasons for why the mass of a bead might affect its ability to accelerate amyloid formation during orbital gyration in a microtiter plate, irrespective of the surface charge, hydrophobicity, or topology of the bead (or any other physical or chemical property). First and foremost, the velocities of different beads are approximately equal during orbital gyration of the microplate—regardless of mass—however, heavier beads will acquire more momentum during orbital gyration compared to beads of lower mass (momentum = mass \times velocity). Thus, the approximate 10-fold greater momentum of a stainless steel bead compared to a polypropylene bead (Table 5.1)

should cause the steel bead to continue orbiting around the microplate well for a longer period of time after the plate reader ceases gyration (in my typical amyloid assay, the Fluoroskan plate reader gyrates the microtiter plate at 360 rpm for 15 seconds, followed by a pause in gyration for 15 seconds, and this process repeats continually for 168 h). Therefore, the heavier beads will undergo more revolutions per minute (on average), over the course of the 168 h experiment. To demonstrate this effect visually, polypropylene beads and stainless steel beads were gyrated in a 96-well microtiter plate at ~ 180 rpm (Figure 5.5A). The stainless steel beads continued gyrating for 5.2 revolutions after the plate ceased gyrating, whereas polypropylene gyrated 2.3 revolutions (Figure 5.5A); I did not include water in each well because doing so interfered with video recording, however, the same qualitative effect was observed in water.

In order to test the “residual momentum” hypothesis, I programmed the Fluoroskan plate reader to gyrate constantly for 40 minutes, with the only pause occurring for 5 seconds during spectroscopic measurements of all wells. Thus, the microplate gyrates at 360 rpm for 40 min, followed by a 5 sec for spectroscopic measurement, and this process repeats for ~ 168 h. If residual momentum effects are significant, this increase in the ratio of gyration time and pause time, from 1:1 to 480:1, should significantly diminish the measured differences in lag time and propagation rate for different types of beads. Thioflavin-T fluorescence amyloid assays were performed again for D90A apo-SOD1 in the presence of stainless steel, Teflon, and acrylic beads under continuous gyration (i.e., three beads that produce fast, medium and slow rates; Figure 5.3A). Continuous gyration did not cause low-mass beads (i.e., acrylic and Teflon) to produce the same lag times as steel beads (Figure 5.5B), and the ratio of lag time at

continuous versus non-continuous gyration were statistically equal for all beads (Figure 5.5C). Continuous gyration accelerated the aggregation of apo-SOD1 in the presence of all three beads (as expected), by ~ 3.5-fold, compared to paused gyration (Figure 5.5B-C).

These results invalidate the “residual momentum” hypothesis of the acceleratory effect of heavy beads on amyloid formation.

Another possible mechanism by which bead mass could affect the aggregation rate of D90A apo-SOD1 is by contact force (pressure) between the bead and bottom and side of the polystyrene microplate. These forces (which I show below are kilopascal in scale) might be sufficient to induce the mechanical fragmentation of oligomers or fibrils, as shear forces have been previously shown to cause oligomer fragmentation and secondary nucleation and elongation.^{201,223}

My calculations of these contact forces, below, take into account the stiffness of the bead and polystyrene microplate and the micrometer-scale deformations that the bead introduces upon the microplate.

A bead with mass m and radius R (a hypothetical ideal sphere) is capable of indenting the surface (due to its weight) of the flat polystyrene microplate (a hypothetical elastic half-plate) at all contact points (Figure 5.6A). The radius of this contact area, r , can be expressed as:

$$r = \sqrt{RL} \quad (\text{Equation 5.2})$$

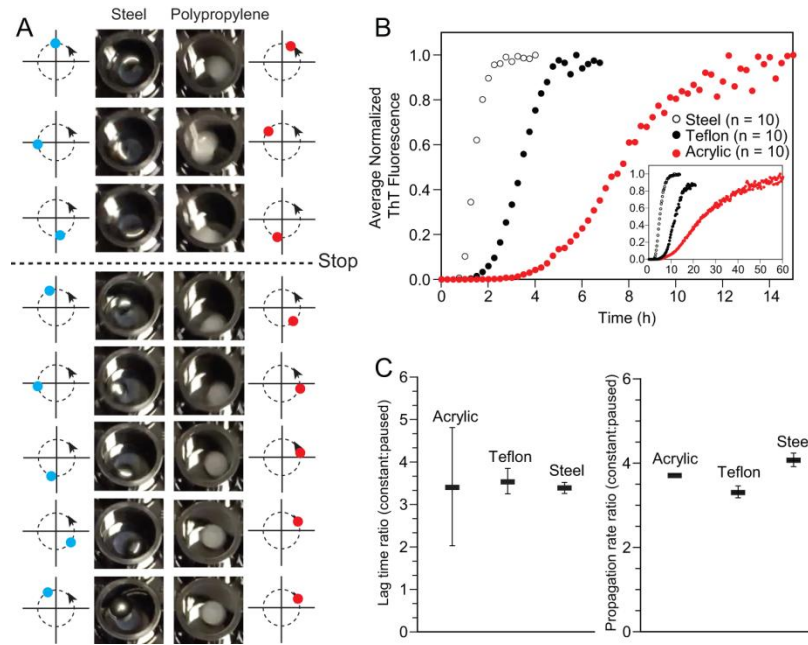


Figure 5.5 Residual angular momentum of heavier beads cannot explain why mass of bead affects amyloid formation. (A) Consecutive images of gyrating steel and polypropylene beads during gyration and after gyration is stopped. Beads were stirred at ~ 180 rpm (0.055 m/s) in a black polystyrene microplate. Circular arrows and blue and red dots next to each image show the trajectory of the moving beads inside the well. (B) Average and normalized ThT fluorescence plots of D90A apo-SOD1 aggregation under continuous gyration of steel, Teflon, and acrylic beads. Inset shows plots of D90A apo-SOD1 aggregation in the presence of same types of beads, but with paused gyration, taken from Figure 5.3A. (C) Comparison plots of aggregation lag time and propagation rate between two different gyration methods.

Where L is the depth of the displacement on the microplate surface due to indentation,²²⁴ as shown in Figure 5.6A (exaggerated for illustration):

$$L = \sqrt[3]{\frac{3(F_g - F_b)}{4E^*R^{0.5}}} \quad (\text{Equation 5.3})$$

Where F_g is the gravitational force exerted by the bead perpendicular to microplate surface, and F_b is the buoyancy force. Thus, if $F_b > F_g$, the bead will float and not touch the bottom of the microplate (Figure 5.6A). E^* is an interfacial stiffness parameter, defined by the physicomaterial properties of both surfaces as:

$$\frac{1}{E^*} = \frac{1-\nu_1^2}{E_1} + \frac{1-\nu_2^2}{E_2} \quad (\text{Equation 5.4})$$

Where E_1 and E_2 are the Young's moduli of bead and polystyrene microplate, and ν_1 and ν_2 are the Poisson's ratios of each bead and the microplate, respectively. The maximum contact pressure on the well surface can be estimated²²⁵ from:

$$P_g = \frac{3(F_g - F_b)}{2\pi r^2} \quad (\text{Equation 5.5})$$

Inspecting the bead trajectory inside the gyrating microplate confirmed that all beads stick to the side of each well and gyrate along with the frame of the plate (Figure 5.6A), meaning that contact occurs on the bottom and side of the well (with the exception of polypropylene and HDPE, which are buoyant). The centrifugal force (F_{cent}) on the side of wells was used to calculate the contact mechanics parameters (r' , L' , p_{cent} ; Figure 5.6A), instead of buoyant and gravitational forces:

$$F_{cent} = m\omega^2 l \quad (\text{Equation 5.6})$$

Where ω is the angular velocity of the rotating bead (360 rpm = 0.11 m/s), and l is the radius of gyration, which is 3 mm in the current experimental setup.

I observed that polypropylene and HDPE beads did not sink when placed in the aggregation solution (i.e., $F_b > F_g$; Figure 5.6A), and did not touch the bottom of the microplate during the course of assay (i.e., p_g is a negative value). Thus, in the case of polypropylene and HDPE, I only calculated the contact parameters in terms of F_{cent} (Figure 5.6A).

Table 8.9 contains the values of r , r' , E_1 , ν_1 , E^* , p_g , and p_{cent} for all studied beads. I calculated the total contact pressure as $p_t = p_g + p_{cent}$ for each bead, and plotted it versus

the corresponding lag time (Figure 5.6B). I point out that although buoyant beads like polypropylene only contact the sides of wells, these beads can produce almost identical total pressure to heavier polymeric beads that sink (e.g., Teflon). For example, the p_{cent} value of polypropylene was 4.8 kPa greater than p_{cent} for Teflon (Table 8.9), however, the p_g of Teflon (6.9 kPa; Table 8.9) renders the two p_t values for polypropylene and Teflon to be similar (Figure 5.6). I point out that although the mass of polypropylene is 3-fold lower than Teflon, the p_{cent} value for polypropylene is greater than Teflon because polypropylene is more stiff than Teflon (Table 8.9) and polypropylene will conform less to the surface of the microplate (which provides less surface area, and thus greater pressure, i.e., pressure = force/area).

Similar to the mass vs. lag time relation (Figure 5.4A), an exponential correlation was observed between p_t and lag time (Figure 5.6B). I note that the linear portion of mass vs. lag time plots (dashed blue trace in Figure 5.4A) did not include any of the polymeric beads (only non-polymeric beads). Taking into account contact mechanics—calculating contact pressures with mass and stiffness—improved the linear correlation (which contained Teflon beads). Nevertheless, Teflon was the only polymeric bead to fall along this linear portion in plots of p_t and lag time (Figure 5.6B; $R^2 = 0.96$). Regarding polymeric beads, there is no general correlation between mass and/or p_t and aggregation lag time (Figure 5.4A and Figure 5.6B). A linear correlation was found between the maximum contact pressure of polymeric and non-polymeric beads, and rate of oligomer propagation (Figure 5.6C).

These results indicate that contact pressure (mechanical stress) are generally dominant forces in nucleation via non-polymeric beads, but are not generally dominant

forces in the case of polymeric beads. Polymeric beads accelerate fibrillization to a lesser degree than I would predict based upon their mass and contact pressure, possibly because of hydrophobic effects.

Surface Adhesion and Hydrophobicity Can Partially Explain the Catalytic Effect of Polymeric Beads on SOD1 Fibrillization:

The insufficiency of mass and total contact pressure (p_t) to explain why polymeric beads have such wide-ranging kinetic effects on apo-SOD1 fibrillization, suggested that surface chemistry might explain lag times observed with polymeric beads. Polymeric beads might interact with monomeric or oligomeric SOD1 species to degrees that non-polymeric beads do not, and these interactions might be dependent upon surface properties (roughness, hydrophobicity) of each bead. To begin to test these hypotheses, I examined how much protein was attached to each bead surface after the end of the amyloid assay. I extensively washed each bead after completion of an amyloid assay, and boiled each bead in 2x Laemmli buffer/4 % β -mercaptoethanol and performed SDS-PAGE on boiled solutions (Figure 5.7A). The greatest amount of protein adhesion was observed for polymeric beads (with the exception of acrylic beads); negligible adhesion was observed for non-polymeric beads; alumina beads showed moderate affinity for SOD1 polypeptides, which is likely due to their positive zeta potential at pH 7.4.²²⁶ The concentration of protein that adhered to polymeric beads during amyloid assays (proportional to band intensities in Figure 5.7A) correlated linearly with the lag time of apo-SOD1 fibrillization (Figure 5.7B; $R^2 = 0.96$), i.e., greater adhesion correlated with faster nucleation. No correlation was found between the band intensity and lag time of non-polymeric beads (Figure 5.7B; open squares, $R^2 = 0.02$). The correlation between

surface adhesion and lag time is interpreted in terms of hydrophobic effects: the surface hydrophobicity (i.e., the water contact angle; Figure 5.7E) of polymeric beads (prior to amyloid assay) correlated with lag time of fibrillization (Figure 5.7C) and the quantity of SOD1 that adhered to beads during amyloid assays (Figure 5.7D).

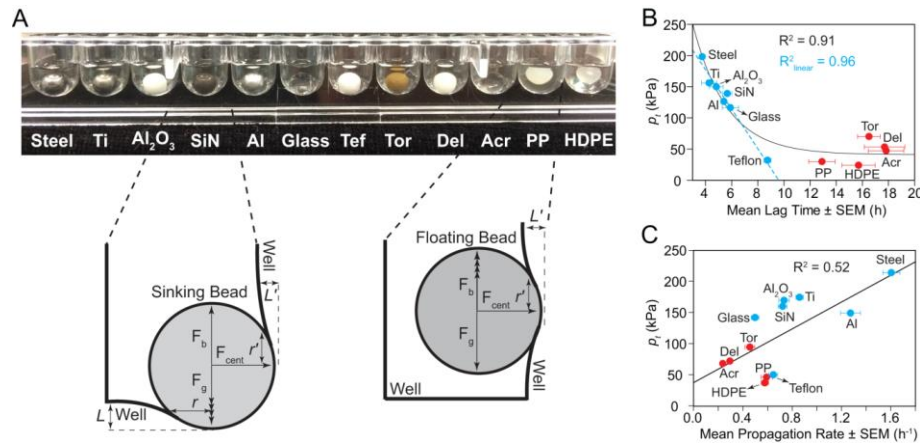


Figure 5.6 Contact mechanics between beads and microplate surface can explain kinetics of amyloid nucleation and propagation. (A) Schematic showing the components of contact forces between bead and microplate well. Two out of twelve beads (i.e., polypropylene and HDPE) did not sink in the solution and contacted only the side of well. Parameters F_g , F_b , F_{cent} , r , L , r' , and L' are described in the main text and are depicted with arbitrary scales and visually exaggerated for clarity. (B-C) Correlation plots of total contact pressure (p_t) versus lag time and propagation rate of D90A apo-SOD1 aggregation. Blue dashed line in (B) indicates the best fit to linear portion of the plot (non-polymeric beads). Note: a transparent microplate (with a concave bottom) was used for demonstrating buoyancy in panel (A).

Together, these results demonstrate that kinetic variations among polymeric beads arise (at least in part) from hydrophobic interactions. The mechanism by which these hydrophobic interactions accelerate fibrillization might involve promotion of primary nucleation events (via increasing the local concentration of SOD1 at the bead surface and/or altering the conformation of SOD1 or its oligomers in ways that accelerate

nucleation). Hydrophobic effects among non-polymeric beads do not appear to be sufficient to explain the kinetic variations in Figure 5.2. Even though some of the non-polymeric beads studied are more hydrophobic than some of the polymeric beads (i.e., aluminum vs. Torlon, Delrin, or acrylic, Table 5.1), non-polymeric beads do not generally bind to SOD1 (open squares in Figure 5.7B), and the contact angle of non-polymeric beads does not correlate in any way with lag time (open squares in Figure 5.7C). Kinetic variations among non-polymeric beads appear to arise not from differences in hydrophobicity but again, from Newtonian mechanical forces. These forces might induce the mechanical breaking of oligomers and fibrils (at the bead-microplate interface), which can promote secondary nucleation processes. Secondary nucleation processes can be induced by mechanical force²⁰¹ and are thought to involve the fragmentation of small, intermediate oligomers to create a higher number of “free-ends” which act as nucleation seeds⁹ and ultimately result in shorter fibrils.^{75,201,223}

In order to test whether non-polymeric beads resulted in shorter, more fragmented fibrils than polymeric beads (which I assume would be the end result of greater continuous fragmentation and secondary nucleation), I performed transmission electron microscopy (TEM) on solutions of fibrils formed in the presence of three different beads: steel, glass, and HDPE (Figure 5.8A). Aggregation of D90A apo-SOD1 resulted in the formation of fibrillar species in the presence of all bead types (Figure 5.8A). Non-polymeric beads caused the formation of a higher number of short, intermittent fibrils (white arrows in Figure 5.8A), where wells with HDPE beads showed mostly long, intertwined fibrils (Figure 5.8A). I also calculated the average fibril length for each bead which showed that shortest fibrils exist in the presence of steel beads (median fibril

length = 70.9 nm), and longest fibrils were formed with HDPE beads (median fibril length = 134.8 nm) (Figure 5.8B). I attribute this higher quantity of short fibrils (in the presence of steel beads) to increased oligomer fragmentation.^{75,201,223} Similar fragmentation-based mechanisms have been observed for other amyloidogenic polypeptides such as $A\beta_{1-42}$.²²⁷ I observed that bead type also affected the formation of amorphous aggregates (the formation of which competes with fibrillization⁹⁸). In general, a higher population of amorphous aggregates was present for polymeric beads compared to non-polymeric beads according to TEM (Figure 8.34 shows representative TEM micrographs for all beads). For example, amorphous SOD1 species were observed to form with HDPE beads (and to a lesser extent, glass beads). Amorphous species were not observed in the presence of steel beads, to the point that products of SOD1 aggregation in the presence of steel beads were almost completely fibrillar (Figure 5.8 and Figure 8.34). This observation demonstrates that higher bead mass—which accelerates the formation of fibrillar species—also disfavors the formation of amorphous aggregates. I interpret this effect to be caused by greater degrees of secondary nucleation with heavier beads. For example, I hypothesize that heavier beads (stainless steel) cause greater degrees of fragmentation of amyloid like oligomers, which promotes further fibrillization and by definition disfavors amorphous aggregation.

In summary, these results do not necessarily imply that surface interactions and hydrophobic effects are not involved at all with non-polymeric beads, or that mechanical forces are not involved in SOD1 fibrillization with polymeric beads, rather that these forces are not sufficiently dominant to explain the kinetic variation within each set of beads.

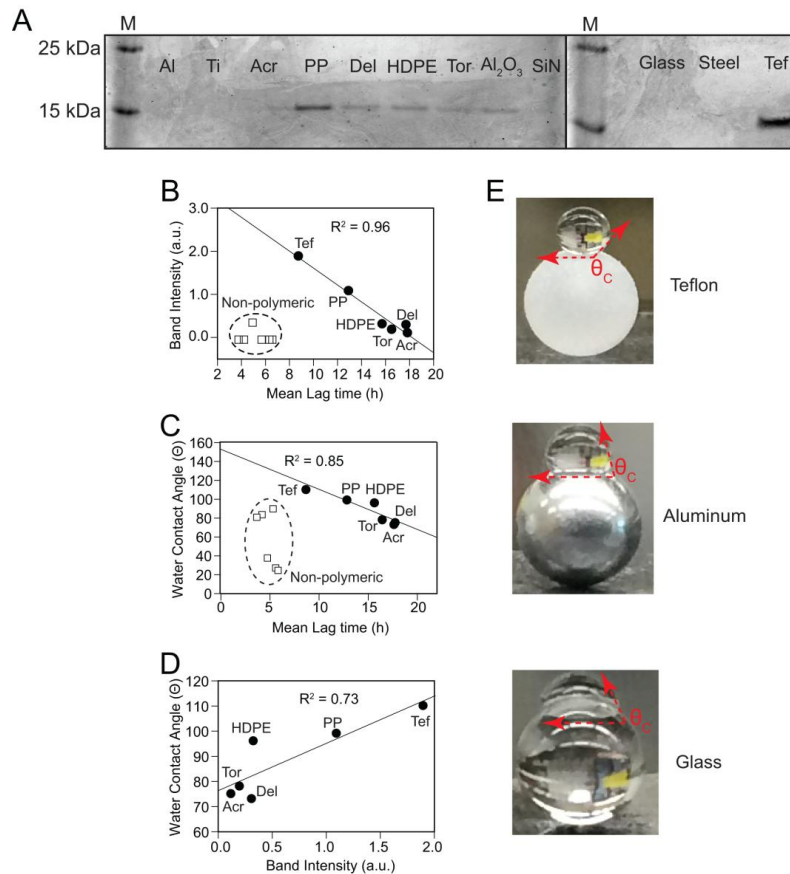


Figure 5.7 Surface adhesion and hydrophobicity can explain kinetic variation among polymeric beads, but not non-polymeric (ceramic, metallic, glass) beads. (A) SDS-PAGE of surface adhered D90A apo-SOD1 recovered from the surface of each washed bead after the termination of ThT aggregation assay (proteins recovered from surface by boiling beads in SDS). Plots of (B) mean band intensity, and (C) water contact angle of bead (prior to beginning assay) vs. mean aggregation lag time of fibrillization for D90A apo-SOD1. (D) Surface hydrophobicity (water contact angle) of bead correlates with the amount of adhered protein to the surface of polymeric beads. Densitometry analyses were carried out using ImageJ® software. (E) Visual demonstration of varying hydrophobicity (θ_c : water contact angle) of beads used in this study.

I was also interested in determining whether altering the surface roughness of smooth, non-polymeric beads would influence aggregation kinetics. This type of experiment has theoretical implications, but I was interested in its practical implications. Do scratches on the surface of beads—scratches that could be introduced during manufacturing, shipping, storage, or handling in laboratory—affect their rates of

aggregation? To answer this question, I coarsened the surface of steel beads using commercial sandpaper (320 grit/X-Fine). I chose steel because it presented the smoothest surface (Figure 5.1). SEM and AFM imaging showed that the surface roughness of steel beads was significantly increased upon sandpapering ($\Delta R_q = 220$ nm; Figure 5.9A). I then performed ThT fluorescence aggregation assays on both smooth (control) and rough (sandpapered) steel beads ($n_{\text{total}} = 104$; Figure 5.9B).

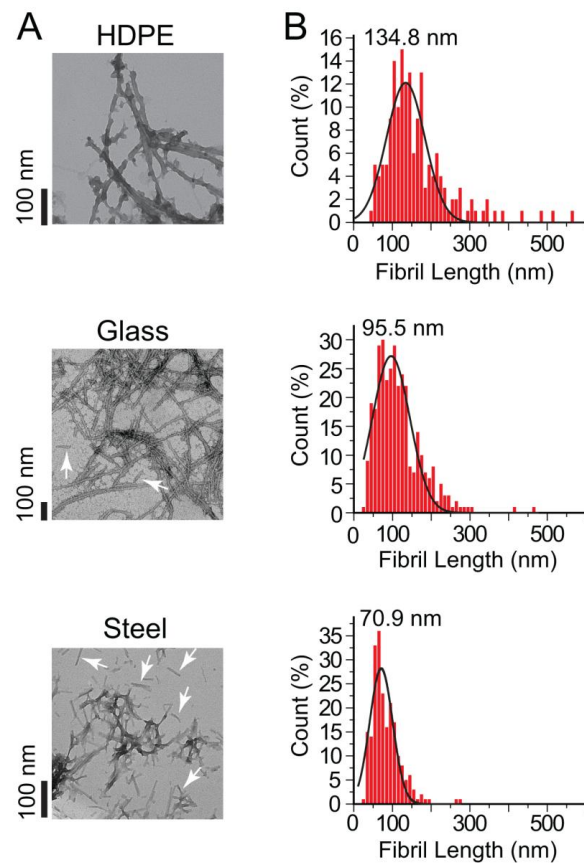


Figure 5.8 Heavier beads promote shorter SOD1 fibrils. (A) Transmission electron micrographs of D90A apo-SOD1 fibrils in the presence of HDPE, borosilicate glass, and stainless steel beads. White arrows point to the short fibril fragments formed in the presence of stainless steel and borosilicate glass beads. (B) Histograms of fibril length ($n_{\text{total}} = 723$) for each bead type. Fibril lengths were measured using cellSens® software and histograms were fit with a 3-parameter Gaussian distribution. The value above each histogram shows the median fibril length.

No significant difference was observed between fibril lag times of control and sandpapered steel beads (Figure 5.9B), supporting the hypothesis that variations in surface roughness do not play a major role in amyloid nucleation with non-polymeric beads. I did, however, observe an acceleratory effect on fibril propagation; D90A apo-SOD1 fibrils propagated faster in the presence of sandpapered steel beads (Figure 5.9B). I interpret this result in terms of higher degrees of oligomer fragmentation in beads with rough surfaces. For example, a rougher surface will have, *ceteris paribus*, fewer contact points with the polystyrene surface of the microplate well, but these fewer contacts will cause greater pressure on points of contact with the polystyrene (as the over-all mass of the bead is not greatly affected by roughening). I found that roughening the surface of steel beads upon sandpapering increased the surface roughness by ~ 25-fold (i.e., $R_{q(\text{steel})} = 9.23 \text{ nm}$, $R_{q(\text{sandpapered})} = 232.0 \text{ nm}$). The average contact pressure that a bead (ideal sphere) exerts on the bottom and sides of polystyrene plate (ideal half-plate) is directly proportional to root mean square of the surface slope i.e., surface roughness (R_q): $p_t \propto R_q$. Thus, sandpapering caused a ~ 25-fold increase in contact pressure between the bead and polystyrene plate ($p_t \propto R_q^{2.25}$). This increased pressure might promote fibril fragmentation and promote secondary nucleation processes. This hypothesis was further tested by measuring the length of SOD1 fibrils in the presence of sandpapered steel beads using TEM imaging. SOD1 fibrils that were formed in the presence of sandpapered steel beads were very short, with an average fibril length of 68.5 nm, which is 2.4 nm smaller than average fibril length in the presence of regular (control) steel beads (Figure 5.9C). These results further demonstrate that increasing contact pressure, upon roughening the surface of beads, leads to a higher degree of fibril fragmentation.

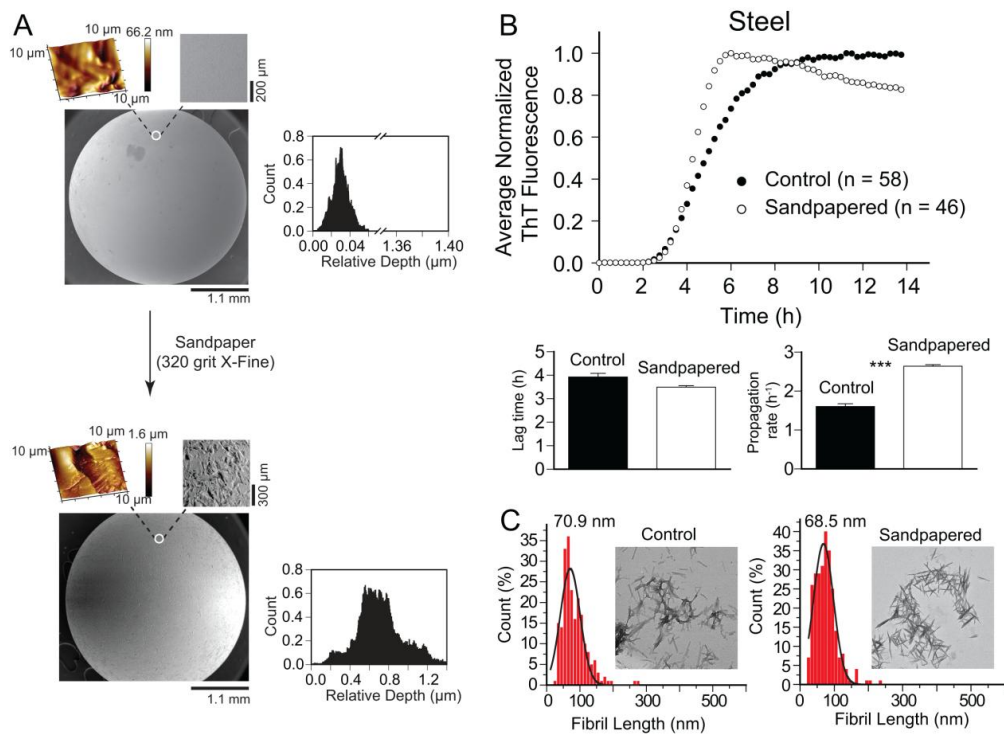


Figure 5.9 Effect of scratching the surface of beads on rate and morphology of fibrillization. (A) SEM and AFM 3D micrographs of the surface of steel beads before and after sandpapering. Color bars next to AFM images represent gradual surface roughness, with lighter colors indicating shallower surfaces. Insets next to each graph show the histogram of relative surface depth, calculated from AFM imaging. (B) Plots of average ThT fluorescence during amyloid assay of D90A apo-SOD1 in the presence of smooth (control) and roughened (sandpapered) steel beads. Bar graphs depict comparison plots of mean lag time and propagation rate ($p < 0.0001^{***}$). (C) Histograms of fibril length ($n_{\text{total}} = 482$) for smooth and sandpapered steel beads. Fibril lengths were measured using cellSens® software and histograms were fit with a 3-parameter Gaussian distribution. The value above each histogram shows the median fibril length. Insets show the TEM micrographs of D90A apo-SOD1 fibrils in the presence of each steel bead.

I also determined whether a correlation existed between the roughness of polymeric beads and aggregation parameters. Values of surface roughness (R_q) of each bead were plotted against corresponding lag time and propagation rate (Figure 8.35). Polymeric beads with rougher surface (higher R_q) cause shorter lag time and faster propagation rate (Figure 8.35). No correlation was found between the surface roughness of non-polymeric beads and kinetic parameters of SOD1 aggregation (Figure 8.35). The

effect of surface roughness of polymeric beads on SOD1 aggregation can be illustrated especially well by comparing Torlon and Delrin beads. These two beads have approximately similar masses, but significantly different surface roughness ($R_{q(\text{Torlon})} \approx 3R_{q(\text{Delrin})}$; Table 5.1). The lag time of SOD1 aggregation is statistically similar in the presence of Torlon and Delrin beads, however, Torlon causes a faster propagation rate than Delrin, possibly due to greater contact pressure which might promote fibril fragmentation (similar to the results obtained for roughened steel beads).

Omniphobicity and Amyloid Formation:

Fluorinated hydrocarbons such as trifluoroethanol (TFE) have been widely used for years to accelerate the rate of amyloid formation²²⁸⁻²³⁰ and control fibril morphology²³¹ during *in vitro* experiments. The chemical mechanisms of action of fluorinated co-solvents on protein structure, folding, and self-assembly are not clearly understood.²³²⁻²³³

The increased rate of fibrillization that I report for a Teflon bead compared to its non-fluorinated analog HDPE, might suggest that similar types of acceleration of fibrillization by RC-F groups is occurring at the surface of Teflon beads (which are omniphobic, i.e., resist interactions with polar and non-polar solvents). One additional difference between Teflon and HDPE beads is that Teflon beads are two-fold higher in mass than HDPE (Table 5.1) and HDPE is ~ 43 % more rigid than Teflon (Table 8.9). These differences offset to produce similar contact pressure for Teflon and HDPE (Figure 5.6B), which do not seem adequate to explain why SOD1 fibrillizes at ~ 16 h in the presence of HDPE beads and ~ 8 h in the presence of Teflon beads (Figure 5.6B).

Contact mechanics thus seems inadequate to explain why Teflon and HDPE beads produce different rates; omniphobic effects between Teflon and the SOD1 protein are of course reasonable explanations.

Hydrodynamic Effects During Microplate Amyloid Assays:

To what degree can hydrodynamic effects—arising perhaps from changes in bead mass or roughness—explain why different types of beads result in different rates of fibrillization? It is well-established that a gyrating bead within a microplate accelerates protein fibrillization via increasing the shear forces upon protein.^{199,234} In the current study, however, the hydrodynamics and type of flow regime (i.e., laminar, transient, or turbulent) of my system remains generally constant regardless of bead type. For example, the Reynolds number of my system is $Re = 328.4$, that is, my system exists under a transient hydrodynamic regime. The Reynolds number does not change per bead type because it is independent of bead's mass or surface properties:

$$Re = \frac{\rho v L}{\mu} \quad (\text{Equation 5.7})$$

Where ρ is fluid density ($\rho_{\text{phosphate buffer}} = 995 \text{ kg/m}^3$), v is the linear gyration speed (0.11 m/s), L is the diameter of circular gyration (0.003 m), and μ is the viscosity of fluid ($\mu_{\text{phosphate buffer}} = 0.0011 \text{ kg/m/s}$). Furthermore, the drag force of the fluid against each bead does not change for different bead types:

$$F_D = \frac{1}{2} \rho v^2 C_D A \quad (\text{Equation 5.8})$$

C_D (drag coefficient) and A (reference area) depend mainly on bead shape, which is constant for the beads used in this study. I note that C_D is also a function of surface

roughness, which does differ among beads used in this study (Table 5.1). However, C_D is only a function of surface roughness under fully turbulent conditions (i.e., $Re > 10^4$). Thus, surface roughness does not have a significant effect on C_D under the transient flow regime of the system in the present study.

Conclusion

I originally initiated this study to find reaction conditions that could increase the rate and reproducibility of amyloid assays for the SOD1 protein. I have succeeded in this effort: the continuous gyration of a stainless steel bead at 360 rpm (with only a 5-second pause for measurement) produces the most rapid, reproducible lag time for apo-SOD1 (1.1 ± 0.08 h, compared to 8.7 ± 0.3 h for the intermittent gyration of a Teflon bead at 360 rpm). However, in the course of assay optimization, I have demonstrated the importance of contact mechanical forces (kilopascal scale) on the nucleation and propagation of SOD1 amyloid fibrils. The best illustration of this point is the ≥ 5 -fold difference in both lag time and propagation rate for stainless steel and acrylic beads (i.e., beads of similar hydrophobicity but different mass; Table 5.1). I attribute the positive correlation between bead mass and rate of amyloidogenesis to the mechanical fragmentation of oligomers by beads.^{195,201} I hypothesize that the greater force imparted on oligomers, at the bead-water-polystyrene interface, leads to increased fragmentation and subsequent secondary nucleation.¹⁹⁵ Previous studies have shown (at the molecular level), that the fibrillization of proteins can be promoted by imparting mechanical and shear force on existing oligomers²³⁴⁻²³⁶ (mechanical stress factors have also been identified as risk factors for different types of protein aggregation diseases²³⁷⁻²³⁸). Thus,

although the study presented in this chapter is performed entirely *in vitro* and would appear to provide little insight into biological processes of SOD1 aggregation, this study establishes the importance of shear force and mechanical stress factors on initiating and propagating SOD1 amyloidogenesis of short fibrils. I also point out that the ability to alter the morphology (i.e., length) of fibrils by simply changing bead type offers a simple, practical method for generating different types of oligomers in order to, for example, test their variable cytotoxicity.

Acknowledgement

Financial support for this research was provided to BFS by the Department of Defense (W81XWH-11-1-0790), the National Science Foundation (CHE: 1352122), and the Welch Foundation (AA-1854). The authors thank Dr. Wilson K. Serem (Materials Characterization Facility, Texas A&M University, College Station, TX) for technical support and useful discussions with atomic force microscopy.

CHAPTER SIX

Metal-Ion-Specific Screening of Charge Effects in Protein Amide H/D Exchange and The Hofmeister Series.

This chapter is published as:

Abdolvahabi A, Gober JL, Mowery RA, Shi Y, Shaw BF (2014) Metal-ion-specific screening of charge effects in protein amide H/D exchange and the Hofmeister series. *Anal. Chem.* **86**, 10303-10310.⁸⁷

Abstract

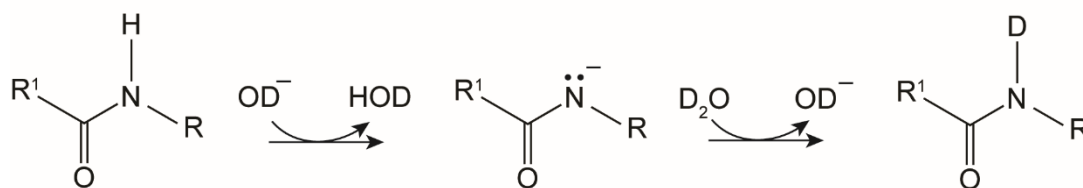
The study presented in this chapter used protein charge ladders and mass spectrometry to quantify how metal cations in the Hofmeister series (Na^+ , K^+ , Li^+ , Mg^{2+} , and Ca^{2+}) permuted the effect of lysine acetylation on the rate of amide H/D exchange in a representative protein (myoglobin, Mb). The successive acetylation of up to 18 Lys- ϵ - NH_3^+ in Mb caused a linear decrease in its global rate of amide H/D exchange (as measured by mass spectrometry) despite also decreasing the thermostability of Mb by > 10 °C. The ability of a metal cation to screen kinetic electrostatic effects during H/D exchange—and abolish the protective effect of acetylation against H/D exchange—was dependent upon the position of the cation in the Hofmeister series. Sodium or K^+ cations did not fully equalize rates of H/D exchange among each “rung” of the charge ladder, however, Mg^{2+} and Ca^{2+} did equalize rates without eliminating the hydrophobic core of the protein; Li^+ exhibited intermediate effects. The ability of Mg^{2+} or Ca^{2+} to completely screen electrostatic effects associated with the H/D exchange of charge isomers of Mb suggests that Mg^{2+} or Ca^{2+} (but not Na^+ or K^+) can be used to quantify the magnitude by which electrostatic charge contributes to observed rates of amide H/D exchange in proteins.

Introduction

The folding of a polypeptide can decrease its rate of backbone amide hydrogen-deuterium (H/D) exchange by a billion-fold.²³⁹⁻²⁴⁰ This deceleration is universally attributed to the formation of hydrogen bonds between amides, and/or their burial from solvent. This paradigm, however useful in studying protein folding and structure, is oversimplified and cannot universally explain rates of amide H/D exchange in folded proteins.^{86,241-242} Certain amides in folded proteins, for example Val38 in rubredoxin,²⁴¹ are not H-bonded or buried from solvent, but nevertheless exchange as if they were. Fundamental physical organic chemistry offers no immediate remedy for this conundrum because the exchange rates of even the smallest amides are perplexing.⁸⁶ The base-catalyzed H/D exchange rate constant (k_{OH}) for 2,5-diketopiperazine—the lowest molecular weight molecule possible with two secondary amides and two α -carbons in series—is ~ 740 times greater than k_{OH} for its mono-amide analog, 2-piperidone.²⁴³

I am interested in determining how large changes in the net surface charge of a folded protein affect its rate of amide H/D exchange. The mechanism of amide H/D exchange at pH 7.4 (Scheme 6.1) and the long-range nature of electrostatic interactions in proteins suggest that the electrostatic environment of an amide NH—its local electrostatic surface potential, and possibly the entire protein's net (or sub-net) charge—will exert some measurable effect on its rate of H/D exchange. For example, the catalyst of amide H/D exchange is an ion (hydroxide at pH > 4; hydronium at pH < 4) whose local concentration at the surface of a protein can be dependent upon the surface potential of the protein.²⁴⁴ The reaction intermediate is also an ion: anionic in the base-catalyzed reaction, and cationic in the acid catalyzed reaction (Scheme 6.1). Finally, electrostatic

interactions in proteins are long-range, occurring across 10 Å through solvent (at ionic strength = 0.1), and possibly further through a protein's interior where the dielectric constant varies from ~ 4 to 20.²⁴⁵ Thus, a cationic functional group at the surface of a protein might increase the rate of amide H/D exchange at pH 7.4 by increasing $[\text{OH}^-]_{\text{local}}$ and/or lowering the free energy of activation (ΔG^\ddagger) of the $\text{R}_0\text{—N}^-\text{—R}_1$ intermediate.



Scheme 6.1 Mechanism of base catalyzed amide H/D exchange.

There are few systematic studies on the correlation between the net charge of a folded protein and its rate of amide H/D exchange.⁸⁶ Most studies altered protein charge by changing solvent pH²⁴⁶⁻²⁴⁷ or altered the Debye radius by changing ionic strength.²⁴⁸⁻²⁴⁹ Discerning the cause of any observed effect in such experiments is complicated by: (i) changes to the intrinsic rate of amide H/D exchange per pH,²⁴⁷ (ii) pH-induced conformational changes,²⁵⁰ and (iii) the under-appreciated difficulty in accurately predicting (or measuring) the net charge of folded proteins across several units of pH.⁶² A more in-depth review of previous investigations into the importance of charge in protein amide H/D exchange can be found in a previous paper by our group.⁸⁶

This previous study by our group utilized lysine-acetyl “protein charge ladders”—chemical derivatives of proteins with systematically altered surface charge and similar structure—to demonstrate that the systematic acetylation of 18 Lys- ϵ -NH₃⁺ on the surface

of bovine carbonic anhydrase II (BCA II) decreased the rate of amide H/D exchange at pH 7.4, in spite of decreasing the conformational stability of BCA II.⁸⁶ The conclusion of our previous study was that the elimination of cationic groups on the surface of BCA II decreased the rate of H/D exchange by diminishing interfacial $[\text{OH}^-]_{\text{local}}$ and/or increasing ΔG^\ddagger of amide H/D exchange by neutralizing cationic groups that stabilize the formation of $\text{R}_0\text{—N:}^- \text{—R}_1$.⁸⁶ One question that remains unanswered from our previous study is why were the presumed electrostatic effects not entirely screened—that is, the disparate rates of H/D exchange of each rung not fully equalized—by the presence of 1 M NaCl? One hypothesis, which I test in this chapter, is that Na^+ and Cl^- ions do not screen electrostatic interactions between OH^- and $\text{Lys-}\epsilon\text{-NH}_3^+$ (or possibly between $\text{R}_0\text{—N:}^- \text{—R}_1$ and $\text{Lys-}\epsilon\text{-NH}_3^+$), because Na^+ and Cl^- interact weakly with the surface of proteins, as understood by their position in the Hofmeister series.²⁵¹

The purpose of this current study is to determine whether and which metal cations in the Hofmeister series²⁵¹ can completely abolish (screen) charge effects in the amide H/D exchange of proteins with similar structure but different net charge. Doing so will not only clarify whether such charge effects can be fully screened, but might identify cations that can be used to determine if perturbations in the rate of H/D exchange (e.g., resulting from non-isoelectric perturbations such as phosphorylation, acetylation, or glycosylation) are caused by a change in charge and/or structure. The results will also deepen my understanding of the Hofmeister series. The molecular underpinnings of the Hofmeister series—e.g., why K^+ is better at “salting-out” proteins than Li^+ —have remained elusive since the effect was first reported in 1888, but appear to involve specific ion-backbone and ion-side-chain interactions,²⁵¹ and the ion’s ability to disrupt the

network of interfacial (not bulk) water.²⁵¹ In this chapter, I used electrospray ionization mass spectrometry (ESI-MS) to test five metal cations in the Hofmeister series for their ability to screen charge effects in the H/D exchange of a Lys-acetyl charge ladder of myoglobin (Mb). I did not study the effect of anions in the Hofmeister series because anions can denature proteins more readily than cations.²⁵¹ I chose horse heart Mb because I wanted to determine if the protective effect of acetylation against amide H/D exchange that I observed in previous studies of BCA II⁸⁶ and human SOD1⁶² occur in other proteins. Myoglobin contains 19 lysine residues and an unacetylated N-terminal α -NH₃⁺. The pI of Mb is 7.3 and the acetylation of each amino group will increase the magnitude of net negative charge at pH 7.4 by \sim -0.9 units instead of -1.0 units (because of charge regulation⁴⁷). The rates of amide H/D exchange of each charge isomer can be measured simultaneously with ESI-MS, under identical solution conditions for H/D in-exchange and back-exchange (Figure 6.1).

Materials and Methods

An expanded version of all experimental details can be found in chapter 8 of this dissertation. Briefly, lysine-NHCOCH₃ protein charge ladders of Mb, denoted Mb-Ac(N) (where N = number of acetylations) were prepared as previously described for other proteins.⁶² The rate of amide H/D exchange was measured with ESI-MS at pH_{read} 6.4, 7.4, and 8.4, and back-exchange controls were carried out as previously described.⁶² The H/D exchange experiments were carried out in the presence and absence of 1 M concentrations of either NaCl, KCl, LiCl, CaCl₂, or MgCl₂. Rates of H/D exchange were also measured at lower concentrations (100-750 mM) of CaCl₂ and MgCl₂ (in D₂O, 99.9

% D) in order to determine the minimal concentration of salt needed to screen charge effects. Deuterated solutions of all Hofmeister salts also contained 50 mM Tris-DCl. Determining the pH_{read} of D_2O solutions (containing molar concentrations of salt) is complicated by electrode instability.²⁵² The pH_{read} of each solution was adjusted, if necessary, to pH_{read} 7.4 prior to H/D exchange by addition of DCl or NaOD. See chapter 8 for details on pH adjustment and colorimetric verification of pH_{read} . Differential scanning calorimetry (DSC), circular dichroism (CD), and capillary electrophoresis (CE) were performed at pH 7.4, as previously described.^{62,67}

Results and Discussion

Acetylation of Lysine Decreases Global Rate of Amide H/D Exchange of Myoglobin Without Increasing Thermostability:

The rate of H/D exchange of the Mb charge ladder at pH_{read} 7.4/ pD 7.8 (without any added salt, apart from the ~ 50 mM Tris buffer and ~ 1 mM citrate buffer) was measured by ESI-MS (Figure 6.2). Throughout the 80 min H/D exchange reaction, the mass spectra of the charge ladders had a similar number of peaks to the mass spectra in H_2O , i.e., 19 peaks in total, with the 20th and 21st rungs being too weak to extract accurate masses (Figure 6.2A). This unimodal mass distribution for each rung in 90 % D_2O suggested that H/D exchange occurred via an EX2 mechanism (Figure 6.2A). An EX1 exchange mechanism would have, in contrast, resulted in a bimodal mass distribution for each rung—totaling 38 peaks—and not a unimodal peak that gradually shifts to higher mass values.⁸⁶ The integration of deconvoluted mass spectra throughout the experimental time course (or in H_2O) revealed a minor fluctuation in signal intensity of each rung of the charge ladder. This fluctuation was minor (\pm 3-12 %), non-progressive, and therefore

not indicative of an EX1 mechanism of H/D exchange (and is likely caused by variations in ionization efficiency and/or computer-assisted deconvolution of raw mass spectra). The predominance of an EX2 mechanism of exchange in the Mb protein charge ladder was confirmed by the pD dependence of its amide H/D exchange (Figure 8.36A-D).

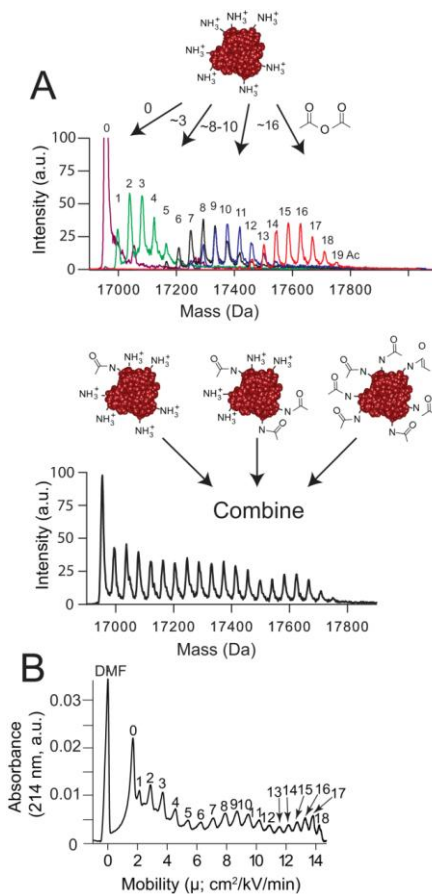


Figure 6.1 (A) Electrospray-ionization mass spectrum of Lys-acetyl “protein charge ladder” of myoglobin (Mb) prepared by the acetylation of surface Lys- ϵ -NH $_3^+$ with acetic anhydride. Variable degrees of acetylation are achieved by adding different molar equivalents of acetic anhydride to aliquots of Mb. Batches of variably acetylated protein can be combined to form the complete charge ladder for Mb. (B) Capillary electropherogram of charge ladder from part (A). Dimethylformamide (DMF) is added to the sample before electrophoresis and functions as a neutral marker of electroosmotic flow.

The rate of amide H/D exchange of each rung is expressed as the number of unexchanged hydrogens with respect to time (Figure 6.2B). The value of unexchanged hydrogens is calculated by subtracting the molecular mass of each rung in D₂O from the mass of the thermally unfolded (perdeuterated) rung, as previously described.⁸⁶ For clarity, I only show the kinetic profile of exchange for every 6th rung; all 19 rungs are shown in Figure 8.37A. Myoglobin retained ~ 36 unexchanged amide hydrogens after 80 min in 90 % D₂O (Figure 6.2B, Figure 8.37). Each additional acetylation of lysine resulted in a constant increase in the number of unexchanged hydrogens throughout the 80 min time course (Figure 6.2B, Figure 8.37A). The hydrogens that become protected from exchange upon lysine acetylation are not likely to be the *side-chain* amides of surface Lys-ε-NHCOCH₃ that resulted from acetylation.⁸⁶ The protective effect of lysine acetylation against amide H/D exchange was first reported for carbonic anhydrase II and was shown to involve backbone amides and not the amide in the introduced Lys-ε-NHCOCH₃ group (which generally exchanged rapidly).⁸⁶ For example, ¹H-¹⁵N HSQC (hetero-nuclear single quantum coherence) NMR and TROSY (transverse relaxation-optimized spectroscopy) of ¹³C-acetylated carbonic anhydrase II showed that most (but intriguingly, not all) side-chain amide groups of Lys-ε-NHCOCH₃ generally underwent rapid H/D exchange before the first HSQC spectra could be collected (i.e., $t_{1/2} \ll 27$ min).⁸⁶

Plotting the number of unexchanged hydrogens at each time point vs. acetylation number, Ac(N)—i.e., plotting the partial derivatives of the trends in Figure 6.2B (i.e., $\partial H_{\text{unex}}/\partial N$)—revealed a linear correlation between the number of unexchanged hydrogens and acetylated lysines (Figure 6.2C).

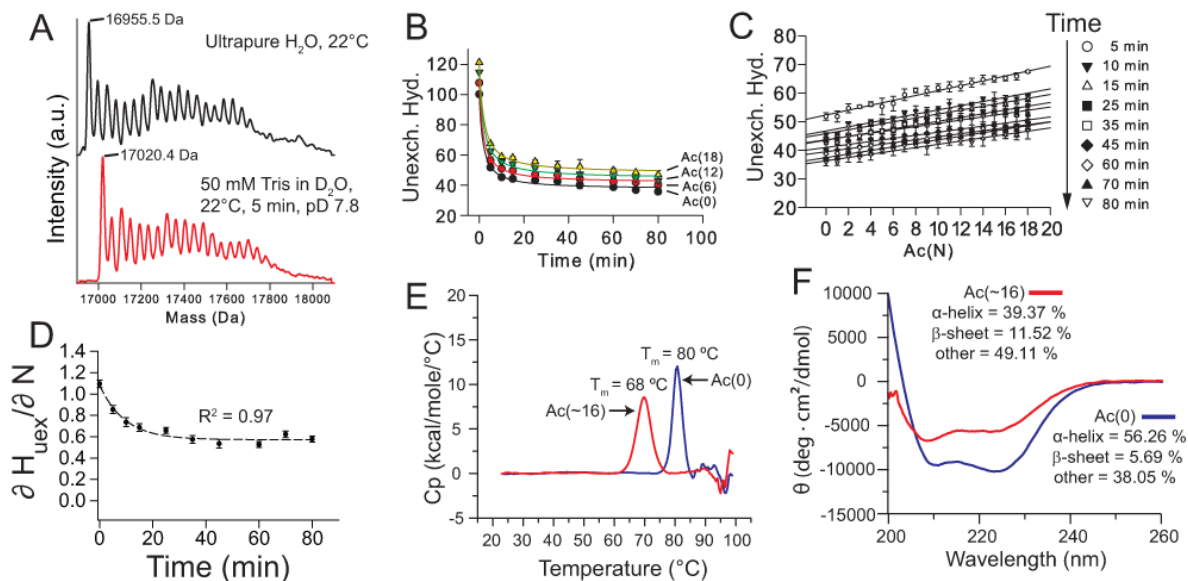


Figure 6.2 Amide H/D exchange of the Mb-Lys-Ac(N) charge ladder at $\text{pH}_{\text{read}} 7.4$ without salt, i.e., $I < 0.1 \text{ M}$. **(A)** Mass spectra of the Mb charge ladder in water at room temperature (top) and in 90 % D_2O after 5 min (bottom). **(B)** Plot of H/D exchange of charge ladder (expressed as unexchanged hydrogen) as a function of time. For clarity, data are only shown for every sixth rung. Error bars are the standard deviation of three replicate measurements. **(C)** Plot of the number of unexchanged hydrogens in each rung of the Mb charge ladder at each time point versus the acetylation number, i.e., a plot of the partial derivative ($\partial H_{\text{uex}}/\partial N$) of plots in part **(B)**, but including all 19 rungs. **(D)** Plot of $\partial H_{\text{uex}}/\partial N$ (i.e., the slope of each line in **(C)**) as a function of time. Error bars are the standard errors associated with the linear fit of $\partial H_{\text{uex}}/\partial N$ from panel **(C)**. **(E)** Differential scanning calorimetry, and **(F)** circular dichroism spectroscopy of unacetylated Mb and Mb-Ac(~ 16), pH 7.4.

The slope of each line in Figure 6.2C ($\partial H_{\text{uex}}/\partial N$) is an expression of the number of amide hydrogens (net) that are protected from H/D exchange in Mb as a result of a single lysine acetylation (at that particular time point in the 80 min experiment). Although these slopes might appear approximately similar for each time point, the slopes are actually decreasing exponentially with respect to time (Figure 6.2D). The magnitude of $\partial H_{\text{uex}}/\partial N$ decreased from 0.85 Da (i.e., 0.85 protected H) per Lys-acetyl at 5 min to 0.57 Da per Lys-Acetyl at 80 min (Figure 6.2D).

This decrease in $\partial H_{\text{uex}}/\partial N$ demonstrated that the protective effect of acetylation against H/D exchange decayed exponentially with time. The fact that $\partial H_{\text{uex}}/\partial N$ decays exponentially with time suggests that lysine acetylation slows the H/D exchange of the rapidly exchanging amides more than slower exchanging amides in the protein's hydrophobic core.

The plot of $\partial H_{\text{uex}}/\partial N$ versus time (Figure 6.2D) was fit with the exponential equation $y = y_0 + ae^{-bx}$. This exponential fit permitted me to extract two constants (ϕ and σ , Table 6.1) that quantify the effect of lysine acetylation upon the rate of H/D exchange in Mb. These constants will be important for quantifying and comparing the magnitude of shielding for each Hofmeister cation. The first constant (denoted ϕ) is “1/b” from the above equation and is referred to as the “shielding” decay constant. The constant ϕ is the mean lifetime (with units of min^{-1}) of the value $\partial H_{\text{uex}}/\partial N$; it expresses the rate at which the protective effect of acetylation against H/D exchange is diminished over time. The constant ϕ also expresses, to some extent, the magnitude by which acetylation slowed the H/D exchange rate of the fastest exchanging hydrogens. The second constant (denoted σ) is “ y_0 ” from the above equation and is referred to as the “penetration” constant (with units of protected hydrogens per acetylation, i.e., $\partial H_{\text{uex}}/\partial N$). The value σ quantifies the degree of protection against H/D exchange that persisted at the end of the 80 min time course. Thus constant σ expresses, to some extent, the magnitude by which acetylation slowed the H/D exchange of the slowest exchanging hydrogens.

Table 6.1 Electrostatic HDX screening constants for cations in the Hofmeister series.

Cation ^a	Shielding Decay Constant, ϕ (min ⁻¹)	Penetration Constant, σ	R ²
No Salt	9.38 ± 0.02 ^b	0.57 ± 0.02 ^b	0.97
K ⁺	32.36 ± 0.01	0.37 ± 0.05	0.97
Na ⁺	21.83 ± 0.02	0.70 ± 0.05	0.92
Li ⁺	6.94 ± 0.03	0.11 ± 0.03	0.93
Mg ²⁺	6.69 ± 0.04	0.05 ± 0.02	0.94
Ca ²⁺	6.65 ± 0.04	0.08 ± 0.03	0.92

^aCounter anion for all cations is chloride.

^bAll data are shown as mean ± SD, n = 3.

It is possible that the acetylation of lysine decreased the rate of amide H/D exchange because acetylation increased the thermostability of Mb and minimized local or global fluctuations in the three dimensional structure of Mb that facilitate H/D exchange.²⁵³ Although the acetylation of lysine residues in folded proteins appears to generally lower their thermostability,^{60,86,254} there are noted exceptions, such as α -amylase.⁶⁰ I measured the thermostability of non-acetylated and acetylated Mb (i.e., Mb-Ac(~16)) with differential scanning calorimetry (DSC) and found that acetylation of nearly all lysine in Mb lowered the melting transition temperature (T_m) from $T_m = 80$ °C for unacetylated Mb-Ac(0) to $T_m = 68$ °C for Mb-Ac(~16) (Figure 6.2E). Acetylation also lowered the absorbance of polarized light at 210 nm by ~ 2500 deg·cm²·dmol⁻¹ and at 225 nm by ~ 4000 deg·cm²·dmol⁻¹. Deconvolution of CD spectra of both unacetylated and acetylated Mb demonstrated that acetylation diminished the α -helicity of Mb by ~ 17 % (i.e., from 56.26 % in the case of Mb-Ac(0) to 39.37 % for Mb-Ac(~16), Figure 6.2F). Lysine acetylation has also been observed to diminish α -helicity of other proteins (α A-crystallin).²⁵⁵ Thus, the acetylation of lysine in Mb slowed the rate of amide H/D exchange in spite of also decreasing Mb thermostability and disrupting secondary

structure. The ability of acetylation to decrease the rate of H/D exchange despite disrupting the protein's secondary structure and lowering its thermostability is contrary to what would be predicted from the H-bonding/solvent accessibility paradigm of amide H/D exchange.

It is unlikely that acetylation of one or more lysine in Mb slowed amide H/D exchange by inducing the aggregation of Mb. The capillary electropherogram of the charge ladder (Figure 6.1B) demonstrated that each rung is soluble, and has similar hydrodynamic drag. An aggregated form of Mb would appear at lower, not higher mobility than Mb-Ac(0). Moreover, lysine acetylation increases the magnitude of net negative charge of Mb, i.e., “supercharges” Mb, which can render proteins impervious to aggregation.³¹ The results of DSC also show that the protein is folded, and the number of unexchanged hydrogen suggests that the protein contains substantial tertiary structure. Nevertheless, I performed native PAGE on highly acetylated Mb (Mb-Ac(~16)). The faster migration of Mb-Ac(~16) compared to Mb-Ac(0) adds further proof of the monomeric structure of Mb-Ac(~16) (Figure 8.38).

I point out that each rung of the charge ladder (except rungs 0 and 21) likely consisted of a mixture of regioisomers. For example, the 1st rung, i.e., Ac(1), has 20 possible regioisomers, while the 9th rung, i.e., Ac(9), has ~ 168,000 possible regioisomers, however, the unique pK_a of each lysine (i.e., its unique reactivity with acetic anhydride) might lower the number of regioisomers by a significant magnitude.⁶⁰ Nevertheless, a single rung of the protein charge ladder is a combinatorial-like array of proteins with equal net charge and number of acetylated lysine, but different patterns of charge. Thus, the measurement of H/D exchange for a single rung reflects the average

global rate of H/D exchange of the entire mixture of regioisomers. The constant increase in unexchanged hydrogen per each rung, suggests that acetylation does not affect the rate of amide H/D exchange by modification of a specific lysine residue (or subset of residues). The drawback to the presence of regioisomers in my experiments is that it complicates the use of rapid proteolysis to identify which regions of the protein become protected in each rung of the ladder. It is unlikely that the rates of H/D exchange that I measured for each rung resulted from the acetylation of a specific lysine residue. Each “rung” of the Lys-acetyl Mb charge ladder is likely composed of a mixture of regioisomers and the rate of amide H/D exchange for each rung is an average of rates for all regioisomers in that rung. For example, the maximum number of different Lys-acetyl regioisomers that are statistically possible in the 7th rung of the charge ladder (Ac6), assuming equal reactivity of all lysine residues, is 27,200.

Additional support for the conclusion that lysine acetylation affects H/D exchange rates by an electrostatic mechanism can be found by comparing the values of $\partial H_{\text{uex}}/\partial N$ at pD 7.8 with values of $\partial H_{\text{uex}}/\partial N$ at pD 6.8 and pD 8.8 (Figure 8.36A-C). The values of $\partial H_{\text{uex}}/\partial N$ at pD 6.8 are higher throughout the 80 min time course, and those at pD 8.8 lower, than values of $\partial H_{\text{uex}}/\partial N$ at pD 7.8. In other words, the acetylation of lysine has less of an effect on amide H/D exchange rates at higher pD. This trend is consistent with the increased deprotonation of lysine at pD 8.8 compared to pD 6.8 and the electrostatic similarity between deprotonated (neutral) Lys- ϵ -NH₂ and Lys- ϵ -NHCOCH₃). Likewise, the values of both ϕ and σ decrease linearly with increasing pD (Figure 8.36D).

Ion Specific Shielding of Charge Effects in Amide H/D Exchange:

The presence of 1 M KCl or NaCl increased the rate of H/D exchange of each rung of the charge ladder (Figure 6.3A and Figure 8.37B), which is an effect that is generally observed with proteins.²⁵⁶ For example, the number of unexchanged hydrogens in the zeroth rung was lowered from ~ 36 unexchanged hydrogens after 80 min in 0 M NaCl, to ~ 30 hydrogens after 80 min in 1 M NaCl (Figure 6.3A).

The presence of 1 M KCl or NaCl did not, however, equalize rates of H/D exchange for each rung, as illustrated by the positive values of $\partial H_{\text{unex}}/\partial N$ throughout the 80 min incubation in D₂O (Figure 6.3B). Thus, 1 M Na⁺ or K⁺ cannot fully abolish the protective effect of lysine acetylation against H/D exchange in Mb. The protective effect of lysine acetylation in the presence of 1 M KCl or NaCl does not exclude the possibility that lysine acetylation is slowing amide H/D exchange by an electrostatic mechanism. Intermolecular electrostatic interactions are not always screened by free salt ions, especially if the interaction requires the desolvation of charged groups, or occurs across distances smaller than the Debye screening length⁴⁷ (i.e., 0.3 nm at 1 M ionic strength). Moreover, electrostatic interactions that occur across the hydrophobic interior of a protein (between charged groups at orthogonal or opposing surfaces) will not necessarily be screened by free ions.²⁵⁷

The presence of Ca²⁺ and Mg²⁺ (1 M) also increased the overall rate of amide H/D exchange in the Mb charge ladder, but unlike Na⁺ and K⁺, both Ca²⁺ and Mg²⁺ equalized rates of H/D exchange for each rung of the charge ladder (Figure 6.3A-B; far right panels). For example, the kinetic profile of H/D exchange for each rung in 1 M Ca²⁺ or Mg²⁺ are superimposable, unlike in the presence of 1 M Na⁺ or K⁺ (Figure 6.3A).

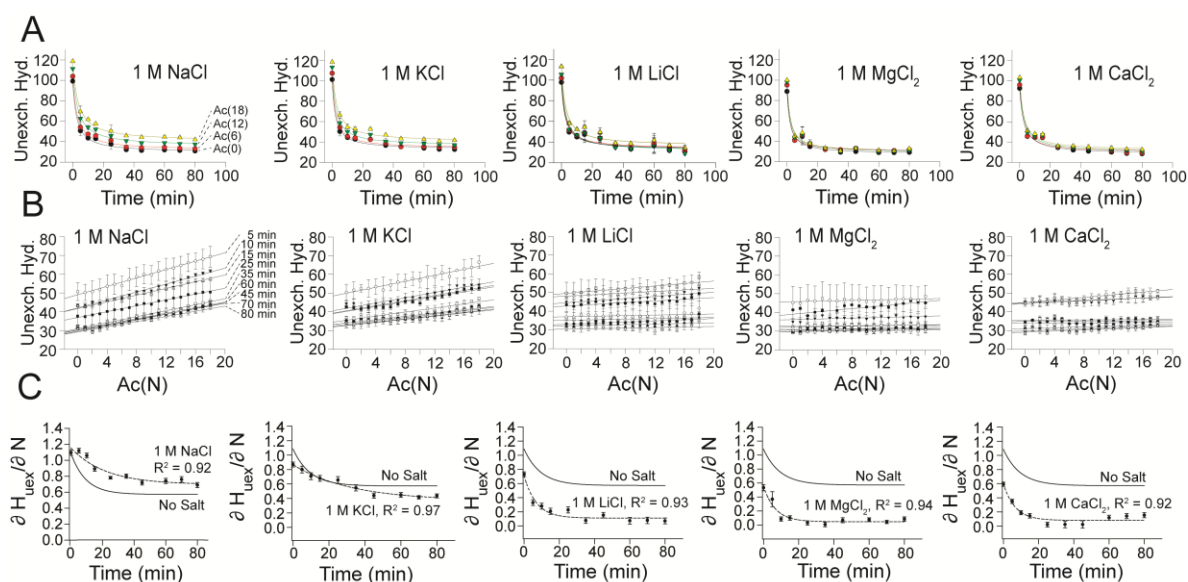


Figure 6.3 Amide H/D exchange of a Mb-Lys-Ac(N) charge ladder in the presence of 1 M metal chloride salts (Na^+ , K^+ , Li^+ , Mg^{2+} , and Ca^{2+}). **(A)** Plots of H/D exchange as a function of time in each salt ($\text{pH}_{\text{read}} = 7.4$; $\text{pD} = 7.8$). Error bars are the standard deviation of triplicate runs. **(B)** Plot of the number of unexchanged hydrogens in each rung of the Mb charge ladder at each time point (5 min to 80 min in D_2O) versus the acetylation number, i.e., a plot of $\partial H_{\text{uex}}/\partial N$ for all 19 “rungs” in the presence of each salt. Error bars are the same standard deviation shown in part **(A)**. **(C)** Plot of $\partial H_{\text{uex}}/\partial N$ (the slope of each line in panel **(B)**) as a function of time. Error bars are the standard errors associated with the linear fit of $\partial H_{\text{uex}}/\partial N$ points from panel **(B)**.

The equal rates of H/D exchange exhibited by each rung in the presence of Ca^{2+} or Mg^{2+} are also illustrated graphically by the small values of $\partial H_{\text{uex}}/\partial N$ (Figure 6.3B) that rapidly approached zero after only 10-30 min in D_2O (Figure 6.3C). A value of zero for $\partial H_{\text{uex}}/\partial N$ indicates that each acetylation did not alter the rate of H/D exchange at that point of time, in the presence of 1 M Ca^{2+} or Mg^{2+} . It is also important to remember that the size of the slow-exchange core or hydrophobic core of Mb-Ac(0) was not largely affected by the presence of 1 M Ca^{2+} and Mg^{2+} , in comparison to 1 M Na^+ and K^+ , as expressed by its number of unexchanged hydrogens. For example, Mb-Ac(0) retained ~ 30-35 unexchanged hydrogens in any of the five salts. In the presence of Ca^{2+} , however,

the highest rung of the ladder (the most acetylated rung) also retained ~ 30 unexchanged hydrogens. This point is subtle, but important because it suggests that Ca^{2+} and Mg^{2+} are completely screening the electrostatic effects and equalizing rates of H/D exchange among all rungs by a mechanism that does not involve protein unfolding. In other words, these data suggest that Ca^{2+} and Mg^{2+} are not equalizing rates of exchange by exposing buried amides to solvent or breaking intramolecular hydrogen bonds, but rather by altering some aspect of the surface chemistry of the protein.

Lithium cation partially screened the electrostatic effect of acetylation on the H/D exchange of Mb, that is, the effect of acetylation on the rate of amide H/D exchange was smaller in the presence of 1 M Li^+ , than in 1 M Na^+ or K^+ , but larger than in the presence of 1 M Ca^{2+} or Mg^{2+} . For example, the slopes of unexchanged hydrogen vs. Ac(N) in 1 M Li^+ are significantly flatter than those observed in 1 M Na^+/K^+ but steeper than those observed in 1 M $\text{Ca}^{2+}/\text{Mg}^{2+}$ (Figure 6.3B). Moreover, the magnitude of $\partial\text{H}_{\text{uex}}/\partial\text{N}$ in the presence of Li^+ decays to 0.11 ± 0.03 H/N after 80 min (Figure 6.3C), which is lower than in Na^+ (0.70 ± 0.05 H/N) but greater than in Ca^{2+} (0.08 ± 0.03 H/N).

In order to graphically compare the screening ability of each cation, I show (in Figure 8.39A) traces of the fit of $y = y_0 + ae^{-bx}$ to each longitudinal plot of $\partial\text{H}_{\text{uex}}/\partial\text{N}$ for each cation (from Figure 6.3C). The “shielding” decay constant (ϕ , Table 6.1) for each cation is a non-equilibrium metric of the screening strength of the cation. A smaller ϕ value demonstrates that the cation more effectively shielded amides from the electrostatic effects of acetylation, causing $\partial\text{H}_{\text{uex}}/\partial\text{N}$ to approach zero more rapidly. The “penetration” constant (σ , Table 6.1) expresses the number of hydrogens per acetylation that continue to be electrostatically protected from exchange in the presence of the cation, even after 80

min in D₂O. The penetration constant σ represents the leveling off point of the plots in Figures 6.3C and 6.4A and is a metric that is closer to equilibrium than ϕ . Thus a smaller value of σ also demonstrates that the cation more effectively screened the electrostatic effects of acetylation on amide H/D exchange.

With respect to values of σ , the five metal cations screened charge effects in the following order: $\text{Na}^+ < \text{K}^+ < \text{Li}^+ < \text{Mg}^{2+} \approx \text{Ca}^{2+}$ (Table 6.1). With respect to values of ϕ , the screening order was: $\text{K}^+ < \text{Na}^+ < \text{Li}^+ \approx \text{Mg}^{2+} \approx \text{Ca}^{2+}$ (Table 6.1). Thus a metal cation's ability to screen surface charge effects during amide H/D exchange, as measured by ϕ correlates approximately (but not perfectly) with the cation's ability to “salt-in” proteins per the Hofmeister series: $\text{K}^+ < \text{Na}^+ < \text{Li}^+ < \text{Mg}^{2+} < \text{Ca}^{2+}$. The trend in values of σ for each cation also follows approximately the Hofmeister series, except that Na^+ and K^+ are in reverse order.

I hypothesize that metal cations such as Li^+ , Mg^{2+} , or Ca^{2+} interact more tightly with higher rungs of the ladder than lower rungs (possibly because of the increased net negative charge of higher rungs) and thereby accelerate the rate of H/D exchange of the higher rungs, so as to be equal to the lower rungs. The most straightforward explanation for the ordering of electrostatic shielding that I observed is that a metal cation such as Li^+ interacts more strongly (albeit still “weakly”) with amides proximal to the site of acetylation than Na^+ (a trend that is supported by molecular dynamic simulations²⁵⁸⁻²⁵⁹). In such a mechanism—which can involve cation interactions with C=O groups of backbone amides²⁶⁰ and presumably C=O groups of amides on surface Lys- ϵ -NHCOCH₃—a Li^+ ion can more effectively act as an electrostatic surrogate for the acylated R- ϵ -NH₃⁺ group of lysine than can the Na^+ ion. Thus, Li^+ might equalize rates of

exchange between acetyl rungs by increasing $[\text{OH}^-]_{\text{local}}$ and/or stabilizing $\text{R}_o\text{—N:}^- \text{—R}_1$. This type of electrostatic interaction of a cation with a backbone or Lys- ϵ -NHCOCH₃ amide would not *necessarily* require physical penetration of cations into the protein's core (and complete desolvation of the cation) because all lysine residues in Mb are located at the protein's surface.

I suspected that the charge density of the cation (Z/r^2) might correlate with the cation's ability to act as an electrostatic surrogate for Lys- ϵ -NH₃⁺, and screen surface charge effects among rungs of the ladder. An exponential correlation was found between the magnitude of ϕ and the charge density of each cation when the ionic radii of the non-hydrated (desolvated) cation were used ($R^2 = 0.97$; Figure 8.39B). This correlation suggests that some type of electrostatic effect between the cation and the protein is partially accounting for the trend that I observed in ϕ for each cation. No correlation (linear, exponential, etc.) was found between the value ϕ and the charge density of the cation, when the hydrated radius of each cation was used to calculate the densities.

An exponential correlation was also found between the magnitude of ϕ and the $\Delta G_{\text{hydration}}$. These correlations suggests that the cation undergoes some degree of desolvation prior to interacting with the surface and screening charge effects among the slowest exchanging amides (presumably in the core of the protein).

There were no linear or exponential correlations found to exist between σ and the charge density or $\Delta G_{\text{hydration}}$ of each cation. The surface of Mb does not contain a coordinate covalent metal binding site²⁶¹ (apart from the heme group) and it is therefore unlikely that Ca²⁺, Mg²⁺, or Li⁺ are equalizing the H/D exchange rates of rungs in the Mb charge ladder by binding tightly (specifically) to a metal binding site or sites on the

protein. If such metal binding interactions were occurring, they would likely increase the T_m of Mb. To confirm the absence of these strong, specific interactions, I compared the thermostabilities of acetylated and unmodified Mb in the presence of Ca^{2+} using differential scanning calorimetry (Figure 8.39).

The T_m of Mb-Ac(0) was ~ 80 °C and the T_m of Mb-Ac(~ 16) was ~ 70 °C in 0 M Ca^{2+} and these two T_m values were unchanged by the addition of 200 mM Ca^{2+} (Figure 8.39). In the presence of 1 M Ca^{2+} , I only observed small differences in the T_m of Mb-Ac(0) and Mb-Ac(~ 16): $T_m = 56$ °C for Mb-Ac(0) and $T_m = 51$ °C for Mb-Ac(~ 16) (Figure 8.39).

Mg²⁺ and Ca²⁺ Completely Screen Electrostatic Effects in the Myoglobin Charge Ladder Only at High Concentration:

In order to determine the concentration of Mg^{2+} or Ca^{2+} required to equalize the rates of H/D exchange throughout the charge ladder, I repeated H/D exchange experiments at progressively lower concentrations of Mg^{2+} (Figure 8.40) and Ca^{2+} (Figure 8.41).

The ability of Ca^{2+} and Mg^{2+} to completely screen charge effects is only observed at concentrations ≥ 500 mM (Figure 8.40 and Figure 8.41), however, $MgCl_2$ almost completely equalized rates of exchange at 200 mM [Mg^{2+}] and this concentration of $MgCl_2$ might be a useful tool for identifying electrostatic effects in the amide H/D exchange of proteins.

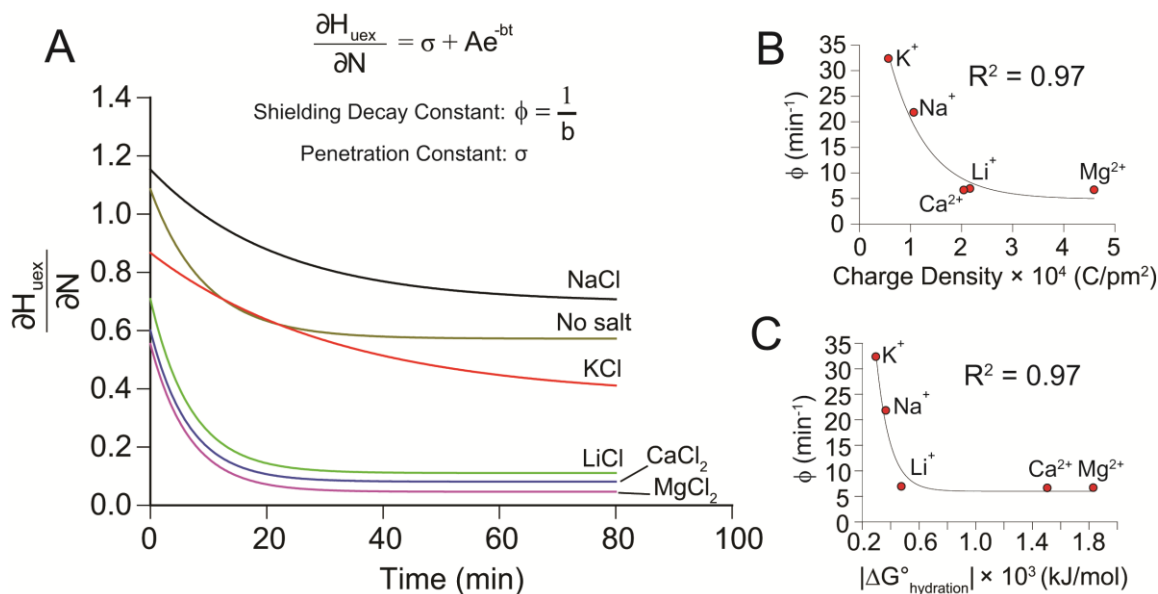


Figure 6.4 (A) Traces of each exponential fit of the plot of $\partial H_{\text{uex}}/\partial N$ versus time for the Mb-Ac(N) charge ladder in the presence of each metal chloride (1 M). Traces are derived from fit of data points in Figure 6.3C. (B) Plot of shielding decay constant (ϕ) for each cation as a function of the cation's charge density. Values of charge density in (B) are calculated from cation's desolvated radii. (C) Plot of shielding decay constant (ϕ) for each cation as a function of its free energy of hydration. A 3-parameter exponential decay function ($y = y_0 + ae^{-bx}$) was used to fit the data in parts (B) and (C).

What Can the H/D Exchange of Protein Charge Ladders Reveal About the Hofmeister Series?

Early cations in the Hofmeister series (K⁺, Na⁺) strengthen hydrophobic interactions between nonpolar groups (“salting-in”), while later cations (Mg²⁺, Ca²⁺) weaken hydrophobic interactions (“salting-out”). Hofmeister ions such as Ca²⁺ are thought to exert their effects by direct interaction with the backbone and side chain functional groups of the protein and by interaction with interfacial water.^{251,262} Recent investigations using vibrational sum frequency generation (VSFG) spectroscopy have shown that later cations such as Mg²⁺ interact more strongly with negatively charged surfaces than cations such as Li⁺ and cause greater disruption of ordered water networks

at the surface-water interface.²⁶² The metal-induced effects that I observed appear to be surface effects that involve the weak association of Mg^{2+} or Ca^{2+} with the net negatively charged surface of Mb. These interactions do not alter the baseline size of the protein's hydrophobic core, that is, each metal cation did not alter the number of unexchanged hydrogens in the zeroth rung of the ladder after 80 min in D_2O . I suspect that the correlation between the magnitude of shielding that I observed for each metal cation, and its approximate position in the Hofmeister series, is not coincidental.

I hypothesize that the ability of a metal cation to shield charge effects in amide H/D is determined by the strength of its interaction with the surface of the protein, its charge density, and its ability to disrupt ordered interfacial water networks (and possibly increase the diffusion of solvent catalyst to and from the protein surface). Although I interpret each cation's ability to screen charge effects in terms of the cation's interaction with the protein, I cannot exclude the importance of the counter ion and interactions involving the ion pair, e.g., $[\text{Ca}^{2+}, 2\text{Cl}^-]$.

These interactions can be important considering the unique effect of each contact ion pair (CIP) on protein structure, as inferred from the “law of matching water affinities”.²⁶³ The ability of Ca^{2+} to interact more strongly with negatively charged surfaces, compared to Na^+ or K^+ , could manifest into faster H/D exchange rates of higher rungs of the ladder by three mechanisms (that are not mutually exclusive). The first two mechanisms are predominantly electrostatic: (i) an electrostatically driven increase in $[\text{OH}^-]_{\text{local}}$ and/or (ii) an electrostatically driven lowering of ΔG^\ddagger of the $\text{R}_o\text{—N}^-\text{—R}_1$ intermediate. A cation such as Ca^{2+} might also increase the rate of H/D exchange of higher rungs, more than Na^+ or K^+ via a third mechanism that involves disruption of the

H-bonded interfacial water network at the protein's surface.²⁶² I presume that disrupting this network would increase the rate of diffusion of solvent catalyst to and from the backbone amides.

Conclusion

The successive acetylation of surface lysine residues in Mb led to a linear increase in the number of amide NH's that are protected from amide H/D exchange, in spite of also decreasing the protein's thermostability and diminishing its secondary structure. This effect is contrary to what would be predicted by the "solvent accessibility and/or H-bonding" paradigm that is used to interpret rates of amide H/D exchange. A series of free cations progressively abolished the protective effect of acetylation in the order: $K^+ \approx Na^+ < Li^+ < Mg^{2+} \approx Ca^{2+}$, which correlates reasonably well with the Hofmeister series: $K^+ < Na^+ < Li^+ < Mg^{2+} < Ca^{2+}$. The exact position of K^+ and Na^+ in my screening series depends upon which screening constant (ϕ or σ) is considered (Figure 8.39). With respect to values of σ , Li^+ exhibited a weaker screening effect than Mg^{2+} and Ca^{2+} (i.e., Li^+ exhibited a 2.2-fold increase in σ compared to Mg^{2+}), and a stronger screening effect than Na^+ and K^+ . Based on values of ϕ , however, Li^+ showed similar screening strengths to Mg^{2+} and Ca^{2+} (Table 6.2). The results of this study explain the previously reported observation⁸⁶ that molar concentrations of NaCl were not capable of completely equalizing the rate of amide H/D exchange among rungs of a lysine-acetyl protein charge ladder.

Although I initiated the study presented in this chapter to investigate previous reports that NaCl cannot screen presumed electrostatic effects during amide H/D

exchange, I suspect that the amide H/D exchange of a protein charge ladder can be a useful tool to study weak interactions between ions and the surfaces of proteins. For example, the magnitude of each cation's shielding decay constant and penetration constant might be a useful metric to quantify weak interactions between the surface of a protein and free ions in solution. Although I only studied a Lys- ϵ -NHCOCH₃ charge ladder in this chapter, other surface properties (hydrophobicity, aromaticity, polarity) can be systematically altered by attaching myriad types of acyl groups to Lys- ϵ -NH₃⁺. This large chemical tool box would be useful for studying the importance of surface chemistry in ion-specific (Hofmeister) effects, which are still far from being fully understood and can, for some proteins, be reversed.²⁵¹

Acknowledgements

B.F.S acknowledges funding from the Department of Defense (W81XWH-11-1-0790), a National Science Foundation CAREER Award (CHE: 1352122), and the Welch Foundation (AA-1854).

CHAPTER SEVEN

Colorimetric and Longitudinal Analysis of Leukocoria in Recreational Photographs of Children with Retinoblastoma

This chapter is published as:

Abdolvahabi A, Taylor BW, Holden RL, Shaw EV, Kentsis A, Rodriguez-Galindo C, Mukai S, Shaw BF (2013) Colorimetric and longitudinal analysis of leukocoria in recreational photographs of children with retinoblastoma. *PLoS One* **8**, e76677.²⁶⁴

Abstract

Retinoblastoma is the most common primary intraocular tumor in children. The first sign that is often reported by parents is the appearance of recurrent *leukocoria* (i.e., “white eye”) in recreational photographs. A quantitative definition or scale of leukocoria—as it appears during recreational photography—has not been established, and the amount of clinical information contained in a leukocoric image (collected by a parent) remains unknown. Moreover, the hypothesis that photographic leukocoria can be a sign of early stage retinoblastoma has not been tested for even a single patient. The study presented in this chapter used commercially available software (Adobe Photoshop®) and standard color space conversion algorithms (operable in Microsoft Excel®) to quantify leukocoria in actual “baby pictures” of 9 children with retinoblastoma (that were collected by parents during recreational activities i.e., in nonclinical settings). One particular patient with bilateral retinoblastoma (“Patient Zero”) was photographed > 7,000 times by his parents (who are authors of this study) over three years: from birth,

through diagnosis, treatment, and remission. This large set of photographs allowed me to determine the longitudinal and lateral frequency of leukocoria throughout the patient's life. This study establishes: (i) that leukocoria can emerge at a low frequency in early-stage retinoblastoma and increase in frequency during disease progression, but decrease upon disease regression, (ii) that Hue, Saturation and Value (i.e., HSV color space) are suitable metrics for quantifying the intensity of retinoblastoma-linked leukocoria; (iii) that different sets of intraocular retinoblastoma tumors can produce distinct leukocoric reflections; and (iv) the Saturation-Value plane of HSV color space represents a convenient scale for quantifying and classifying pupillary reflections as they appear during recreational photography.

Introduction

Retinoblastoma (Rb) is an aggressive cancer that forms rapidly in the developing retina of children, typically before the age of five years.²⁶⁵⁻²⁶⁷ Epidemiology estimates that ~ 7000-8000 children develop Rb throughout the world each year, and 3000-4000 children die annually.²⁶⁸ The median age of diagnosis in the U.S. is ~ 24 months for unilateral disease and ~ 9-12 months for bilateral disease.^{267,269-271} Survival rates are high in developed countries (e.g., ~ 95 % survival in the U.S.²⁷¹⁻²⁷³) but drop in resource limited settings (e.g., 48 % in India;²⁷⁴ 46 % in Namibia²⁷⁵⁻²⁷⁶). Lower survival rates are attributed to delayed diagnosis and the development of extra-ocular and metastatic disease.²⁷⁷ Survivors typically experience moderate to severe vision loss; however, early diagnosis can increase the rate of vision preservation and survival.²⁷⁸⁻²⁸² Diagnosing Rb continues to be a major challenge. The incidence of this cancer in the U.S. is sufficiently

high (i.e., 1:16,000-18,000 births²⁷¹) that pediatricians are advised to screen for Rb by performing the “red reflex” test with an ophthalmoscope.²⁸³⁻²⁸⁴ In spite of pediatric screening, one of the most effective methods for detecting Rb appears to be amateur photography: the diagnosis of a large proportion of Rb cases in the U.S. (e.g., ~ 80 % in one study²⁸⁵) appears to be initiated by a parent’s concern over recurrent leukocoria in photographs of their child²⁸⁶ (see Figure 7.1B for an example of Rb-linked leukocoria). Although other rare eye conditions can also result in recurrent leukocoria²⁸⁷ (e.g., Coats’ disease,²⁸⁸ pediatric cataract,²⁸⁹ chorioretinitis,²⁹⁰ and persistent fetal vasculature²⁹¹), the most common cause of *persistent* leukocoria in children under the age of 5 years old is historically considered to be Rb.²⁹²⁻²⁹⁴

Leukocoria (from Greek meaning “white pupil” colloquially referred to as “white eye” or “cat eye”) has been historically associated with advanced Rb and low rates of ocular salvage,²⁸⁵ however, the age of emergence and longitudinal frequency of leukocoria has never been determined for even a single patient. Thus, the correlation between the emergence and frequency of leukocoria (detected by parents during recreational photography) and disease onset, progression and remission remains unknown. I suspect that photographic leukocoria might emerge earlier in disease progression than tacitly assumed, but that it initially occurs at a low frequency because of the small size or eccentric position of the tumor(s), and becomes progressively more frequent (and thus easily noticed by parents) as tumors increase in size and number.

Despite the effective—albeit, anecdotal—use of digital photography by parents to detect Rb-linked leukocoria,²⁸⁵ there have been no efforts to develop tools that might increase the effectiveness of digital photography in screening Rb (e.g., software that is

embedded in a camera or computing device that can detect leukocoria). The recreational photographs of Rb patients with leukocoria have never been analyzed with basic tools in computer graphics that can quantify the colorimetric properties of the leukocoric reflection, e.g., the Hue (color), Saturation (color concentration) and Value (brightness). Thus, a quantitative definition and scale of leukocoria does not exist and the correlation between the clinical severity of Rb (i.e., size, position, and number of tumors) and the colorimetric properties of its leukocoric reflection remains undetermined. I hypothesize that photographs of children with Rb—of the type that parents collect—do contain more clinically relevant information than a simple binary detection of “white-eye”. This information (if present and readily quantifiable) might be useful to a pediatric clinician or ophthalmologist, and could be instantly transmitted out of environments with limited resources where most deaths occur.

I presume that amateur photography has been overlooked as a quantitative tool for screening Rb because amateur recreational photography involves untrained (or unsuspecting) users who are operating dozens of different devices in diverse settings (i.e., at multiple angles, focal apertures, light intensities, etc.). Nevertheless, despite the optically diverse nature of recreational photography, parents have inarguably proven that this practice of photography is as effective at detecting Rb as pediatric examinations (if not more effective, because parents photograph their children more often than they are examined by a clinician and/or possibly because flash photography involves a rapid flash pulse, $t < 500$ ms, that will not necessarily contract the pupil and impede the reflection of light off peripheral tumors, Figure 7.1). In this chapter, my colleague and I analyzed > 7000 recreational photographs of nine Rb patients and 19 control children (who were

photographed alongside patients, i.e., were “playmates”). I show that the intensity of a leukocoric reflection can be quantified in HSV color space; I also show that the lateral and longitudinal frequency of leukocoria can correlate with the clinical severity of Rb and its progression and remission. The results suggests that leukocoria can emerge in the earliest stages of Rb (e.g., at 12 days old in one patient), but occurs initially at low frequency and is, presumably, easily overlooked by a parent. Finally, I propose a quantitative scale by which leukocoria intensity can be graded.

With regard to this study, it must be remembered that the recreational photography of an infant and toddler by his parents is *not* by nature optically random. For example, a parent will typically photograph an infant or toddler at a finite range of focal lengths and will favor certain positions and angles of the child over other angles (i.e., top-down pictures are more often collected than bottom-up). As I show in this chapter, thousands of recreational photographs collected over several years can have similar exposure times, focal apertures, and depending upon the camera, a consistent flash pulse and aspect ratio.

Methods

Collection of Donated Photographs of Retinoblastoma Patients and Healthy Control

Subjects:

Photographs of nine children with Rb (2 girls, 7 boys) were donated by their parents. The parents of eight of the children only donated images that they had judged to be leukocoric; these sets of photographs were small (i.e., < 10 images per child) and were not longitudinal in nature. The parents of a ninth child (a male, referred to as “Patient Zero”), who are the corresponding authors of this study, donated their entire library of

photographs that consisted of an unsorted set of 9493 digital photographs in JPEG (Joint Photographic Experts Group) format. Out of this library, 7377 photographs contained the patient's face and thus were used in analysis. The photographs of Patient Zero also contained images of 19 different children (approximately age-matched) who functioned as embedded controls.

The metadata tags included in the EXIF (Exchangeable Image File) data of each leukocoric JPEG file from each patient were analyzed in order to determine: (i) the date that each picture was collected (i.e., the age of the patient), (ii) whether a flash was used, (iii) whether "Red Eye Reduction" was in effect, (iv) the make and model of the camera, and (v) photographic parameters such as exposure time and focal aperture.

A total of fourteen different digital cameras were used to collect the photographs in this study. Two cameras were used contiguously to collect images of Patient Zero: (i) a Canon Power Shot SD750® (Canon USA, Lake Success, NY), from age 0-16 months, and (ii) a Nikon D3000® (Nikon Inc., Melville, NY) from age 16-36 months. Both cameras were equipped with a xenon flash tube and contained "Red Eye Reduction" and "Red Eye Removal" technologies.

Nine digital cameras that were used to photograph the remaining eight patients were: Apple iPhone 4® (Apple Inc., Cupertino, CA) for Patient 1, n = 9 leukocoric photographs; Panasonic DMC-FS3® (Panasonic Inc., Secaucus, NJ), Canon Powershot SD300®, and Canon EOS Digital Rebel XSi® for Patient 3, n = 4; Nikon D60® and Blackberry 8330® (Blackberry, Ontario, Canada) for Patient 4, n = 9; Blackberry 8330® for Patient 5, n = 9; Nikon D60® for Patient 6, n = 3; Canon Powershot A80® and Canon Powershot A2000 IS® for Patient 7, n = 3; and Panasonic DMC-LZ2® for Patient 8, n =

7. The digital camera used to photograph Patient 2 could not be determined. The following three digital camera phones were used to generate 72 photographs of a healthy adult that exhibited “pseudo-leukocoria”: Samsung SGH-I997; Apple iPhone 4; and Droid Razr® (Motorola). Because anecdotal evidence suggests that “pseudo-leukocoria” occurs more frequently in low-light conditions, I collected “pseudo-leukocoric” images under low-light conditions (i.e., a dimly lit room) characterized by a light intensity of $0.0259 \pm 0.0074 \mu\text{E}/\text{m}^2/\text{s}$, as measured by a digital light meter (*LX1010B*, Dr. Meter). A flash was emitted during the collection of each “pseudo-leukocoric” image.

Colorimetric Analysis of Pupillary Reflexes:

The average HSV color space parameters (Hue, Saturation, and Value) of each pupil were determined in the following manner: (i) each pupil was cropped in its entirety and the total pixel count was determined using Adobe Photoshop® (Adobe, San Jose, CA; CS5 Extended, version 12.0.4 x64); (ii) the number of pixels with a given intensity in three color-channels (red, green, and blue; RGB) was then determined for each pupil; (iii) the average RGB coordinates of each cropped pupil was calculated using Microsoft Excel® (Microsoft Inc., Redmond, WA); (iv) these RGB coordinates were then transformed to the HSV cylindrical coordinate system using the standard RGB-HSV conversion algorithm introduced by Smith²⁹⁵ (which is operable in Microsoft Excel®). Photographs that contain pupils comprised of 10 pixels or fewer were not analyzed because of their low resolution. I chose to express and quantify leukocoria in HSV color space (instead of RGB) because HSV specifies the color in terms that are more intuitive (to us) and thus much easier to interpret and communicate. For instance, the HSV system

defines a basic color of the visible range of the electromagnetic spectrum (Hue), the concentration of that color, i.e., from pink to red (Saturation), and thirdly, the brightness of the color (Value). The RGB system, on the other hand, partitions a single color into color channels designated "Red", "Green" and "Blue" that correspond to the additive color components, which make up the single color. While both HSV and RGB can specify a color to the same precision, RGB requires knowledge of additive colors in order to understand how changes in one channel affect the overall appearance of color. Thus, in my opinion, this feature makes RGB more complicated and less intuitive comparing to HSV color space.²⁹⁵ Moreover, consumers (parents) are often self-educated in HSV color space during the use of electronic image displays (i.e., computer screens, flat screen televisions, etc.).

In the case of Patient Zero, I did not crop and quantify the HSV of *every* pupil in each of the 7377 facial photographs. Instead, I manually inspected each photograph for pupils that were suspicious for leukocoria (i.e., pupils that were not obviously black or dark red in appearance). The entire process of cropping pupils and quantifying HSV parameters for each pupil in this subset was then performed in duplicate by separate researchers.

Clinical Description of Patient Zero:

Patient Zero was diagnosed with bilateral Rb by an ophthalmologist at 123 days of age. The only presenting sign was leukocoria, which the parents had reported noticing for three weeks prior to diagnosis. A diagnosis of Group B disease by the International Classification of Retinoblastoma²⁶⁹ was made in both eyes, which was based on

examination of the dilated eyes and fundus photography. The position and size of tumors were, however, significantly different in each eye. The tumors in the left eye were generally smaller, and although they were posterior with one near the optic nerve and one in the macula (but outside of the fovea), none involved the center of the macula. The right eye contained two tumors: the larger tumor (diameter = 15 mm) was centrally located, and involved the entirety of the macula; the smaller tumor (diameter = 1.5 mm) was more peripheral, located at 4 o'clock. The left eye contained three posterior tumors, as described above, with diameters of 6 mm, 1.5 mm, and 0.4 mm.

Over a period of 5 months after diagnosis, Patient Zero received five different types of treatment. In chronological order, the treatments were: (i) systemic vincristine and carboplatin (age: 132-196 days), (ii) focal cryotherapy to right and left eye (age: 200 and 207 days), (iii) focal laser photoablation to right eye (age: 207 days) and left eye (age: 207, 220, 264 days), (iv) enucleation of right eye (age: 220 days, after progression to Group D with vitreous seeding), and (v) proton beam radiation to left eye (age: 222-258 days). Systemic chemotherapy along with cryotherapy and laser consolidation slowed the growth of existing tumors, but failed to reduce their size, and did not prevent the appearance of new tumors, however, treatment with proton beam radiotherapy resulted in an excellent response.

Ethics Statement:

This study was determined to be exempt from review by an Institutional Review Board at Baylor University. Permission to publish images of two children (Patient Zero and healthy controls) was obtained from both parents of each child.

Results and Discussion

I reiterate that the images in this chapter are photographically diverse (i.e., pictures were collected at multiple photographic angles, poses, settings, and lighting conditions) and thus accurately reflect typical recreational photographs of infants and toddlers in typical recreational activities (i.e., crawling, eating, crying, etc.). This photographic diversity is by no means a limitation or liability to this study—or to the utility of photography in detecting Rb—but increases the probability that light will sample the tumor surface and be reflected back towards the camera lens, regardless—to some degree—of tumor position or size (Figure 7.1A). Moreover, the parents of each child did not anticipate, during photography, that a photograph might be used for a scientific study. The photographs thus represent an authentic set of “family pictures,” of the sort that might initiate a diagnosis of Rb, and in the case of Patient Zero, did in fact initiate diagnosis (Figure 7.1B).

The large number and longitudinal nature of available photographs of Patient Zero allowed me to determine the longitudinal frequency of leukocoria as a function of age and whether the colorimetric properties of leukocoria were statistically different in the right versus left eye. It should be noted that the smaller sets of photographs of the other eight patients are not longitudinal in nature, or large enough (in my opinion) to justify a statistically significant comparison between leukocoria intensity and clinical severity, but are useful for surveying the possible range of Rb-linked leukocoria in HSV color space.

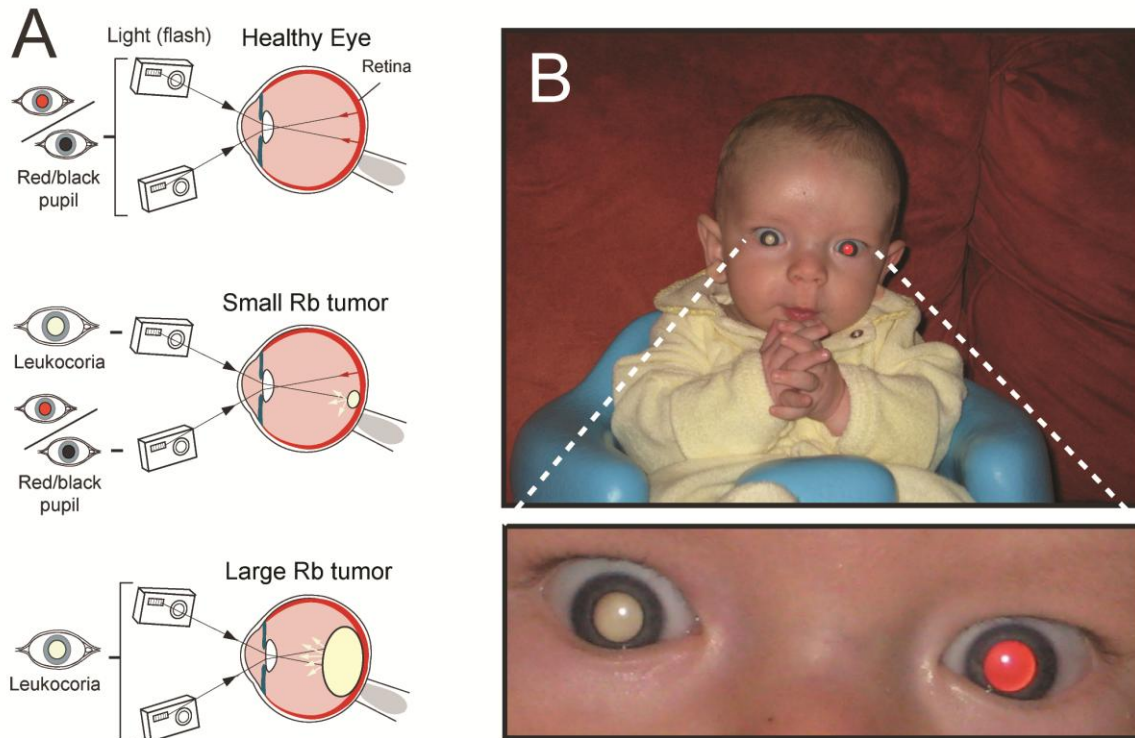


Figure 7.1 (A) The reflection of visible light by an intraocular Rb tumor can cause the pupil to appear white (*leukocoric*) during photography; an increase in the size of a tumor will generally increase the number of photographic angles that will produce leukocoria during recreational photography. **(B)** An example of a leukocoric picture from a set of 7377 pictures of a patient (Patient Zero) with bilateral Rb. Images of Patient Zero were donated by his parents.

Longitudinal Frequency of Leukocoria in “Patient Zero”: From Birth through Diagnosis and Remission:

The longitudinal frequency of photographs of Patient Zero is shown in Figure 7.2A. The parents collected photographs consistently over a period of three years. I manually analyzed this entire set of photographs and found that 237 out of 7377 pictures contained at least one leukocoric pupil; leukocoria was detected in 120 left pupils and 146 right pupils. Approximately 80 % of the leukocoric pictures were taken with a Canon PowerShot SD750 (shown in Figure 7.2B). A pupil was classified as leukocoric if it exhibited an abnormal reflection with a Value ≥ 0.50 , and a Saturation that was ≤ 0.60 (in

HSV color space). Approximately 10 % of pupils that were categorized as leukocoric exhibited an average pixel Value ≤ 0.5 or Saturation ≥ 0.60 , but were nonetheless classified as leukocoric because only a portion of the pupil exhibited abnormal Saturation or Value. In contrast, many non-leukocoric pupils (from Patient Zero and control subjects) contained a specular reflection of the cornea (which is not indicative of disease) that caused the average pixel brightness to be > 0.5 . This type of specular reflection is common in flash photography and appears as a white dot in the pupil, iris or sclera. I did not attempt to subtract specular reflections from images of any patient or control subjects because my goal is to determine how effective digital photography—as practiced by amateurs during recreation—can be at quantifying leukocoria.

Examples of leukocoria from the donated set of photographs of Patient Zero are shown in Figures 7.1 and 7.2. In addition, approximately 300 cropped images of pupils from Patient Zero and healthy control subjects are grouped according to gross shade and arranged into spirals (Figure 7.3). Each spiral contains: (i) cropped pupils of Patient Zero that exhibited leukocoria (denoted “Lk+/Rb+”); (ii) non-leukocoric pupils from the patient (which appear black or red, denoted “Lk-/Rb+”); and (iii) cropped pupils from healthy subjects that appeared red or black (denoted “Lk-/Rb-” in Figure 7.3). Leukocoric pupillary reflections were not detected in healthy control subjects (however, leukocoria can occur rarely in children who do not have any known eye disease, presumably during off-axis photography and reflection of the optic nerve²⁹⁶⁻²⁹⁷).

The gross appearance of leukocoric pupillary reflections in Patient Zero was often white or gray (Figure 7.3A), but leukocoria also appeared with yellow Hues (Figure 7.3B), pink Hues (Figure 7.3C) and orange Hues (Figure 7.3D). The photographic

reflection of Rb tumors might, therefore, be more accurately described by a general term such as “photocoria” (Greek: light pupil), instead of leukocoria, because the abnormal reflections do not necessarily *appear* white.²⁹⁸ I attribute the differences in the gross appearance of photocoric pupils to be caused by different angles of photography, which result in variable mixtures of light reflected from the healthy regions of the retina and optic nerve, and light reflected by the surface of a tumor.

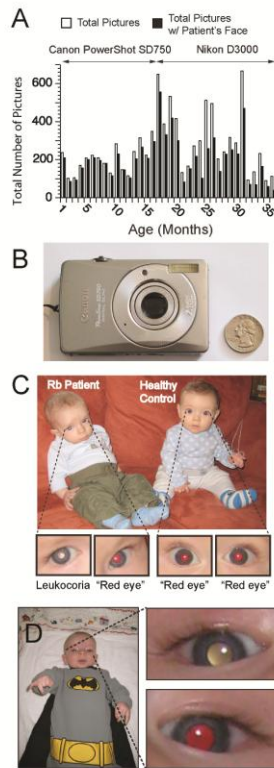


Figure 7.2 (A) Longitudinal frequency of photography of “Patient Zero” by parents over a three year period (i.e., from birth to 3 years old; 7377 photographs). (B) The majority of leukocoric pictures (~ 80 %) were collected with this compact 7.1 megapixel Canon PowerShot SD750 camera. (C) Digital picture of Patient Zero (i.e., child on left, exhibiting leukocoria in left eye) and a healthy playmate (i.e., child on right, exhibiting a red reflex in both eyes). (D) Example of a digital picture of Patient Zero; right eye exhibited leukocoria, and the left eye exhibited a red reflex. Photographs in C&D were taken with Canon Power Shot SD750. Permission to include images of the healthy control child was granted by both parents.

A timeline of the diagnosis, treatment, and remission of the Patient Zero is described in Figure 7.4, and compared with the daily and monthly frequency of leukocoria. Leukocoria first occurred at 12 days old (Figure 7.4A-C)—several months before the parents first noticed leukocoria—but only occurred in $< 5\%$ of facial pictures taken during the first month of life (Figure 7.4B,D). Leukocoria increased in frequency during disease progression (reaching as high as 100% of pictures per day and 25% of pictures taken per month, Figure 7.4B,D), even in spite of systemic chemotherapy, laser photoablation therapy and cryotherapy. The increase in frequency, despite chemotherapy, is consistent with clinical observations that systemic chemotherapy did not significantly reduce tumor size, or prevent the formation of new small tumors (which were immediately and successfully treated with cryotherapy or laser photoablation therapy). The treatment of the patient's left eye with proton beam radiation and laser photoablation (which resulted in long term tumor regression) decreased the frequency of leukocoria to $< 2\%$ per month (Figure 7.4D). Leukocoria frequency remained $< 2\%$ per month throughout the period of remission. The lateral distribution of leukocoria in Patient Zero is shown in Figure 7.4E. The right eye accounted for 60-85% of all detected leukocoria (until it was enucleated at 9 months of age). I attribute this higher frequency to the greater total surface area of tumors in the right eye and its central location, which might increase the probability (during recreational photography at multiple angles) that light will reflect off the surface and into the camera lens (Figure 7.1A). The total surface area of tumors in the right eye was calculated to be ~ 4 -fold greater than the surface area of tumors in the left eye. The lateral ratio of the total surface area of tumors in the right and left eye was approximated using the measured height and diameter of tumors from fundus

photography performed at age 129 days, and 199 days; a semi-spherical geometry was assumed when calculating the surface area of each tumor, as previously described.²⁹⁹ The correlation between the frequency of leukocoria and the progression and remission of disease and also the greater frequency in the more severely affected eye suggests that the leukocoria observed in these images are clinically relevant.

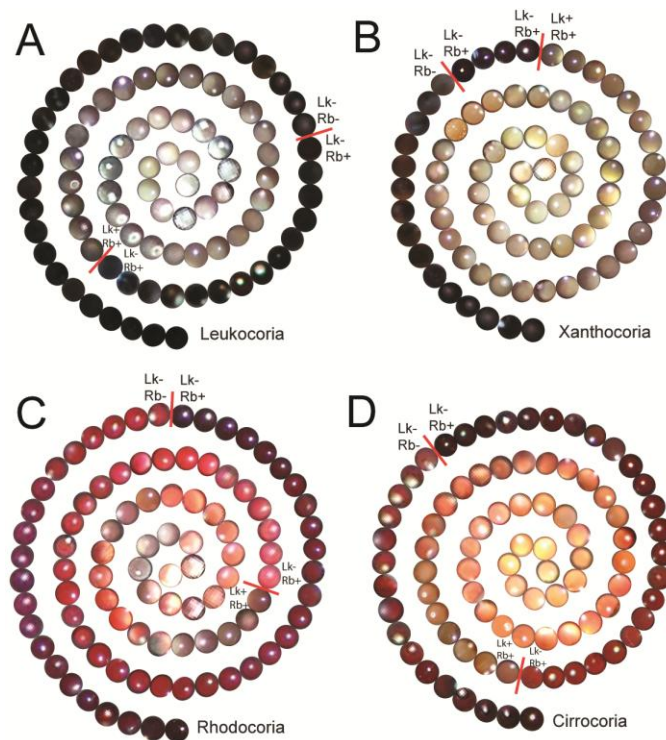


Figure 7.3 Examples of cropped leukocoric and non-leukocoric pupils from a set of 7377 pictures of Patient Zero (and control children who were photographed alongside patient). Each spiral contains: (i) cropped leukocoric pictures from Patient Zero (denoted Lk+/Rb+), (ii) non-leukocoric pupils from Patient Zero (Lk-/Rb+), and (iii) non-leukocoric pupils from healthy control subjects (Lk-/Rb-). Cropped leukocoric pupils that exhibit a gray scale (classic leukocoria) are shown in **(A)**; cropped leukocoric pupils with non-black and white appearance are also shown: **(B)** yellow, i.e., “xanthocoria”; **(C)** pink, i.e., “rhodocoria”; **(D)** orange, i.e., “cirrocoria”. Many pupils in **(A-D)** contain specular reflections of cornea that appear as a white dot and are not indicative of disease.

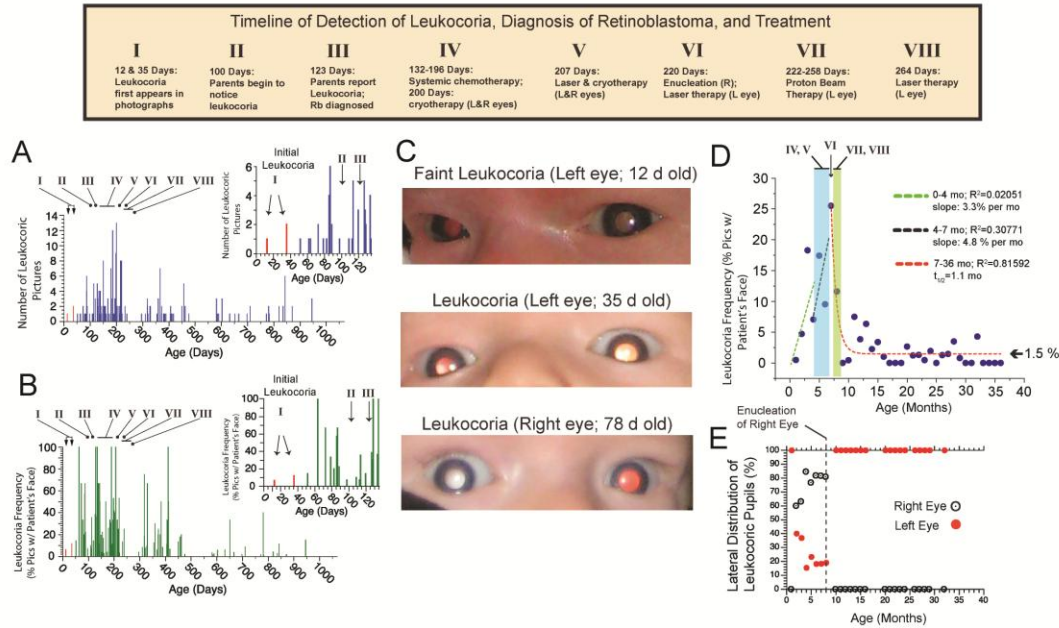


Figure 7.4 Comparison of frequency of leukocoria with age of Patient Zero and timeline of treatment. **(A)** Number of leukocoric pictures plotted as a function of age. Inset shows expansion of age 0-135 days. **(B)** Daily frequency of leukocoric pictures from a set of 7377 facial pictures plotted as a function of age. Inset shows expansion of age 0-135 days. **(C)** First leukocoric pictures of patient at 12, 35, and 78 days old. **(D)** Comparison of monthly frequency of leukocoria with treatment of patient. **(E)** Lateral distribution of leukocoria in 7377 photographs of Patient Zero. After the first month of life, the right eye accounted for the majority of leukocoric pupils that were observed until the right eye was enucleated.

Right Leukocoric Pupils of Patient Zero Exhibited Lower Saturation and Value than Left Pupils:

The Saturation and Value of the right and left leukocoric pupils from Patient Zero are plotted in Figure 7.5 (as a per-pixel average, red circles). The average Hue versus Value of each leukocoric pupil is also plotted on a polar coordinate plane (Figure 7.6, red circles). Because the HSV quantities are expressed as a per-pixel average (the average number of pixels analyzed was 308.11), they are independent of image resolution. I also calculated the mean Hue, Saturation, and Value of right and left leukocoric pupils over the entire three-year period of photography (Table 7.1). These colorimetric (and

statistical) analyses of pupils demonstrate that the Saturation and Value, but not the Hue of right leukocoric pupils, are different than left leukocoric pupils in Patient Zero. For example, the three-year aggregate mean Saturation of right leukocoric (RL) pupils ($S_{RL} = 0.234$) is 46 % lower than left leukocoric (LL) pupils ($S_{LL} = 0.436$; $p < 0.0001^*$). The aggregate mean Value of the right leukocoric pupils ($V_{RL} = 0.677$) is 17 % lower than left pupils ($V_{LL} = 0.818$; $p < 0.0001^*$). The right and left pupils did not show differences in Hue: the three-year aggregate mean Hue of right leukocoric pupils ($H_{RL} = 21.1^\circ$, i.e., yellow) were nearly identical to left leukocoric pupils ($H_{LL} = 21.0^\circ$). The derivation of the p values and statistical significance of differences in the HSV quantities of right and left eyes are discussed below. The ability to detect variations in the average colorimetric properties of leukocoric reflection from different ocular sets of Rb tumors with a pocket-sized digital camera (Figure 7.2B), during recreational photography is remarkable. I hypothesize that the lower Saturation of leukocoric reflections from the right eye, compared to the left for Patient Zero, is caused by the greater degree of retinal eclipsing by the larger surface area of the tumors in the right eye compared to the left eye.

Right and Left Pupils are Colorimetrically Identical in Healthy Children:

It is possible that the bilateral differences in Saturation and Value of leukocoria in Patient Zero resulted from a photographic clustering artifact, i.e., images were collected at a constant angle, lighting, pose, or setting which may lead to a measurable amount of clinically irrelevant leukocoria (i.e., pseudo-leukocoria²⁹⁶). To begin to rule out this possibility and to establish quantitative and colorimetric definitions of healthy pupillary reflexes, I measured the Hue, Saturation, and Value of right and left pupils from

19 healthy children (without having any known eye diseases; 305 pupils in total; 166 left pupils; 139 right pupils; mean age = 39.5 months old, median age = 20 months old, as adjusted to their frequency of appearance alongside Patient Zero in photographs).

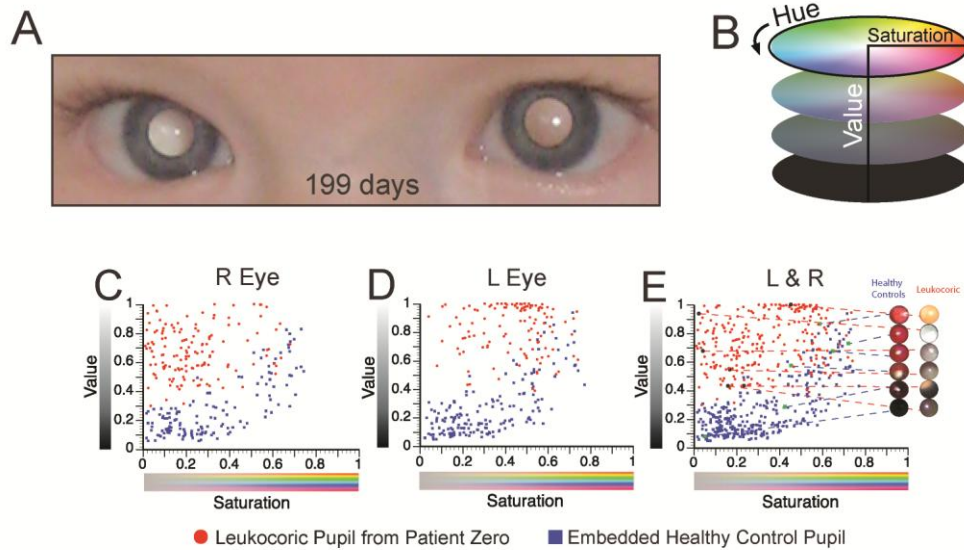


Figure 7.5 Quantification of Saturation and Value of right and left leukocoric pupils of Patient Zero, and 19 healthy control children. **(A)** Digital image showing bilateral leukocoria in Patient Zero taken at the age of 199 days. **(B)** Illustration of cylindrical HSV (Hue, Saturation, Value) color space. **(C)** Plot of average Saturation and Value of cropped leukocoric and control pupils from right eyes of Patient Zero (red circles) and 19 control subjects (blue squares). **(D)** Plot of average Saturation and Value of cropped leukocoric and control pupils from left eyes of patient (red circles) and 19 control subjects (blue squares). **(E)** Saturation and Value from right and left leukocoric and control pupils (a combination of plots **(C)** and **(D)**). Images of cropped pupils are matched to enlarged data points in order to illustrate the range of Saturation and Value of leukocoric and control pupils.

The images of these children represent a convenient set of internal controls from which I could determine the average HSV in healthy pupillary reflections and also further ascertain if the two cameras used resulted in high levels of clinically irrelevant “pseudo-leukocoria” (caused, for example, by reflection of optic nerve). As an instance, each

control child was—by virtue of being photographed alongside Patient Zero—also photographed with the same camera as Patient Zero, under the same lighting conditions, exposure time, flash pulse duration, and aperture. The HSV were determined for pupils from each healthy child in the same manner as leukocoric pictures and regardless of the gross appearance of the healthy child’s pupil. The colorimetric properties of control pupils should be identical among the right and left eyes of these children, so long as no photographic clustering artifact (pseudo-leukocoria) is present in these data.

Plots of the Saturation and Value of right and left control pupils are shown in Figure 7.5 (blue squares). Polar plots of Hue (angular) and Value (radial) of right and left control pupils are shown in Figure 7.6 (blue squares). The aggregate mean Hue, Saturation and Value for all 139 right and 166 left control pupils that were photographed over the three-year period are listed in Table 7.1. These quantities represent a reasonable starting point for establishing standard colorimetric properties of pupillary reflexes of healthy children (at the age of Rb susceptibility) during digital photography.

The mean Hue, Saturation, and Value for all right control pupils were nearly identical to those of the left control pupils. For example, the mean Hue of right control (RC) pupils ($H_{RC} = 350.2^\circ$) differed only 6.4° from left control (LC) pupils ($H_{LC} = 343.8^\circ$; $p > 0.05$); the bilateral Saturation differed by only 2 % ($p = 0.9845$) and the Value by 6 % ($p = 0.4508$).

The similarities in the HSV of right and left control pupils suggest that: (i) leukocoria detected in this study is only observed in a patient with Rb and thus is clinically relevant, (ii) the cropped pupils from 19 different control subjects have similar colorimetric properties (Table 7.1), and most importantly, (iii) any differences that are

detected in HSV quantities of right and left leukocoric pupils from Patient Zero are not caused by photographic clustering artifacts, but are instead, caused by clinical differences in each eye.

Statistical Significance of Bilateral and Longitudinal Differences in Hue, Saturation, and Value of Cropped Pupils From Patient Zero and Healthy Control Subjects.

In order to determine if the Saturation and Value of each set of right and left cropped pupils (from Patient Zero and healthy control subjects) were normally distributed, I performed a Shapiro-Wilk test. I did not perform a similar statistical analysis on photographs of other patients with Rb because of the small number of photographs (i.e., < 10) of each child.

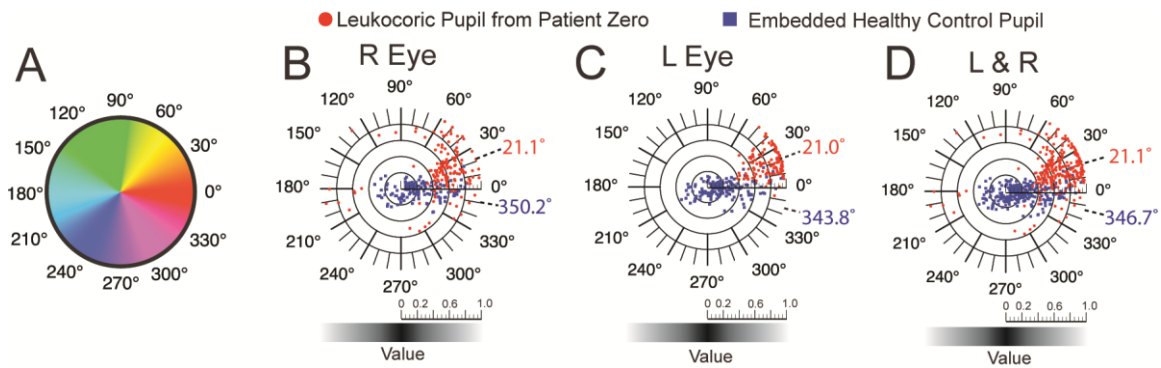


Figure 7.6 Quantification of Hue and Value of right and left leukocoric pupils of Patient Zero. **(A)** Depiction of Hue as an angular quantity. **(B)** Polar plots of average Hue, per pixel (angular dimension) and average Value, per pixel (radial dimension) for right eye of patient that exhibited leukocoria (red circles), and right eye from 19 healthy children (blue squares). **(C)** Polar plots of average Hue, per pixel (angular dimension) and average Value, per pixel (radial dimension) for left eye of patient that exhibited leukocoria (red circles), and left eye from 19 healthy children (blue squares). **(D)** Combination of data points from plots (C) and (B).

Table 7.1 Mean HSV Quantities of Leukocoria in “Patient Zero” and Control Pupils Over 3 Years.

	Leukocoric, left n = 120	Leukocoric, right n = 146	Control, left n = 166	Control, right n = 139
Hue ^{a,d}	21.0° (0.033°)	21.1° (0.215°)	343.8° (1.060°)	350.2° (0.877°)
Saturation ^b	0.436 (0.159)	0.234 (0.166)	0.317 (0.194)	0.322 (0.216)
Value ^c	0.818 (0.168)	0.677 (0.166)	0.280 (0.210)	0.297 (0.216)

^aFor Hue of R and L non-leukocoric controls, $p > 0.05$; for Hue of R and L leukocoric pupils, $p < 0.05^*$; p-values for Hue were calculated with Wheeler-Watson test.

^bFor Saturation of R and L controls $p = 0.9845$; for Saturation of right and left leukocoric pupils $p < 0.0001^*$.

^cFor Value of R and L controls, $p = 0.4508$; for Value of R and L leukocoric pupils $p < 0.0001^*$.

^dError values in parentheses are standard deviation, except for those of Hue, which are circular standard deviation (CSD). CSD is a circular statistical analogue of standard deviation which measures the spread of the data points about the average center.

The results of the Shapiro-Wilk test demonstrated that the quantities of both Saturation and Value of right and left pupils were characterized by a non-normal distribution ($p < 0.005^*$). The absence of a normal distribution demonstrates that a non-parametric statistical test (e.g., the van der Waerden test) is most appropriate to compare the statistical similarity of the Saturation or Value of cropped pupils from each eye of the patient and control subjects. I therefore used the van der Waerden test to determine p-values of Saturation and Value between right and left pupils, and to determine if the Saturation of right leukocoric pupils is associated with the same mathematical distribution as Saturation of left leukocoric pupils. The results demonstrate that the differences in Saturation and Value of right and left pupils from Patient Zero are statistically significant (Table 7.1).

In order to determine if the differences in the Hue of right and left pupils were statistically significant, I used the Wheeler-Watson test. Because the Hue of cropped pupils is expressed as a directional (circular) statistic, the Shapiro-Wilk test for normality and the van der Waerden test—which were designed for use on non-directional data—are not applicable. The Wheeler-Watson test is a non-parametric test designed to determine statistical similarity between the distributions of different sets of directional data, and is thus appropriate for comparing Hue of right and left eyes, etc. The Hue of right and left pupils were not significantly different (Table 7.1).

The Average Hue of Leukocoria in Patient Zero is Yellow:

The three-year mean Hue of right and left leukocoric pupils of Patient Zero exhibited a yellow Hue, in comparison to right and left pupils from control subjects, which exhibited a red Hue (Figure 7.6). I hypothesize—but cannot prove—that the yellow Hue associated with this patient’s leukocoria resulted from the chemical composition and/or surface properties of the Rb tumor. While this hypothesis is bold, it is by no means capricious. For example, the diverse chemical composition of the *tapetum lucidum* (e.g., guanine, collagen, or riboflavin) among nocturnal animals is thought to cause the variably colored eye-shine (i.e., retinal reflexes) that are commonly observed among these animals (ranging from blue in bovine to yellow-green in canine).³⁰⁰ The *tapetum lucidum* is a reflective layer of retinal tissue (not present in humans) that functions as a biologic reflector system to enhance visual sensitivity in low-light conditions.³⁰⁰

Previous analyses of Rb tumors from both fundus photography and pathological analyses of surgical specimen from enucleated eyes show that Rb tumors can be white,

“off-white”, tan, or yellow in appearance.³⁰¹ Rb tumors (or regions of tumors) that are yellow have been associated with hemorrhage, macular yellow pigment, calcification, and necrosis,³⁰¹ however, it is possible that the yellow color I detect arises from the lipid composition of the plasma membrane of tumor cells. The lipid constituents of Rb cells have not been determined exactly and categorically, and the lipid content of cultured Rb cells can vary among different *Rb*/*Rb*⁻ cell lines.³⁰² Retinoblastoma tumors have been reported to possess increased levels of unsaturated fatty acids,³⁰³⁻³⁰⁶ as well as a higher content of cholesterol than healthy cells in the retina.³⁰⁷ Intraocular cholesterosis (abnormal deposition of cholesterol) has also been reported in children with Rb after systemic chemotherapy, cryotherapy and laser photoablation.³⁰⁸ No clinical deposition of cholesterol (e.g., hard exudation) was observed in the eyes of Patient Zero.

Saturation and Value of Right Pupils From Patient Zero Remain Different From Left Pupils Throughout Three-Year Period of Treatment:

Because the right and left eyes of Patient Zero received different types of treatment (e.g., the right eye was not treated with proton beam radiation therapy, but was instead enucleated), it is possible that the colorimetric differences in right and left leukocoria are not caused by differences in tumor surface area or position, but instead are caused by changes in the surface properties of tumors (e.g., calcification) or retina that resulted from radiation or photoablation therapy. The calcification of the large tumor in the left eye, and laser photoablation of the two small tumors (at 6 o'clock and 9 o'clock), can be seen from clinical images of the left retina that were obtained with fundus photography (Figure 7.7).

In order to test the hypothesis that bilateral colorimetric differences are caused by treatment, I compared the longitudinal changes in the HSV properties of right and left leukocoric pupils over the three-year period of photography. First, I divided images into three longitudinal groups based upon the time of photography: (i) before treatment began (Period 1, age: 0-131 days), (ii) after chemotherapy, laser photoablation and cryotherapy (Period 2, age: 132-221 days), and (iii) after proton beam therapy and final treatment with laser photoablation therapy (Period 3, age: 259-945 days). In order to examine the variation of the HSV of each right and left leukocoric reflection, from day to day and throughout all three time periods, I plotted the HSV of each leukocoric pupil as a function of the patient's age (Figure 7.8). A linear fit was applied to the HSV data points for each treatment period in each eye (dashed lines in Figure 7.8).

The mean Saturation of left leukocoric pupils only varied from 0.400-0.459 (i.e., 13 % variation) throughout all three periods of treatment (Table 7.2). The mean Saturation of the right leukocoric pupil from Periods 1 and 2 were 0.226 and 0.265 (i.e., 15 % variation; $p = 0.1606$); the right eye was enucleated before the beginning of Period 3. Throughout all three periods of treatment, the mean Value of left leukocoric pupils varied only 0.822-0.835 (i.e., 2 % variation); the mean Value of the right leukocoric pupil from Periods 1 and 2 were 0.641 and 0.696, respectively (i.e., 8 % variation, $p = 0.1407$). The persistent difference in Saturation or Value of right and left leukocoric pupils throughout the entire three-year period suggests that the colorimetric differences between right and left leukocoric pupils are not caused by treatment, but are instead the result of differences in the surface area and/or the position of tumors in the right versus left eye.

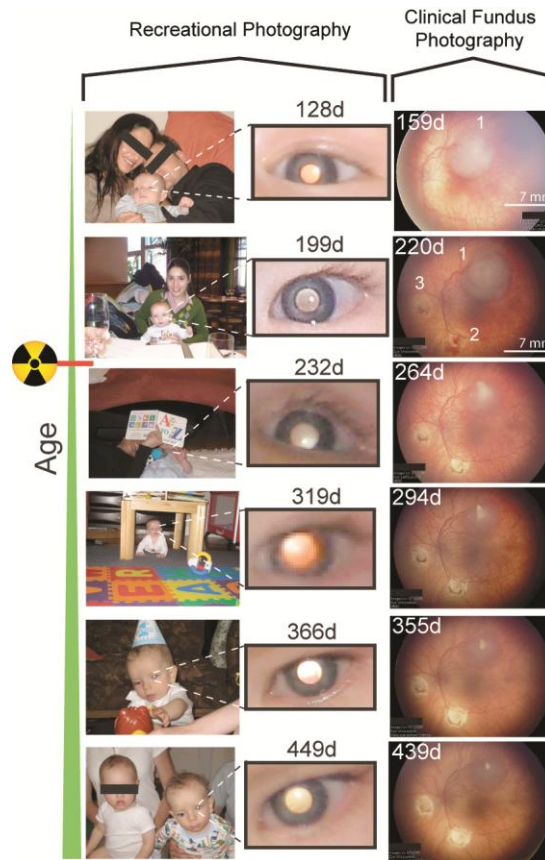


Figure 7.7 A comparison of clinical images of the left retina of Patient Zero collected with fundus photography and leukocoria in left pupil (age of patient is listed in days). The left retina contains three tumors; one large tumor at 12 o'clock, and two smaller tumors at 6 o'clock and 9 o'clock (the two smaller tumors were treated with laser photoablation therapy which resulted in tumor eradication and exposure of the sclera). The radiation symbol denotes the point in time when proton beam radiation therapy was administered to the left eye.

In conclusion, the colorimetric properties of the right and left eye of Patient Zero were different from each other before and after radiation therapy, and were generally stable over the three-year period of photography. The administering of proton beam therapy to the left eye cannot entirely explain the differences in the Saturation or Value of left and right leukocoric pupils. I also do not believe that the greater Value observed in the left eye arose from the exposure of sclera that resulted from photoablation of the two

small tumors at 6 o'clock and 9 o'clock (see fundus photographs in Figure 7.7). For example, the Value (or Saturation) of leukocoric pupils did not change significantly as a result of laser photoablation therapy and exposure of the sclera (possibly because the bare sclera and tumor reflect similarly during flash photography). I conclude that the longitudinal stability of the colorimetric properties over the three-year period of photography is due to the stabilization of growth of the predominant tumor in each eye that was quickly accomplished for this patient by his early diagnosis at age 4 months.

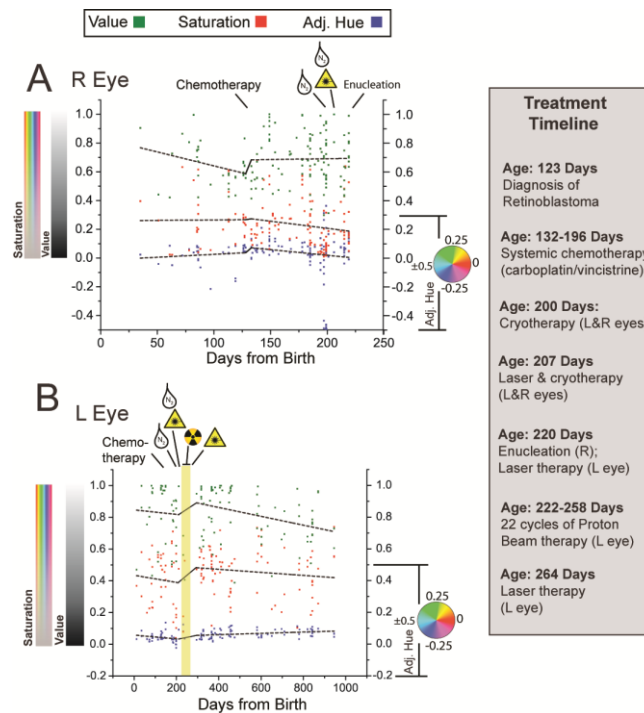


Figure 7.8 Longitudinal plot of HSV quantities of leukocoria in Patient Zero and treatment timeline listed at right. In order to project quantities of Hue in a Cartesian coordinate, I converted quantities of Hue to a linear scale. **(A)** Plot of average HSV (per pixel) for leukocoric pupils from right eye. A linear fit of data points was made for two time periods: before and after systemic chemotherapy. **(B)** Plot of average HSV (per pixel) for leukocoric pupils from left eye throughout the three-year period of photography. A linear fit of data points was made for two time periods: before the administering of proton beam radiation therapy, and after the completion of therapy.

Table 7.2 HSV Properties of Leukocoric Pupils in “Patient Zero” During Three Periods of Treatment.

Treatment Period	Left Eye			Right Eye		
	Hue ^c	Sat.	Value	Hue	Sat.	Value
Period 1 age: days 0-131 (n = 19 left, 37 right) ^{a,b}	16.5° (0.013°)	0.411 (0.145)	0.835 (0.194)	10.7° (0.156)	0.265 (0.171)	0.641 (0.145)
Period 2 age: days 132-221 (n = 21 left, 109 right) ^{a,b,c}	13.9° (0.048°)	0.400 (0.195)	0.822 (0.170)	25.5° (0.244)	0.226 (0.166)	0.696 (0.170)
Period 3 age: days 259-945 (n = 77 left) ^c	23.8° (0.024°)	0.459 (0.144)	0.823 (0.157)	n/a ^d	n/a ^d	n/a ^d

^aFor the right eye, a comparison of Periods 1 and 2 yielded p-values of p > 0.05 for Hue, p = 0.1606 for Saturation, and p = 0.1407 for Value.

^bFor the left eye, a comparison of Periods 1 and 2 yielded p-values of p > 0.05 for Hue, p = 0.7370 for Saturation, and p = 0.7622 for Value.

^cFor the left eye, a comparison of treatment Periods 2 and 3 yielded p-values of p < 0.05* for Hue, p = 0.1484 for Saturation, and p = 0.9930 for Value.

^dTreatment Period 3 was post-enucleation of the right eye.

*Entries with asterisk indicate the given colorimetric property is statistically different between the two sets being compared at a 0.05 significance level.

^eFor Hue, comparisons were made using the Wheeler-Watson test. Error values in parentheses are standard deviation, except for those of Hue, which are circular standard deviation (CSD). CSD is a circular statistical analogue of standard deviation, which measures the spread of the data points about the average center.

The Colorimetric Differences Between Right and Left Leukocoric Pupils of Patient Zero Are Not Artifacts of Photography:

The photographic settings for each photograph are embedded as EXIF data in each JPEG file, and can be viewed when the JPEG file is analyzed in software programs such as Picassa® (Google Inc., Mountain View, CA). The average time of exposure and average focal aperture were calculated for right and left leukocoric pupils, and were found to be statistically similar. The colorimetric differences between right and left eye are therefore clinically relevant. For example, the average time of exposure (t_{exp}) of the

120 photographs with left leukocoric pupils was $t_{\text{exp}} = 16.9 \pm 4.1$ msec, *versus* $t_{\text{exp}} = 18.6 \pm 4.1$ msec for the 146 photographs with a right leukocoric pupil. Likewise, the average focal apertures (f) were similar: $f = 3.7 \pm 1.0$ for photographs with left leukocoric pupils; $f = 3.9 \pm 1.4$ for photographs with right leukocoric pupils. The EXIF data also documented that a flash pulse (from the xenon flash tube) was emitted during the collection of every leukocoric picture.

To ensure that the cropping of leukocoric pupils in this study is reproducible, I had two different researchers (AA and BT) crop the entire set of photographs and quantify the pupils in HSV color space (Table 7.3). The mean colorimetric properties of both eyes for Patient Zero and all controls are statistically similar ($p < 0.05^*$) regardless of which researcher performed the analyses (denoted as “Trial 1” and “Trial 2” in Table 7.3). This similarity illustrates that colorimetric variations in leukocoric and non-leukocoric pupils are not the artifacts caused by variations in the practice of pupil cropping.

Colorimetric Analysis of Leukocoric Photographs from Eight Additional Patients with Rb:

As a first step in determining the range of HSV coordinates that will generally describe Rb-linked leukocoria in recreational photography, I plotted the Hue, Value, and Saturation of leukocoric pupils for all the nine patients in this study (Figure 7.10). As shown in Figure 7.10, the average Value and Saturation of leukocoric pupils from each patient are Value > 0.3 , and Saturation < 0.6 . The leukocoria in all but one of the patients was characterized by a red-yellow hue.

In order to begin to establish a quantitative scale of leukocoria, and a means of interpreting the colorimetric properties of pupillary reflexes in digital photographs, I

sectioned the Saturation-Value plane of HSV color space into five regions (Figure 7.10): (i) 1° leukocoria, (ii) 2° leukocoria, (iii) 3° leukocoria, (iv) “black” eye, and (v) “red” eye. The exact boundaries of the regions that I propose in this scale of leukocoria are by no means definitive, and will likely change (slightly) as I analyze more photographs from more patients. In this particular scale, first degree leukocoria represents the most intense level of leukocoria, i.e., the brightest, least colored leukocoria. I therefore present this scale as a tentative first step in developing methods for quantitatively interpreting leukocoria.

Table 7.3 Mean Colorimetric Properties Calculated From Images Containing Leukocoric and Healthy Control Pupils and Cropped by Two Different Researchers (Trials)

Eye	Hue ^a (Trial1) _c	Hue (Trial2) _c	Sat. ^b (Trial1)	Sat. (Trial2)	Sat. % dev _d	Value ^b (Trial1)	Value (Trial2)	Val ue % dev
R (Lk ^e)	21.1° (0.215°)	17.7° (0.189°)	0.234 (0.166)	0.266 (0.188)	12. 80	0.677 0.16580	0.665 (0.166)	1.79
L (Lk)	21.0° (0.033°)	20.7° (0.034°)	0.436 (0.159)	0.438 (0.156)	0.4 6	0.818 (0.168)	0.808 (0.174)	1.23
R&L (Lk)	21.1° (0.035°)	19.0° (0.109°)	0.325 (0.191)	0.344 (0.194)	5.6 8	0.741 (0.181)	0.729 (0.184)	1.63
R&L (Control)	347° (0.978°)	348° (0.647°)	0.319 (0.204)	0.318 (0.203)	0.3 2	0.288 (0.212)	0.267 (0.196)	7.57

^aFor each entry of Hue, the number in parentheses is the circular standard deviation (CSD) of the crops in that data set. CSD is a circular statistical analogue of standard deviation which measures the spread of the data points about the average center.

^bFor each entry of Value and Saturation, the number in parentheses is the standard deviation of the crops in that data set.

^cTrial 1 was cropped by Brandon W. Taylor and Trial 2 by Alireza Abdolvahabi.

^dPercent deviations (% dev) are calculated using: $\frac{|x_1 - x_2|}{\frac{1}{2}(x_1 + x_2)} \times 100$.

^eLk: Leukocoric

There is growing concern among clinicians that Red Eye Reduction and Red Eye Removal technologies will inhibit the ability of a digital camera to detect leukocoria,³⁰⁹ and possibly cause significant delays in the diagnosis of Rb. I point out that the two cameras used to collect photographs of Patient Zero were equipped with optional “Red Eye Removal” and “Red Eye Reduction” technologies (which are two entirely different types of technology), however, these technologies were not generally used by parents in this study. For example, the parents of Patient Zero utilized Red Eye Reduction flash mode in only ~ 5 % of the leukocoric pictures they collected (as determined by analysis of the EXIF data for each JPEG image), and the parents did not edit any of the images with Red Eye Removal software. Red Eye *Reduction* technology employs a flash with a series of two light pulses: the first pulse is intended to contract the pupil (immediately prior to the collection of the image), and the second pulse provides lighting during exposure. In contrast, Red Eye *Removal* technology is a software feature that edits a photograph (i.e., removes red eye) *after* it is collected. I conclude that the Red Eye Reduction feature did not *entirely* inhibit leukocoria in Patient Zero, possibly because the centrally located tumors blocked light from bombarding the retina, and inhibited the contraction of the pupil during the first flash pulse.

Occurrence of Clinically Irrelevant “Pseudo-leukocoria” During Flash Photography:

In contrast to the possibility that Red Eye Reduction technology might inhibit the occurrence of leukocoria, there is also evidence suggesting that new models of digital cameras (such as the camera embedded within the Apple iPhone®) are causing clinically *irrelevant* leukocoria to occur in healthy children and adults (who do not have any known

eye disease) at a higher rate than previous models of digital cameras. The cause(s) of this alarming increase in pseudo-leukocoria—alarming because it might cause parents to begin to overlook leukocoria that *is* clinically relevant—is not known. I hypothesize that this increase in pseudo-leukocoria is caused by: (i) errors in post-processing of the image after collection (i.e., “Red Eye Removal”), (ii) the type of “flash” or light source (i.e., a Light Emitting Diode (LED) in newer cameras such as the iPhone® vs. a xenon flash tube in older cameras), and/or (iii) the proximity of the light source to the lens (a general rule of thumb in photography is that retinal reflections are minimized by moving the flash source away from the camera lens which is of course impossible in compact cameras).



Figure 7.9 Examples of “pseudo-leukocoria” (bilateral or unilateral) in a healthy adult without any known eye disease. Upper panel: photograph collected with a Motorola Droid Razr® and “pseudo-leukocoria” which can be seen in the right eye (unilateral). Middle panel: photograph collected with a Samsung SGH-I997® and with “pseudo-leukocoria” observable in the left eye (unilateral). Lower panel: photograph collected with an Apple iPhone 4® and “pseudo-leukocoria” can be partially seen in both eyes (bilateral). As described in the text, all photographs were taken in the same low-light conditions i.e., intensity of $0.0259 \pm 0.0074 \mu\text{E}/\text{m}^2/\text{s}$.

Leukocoria Can Occur in Spite of “Red Eye Reduction” Technology:

Nevertheless, the leukocoric reflections that I detect in this study are clinically relevant, that is, are not likely to be caused by reflection of the optic nerve,²⁹⁶ or artifacts of advanced camera technologies. This conclusion is based on: (i) the absence of leukocoria in 305 images of pupils from 19 healthy control subjects, and the absence of leukocoria in adults that were photographed alongside each patient (data not shown), (ii) the correlation between the longitudinal frequency of leukocoria in Patient Zero and the progression/remission of disease, and (iii) the bilateral correlation between the lateral frequency and intensity of leukocoria and the clinical severity of each eye (Figures 7.4 and 7.5).

In order to determine if pseudo-leukocoria can be easily distinguished (colorimetrically) from Rb-linked leukocoria, I collected and analyzed 72 pseudo-leukocoric images (of a healthy adult male) using three different digital camera phones equipped with a flash or light source (Figures 7.9 and 7.10; see Methods section of this chapter for more details on the type of cameras used). I determined that pseudo-leukocoria only occurred under low-light conditions, i.e., at $0.0259 \pm 0.0074 \mu\text{E}/\text{m}^2/\text{s}$ (according to measurement with a digital light meter). This low-light setting was established by simply turning off overhead cool fluorescent lights in a windowed office. I found that “pseudo-leukocoria” did not occur during flash photography in the same room when the lights were turned on i.e., at $10.4 \pm 0.0074 \mu\text{E}/\text{m}^2/\text{s}$ in the presence of a higher light intensity. The average colorimetric quantities of pseudo-leukocoric reflections (denoted “PL” in Figure 7.10) from all three cameras were grouped in similar color space (i.e., Hue: 15°-30°; Saturation: 0.3-0.4; and Value: 0.9-0.7), and were similar to the HSV

properties of some Rb patients with 3° leukocoria. The similarity between Rb-linked leukocoria and pseudo-leukocoria suggests that any type of leukocoria detection software that might be engineered to alert users of digital cameras to the presence of leukocoria will need to discriminate between pseudo-leukocoria and Rb-linked leukocoria based (in part) on the higher rate at which leukocoria is likely to occur during the photography of a child with Rb compared to a healthy subject.

Over the past decade, the timing of diagnosis of Rb in underdeveloped countries has been improved by campaigns that increase the public awareness of Rb, and facilitate referral of children who might have Rb.^{277,310} The growing prevalence of digital cameras in developing nations (e.g., in India, which is predicted to have a compounded annual growth rate (CAGR) of ~ 27 % in its camera market in the next five years, outpacing the market growth in the USA),³¹¹⁻³¹² and their growing use in telemedicine³¹³⁻³¹⁴ suggests that digital photography can play an increasingly large role in these types of ongoing Rb campaigns.

Improving the Timing of Diagnosis of Retinoblastoma in Developing Nations with Digital Photography:

I find it reasonable to predict that access to digital photographic devices will continue to increase for many families in developing nations³³⁰ at a faster rate than access to pediatric clinicians who can screen for Rb with conventional methods. The photography of children by *parents* in resource-limited settings might, therefore, represent a rapid, economical, and effective method for decreasing the age of diagnosis of Rb in these environments.

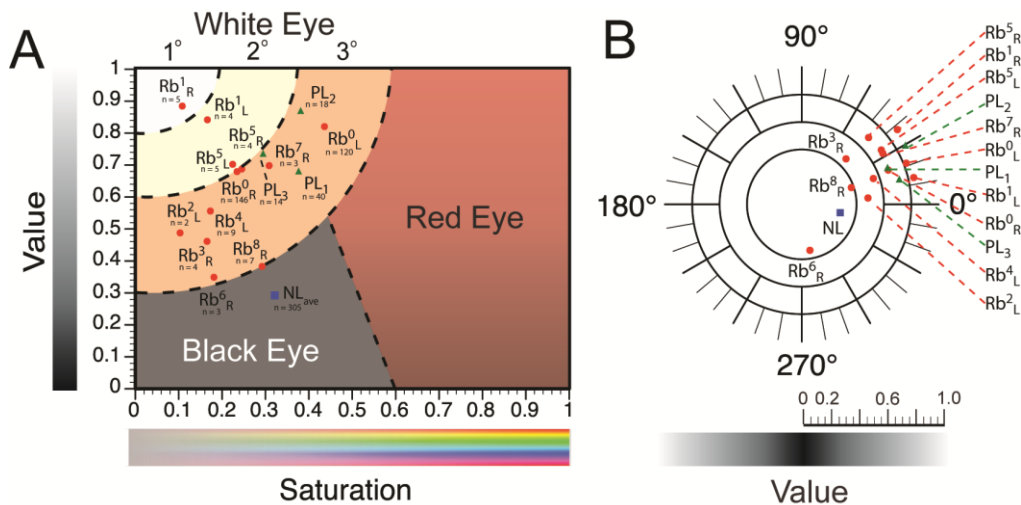


Figure 7.10 (A) Sectioning the Saturation-Value plane of HSV color space into a useful scale for classifying pupillary reflexes in recreational photographs. In this proposed scale, leukocoria is divided into differing degrees of brightness and color concentration (1° being the brightest, least colored; 3° is the least bright and most colored); areas that likely represent a typical “red” or “black” pupillary reflex are indicated. Each data point labeled “Rb” refers to the average H, S, or V of all leukocoric images of one of nine patients; the superscript of each label refers to the patient number (beginning with zero); subscript text refers to right or left pupil. “PL” refers to Pseudo-Leukocoria from images of a healthy individual that were collected with one of three different camera phones; the subscript refers to the camera that was used to photograph the individual (see text). “NL” refers to Non-Leukocoric controls (average of right and left pupils) from healthy children (i.e., data contained in Figure 7.5 and Table 7.1). The value “n” below each Rb, NL, and PL point refers to the number of pictures from which each average was calculated. **(B)** Plot showing the average Hue of cropped pupils from panel (A).

Can the Digital Camera Help Preserve Vision of Rb Patients in Highly Developed Nations?

Diagnostic challenges also continue to exist in highly developed nations, despite the high rate of survival. Improving the timing of diagnosis in developed nations will not lead to enormous increases in the (already high) survival rate, however, removing delays in diagnosis can result in greater degrees of vision preservation.²⁷⁸⁻²⁸² Recent reports have described great deficiencies in the ability of pediatricians to detect Rb, possibly due to inconsistencies in the administering of the “red reflex” test, or simply because a child

only receives (typically) ~ 12 examinations by a pediatrician during the first two years of life.³¹⁵ Moreover, regular examinations of a child's vision—which might also detect Rb—typically begin after the age of 3 years, which is outside the typical age of diagnosis.³¹⁵ In contrast to this limited number of pediatric examinations, a child who lives in a highly developed nation will be photographed hundreds or thousands of times by parents, guardians, relatives, or acquaintances during the first two years of life.

I point out that although many individuals own digital cameras in developed nations, a significant portion do not, and their increasing access to digital photography over time might lead to improvements in the use of digital photography to detect Rb. For example, it is estimated that ~ 10 % of individuals in the USA do not have access to a digital camera (either as a standalone camera or as a camera phone³¹⁶).

The use of the digital cameras to detect intraocular abnormalities might represent the most economical and rapid method for improving Rb diagnosis in developed nations. The potential of digital photography cannot be overestimated, in my opinion, because the detection limits of digital photography have not even been established, and might be much higher than currently appreciated. For example, digital photography appears to be able to detect early stage Rb that presents with a “gray” pupil (Figure 7.3)—which might not seem abnormal to a parent or clinician—prior to the presentation of classic “white” (or yellow) leukocoria. Utilizing the full potential of digital photography in screening Rb will likely require the development of computer software that can alert the photographer (or viewer of the image) to the presence of an abnormal pupillary reflection that might or might not be obvious to the naked eye.

Conclusion

The primary *clinical* result of this study suggests that a leukocoric photograph of a child with Rb can provide more information than a binary readout of leukocoria. I have shown that the quantity of Saturation and Value of a leukocoric pupillary reflection (in HSV color space) might be a crude metric for approximating the degree of leukocoria, which might be—for tumors in certain positions—a convenient expression of the total reflective surface area of intraocular Rb tumors.

This study also shows that “low frequency” leukocoria can be overlooked more easily by parents than “high frequency” leukocoria. For example, the parents of Patient Zero did not notice leukocoria until it appeared in > 60 % of pictures per day, and > 10 % of pictures per month; in fact, approximately 3 months elapsed from the time leukocoria emerged to the time it had increased to sufficient frequency that parents began to notice leukocoria. Increasing public awareness about leukocoria can accelerate diagnosis by preventing parents from overlooking sporadic leukocoria during the early stages of Rb. For example, although “Patient Zero” was diagnosed 5-8 months earlier than the average age of diagnosis for bilateral Rb,^{280,317} it is reasonable to predict that an earlier diagnosis at 12 or 35 days old—when the leukocoria first emerged—would have improved the patient’s outcome. This study only examined photographs of 9 patients with Rb (and only a single patient in longitudinal and bilateral detail), however, I suspect that the primary clinical finding of this study—that distinct ocular sets of Rb tumors produce distinct colorimetric patterns during amateur photography—will be found to be generally applicable, to some degree, with leukocoric photographs of other children with Rb. This zeroth order approximation is based on the assumption that: (i) the possible position of

Rb tumors, in both time and space, is quite narrow (i.e., the surface area of a child's retina is $< 11 \text{ cm}^2$, and Rb tumors typically form before the age of 5 years), and (ii) the photography of children by parents occurs at multiple angles, which will increase the probability that light will bombard tumors in both central or peripheral positions. I believe that the optical diversity of recreational photography—the collection of images at different angles and lighting conditions—by no means lowers its utility in Rb detection, but actually improves its applicability by increasing the probability that leukocoria will be eventually observed, regardless of the tumor position.

Analyzing additional libraries of photographs—similar in size to the library of Patient Zero—from more Rb patients will be necessary to determine whether the colorimetric properties of leukocoria have general clinical relevance, and to fully interpret the clinical implications of HSV quantities of a leukocoric image. The software that I used to analyze photographs (Adobe Photoshop®) is readily available, and the algorithm for converting RGB to HSV color space is operable in Microsoft Excel®. Researchers or clinicians without expertise in computer science should, therefore, be able to carry out the colorimetric analyses that I describe on photographs of other patients. Collecting a database of HSV coordinates of leukocoria from other patients will help establish a quantitative definition and scale of leukocoria, which might prove useful for quickly approximating the clinical severity of Rb when a parent reports leukocoria.

The digital photography of children in recreational settings is by no means as useful as high-resolution clinical methods for examining and imaging the retina (e.g., ophthalmoscopy and fundus photography). This technical disparity notwithstanding, the high frequency of photography of children by parents throughout the entire five-year

period of Rb susceptibility, combined with the growing prevalence of digital photography, is resulting in the accumulation of enormous, longitudinal sets of images that represent crude retinal scans. The colorimetric analysis of these types of large photographic libraries—over 7,000 images for the single patient in this study—might be, as an aggregate, useful for screening or assessing Rb. My colleagues and I envision that the creation of computer software that can automatically detect and quantify leukocoria—within thousands of images from a parent’s library of “baby pictures” or during photography or web-based social networking—will facilitate the automated and instantaneous screening of leukocoria in children throughout the entire period of their Rb susceptibility.

Acknowledgements

B.F.S acknowledges a generous startup fund from Baylor University; SM acknowledges support from the Mukai Fund at Massachusetts Eye and Ear Infirmary. The authors would like to thank the families who donated digital photographs for this study. The authors also acknowledge Dr. Erich Baker and Dr. Greg Hamerly for helpful discussions.

CHAPTER EIGHT

Supporting Information

Arresting Amyloid with Coulomb's Law: Acetylation of ALS-Linked SOD1 by Aspirin Impedes Aggregation.

Supporting Materials and Methods

Acetylation of Native Apo-SOD1 with Aspirin:

As briefly described in chapter 2 of this dissertation, successive acetylation of lysine residues in WT and ALS-variant native apo-SOD1 by aspirin was performed by dissolving acetylsalicylic acid crystalline directly in solutions of apo-SOD1 (5 μ M SOD1 dimer) in 100 mM HEPBS (N-2-hydroxyethyl piperazine-N'-4-buthanesulfonic acid), pH 9.0. The final concentration of aspirin was 25 mM, 50 mM, and 150 mM. The solutions of apo-SOD1 and acetylsalicylic acid were stirred for 48 hr at 4 °C. Throughout the acetylation and hydrolysis reactions, both of which produce acetic acid, the pH was maintained at pH 8-9 by addition of 3 M KOH. As a control, solutions of unacetylated apo-SOD1 were incubated alongside acetylated proteins, in the identical HEPBS buffer as the acetylated proteins, wherein no acetylsalicylic acid was added. Thus, the unmodified apo-SOD1 proteins were processed under the exact same solution conditions as the acetylated proteins. Reaction by-products (i.e., acetic acid and salicylic acid) and unreacted acetylsalicylic acid were removed with centrifugal filtration devices (5 kDa molecular weight cut-off, Corning® Spin-X® UF). Centrifugal filtration was also used to transfer proteins into an "aggregation buffer" consisting of 10 mM potassium phosphate, 5 mM EDTA, pH 7.4 (for carrying out thioflavin-T fluorescence amyloid assays).

Centrifugal filtration consisted of diluting protein solutions (ten-fold) into the aggregation buffer and concentrating ten-fold (typically from 25 mL to 2.5 mL). This ten-fold concentration and dilution cycle was performed seven times for each sample.

Acetylation of Fibrillar SOD1 with Aspirin:

In order to prepare peracetylated apo-SOD1 fibrils (i.e., acetylating SOD1 after fibrillization), I combined 1.62 g of acetylsalicylic acid to 3.0 mL of unacetylated fibril homogenate (containing ~ 240 μ M SOD1 polypeptide). The fibrils were prepared from 3.0 mL of 60 μ M apo-SOD1 monomer as described for ThT fluorescence assays. Negative control samples contained the same amount of fibrils without the addition of aspirin. During the course of acetylation, the pH of the solution of acetylated fibrils drops as acetic acid is produced from hydrolysis of aspirin. The pH of the reaction was therefore maintained between pH ~ 8-9 by addition of 12 M KOH. Both acetylated and control samples were gently stirred with a stir bar (at room temperature, ~ 23 °C) during the course of reaction. In order to ensure that total protein concentrations were identical for control and acetylated samples, an aliquot of aggregation buffer (10 mM potassium phosphate, 5 mM EDTA, pH 7.4) was added to the control sample to keep its volume equal to that of the acetylated sample (the volume of which increased over time as KOH was added). After dissolution of aspirin (~ 1 hr), both acetylated and control samples were gently stirred for an additional 48 hr at 4 °C, pH 9.5. The pH of the acetylated sample was maintained at ~ 9.5 by periodic addition of 3 M KOH. After 48 hr, the acetylated sample underwent 10 cycles of washing with aggregation buffer (10 mM potassium phosphate, 5 mM EDTA, pH 7.4) to remove salicylic acid, acetic acid, and any

unreacted acetylsalicylic acid or non-aggregated SOD1. The washing process was as follows: centrifugation at $16,200 \times g$ ($4\text{ }^{\circ}\text{C}$), followed by removal of supernatant, addition of fresh buffer to the pellet, and additional centrifugation. The removal of salicylic acid was monitored with UV-Vis spectrophotometry (UV-2550, Shimadzu Corp., Kyoto, Japan) by the diminishing absorbance at 280 nm, i.e., salicylic acid absorbs strongly at 280 nm.³¹⁸ Washed samples were then separated into either 200 μL or 500 μL aliquots to be used for thermal stability assays and mass spectrometry.

Capillary Electrophoresis (CE):

CE experiments were performed on a Beckman Coulter Inc. P/ACE electrophoresis instrument, in order to confirm the acetylation of apo-SOD1 as well as determining the number of acetylated lysine residues, as previously described.⁶⁷ Potassium phosphate buffer was used as the running buffer (10 mM potassium phosphate, pH 7.4). Dimethylformamide (DMF) was added to each solution of protein (immediately prior to injection) as a neutral marker of electroosmotic flow, as previously described.⁶⁷

Hydrogen/Deuterium exchange:

The rate of amide hydrogen/deuterium exchange (HDX) of apo-SOD1^{S-S} was measured with ESI-MS as previously described⁸⁷ using a LTQ LX/Orbitrap Discovery LC/MS (Thermo Scientific). Samples of each acetylated apo-SOD1 protein were concentrated in potassium phosphate buffer (100 mM phosphate, pH 7.4). Each sample was diluted 1:10 into D₂O and aliquots were then measured at three time points: 3 min, 60 min, and 120 min after dilution (seven replicates each). This exchange reaction was

performed at room temperature and the samples were flash frozen at each time point. At the end of the H/D exchange experiment, the remaining solution was divided into seven aliquots for the purpose of SOD1 denaturation (perdeuteration) and measuring the extent of deuterium/hydrogen back-exchange. The specific temperatures that were used to perdeuterate WT, D90A, and A4V apo-SOD1 scaled with their relative thermostability and were 50 °C (for WT and D90A) and 37 °C (for A4V). The perdeuterated samples were then flash frozen in liquid nitrogen. All deuterated samples were then rapidly thawed (individually), and diluted 1:20 with ice-chilled formic acid (0.1%, in H₂O) and measured with ESI-MS. The ESI-MS was equipped with a desalting column (submerged in ice to minimize back-exchange) that was attached to an external, free standing Rheodyne injector that was also submerged in ice. Protonated solvents were used for ESI-MS, as previously described.⁸⁷

Differential Scanning Calorimetry:

The effect of acetylation on the thermostability of apo-SOD1 was measured with differential scanning calorimetry (DSC). Calorimetry was performed on acetylated apo-SOD1 (without the addition of reducing agent) in potassium phosphate buffer (10 mM potassium phosphate, pH 7.4, [SOD1] = 2 mg/mL) using a Microcal LLC VP-DSC (Microcal/GE-Healthcare), as previously described.⁶⁴

The melting transition temperature (T_m) that was reported for each protein was an average of three separate measurements.

Transmission Electron Microscopy:

To determine whether aggregates of acetylated and unacetylated native WT and ALS-variant apo-SOD1 were fibrillar in nature, and to assess morphological characteristics of fibrils (e.g., fibril diameter and length), I analyzed aggregated solutions with Transmission Electron Microscopy (TEM) at the end of the 10-day aggregation assay, as previously described.⁶⁴ Imaging with TEM was also used to determine whether non-sedimentable oligomers remained in the supernatant of melted fibrils after completion of the thermal stability assays and filtration with a 0.2 μm filter (thermal stability assays are described in the main text). All samples were imaged using a JEOL 1230 High Contrast Transmission Electron Microscope operating at 80 kV and samples were prepared as previously described.⁶⁴

Liquid Chromatography and Mass Spectrometry:

The number of acetylated amino acid residues in apo-SOD1 was confirmed with electrospray ionization-mass spectrometry (ESI-MS) using a LTQ LX/Orbitrap Discovery LC/MS (Thermo Scientific). In order to determine the identity of the residues that were acetylated in native (non-fibrillar) SOD1, I sequenced acetylated SOD1 with ESI-MS/MS after proteolysis with trypsin (Trypsin Gold, Mass Spectrometry Grade, Promega Corp.) and porcine pepsin (Sigma-Aldrich®). Trypsin and pepsin proteolysis was performed on separate aliquots of apo-SOD1, and not in tandem. Aliquots of the proteolytic digest of acetylated apo-SOD1 (10 μL , [SOD1] = 1 mg/mL) were loaded onto a C-18 Zorbax column using the same water/acetonitrile gradient described previously.⁶⁷ All MS/MS spectra were analyzed using Proteome Discoverer 1.3.

Thioflavin-T Aggregation Assays:

Assays were performed at pH 7.4, 37 °C, in a 96-well black polystyrene plate with a Thermo Scientific Fluoroskan Ascent 2.5 Fluorescence spectrophotometer; fibrillization was initiated by the addition of a Teflon® bead to each solution, in each well of the microplate. I performed 18 replicates of ThT assays for each of the three apo-SOD1 proteins and the four sets of acetylated derivatives, in the presence and absence of 100 mM NaCl, a total of 432 separate assays. In order to extract the kinetic parameters of each aggregation assay, a sigmoidal function (Equation 8.1 and Figure 8.1) was fit to plots of fluorescence vs. time (each plot consisted of 1000 scans for each well) using SigmaPlot™, version 11.0 (Systat Software Inc., Chicago, IL, USA).

$$f = y_0 + \frac{a}{1 + e^{-\frac{(x-x_0)}{b}}} \quad \text{(Equation 8.1)}$$

In Equation 8.1, f = fluorescence intensity (arbitrary units; a.u.); a = maximum emission intensity; y_0 = starting emission intensity; x = time in hours; and x_0 = time of 1/2 maximum emission intensity. As a template, I show a graphical representation of these parameters within a typical sigmoidal function (Figure 8.1). The two most important parameters (for quantifying the rate of aggregation) are “ $x_0 - 2b$ ”, which I refer to as “lag time” and “ b ”, which is equal to the reciprocal rate constant of fibril propagation ($1/k$), where k represents the fibrillization rate constant. I refer to “ b ” as “reciprocal rate constant of propagation” or simply “inverse propagation constant”. Kinetic parameters were extracted from sigmoidal fits of all 18 replicate plots for each acetylated and unacetylated apo-SOD1 protein. Average kinetic parameters were reported as mean values and error values were reported as standard error of the mean (SEM). The statistical

significance of measured differences in the kinetic parameters of aggregation between acetylated and unacetylated proteins was determined with an unpaired Student's t-test, using GraphPad Prism® software (GraphPad Inc., La Jolla, CA, USA). A threshold of significance of $p < 0.05^*$ (at a 95 % confidence interval) was used to establish the statistical significance of differences between the mean kinetic parameters of fibrillization of acetylated and unacetylated proteins.

The amount of apo-SOD1 that remained in solution at the end of ~ 10-day aggregation assay was determined with SDS-PAGE in order to ensure that aggregation proceeded to completion, without any remaining soluble SOD1. For this analysis, solutions of aggregated apo-SOD1 were pelleted with centrifugation at $16200 \times g$ for ten minutes (on a Fisher Scientific™ accuSpin™ Micro 17/Micro 17R microcentrifuge) and SDS-PAGE was performed on the resulting supernatant, as previously described.⁶⁴

Size-Exclusion Chromatography and Native Polyacrylamide Gel Electrophoresis:

In order to characterize the non-sedimentable oligomers of apo-SOD1 after thermal defibrillization assays, I performed size-exclusion chromatography and native PAGE. Prior to SE-LC, the supernatant of the heated samples were immediately combined with pure (14.3 M) β -mercaptoethanol (β -ME) in a 60:1 (v/v) ratio (sample: β -ME) to prevent the formation of disulfide cross-links. Defibrillized solutions (300 μ L) were injected into a 25 cm Zorbax Bio Series G-250 column (Agilent Technologies, Santa Clara, CA, USA); internal diameter = 4.6 mm; resolving range = 4-400 kDa. The aggregation buffer (10 mM potassium phosphate, 5 mM EDTA, pH 7.4) was used as a running buffer with a flow rate of 0.2 mL/min. The total run time was 40 minutes and the

void volume (V_o) of the column was calculated to be 1.38 mL. Eluted species were detected at 280 nm using a photodiode array (PDA) detector. In order to approximate the molecular weight of the thermally defibrillized apo-SOD1 proteins that were generated during thermal melting experiments, I generated a calibration curve using a mixture of 5 different proteins with known molecular weights: phosphorylase b, lactate dehydrogenase (tetramer), albumin, WT apo-SOD1 (dimer), and ubiquitin. The concentration of each protein in the standard was 50 μ M, except ubiquitin, which was prepared at 100 μ M, because of its low absorbance at 280 nm.

For native PAGE experiments, defibrillized samples (containing β -ME) and native WT apo-SOD1 (dimer, used as a control) were diluted two-fold with native 2X buffer (Bio-Rad Laboratories Inc., Hercules, CA, USA) and loaded on a 10 % polyacrylamide gel. Electrophoresis was performed at 90 V (4 °C). Gels were then stained with Coomassie blue, followed by destaining and visualization using a charge-coupled device (CCD) camera.

Calculating the Formal Net Charge of Fibrillar SOD1:

As described in the main text, I first determined the number of SOD1 polypeptide chains in an average-sized fibril; to do so, I approximated the volume (V_{SOD1}) and diameter (d_{SOD1}) that a single SOD1 polypeptide would occupy in the fibril according to previously proposed spherical approximation⁷⁰ (M represents the molecular weight of the protein)

$$V = (1.212 \times 10^{-3}) \times M$$

$$V_{\text{SOD1}} = (1.212 \times 10^{-3}) \times (15845 \text{ Da}) = 19.2 \text{ nm}^3$$

$$d_{\text{SOD1}} = 2 \times \left(\frac{3 \times (19.2)}{4\pi} \right)^{1/3} = 3.32 \text{ nm}$$
(Equation 8.2)

I then approximated a representative length of SOD1 fibrils (L_f) based on TEM images for all three proteins, as well as the average diameter of fibrils (d_f) for each SOD1 protein (d_{avg} in Figure 2.5E) in order to calculate the volume of the fibrils (V_f) by assuming a cylindrical geometry for the fibrils:

$$V_f = \pi \left(\frac{d_f}{2} \right)^2 \times L_f$$
(Equation 8.3)

Thus, the number of monomeric SOD1 proteins embedded in a fibril with the volume of V_f can be calculated as:

$$N_{\text{SOD1}} = \frac{V_f}{V_{\text{SOD1}}} = \frac{V_f}{19.2}$$
(Equation 8.4)

Because there are 11 lysine residues per SOD1 monomer, the total number of lysines per fibril can be estimated as:

$$N_{\text{Lys}} = 11 \times \frac{V_f}{19.2} = (0.6)V_f$$
(Equation 8.5)

I can then estimate the magnitude of increase in the net negative charge upon “supercharging” of the fibrils directly from the number of lysine residues (since all the lysines become acetylated upon peracetylation, Figure 2.6A-C):

$$\Delta Z_f = (0.9)N_{\text{Lys}} = (0.9) \times (11 \times \frac{V_f}{19.2}) = (0.52)V_f$$
(Equation 8.6)

In Equation 8.6, the constant 0.9 represents the fact that each lysine acetylation increases the net charge of the SOD1 polypeptide by 0.9 units.

Supporting Results and Discussion

Acetylation of Lysine in SOD1 by Aspirin is Semi-Random:

I expected that the acetylation of the lysine residues in apo-SOD1 with aspirin would be random, with the possible exception of Lys-3 and Lys-91. Nine out of the eleven lysine residues in WT and D90A apo-SOD1 were found to be acetylated (according to MS/MS) regardless of the amount of aspirin added to the solutions, that is, each peak or “rung” in the capillary electropherograms and mass spectra in Figure 2.2 were comprised of multiple regioisomers. Approximately 95 % of the apo-SOD1 sequence was observed in the resulting MS/MS spectra, and the statistical scores (X_{COR} , Sequest 1.2) used to grade each MS/MS spectrum were uniformly > 3.0 . Lysine-3 was not measured to be acetylated in any WT sample, and Lys-91 was only found to be acetylated in WT apo-SOD1 after addition of the maximum amount of aspirin (Table 8.1). Because Lys-91 is exposed to solvent, I suspect that it is protected from acetylation because it is located (upon the folding of SOD1) in the most negatively charged region of native SOD1, which will likely raise the pK_a of $Lys-\epsilon-NH_3^+$ and disfavor acetylation.³¹⁹ Lysine-91 has been previously shown to be protected from acetylation by acetic anhydride.⁶⁷ Lysine-3 is located at the dimer interface and might be sterically shielded from reaction.

In the case of A4V apo-SOD1, all lysine residues were found to be acetylated (even Lys-3 and Lys-91) regardless of the concentration of aspirin (Table 8.1). The ability of aspirin to acetylate Lys-3 and Lys-91 in A4V apo-SOD1 might be facilitated by the conformational instability and high degree of disorder associated with this ALS-variant.^{30,71}

Supporting Figures and Tables

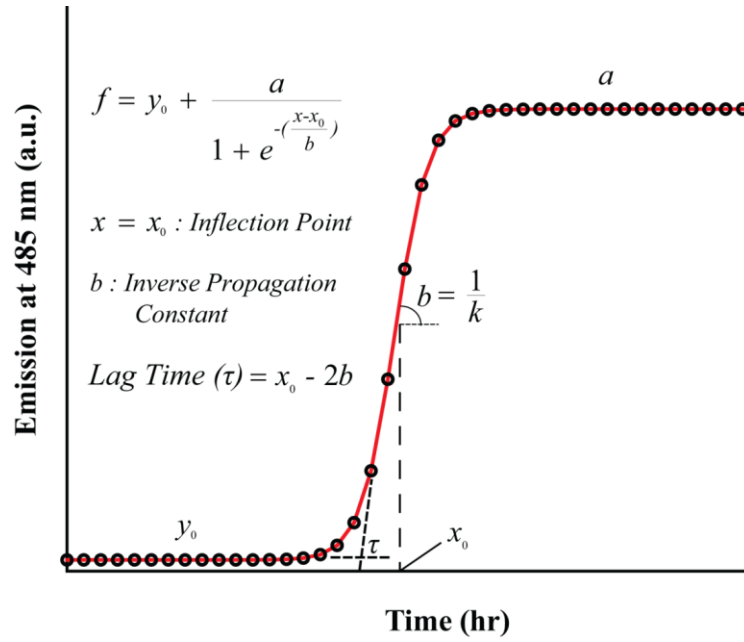


Figure 8.1 Sigmoidal curve used to fit fibrillization kinetics of apo-SOD1 protein variants as measured by an increase in thioflavin-T (ThT) fluorescence at 485 nm.

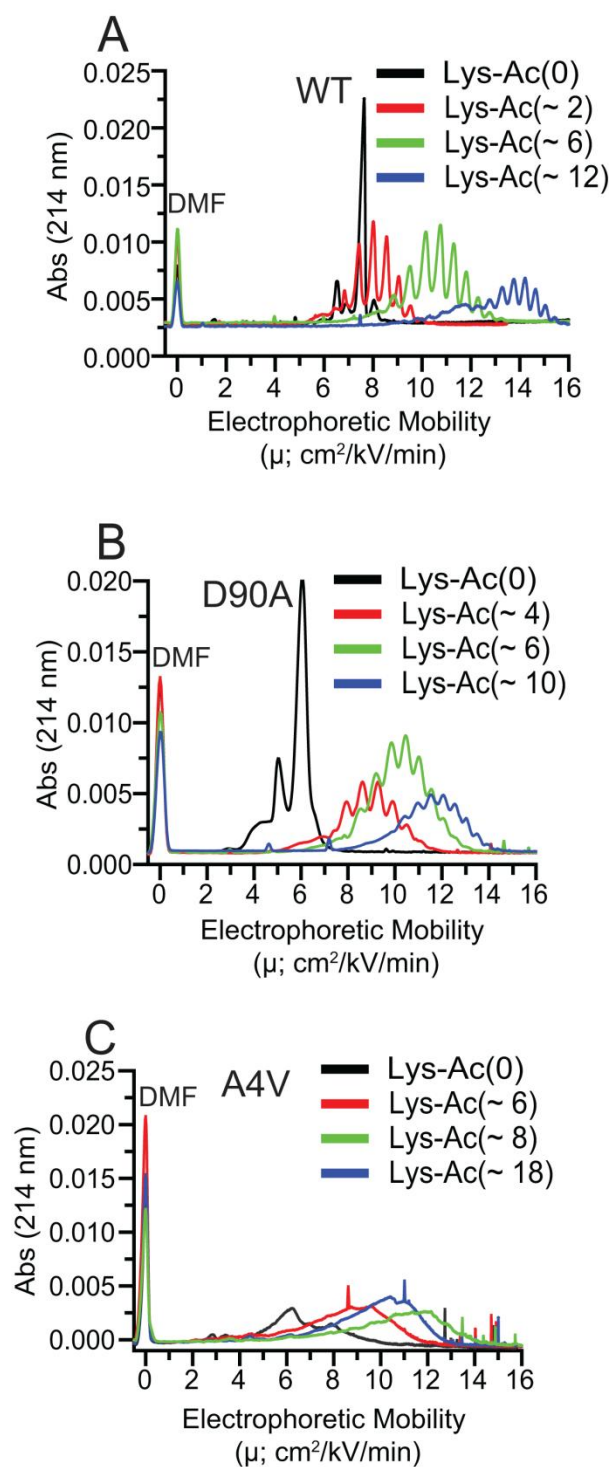


Figure 8.2 Aspirin acetylates lysine residues in WT and ALS-variant apo-SOD1. Capillary electropherograms of soluble (A) WT, (B) D90A, and (C) A4V apo-SOD1 after reaction with different concentrations of aspirin (in aqueous buffer). The mean numbers of acetylated lysines are denoted as “Lys-Ac(~N)”, and are listed per apo-SOD1 dimer. DMF (dimethylformamide) was added as a neutral marker of electroosmotic flow.

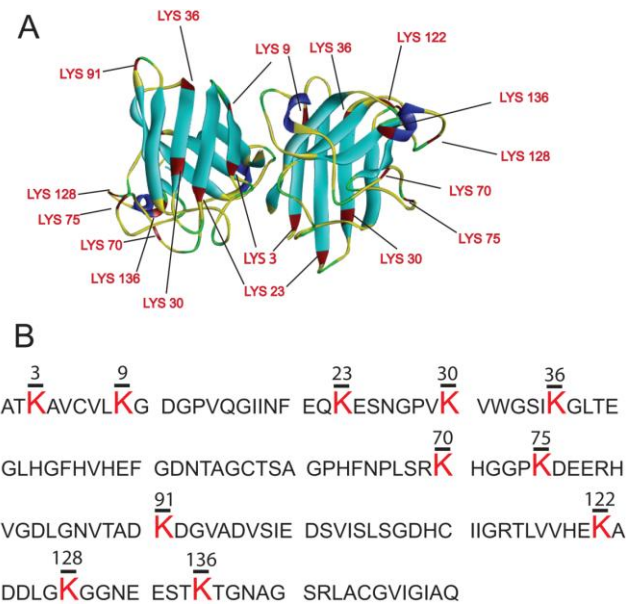


Figure 8.3 Three dimensional structure and amino acid sequence of human SOD1. (A) Three dimensional ribbon structure of WT human SOD1 dimer (PDB entry: 2V0A). (B) Amino acid sequence of WT human SOD1 (Uniprot entry: SODC_Human). Lysine residues are numbered and colored in red.

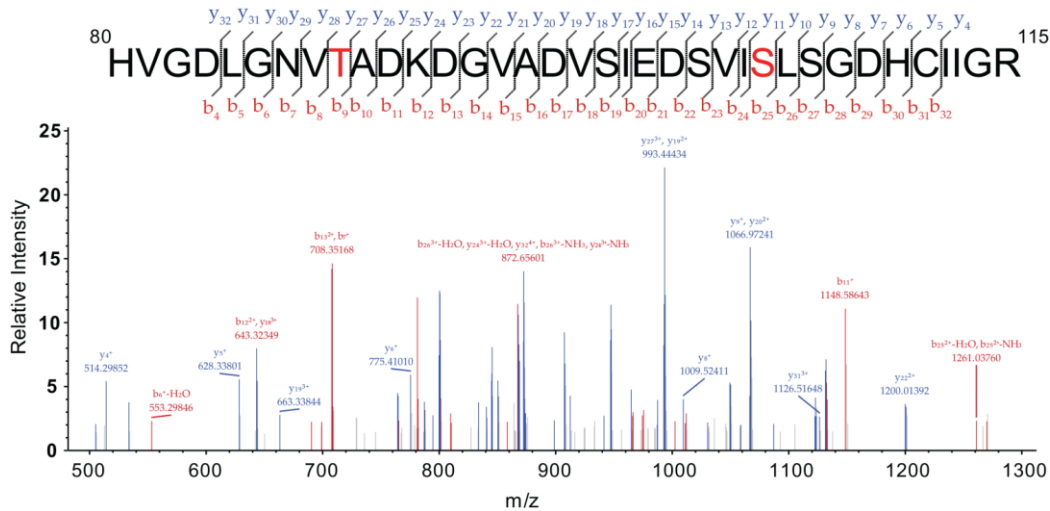


Figure 8.4 High concentration of aspirin can acetylate serine and threonine residues in A4V apo-SOD1. MS/MS spectrum of acetylated peptide 80-115, showing the acetylation of Thr-88 and Ser-105. This peptide was derived from trypsinization of A4V apo-SOD1 that was reacted with 150 mM acetylsalicylic acid (before fibrillization).

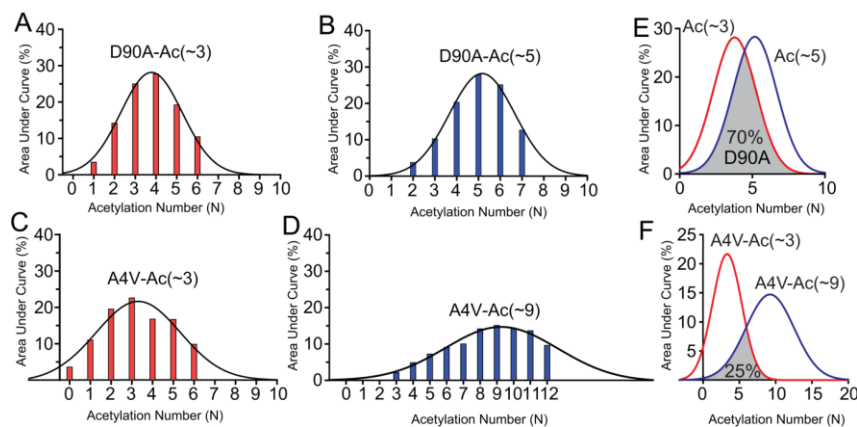


Figure 8.5 Relative concentration of each acetyl derivative in solutions of D90A and A4V apo-SOD1 that were acetylated with aspirin before fibrillization. Percentages were calculated from integration of the mass spectra of (A-B) D90A and (C-D) A4V apo-SOD1 (these spectra are shown in Figure 2.2). Gaussian distribution for each mass envelope is plotted with $R^2 > 0.99$. The degree by which MS Gaussian distributions overlap for each acetylation number (median) is illustrated for (E) D90A and (F) A4V apo-SOD1.

WT (0 mM NaCl)

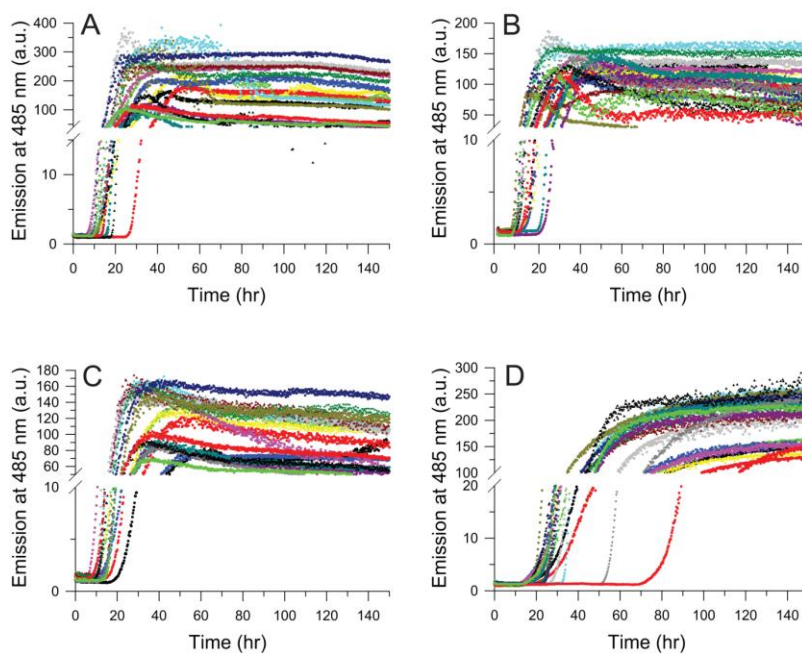


Figure 8.6 Fibrillization of unacetylated and acetylated WT apo-SOD1 as measured by thioflavin-T fluorescence in a 96-well microplate in 0 mM NaCl. (A-D) Raw, unnormalized thioflavin-T fluorescence amyloid assays for all 18 replicates of unacetylated and acetylated WT apo-SOD1 at pH 7.4 in 0 mM NaCl. (A) Lys-Ac(0), (B) Lys-Ac(~1), (C) Lys-Ac(~3), and (D) Lys-Ac(~6). The number of acetylated lysine residues is listed per apo-SOD1 monomer.

WT (100 mM NaCl)

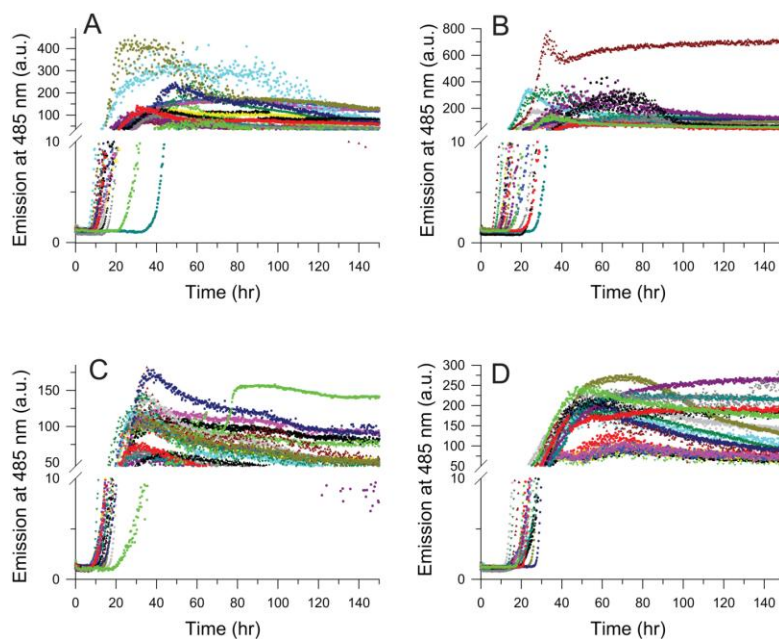


Figure 8.7 Fibrillization of unacetylated and acetylated WT apo-SOD1 as measured by thioflavin-T fluorescence in a 96-well microplate in 100 mM NaCl. (A-D) Raw, unnormalized thioflavin-T fluorescence amyloid assays for all 18 replicates of unacetylated and acetylated WT apo-SOD1 at pH 7.4 in 100 mM NaCl. (A) Lys-Ac(0), (B) Lys-Ac(~1), (C) Lys-Ac(~3), and (D) Lys-Ac(~6). The number of acetylated lysine residues is listed per apo-SOD1 monomer.

D90A (0 mM NaCl)

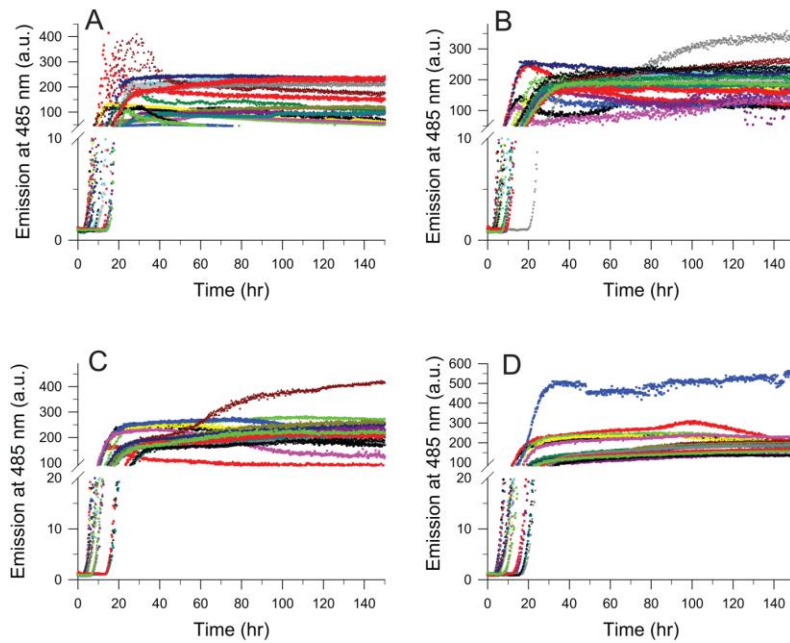


Figure 8.8 Fibrillization of unacetylated and acetylated D90A apo-SOD1 as measured by thioflavin-T fluorescence in a 96-well microplate in 0 mM NaCl. (A-D) Raw, unnormalized thioflavin-T fluorescence amyloid assays for all 18 replicates of unacetylated and acetylated D90A apo-SOD1 at pH 7.4 in 0 mM NaCl. **(A)** Lys-Ac(0), **(B)** Lys-Ac(~1), **(C)** Lys-Ac(~3), and **(D)** Lys-Ac(~6). The number of acetylated lysine residues is listed per apo-SOD1 monomer.

D90A (100 mM NaCl)

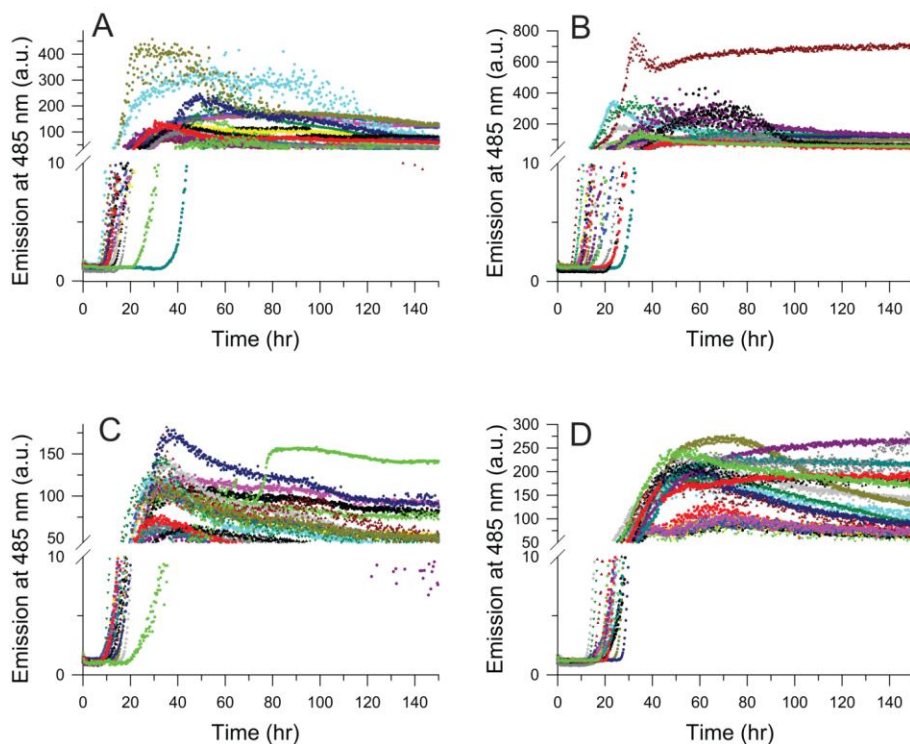


Figure 8.9 Fibrillization of unacetylated and acetylated D90A apo-SOD1 as measured by thioflavin-T fluorescence in a 96-well microplate in 100 mM NaCl. (A-D) Raw, unnormalized thioflavin-T fluorescence amyloid assays for all 18 replicates of unacetylated and acetylated D90A apo-SOD1 at pH 7.4 in 100 mM NaCl. (A) Lys-Ac(0), (B) Lys-Ac(~1), (C) Lys-Ac(~3), and (D) Lys-Ac(~6). The number of acetylated lysine residues is listed per apo-SOD1 monomer.

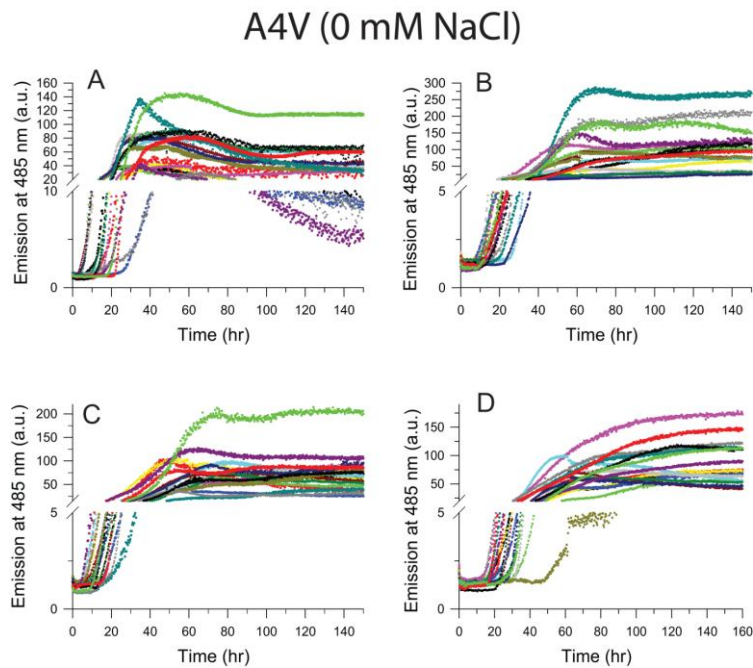


Figure 8.10 Fibrillization of unacetylated and acetylated A4V apo-SOD1 as measured by thioflavin-T fluorescence in a 96-well microplate in 0 mM NaCl. (A-D) Raw, unnormalized thioflavin-T fluorescence amyloid assays for all 18 replicates of unacetylated and acetylated A4V apo-SOD1 at pH 7.4 in 0 mM NaCl. **(A)** Lys-Ac(0), **(B)** Lys-Ac(~1), **(C)** Lys-Ac(~3), and **(D)** Lys-Ac(~6). The number of acetylated lysine residues is listed per apo-SOD1 monomer.

A4V (100 mM NaCl)

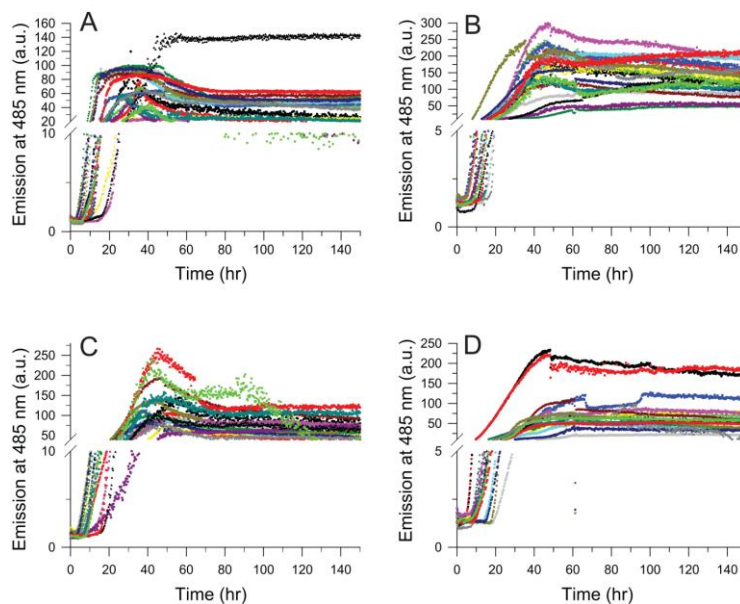


Figure 8.11 Fibrillization of unacetylated and acetylated A4V apo-SOD1 as measured by thioflavin-T fluorescence in a 96-well microplate in 100 mM NaCl. (A-D) Raw, unnormalized thioflavin-T fluorescence amyloid assays for all 18 replicates of unacetylated and acetylated A4V apo-SOD1 at pH 7.4 in 100 mM NaCl. (A) Lys-Ac(0), (B) Lys-Ac(~1), (C) Lys-Ac(~3), and (D) Lys-Ac(~6). The number of acetylated lysine residues is listed per apo-SOD1 monomer.

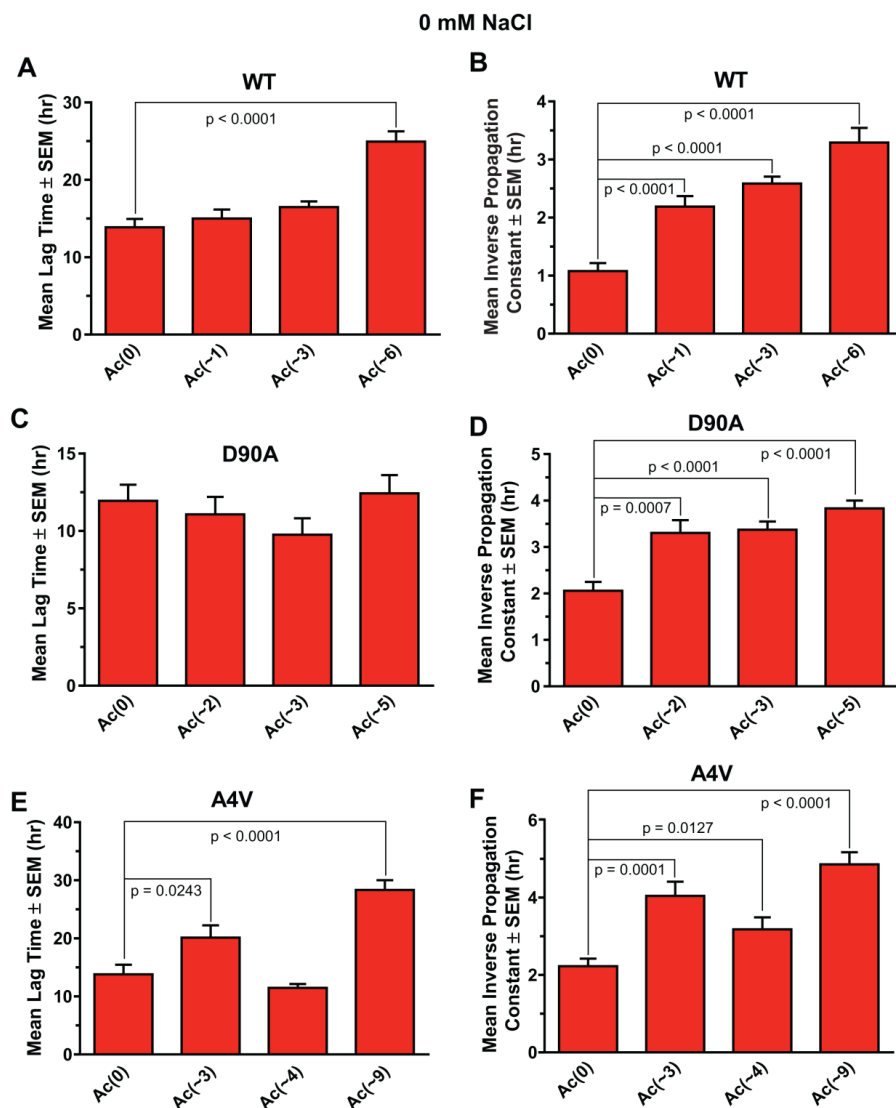


Figure 8.12 Statistical comparison of mean lag time and mean inverse propagation constant (from Table 2.1) for fibrillation of unacetylated and acetylated apo-SOD1 proteins in 0 mM NaCl. (A-B) WT, (C-D) D90A, and (E-F) A4V apo-SOD1 at different degrees of acetylation (in 0 mM NaCl). P-values compare the acetylated derivative with the unacetylated protein, and were calculated with a Student's unpaired t-test at a 95 % confidence interval. The number of acetylated lysine residues is listed per apo-SOD1 monomer. A lack of statistical significance ($p > 0.05$) between the unacetylated form of each protein, and anyone of its acetylated derivatives is indicated by the absence of a listed p-value and the absence of a connecting line. Data represent the calculated mean \pm SEM for 18 replicates ($n = 18$).

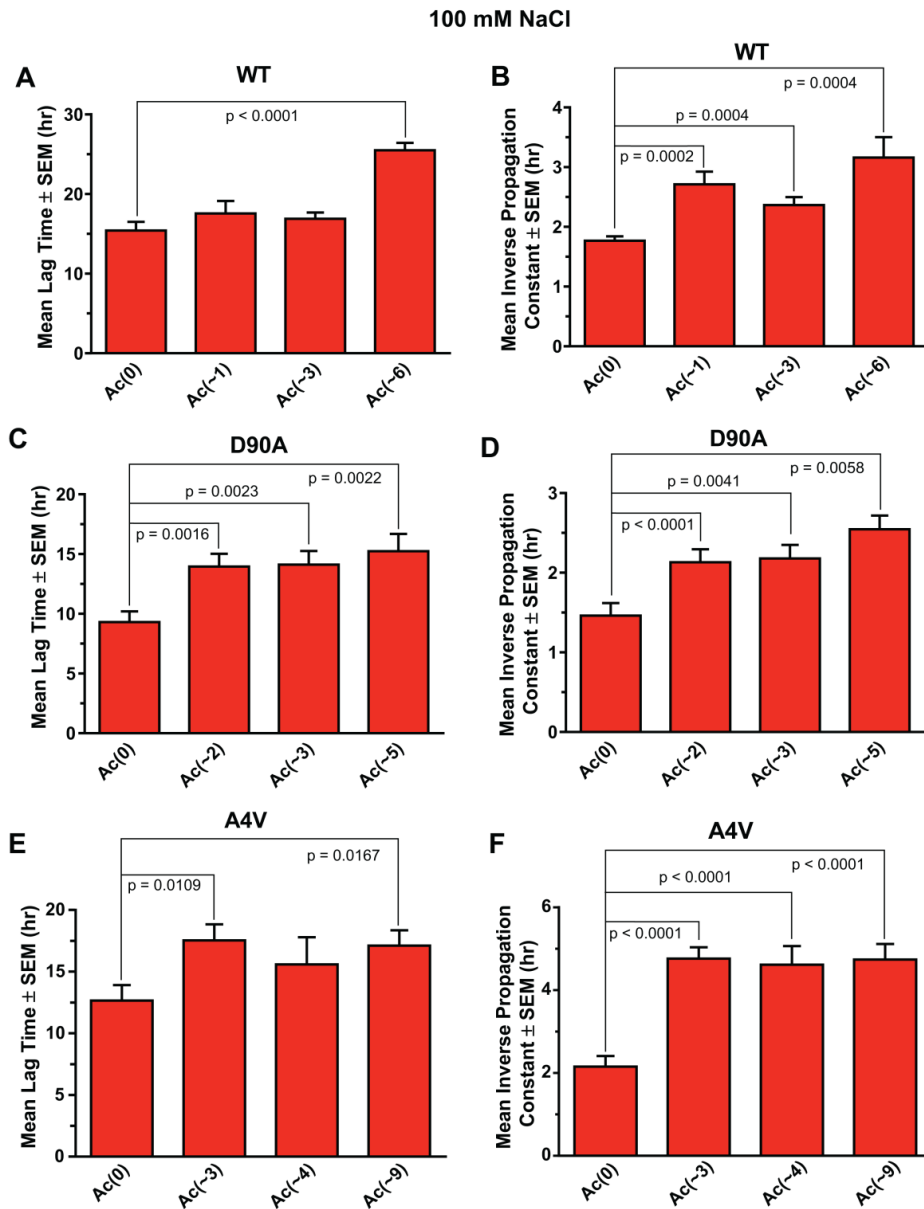


Figure 8.13 Statistical comparison of mean lag time and mean inverse propagation constant (from Table 2.1) for fibrillation of unacetylated and acetylated apo-SOD1 proteins in 100 mM NaCl. (A-B) WT, (C-D) D90A, and (E-F) A4V apo-SOD1 at different degrees of acetylation (in 100 mM NaCl). P-values compare the acetylated derivative with the unacetylated protein, and were calculated with a Student's unpaired t-test at a 95 % confidence interval. The number of acetylated lysine residues is listed per apo-SOD1 monomer. A lack of statistical significance ($p > 0.05$) between the unacetylated form of each protein, and any one of its acetylated derivatives is indicated by the absence of a listed p-value and the absence of a connecting line. Data represent the calculated mean \pm SEM for 18 replicates ($n = 18$).

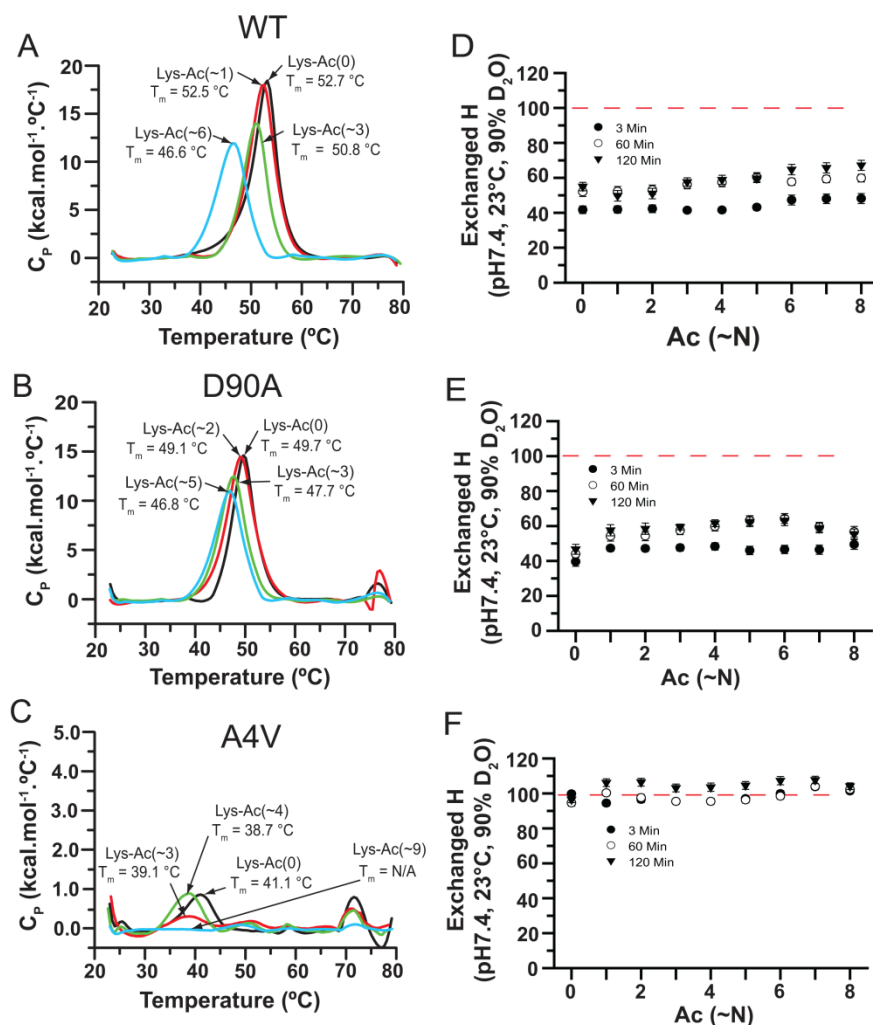


Figure 8.14 Differential scanning calorimetry and H/D exchange of unacetylated and acetylated apo-SOD1 proteins. (A-C) Thermograms of WT, D90A, and A4V apo-SOD1 are shown as a function of acetylated lysines. (D-F) Plots of number of exchanged hydrogens versus acetylation number for WT, D90A, and A4V apo-SOD1. Samples were incubated in 90 % D₂O at three different time points. Red dashed line indicates the experimental limit of deuteration (i.e., the number of exchanged hydrogen in the thermally denatured and perdeuterated protein). The extent of back-exchange for each acetylated derivative of each protein was measured. Typical values of back-exchange were 38 % (WT), 29 % (D90A), and 24 % (A4V) and the rate of back-exchange was not affected by the extent of acetylation. Mean number of acetylated lysine residues is denoted as Lys-Ac(~N) in each panel. In panel (C), the endothermic transitions of unmodified and minimally acetylated A4V were low in intensity to begin with, which suggested that the A4V apo-SOD1 protein was populating folded and unfolded states (as previously reported for this unstable ALS-variant³²⁰). A similar conclusion about low stability of A4V apo-SOD1 protein can be deduced from plots of HDX in panel (F). The number of acetylated lysine residues is listed per apo-SOD1 monomer.

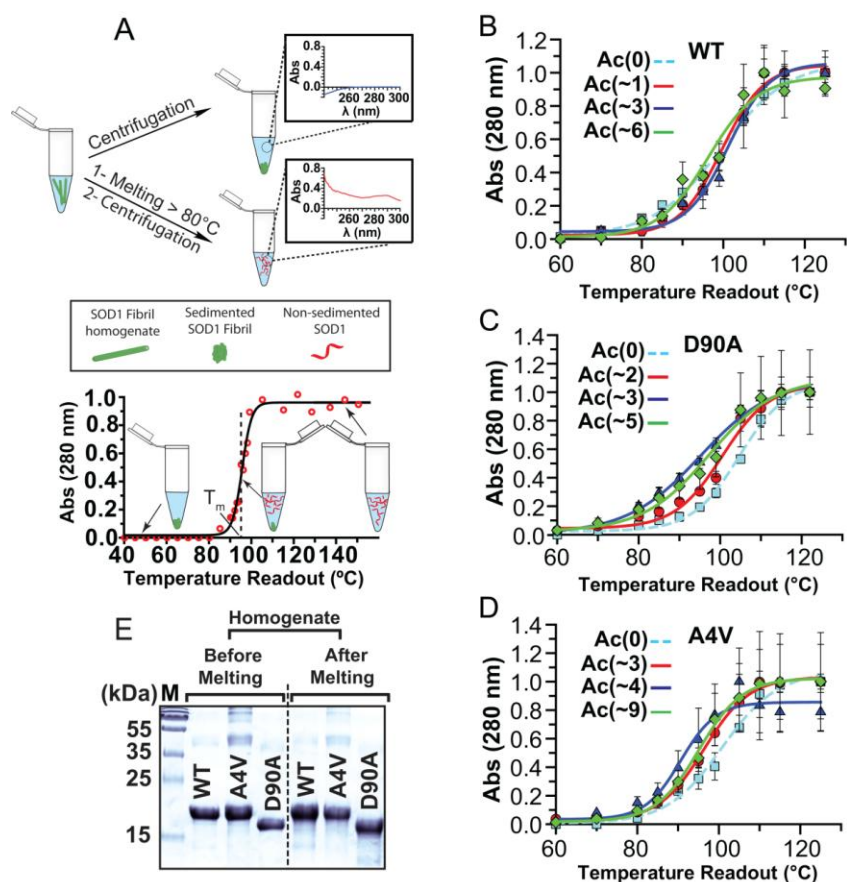


Figure 8.15 Effect of lysine acetylation in native apo-SOD1 on thermostability of resulting amyloid fibrils (i.e., acetylation before fibrillization). (A) Schematic illustration of thermal defibrillation assay for determining melting temperature of fibrillar apo-SOD1. Solutions of fibrillar SOD1 are heated, centrifuged, and the supernatant is analyzed with UV-Vis spectrophotometry. Soluble SOD1 proteins are retained in supernatant upon thermal defibrillation. T_m values (lower panel) were calculated as the inflection point of the sigmoid (x_0 in Equation 8.1). (B-D) Thermal defibrillation curves of fibrils formed from unacetylated and acetylated (B) WT, (C) D90A, and (D) A4V native apo-SOD1 proteins. Number of acetylated lysines is listed per apo-SOD1 monomer. Data are presented as mean \pm SEM ($n = 4$), and all fittings resulted in $R^2 = 0.99$. (E) Reducing SDS-PAGE on unacetylated apo-SOD1 amyloid fibrils before melting (left) and after the completion of melting (right). Intermediate increases in the mean number of acetylated lysines did not consistently result in statistically significant differences in fibril T_m . I suspect that these similarities in fibril T_m occurred because these mixtures have overlapping degrees of acetylation in spite of different mean number of acetylation. For example, the T_m of D90A-Ac(~ 3) apo-SOD1 fibrils is statistically similar to the T_m of D90A-Ac(~ 5) fibrils ($p > 0.05$, Table 8.5). The T_m values for A4V-Ac(~ 3) and A4V-Ac(~ 9) are statistically similar ($p > 0.05$, Table 8.5). Accordingly, I found ~ 70 % overlap between the distribution of acetyl groups of D90A apo-SOD1-Ac(~ 3) and D90A apo-SOD1-Ac(~ 5) and ~ 25 % overlap between A4V apo-SOD1-Ac(~ 3) and A4V apo-SOD1-Ac(~ 9). This overlap might explain the statistically similar average T_m values between these different mixtures.

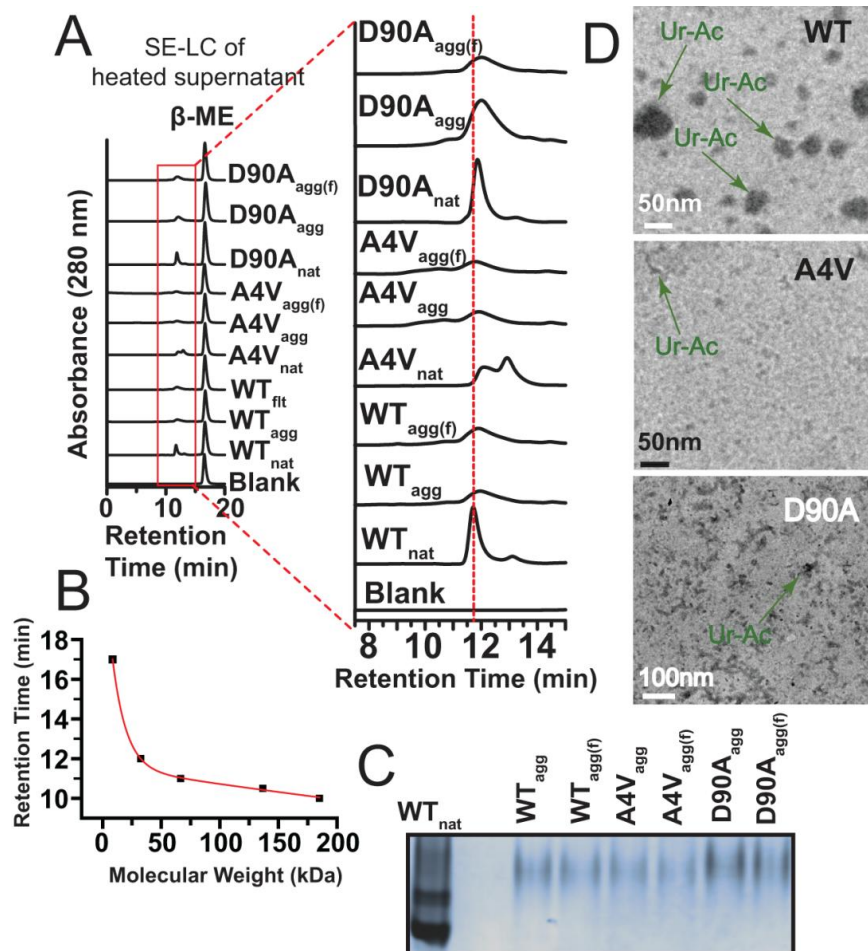


Figure 8.16 Characterization of state of oligomerization of WT and ALS-linked apo-SOD1 after thermal defibrillation of amyloid fibrils of apo-SOD1. (A) Size-exclusion chromatograms of supernatants of heated fibrils with native state (dimer) of each protein as control; β -ME stands for β -mercaptoethanol. Supernatants of samples heated at 125 °C (defibrillized proteins) were combined with β -mercaptoethanol (60:1 v/v ratio) to prevent disulfide cross-linking between cysteine residues during cooling period. (B) Calibration curve used for size determination of thermally defibrillized species in supernatants. (C) Native PAGE (10 %) performed on supernatant of melted fibrils with WT apo-SOD1 (dimer) as control. (D) TEM images of melted fibrils from supernatant. Ur-Ac indicates the clusters of uranyl acetate dye. Scale bars in (D) are 50 nm in case of WT and A4V and 100 nm in case of D90A. Subscripts “agg” and “agg(f)” in (A-C) indicate melted unfiltered protein aggregates and those that were filtered with a 0.2 μ m filter, respectively. Subscript “nat” in (A) and (C) designates the native protein.

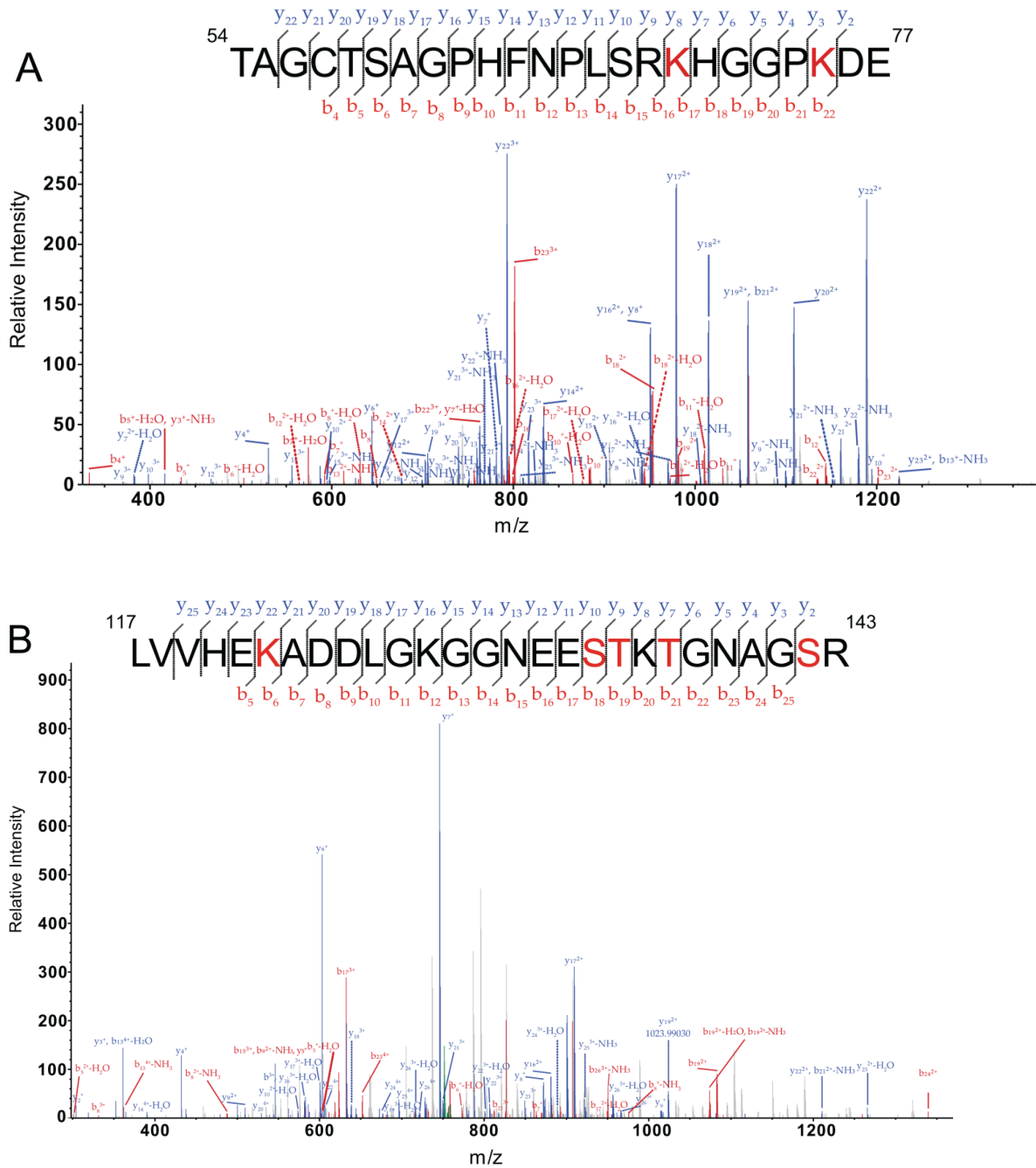


Figure 8.17 MS/MS spectra of tryptic SOD1 peptides from WT apo-SOD1 fibrils that were acetylated with aspirin after fibrillization. (A) MS/MS spectrum of peptide comprised of residues 54-77; (B) MS/MS spectrum of residues 117-143.

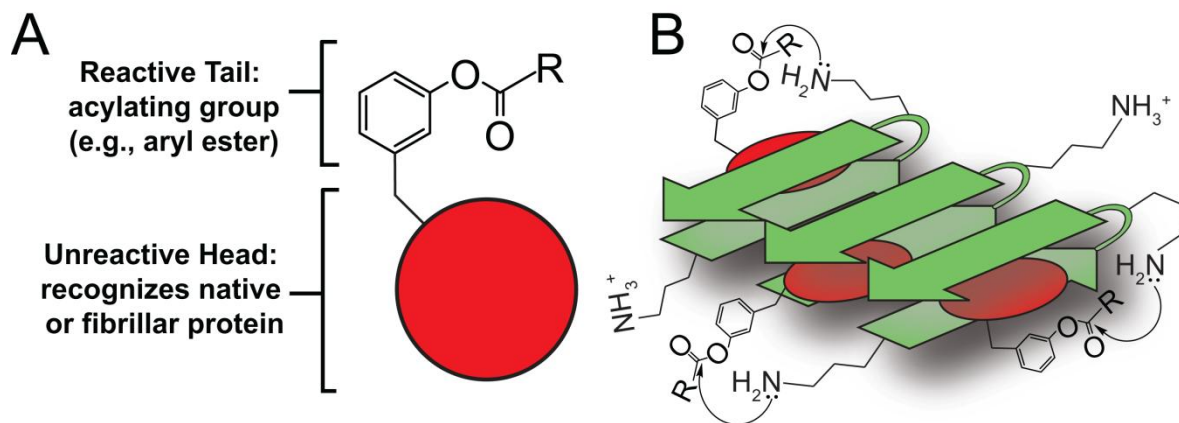


Figure 8.18 (A) Chemical anatomy of a prototype “charge boosting” drug that contains a “head” that either binds to a native protein or partitions to an amyloid-like oligomer, and an acylating “tail” that modifies nearby lysine residues. (B) The “head” does not become covalently attached to the protein, and can be displaced over time to allow for the binding and reaction of additional “charge boosters”. This scheme does not intend to indicate a preferred mode of binding (perpendicular or parallel to β -sheets). Designing acylating agents that specifically bind to and acylate lysine in anionic amyloid-like oligomers is certainly feasible. Several natural and synthetic small-molecules have been shown to bind to amyloid fibrils formed from different proteins.⁸⁸ I hypothesize that synthetically linking aryl ester moieties to these amyloid-binding molecules might enable the selective (and successive) acylation of amyloid fibrils.

Table 8.1 Results of tandem mass spectrometry of trypsin and pepsin digests of WT and ALS-variant apo-SOD1 at varying degrees of acetylation; (•) represents the acetylated lysine residues in digested fragments. N represents the number of acetylated lysine residues listed per apo-SOD1 monomer.

WT	Mean	Lysine residue number										
	Ac(~N)	3	9	23	30	36	70	75	91	122	128	136
	0											
	1		•	•	•	•	•	•		•	•	•
	3		•	•	•	•	•	•		•	•	•
	6		•	•	•	•	•	•	•	•	•	•
D90A	Mean	Lysine residue number										
	Ac(~N)	3	9	23	30	36	70	75	91	122	128	136
	0											
	2		•	•	•	•	•	•		•	•	•
	3		•	•	•	•	•	•		•	•	•
	5		•	•	•	•	•	•		•	•	•
A4V	Mean	Lysine residue number										
	Ac(~N)	3	9	23	30	36	70	75	91	122	128	136
	0											
	3	•	•	•	•	•	•	•	•	•	•	•
	4	•	•	•	•	•	•	•	•	•	•	•
	9	•	•	•	•	•	•	•	•	•	•	

Table 8.2 Average kinetic parameters of ThT aggregation assays for acetylated and unacetylated WT SOD1, in 0 mM and 100 mM NaCl. All data are presented as mean \pm SEM, n = 18. The number of acetylated lysine residues is listed per apo-SOD1 monomer.

SOD1	a (maximum) (a.u.)	x₀ (hr)	b (hr)	Lag time (hr)	Average R²
WT-Ac(0)	199.2 \pm 18.1	16.0 \pm 1.1	1.1 \pm 0.1	13.9 \pm 1.1	0.99
WT-Ac(~1)	127.3 \pm 5.5	19.4 \pm 1.4	2.2 \pm 0.2	15.0 \pm 1.2	0.99
WT-Ac(~3)	116.9 \pm 8.0	21.6 \pm 0.9	2.6 \pm 0.1	16.5 \pm 0.7	0.99
WT-Ac(~6)	205.9 \pm 11.1	31.5 \pm 1.3	3.3 \pm 0.3	24.9 \pm 1.3	0.99
WT-Ac(0) (100 mM NaCl)	166.7 \pm 25.8	18.9 \pm 1.1	1.8 \pm 0.1	15.4 \pm 1.1	0.98
WT-Ac(~1) (100 mM NaCl)	191.4 \pm 36.4	23.0 \pm 1.7	2.7 \pm 0.2	17.6 \pm 1.6	0.98
WT-Ac(~3) (100 mM NaCl)	98.6 \pm 6.8	21.6 \pm 0.8	2.4 \pm 0.1	16.9 \pm 0.8	0.98
WT-Ac(~6) (100 mM NaCl)	169.6 \pm 16.7	31.8 \pm 1.1	3.2 \pm 0.3	25.5 \pm 0.9	0.99

Table 8.3 Average kinetic parameters of ThT aggregation assays for acetylated and unacetylated D90A apo-SOD1, in 0 mM and 100 mM NaCl. All data are presented as mean \pm SEM, n = 18. The number of acetylated lysine residues is listed per apo-SOD1 monomer.

SOD1	a (maximum (a.u.))	x₀ (hr)	b (hr)	Lag time (hr)	Average R²
D90A-Ac(0)	154.6 \pm 20.2	16.1 \pm 1.3	2.1 \pm 0.2	11.9 \pm 1.0	0.98
D90A-Ac(~2)	189.4 \pm 8.9	17.7 \pm 1.3	3.3 \pm 0.3	11.1 \pm 1.1	0.99
D90A-Ac(~3)	188.4 \pm 11.8	16.5 \pm 1.1	3.4 \pm 0.2	9.8 \pm 1.1	0.99
D90A-Ac(~5)	187.4 \pm 21.2	20.1 \pm 1.1	3.8 \pm 0.2	12.4 \pm 1.2	0.98
D90A-Ac(0) (100 mM NaCl)	150.5 \pm 30.9	12.2 \pm 1.0	1.5 \pm 0.2	9.3 \pm 0.9	0.99
D90A-Ac(~2) (100 mM NaCl)	271.6 \pm 29.6	18.2 \pm 1.3	2.1 \pm 0.2	14.0 \pm 1.1	0.99
D90A-Ac(~3) (100 mM NaCl)	233.1 \pm 21.8	18.5 \pm 1.3	2.2 \pm 0.2	14.1 \pm 1.1	0.98
D90A-Ac(~5) (100 mM NaCl)	160.4 \pm 25.6	20.3 \pm 1.5	2.6 \pm 0.2	15.2 \pm 1.4	0.98

Table 8.4 Average kinetic parameters of ThT aggregation assays for acetylated and unacetylated A4V SOD1, in 0 mM and 100 mM NaCl. All data are presented as mean \pm SEM, n = 18. The number of acetylated lysine residues is listed per apo-SOD1 monomer.

SOD1	a (maximum) (a.u.)	x₀ (hr)	b (hr)	Lag time (hr)	Average R²
A4V-Ac(0)	67.4 \pm 8.1	18.3 \pm 1.8	2.2 \pm 0.2	13.8 \pm 1.7	0.99
A4V-Ac(~3)	101.6 \pm 16	28.2 \pm 2.4	4.1 \pm 0.4	20.1 \pm 2.1	0.99
A4V-Ac(~4)	91.7 \pm 8.8	17.8 \pm 0.5	3.2 \pm 0.3	11.5 \pm 0.7	0.99
A4V-Ac(~9)	84.1 \pm 13.9	38.0 \pm 1.7	4.9 \pm 0.3	28.3 \pm 1.7	0.99
<hr/>					
A4V-Ac(0) (100 mM NaCl)	75.9 \pm 6.4	16.9 \pm 1.6	2.2 \pm 0.3	12.7 \pm 1.3	0.98
A4V-Ac(~3) (100 mM NaCl)	169.1 \pm 17.4	27.1 \pm 1.5	4.8 \pm 0.3	17.5 \pm 1.3	0.99
A4V-Ac(~4) (100 mM NaCl)	127.2 \pm 12.6	24.8 \pm 2.4	4.6 \pm 0.5	15.6 \pm 2.2	0.99
A4V-Ac(~9) (100 mM NaCl)	86.0 \pm 16.0	26.6 \pm 1.5	4.7 \pm 0.4	17.1 \pm 1.2	0.99

Table 8.5 Thermostability of native and amyloid WT and ALS-variant apo-SOD1 as a function of lysine acetylation. All of the T_m values are presented as mean \pm SEM, n = 4.

SOD1	Ac ^a (~N)	Native T_m (°C)	ΔT_m (°C) ^b	Amyloid T_m (°C)	ΔT_m (°C) ^b
WT	0	52.70 \pm 0.05	—	99.42 \pm 0.89	—
	1	52.50 \pm 0.03	-0.02 \pm 0.06	99.64 \pm 0.76	-0.22 \pm 1.17
	3	50.80 \pm 0.03	-1.90 \pm 0.06	101.34 \pm 0.88	1.92 \pm 0.88
	6	46.60 \pm 0.03	-6.10 \pm 0.06	96.27 \pm 0.66	-3.15 \pm 1.1
	11	—	—	91.66 \pm 0.78	-7.76 \pm 1.18
D90A	0	49.70 \pm 0.04	—	104.69 \pm 0.24	—
	2	49.10 \pm 0.06	-0.60 \pm 0.07	100.11 \pm 0.97	-4.58 \pm 0.99
	3	47.70 \pm 0.02	-2.00 \pm 0.04	96.02 \pm 0.97	-8.67 \pm 0.99
	5	46.80 \pm 0.04	-2.90 \pm 0.04	97.62 \pm 0.60	-7.07 \pm 0.64
	11	—	—	84.49 \pm 0.42	-20.2 \pm 0.48
A4V	0	41.10 \pm 0.32	—	99.85 \pm 0.48	—
	3	39.10 \pm 0.36	-2.00 \pm 0.48	95.98 \pm 1.71	-3.87 \pm 1.77
	4	38.70 \pm 0.23	-2.40 \pm 0.39	92.26 \pm 1.31	-7.59 \pm 1.39
	9	—	—	95.07 \pm 0.33	-4.78 \pm 0.58
	11	—	—	95.29 \pm 0.50	-4.56 \pm 0.69

^aMean number of acetylated lysines in apo-SOD1 prior to fibrillization, except Ac(~11), which was acetylated in fibrillar form. Number of acetyl modifications is listed per apo-SOD1 monomer. ^b ΔT_m values for native and amyloid SOD1 are expressed relative to Ac(0) for each protein. All values and errors are listed as mean \pm SEM, n = 4.

*Stochastic Formation of Fibrillar and Amorphous Superoxide Dismutase Oligomers
Linked to Amyotrophic Lateral Sclerosis.*

Supporting Methods

*Thioflavin-T (ThT) and 1-Anilino-8-Naphthalene Sulfonate (ANS) Fluorescence
Aggregation Assays:*

The aggregation of WT and ALS-variant apo-SOD1 proteins into amyloid was monitored using high-throughput ThT fluorescence assays in a 96-well black polystyrene plate (measured with a Thermo Scientific Fluoroskan Ascent 2.5 Fluorescence spectrophotometer), and data were analyzed as previously described.⁴⁵ Assays were carried out at a protein concentration of 60 μ M (per monomer), 20 μ M ThT, 0 mM or 150 mM NaCl, 10 mM potassium phosphate, pH 7.4, 37 °C, 10 mM or 100 mM TCEP, and 5 mM EDTA. Excitation and emission wavelength pairs were 444 nm/485 nm for ThT and 350 nm/500 nm for ANS. A 3.18 mm Teflon bead was added to each well of the microplate (maximum of 60 wells out of 96, since I did not use outside wells which sometimes form faulty seals with polypropylene sheets). The plate was carefully sealed with a pre-warmed polypropylene seal. I note that the calculated diffusion of O₂ through the polypropylene seal at 37 °C will occur at $\approx 4.3 \times 10^{-7}$ mg/hr which can theoretically oxidize only 0.4 nmol of TCEP—out of 2000 nmol present (0.02 %)—during the 168 hr assay in each well. Fibrillization was initiated by automated gyration of the microplate at 360 rpm. This gyration does not occur throughout the entire ThT assay, but occurs in bursts of 15 sec, followed by a pause of 15 sec; the radius of gyration is 3 mm. Fluorescence was measured every 15 min, for 168 hr. In order to determine how reaction conditions affected the stochastic nature (and rate) of amyloid formation, reaction

conditions were varied (i.e., temperature, protein concentration, ionic strength, and speed of plate gyration). Prior to initiating the ThT kinetic assays, all apo-SOD1 solutions were filtered with a 0.2 μm filter (to remove pre-formed oligomers that can seed aggregation), and pipetted into different wells of a 96-well plate. The absence of any residuals of soluble protein at the end of aggregation assays was confirmed with SDS-PAGE on the supernatant of centrifuged fibril homogenates, as previously described.⁴⁵ The gross morphology of formed aggregates was determined with transmission electron microscopy, as previously described.⁴⁵

All sets of ThT and ANS kinetic data were fit with a 4-parameter sigmoidal function (Equation 8.7):

$$f = f_0 + \frac{f_{\max}}{1 + e^{\frac{t-t_0}{b}}} \quad (\text{Equation 8.7})$$

Where f is ThT emission intensity at 485 nm, f_0 and f_{\max} are minimum and maximum fluorescence intensities, respectively, t_0 is the time where $f = 1/2(f_{\max})$, and b is defined as inverse propagation constant ($1/k$) with the unit of hr. Lag time (τ) of apo-SOD1 aggregation was calculated as $\tau = t_0 - 2b$, and average values of τ and b were determined by individually fitting replicate traces, not by a single fit to an average sigmoid, as previously described.⁴⁵

Well and Bead-Specific Aggregation Assays:

A 96-well plate that contained wells with outlier kinetic sigmoids was chosen and cooled down to 4 °C immediately after the termination of the assay. These wells were then emptied, beads were removed, and both were then washed with detergent, guanidinium hydrochloride (GdmHCl), and pepsin, to remove any aggregates that were

adhered to the wells. The washing protocol was as follows: wells were washed with MilliQ water with 5 volumes, and then filled with 250 μ L of boiling 2x Laemmli buffer containing 2.1 % SDS. The plate was then sealed with a polypropylene sealing film and stored for 10 min at 50 $^{\circ}$ C with constant shaking.

A similar volume of 2x Laemmli buffer was added to the vials containing beads and vials were boiled at 95 $^{\circ}$ C for 10 min. All wells and beads were washed thoroughly with MilliQ water prior to incubation with 6.5 M GdmHCl and 20 mM DTT for 12 hr at 50 $^{\circ}$ C with gentle shaking. After 12 hr, wells and beads were washed several times with MilliQ water to remove all residual GdmHCl and DTT.

Finally, in order to completely remove any remnants of small misfolded proteins or oligomers that might seed SOD1 fibrillization, 250 μ L of 1 mg/mL pepsin solution (100 mM KPO₄, pH 2.5) was added to each well (that contained the corresponding bead) and the plate was gently shaken at 37 $^{\circ}$ C for 24 hr. Wells and beads were then washed several times with MilliQ water, dried and sealed until the initiation of a replicate aggregation assay. The new assay was performed in a similar condition as the first assay.

Statistical Analyses of Lag Time and Inverse Propagation Rate Histograms of Apo-SOD1 Aggregation:

The log-normal distribution functions that were used to fit the non-normal histograms were as follows:

The 3-parameter log-normal distribution:

$$y = \frac{a}{x} e^{-0.5 \left[\frac{\ln\left(\frac{x}{x_0}\right)}{b} \right]^2} \quad \text{(Equation 8.8a)}$$

And the 4-parameter log-normal distribution:

$$y = y_0 + \frac{a}{x} e^{\left[-0.5 \left(\frac{\ln\left(\frac{x}{x_0}\right)}{b} \right)^2 \right]} \quad (\text{Equation 8.8b})$$

Where $x_0 = \mu$ and $b = \sigma$ with μ and σ are the mean and standard deviation of natural logarithm of x , respectively, and $a = \sigma(2\pi)^{1/2}$.

A bimodal Lorentzian function was applied to non-normal bimodal histograms as follows:

$$y = y_0 + \left(2 \frac{A}{\pi}\right) \left(\frac{W}{4(x - x_0)^2 + W^2} \right) \quad (\text{Equation 8.9})$$

Where A is the total area under the curve from the baseline and W represents the peak width.

Exponential plots of ANS fluorescence were fit using Equation 8.10 as follows:

$$f_{ANS} = (f_0)_{ANS} + \varphi(1 - e^{-\delta x}) \quad (\text{Equation 8.10})$$

Where f_{ANS} is ANS emission intensity at 500 nm, $(f_0)_{ANS}$ and φ are minimum and maximum fluorescence intensities, respectively, and δ is the growth rate of amorphous species.

Supporting Figures and Tables

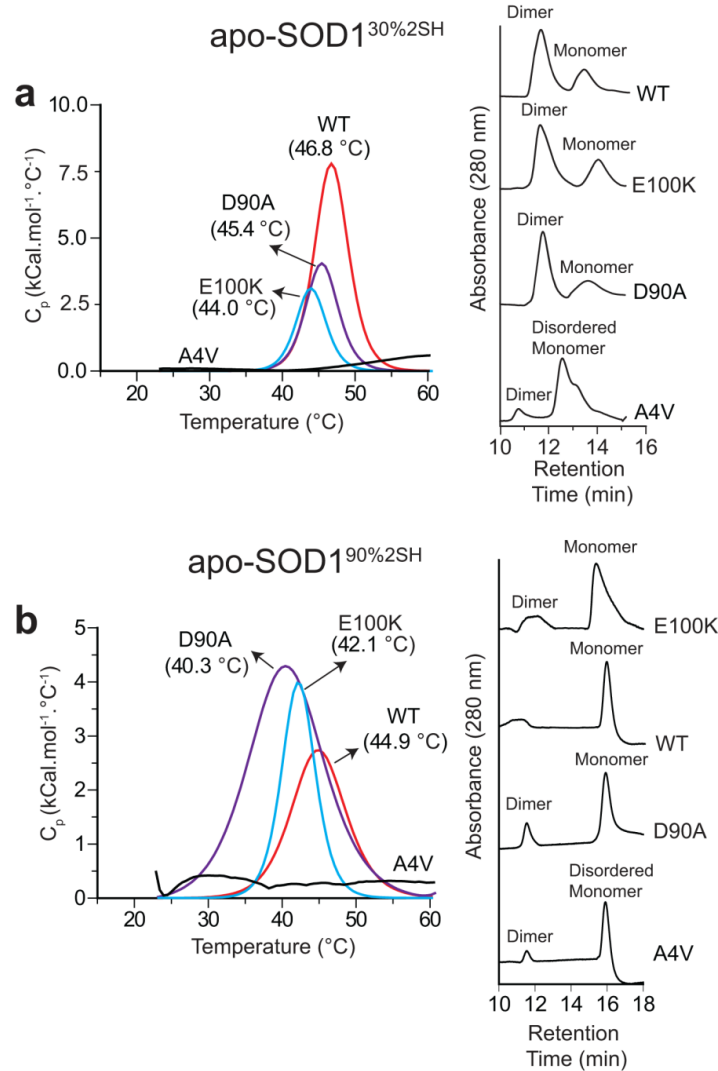


Figure 8.19 DSC thermograms and size-exclusion chromatograms of (a) apo-SOD1^{30%2SH} and (b) apo-SOD1^{90%2SH} after incubation in 10 and 100 mM TCEP for 6 hr, respectively. A4V did not exhibit a thermogram (flat line) because of its disordered state.⁷¹ Percents reduction was calculated based on area under curve (AUC) ratio of size-exclusion chromatograms for dimeric and monomeric apo-SOD1.

Apo-SOD1^{30%2SH}

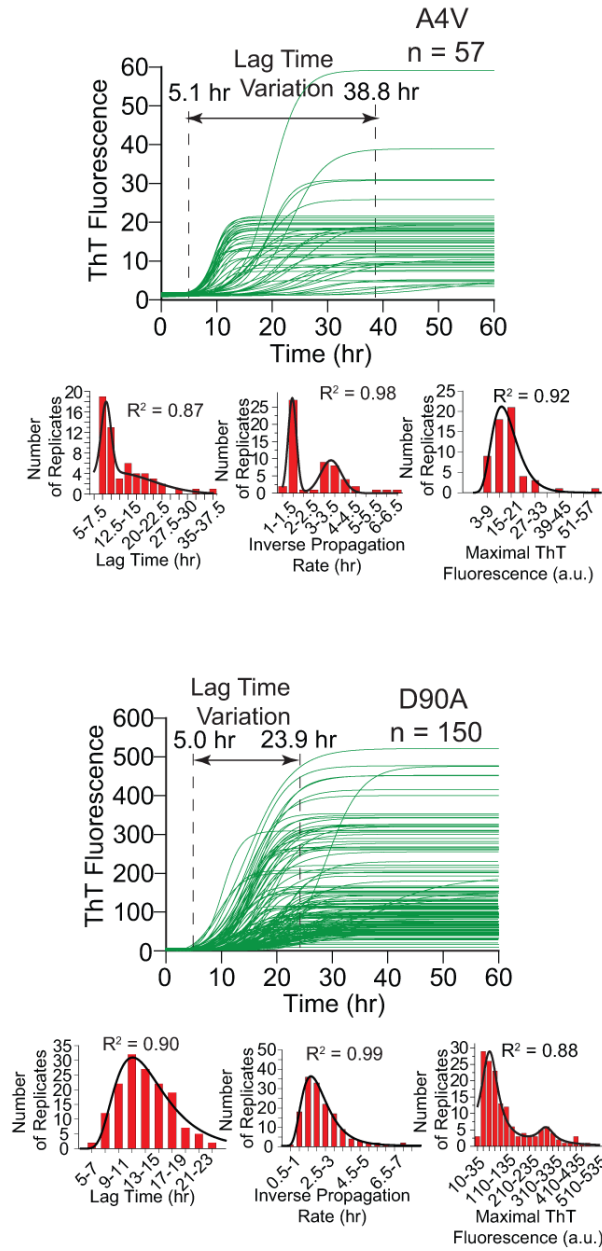


Figure 8.20 Sigmoidal fits of ThT fluorescence of replicate assays of A4V and D90A apo-SOD1^{30%2SH}. Histograms of iterate lag time, inverse propagation rate, and maximal ThT fluorescence are shown as insets below each plot.

Apo-SOD1^{90%2SH}

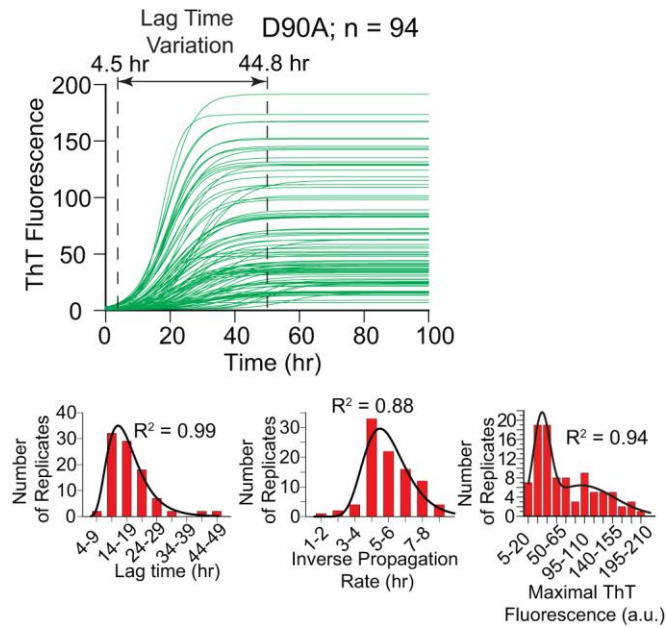
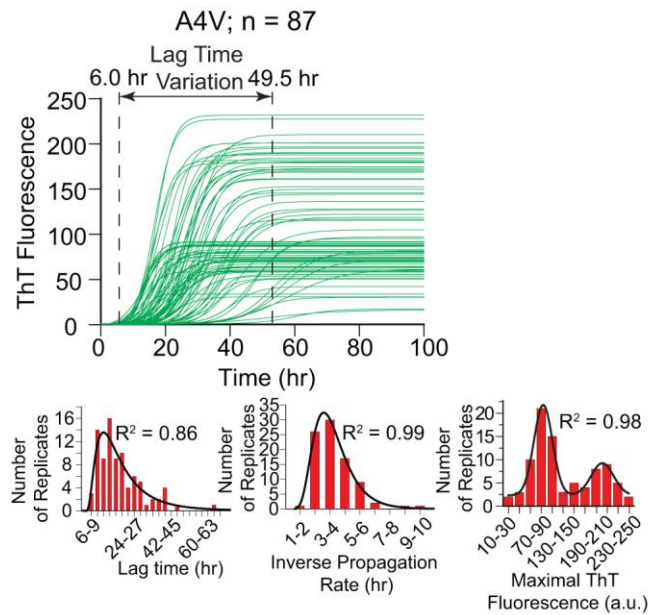


Figure 8.21 Sigmoidal fits of ThT fluorescence of replicate assays of A4V and D90A apo-SOD1^{90%2SH}. Histograms of iterate lag time, inverse propagation rate, and maximal ThT fluorescence are shown as insets below each plot.

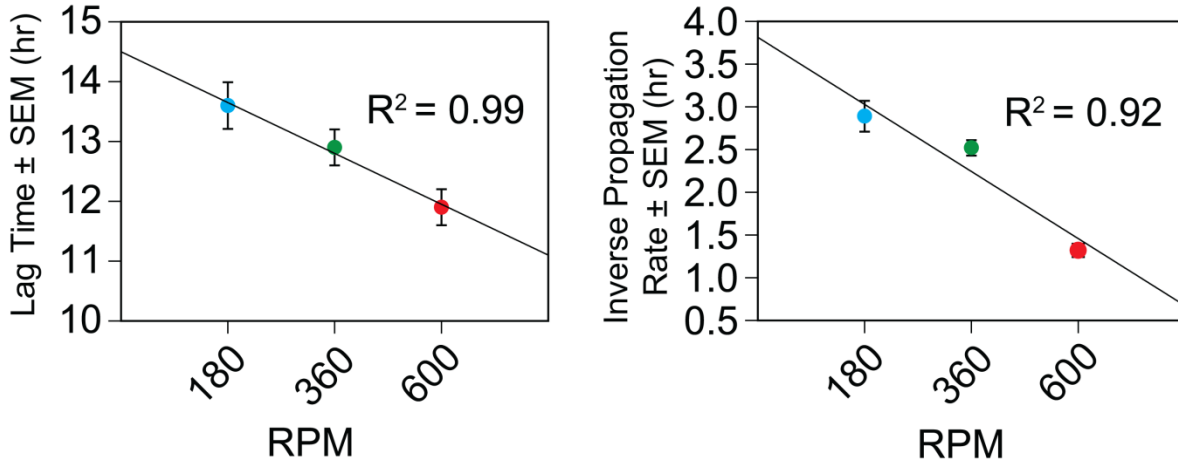


Figure 8.22 Average rate of nucleation and propagation of D90A apo-SOD1^{30%2SH} decreases linearly with increasing gyration speed.

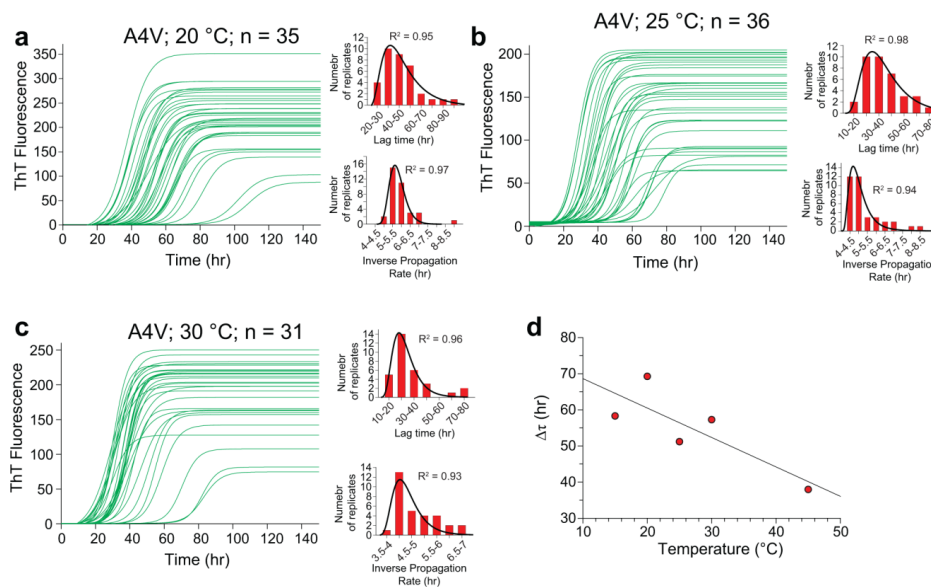


Figure 8.23 Fit traces of all replicates of ThT aggregation assays for A4V apo-SOD1^{90%2SH} in 100 mM TCEP at (a) T = 20 °C, (b) 25 °C, and (c) 30 °C (n_{total} = 102). Insets show the histograms of lag time and inverse propagation rate in each temperature. (d) Temperature-dependent range of lag time ($\Delta\tau$), i.e., the difference between maximum and minimum lag times (outlier replicates) in a single kinetic assay of A4V apo-SOD1^{90%2SH}. Histograms in (a-c) were fit with a 3-parameter log-normal function (Equation 8.8a).

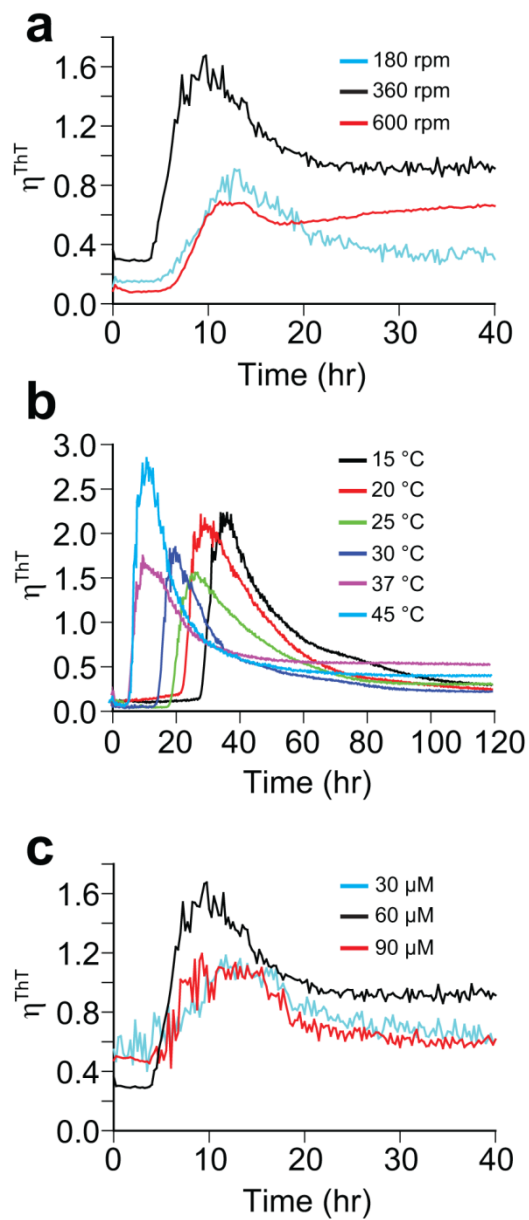


Figure 8.24 Noise plots of (a) D90A apo-SOD1^{30%2SH} during ThT assays at different shaking speeds, (b) ThT assays of A4V apo-SOD1^{90%2SH} at different temperatures, and (c) ThT assays of D90A apo-SOD1^{30%2SH} at different monomer concentrations.

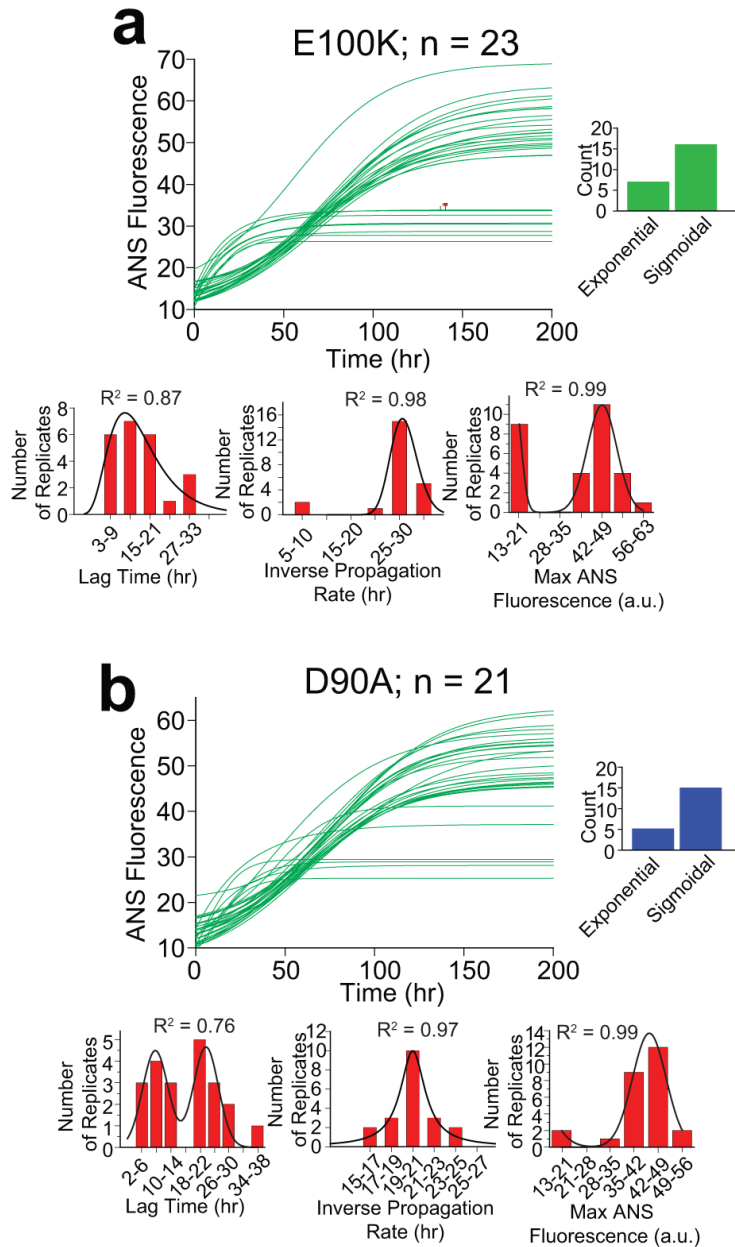


Figure 8.25 Plots of ANS fluorescence for **(a)** E100K, and **(b)** D90A apo-SOD1^{90%2SH} ($n_{\text{total}} = 44$). Insets below each plot illustrate the histograms for lag time and inverse propagation rate. Inset next to each plot shows the comparison between the number of exponential and sigmoidal traces.

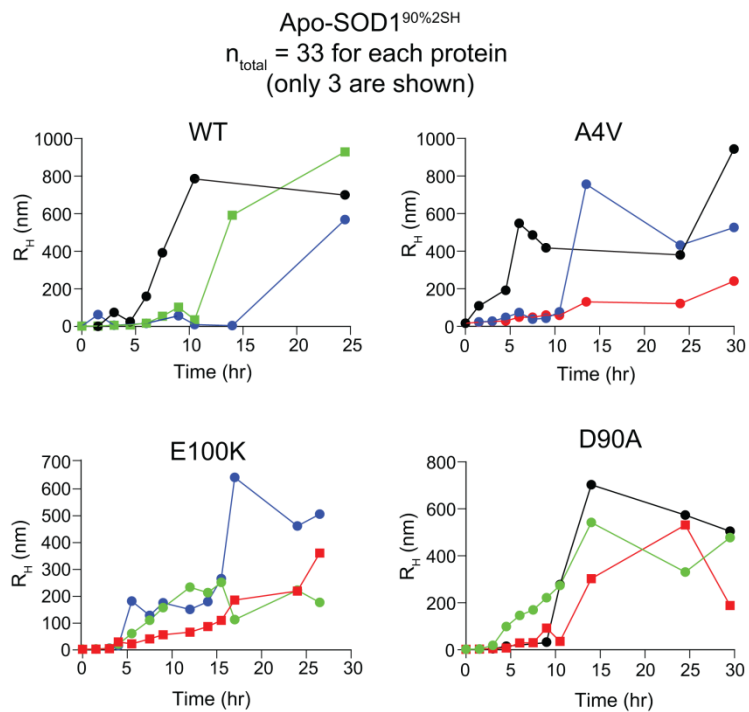


Figure 8.26 Selected replicate aggregation assays (as measured by DLS) for WT and three ALS-variant apo-SOD1^{90%2SH} proteins show a high degree of stochasticity among different replicates. R_H = hydrodynamic radius of all species in solution (including monomeric SOD1).

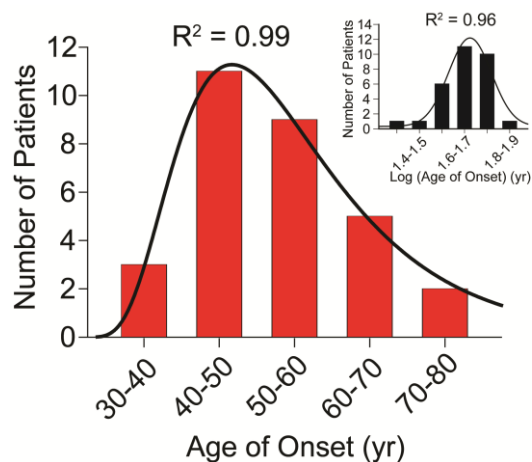


Figure 8.27 Histogram of age of disease onset for ALS patients with L144F *SOD1* mutation ($n = 30$) shows a log-normal distribution (fit with a 3-parameter log-normal function, Equation 8.8a). Inset shows the normal distribution of logarithm of age of disease onset data, which mathematically confirms the authenticity of observed log-normal behavior. Data for age of disease onset were taken from Abel et al.²⁹

Table 8.6 Metal content of WT and ALS-variant apo-SOD1 proteins before initiating the aggregation assay measured with ICP-MS.

apo-SOD1	Zn ²⁺ (per monomer)	Cu ²⁺ (per monomer)
WT	0.08	0.04
A4V	0.03	0.01
D90A	0.07	0.03
E100K	0.08	0.05

Table 8.7 Kinetic parameters of fibrillization of WT and ALS-variant apo-SOD1^{30%2SH} and apo-SOD1^{90%2SH} in 150 mM NaCl. Data are shown as mean \pm SEM. Average R² of sigmoidal fits for all replicate assays was 0.98.

SOD1 Variant	apo-SOD1 ^{30%2SH} (n _{total} = 410)			apo-SOD1 ^{90%2SH} (n _{total} = 345)		
	Lag time, (τ) (hr)	1/k, (hr)	f, (a.u.)	Lag time, (τ) (hr)	1/k, (hr)	f, (a.u.)
WT	12.9 \pm 0.4 (n = 88)	2.4 \pm 0.1	30.7 \pm 2.6	13.4 \pm 0.9 (n = 89)	5.6 \pm 0.2	45.3 \pm 3.6
A4V	12.35 \pm 0.9 (n = 57)	2.3 \pm 0.2	13.7 \pm 1.2	19.8 \pm 1.1 (n = 87)	3.8 \pm 0.1	110.7 \pm 6.1
E100K	11.2 \pm 0.5 (n = 107)	1.7 \pm 0.1	177.5 \pm 11.9	20.8 \pm 1.3 (n = 75)	7.3 \pm 0.2	44.6 \pm 3.9
D90A	12.8 \pm 0.3 (n = 150)	2.5 \pm 0.1	139.4 \pm 9.5	13.9 \pm 0.8 (n = 94)	5.9 \pm 0.1	65.9 \pm 4.9

Table 8.8 Kinetic parameters of aggregation of WT and ALS-variant apo-SOD1^{90%2SH} in 150 mM NaCl measured with ANS fluorescence. Data are shown as mean \pm SEM.

SOD1 Variant	Sigmoidal ^a (n _{total} = 71)			Exponential ^a (n _{total} = 21)	
	Lag time, (τ) (hr)	$1/k$, (hr)	f , (a.u.)	ϕ^b (hr)	δ^b (hr)
WT	12.6 \pm 2.0 (n = 18)	25.9 \pm 1.3	40.4 \pm 1.7	15.8 \pm 0.6 (n = 3)	0.072 \pm 0.003
A4V	18.7 \pm 1.7 (n = 20)	19.4 \pm 1.6	27.1 \pm 2.2	9.8 \pm 1.0 (n = 7)	0.070 \pm 0.007
E100K	12.2 \pm 1.6 (n = 17)	26.4 \pm 1.4	40.4 \pm 2.4	18.7 \pm 0.7 (n = 6)	0.049 \pm 0.004
D90A	14.4 \pm 2.0 (n = 16)	26.5 \pm 0.7	41.3 \pm 0.9	20.6 \pm 1.2 (n = 5)	0.047 \pm 0.005

^aAverage R² of sigmoidal fits for all replicate assays was 0.99.

^bExponential plots were fit with an exponential growth function using Equation 8.10.

Kaplan-Meier Meets Chemical Kinetics: Intrinsic Rate of SOD1 Amyloidogenesis Decreased by Subset of ALS Mutations and Cannot Fully Explain Age of Disease Onset.

Supporting Results and Discussion

Variations in Assay Conditions Cannot Explain the Discrepancies in Reported Rates of WT and ALS-Variant SOD1 Aggregation:

To determine if differences in assay conditions utilized by different research groups could affect discrepancies in reported rates of WT and ALS-variant SOD1 aggregation, we performed aggregation assays on E100G and G37R apo-SOD1 across a wide range of experimental conditions (e.g., pH 5.5-7.4, and gyration rates = 120-360 rpm). For example, G37R apo-SOD1 fibrillized 3-fold slower than WT at pH 5.5, whereas E100G apo-SOD1 showed statistically similar lag times to WT protein (Figure S5a,d). At pH 6.5, G37R apo-SOD1 fibrillized faster than WT apo-SOD1 (Figure S5b,e), whereas E100G and WT apo-SOD1 exhibit similar lag times at pH 6.5 (Figure S5b,e). Changing the agitation velocity of the microplate partially altered kinetic differences between WT and ALS-variant SOD1 fibrillization. Decreasing the agitation speed (by ~ 66 %; i.e., to 120 rpm) caused a ~ 2-fold decrease in the nucleation and propagation rate of WT and G37R apo-SOD1 proteins (Figure S5c,f). Mean lag times and propagation rates of fibrillization were statistically identical for both WT and G37R apo-SOD1 when shaken at 120 rpm (Figure S5c,f). Together, these results show that differences in assay conditions do not explain the discrepancies in rates of SOD1 aggregation in this study and previous reports.

Supporting Figures

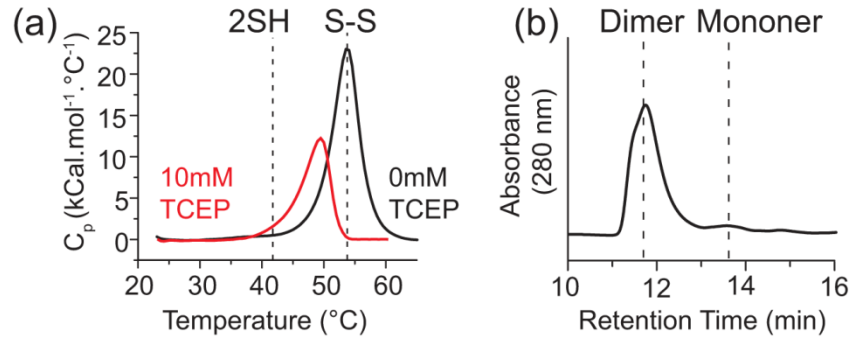


Figure 8.28 (a) DSC thermograms of fully disulfide oxidized (black) and partially reduced (red) WT apo-SOD1. (b) Size exclusion chromatogram of partially reduced WT apo-SOD1. Partial disulfide reduction (~ 10 %) was achieved by incubating fully oxidized WT apo-SOD1 in 10 mM TCEP for 30 min at 22 °C, without shaking. S-S: fully oxidized; 2SH: fully reduced.

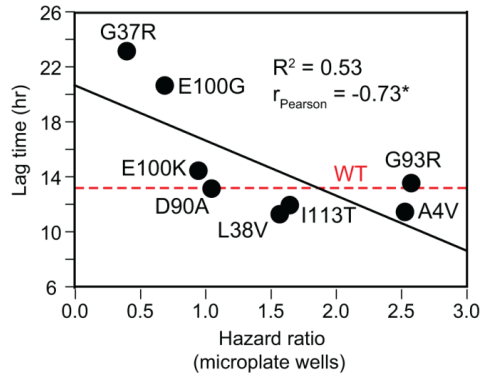


Figure 8.29 Correlation between mean lag times of apo-SOD1 fibrillization and Hazard ratios of apo-SOD1 fibrillization. Dashed red line indicates the lag time of WT apo-SOD1.

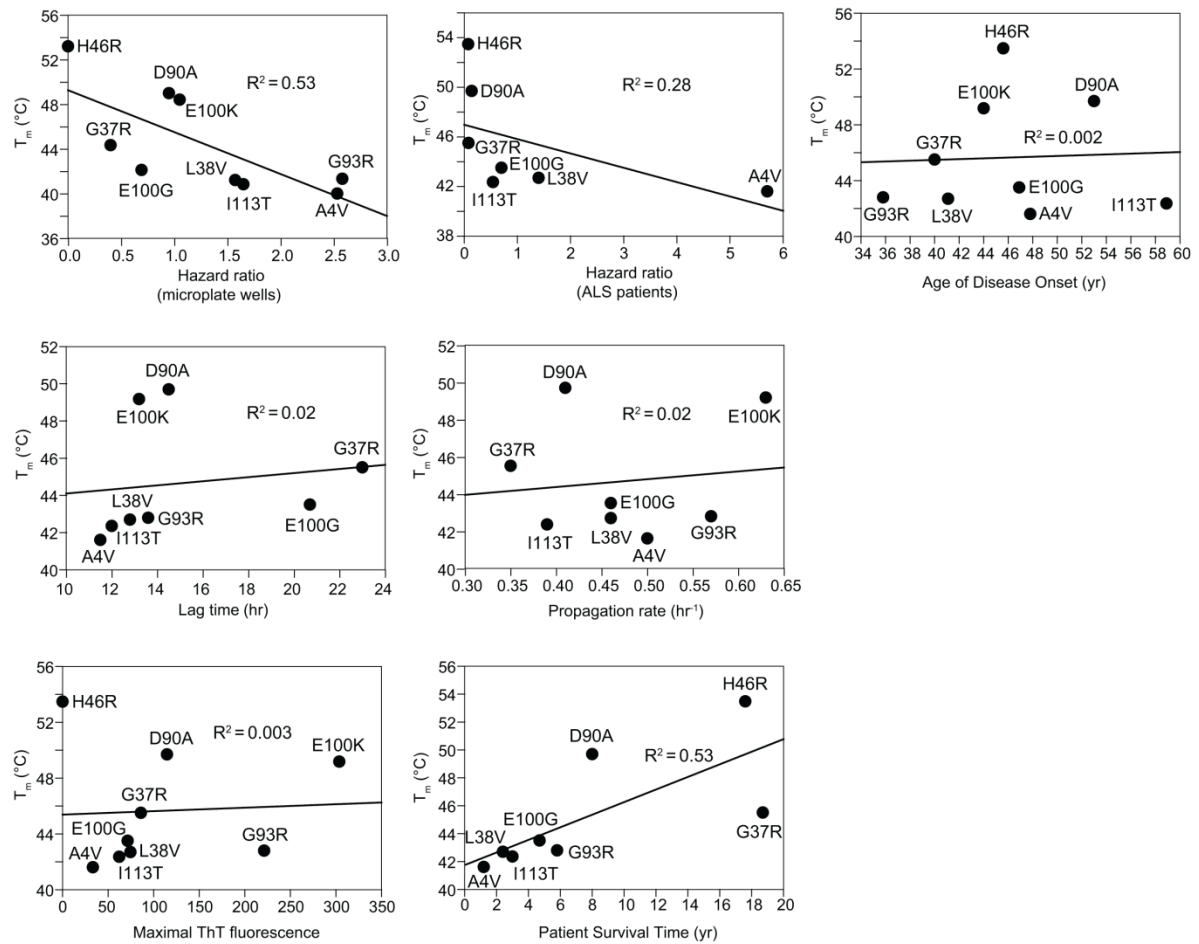


Figure 8.30 Correlations between mean lag time and propagation rate of *in vitro* apo-SOD1 fibrillization and clinical phenotypes of ALS patients. Dashed red lines indicate the lag time and propagation rate of WT apo-SOD1. Note: Hazard ratios are not available for G93R and E100K variants because of low patient number.

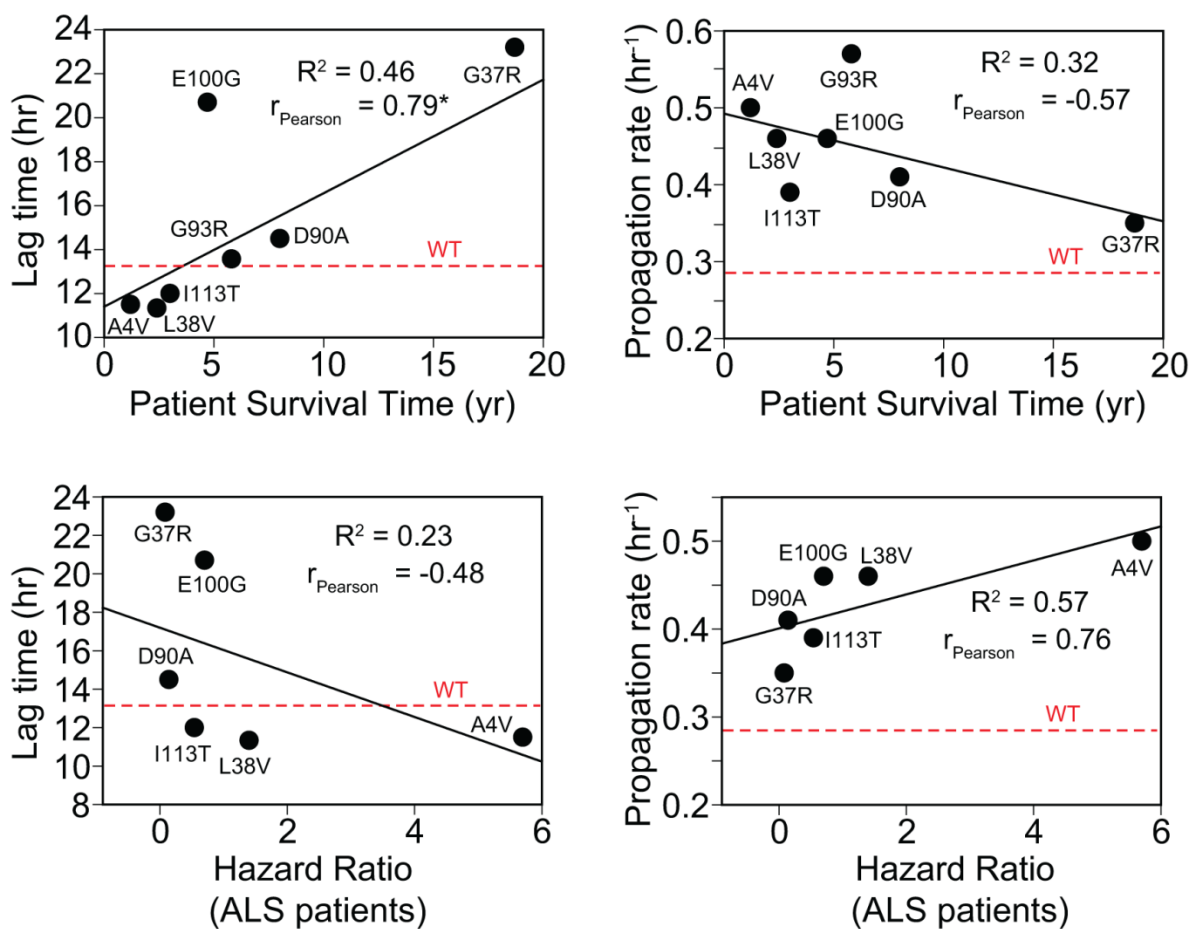


Figure 8.31 Correlation plots of thermostability of ALS variants of apo-SOD1, fibrillization rates, and clinical phenotypes. Plots of melting temperature of ALS variants of SOD1 versus *in vitro* kinetic parameters of SOD1 aggregation and clinical data from ALS patients.

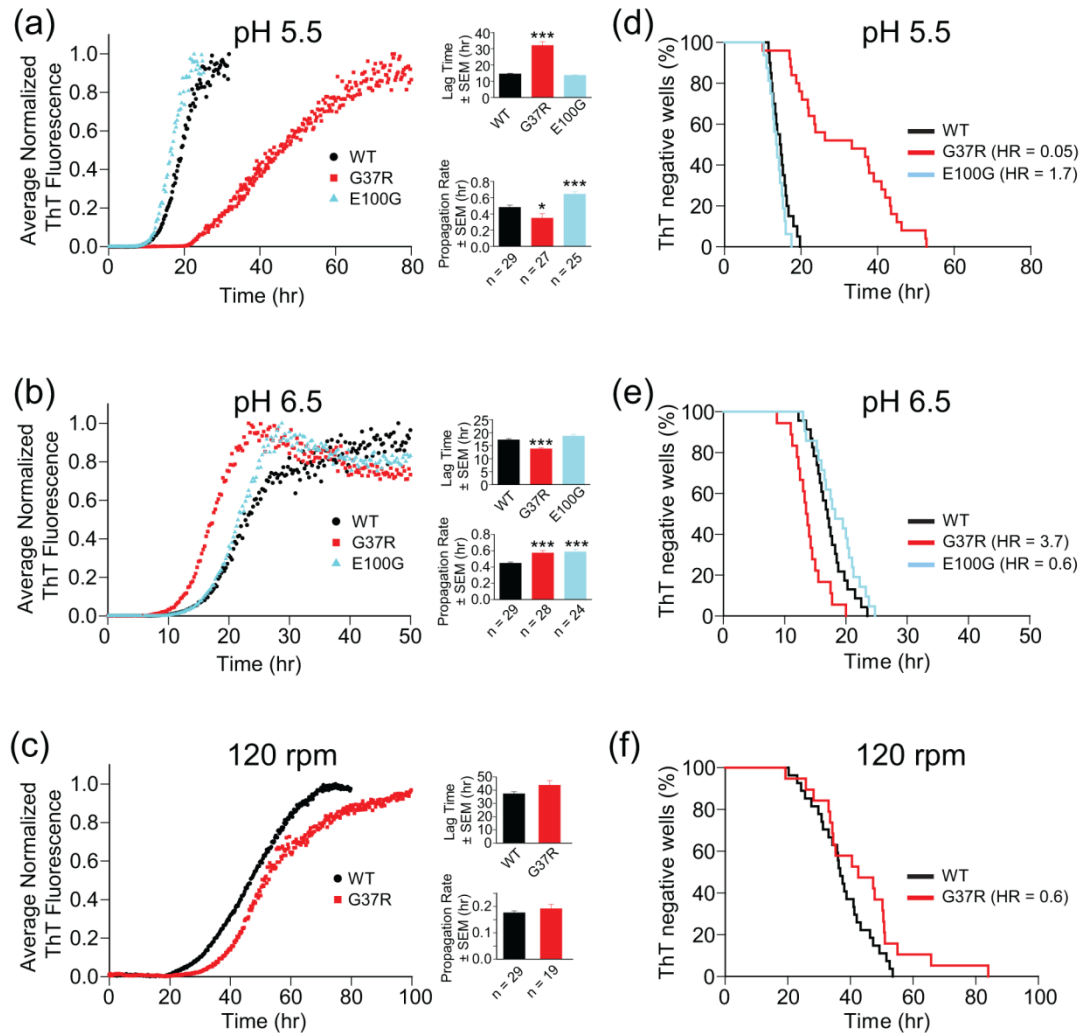


Figure 8.32 Rate of ALS mutant apo-SOD1 fibrillization remains equal to or slower than WT apo-SOD1 fibrillization under different experimental conditions. Average plots of ThT fluorescence for the fibrillization of WT, E100G, and G37R apo-SOD1 at (a) pH 5.5, (b) pH 6.5, and (c) WT and G37R under agitation speed of 120 rpm, pH 7.4 (all other experiments are performed at 360 rpm, unless otherwise stated). All experiments were performed at 37 °C (* = $p < 0.01$; *** = $p < 0.0001$). (d-f) Plots of Kaplan-Meier analysis for each reaction condition. HR: Hazard ratio.

How Do Gyration Beads Accelerate Amyloid Fibrillization?

Supporting Figures and Tables

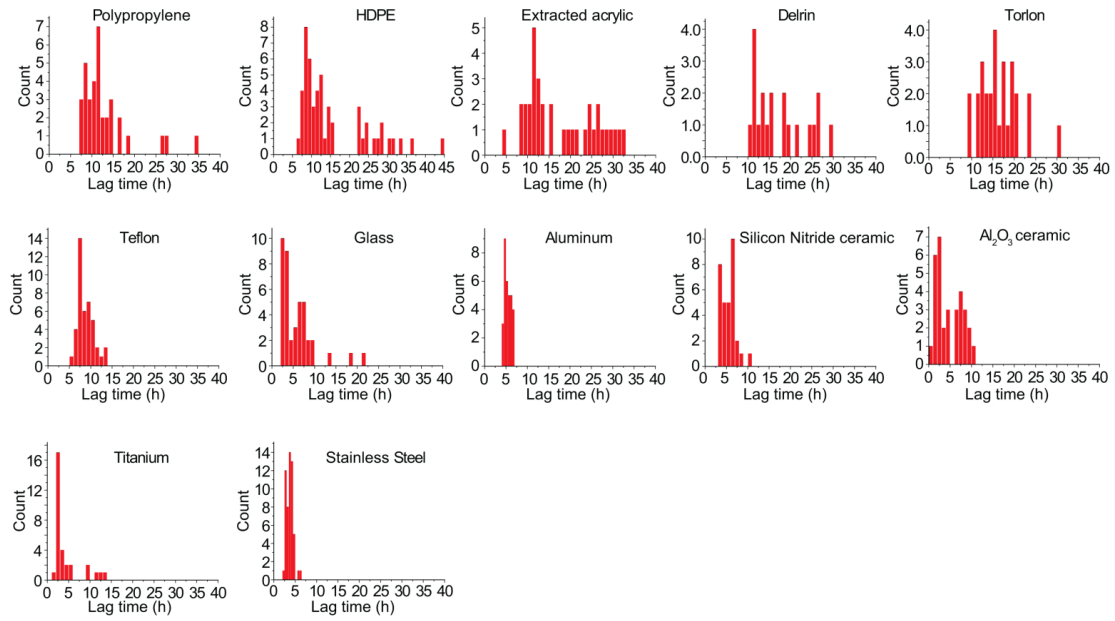


Figure 8.33 Histograms of lag time of D90A apo-SOD1 aggregation in the presence of different bead types.

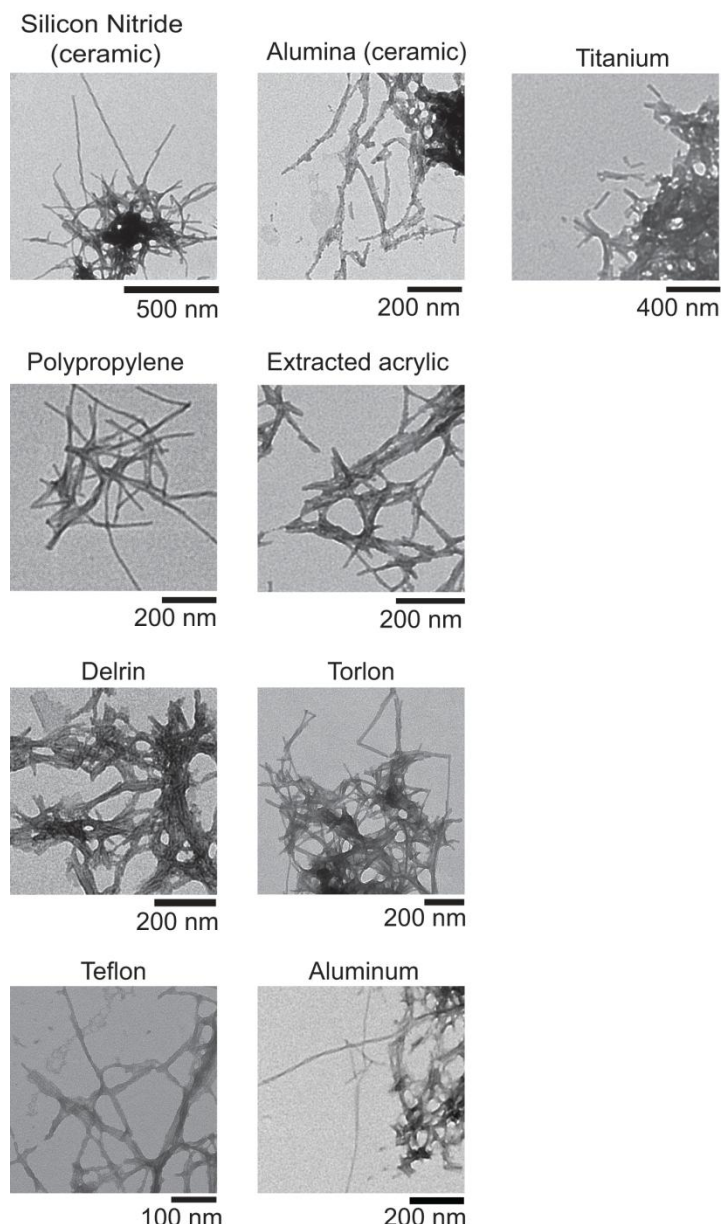


Figure 8.34 Transmission electron micrographs of D90A apo-SOD1 aggregates in the presence of different beads. TEM micrographs of apo-SOD1 fibrils in the presence of HDPE, glass, and steel beads are shown in the Figure 5.8A.

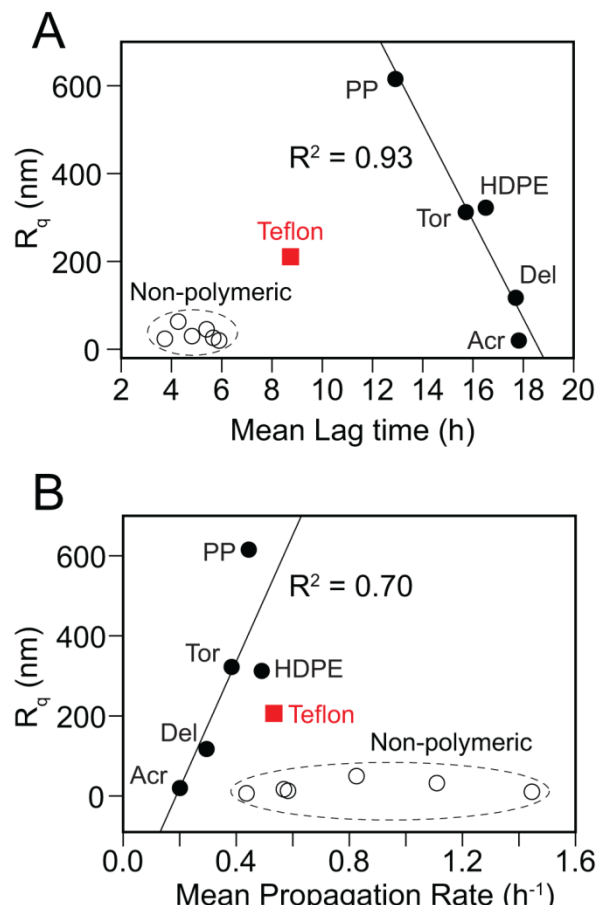


Figure 8.35 Correlation plots of bead surface roughness vs. (A) lag time, and (B) propagation rate of apo-SOD1 aggregation. Teflon was an outlier in this correlation and was excluded from fits in both plots.

Table 8.9 Physicomechanical properties of all studied beads in chapter five. Values for E^* , r , r' , p_g , and p_{cent} are calculated according to formalism described in the main text of chapter five (Equations 5.2-5.6).

Bead	E_1 (GPa)	ν_1	E^* (GPa) ^a	r (μm)	r' (μm)	p_g (kPa)	p_{cent} (kPa)
Polypropylene	1.2	0.45	1.07	69.5	137.2	—	29.9
HDPE	0.8	0.43	0.77	77.6	153.1	—	24.1
Extracted acrylic	2.5	0.40	1.65	66.2	130.6	3.6	43.9
Polyoxymethylene (Delrin)	2.8	0.35	1.71	67.4	133.0	6.9	46.4
Polyamide-imide (Torlon)	6.6	0.41	2.53	59.9	118.2	9.4	60.7
PTFE (Teflon)	0.5	0.46	0.54	115.2	227.3	6.9	25.1
Borosilicate glass	70	0.22	3.53	64.3	126.9	25.3	91.1
Aluminum	69	0.33	3.54	67.4	132.9	30.6	95.6
Silicon nitride (ceramic)	310	0.27	3.66	69.8	137.7	36.4	102.7
Alumina (ceramic)	300	0.21	3.66	74.1	146.2	40.9	108.9
Titanium	112.5	0.32	3.59	77.6	153.1	43.9	112.0
Stainless steel	200	0.31	3.64	94.1	185.7	60.4	137.6

^aValues for E^* are calculated from Equation 5.4 with $E_2 = 3.2$ GPa and $\nu_2 = 0.34$ for black polystyrene.

Metal Ion-Specific Screening of Charge Effects in Protein Amide H/D Exchange Follows the Hofmeister Series

Materials and Methods

Preparation of Lys-Acetyl Charge Ladders for Mb:

Approximately 100 mg of Mb (isolated from horse heart, Sigma-Aldrich®, St. Louis, MO, USA) was dissolved in 150 mL of 100 mM HEPBS buffer (N-(2-Hydroxyethyl)piperazine-N'-(4-butasulfonic acid)), pH 9.0. The resulting solution was divided into six fractions and increasing aliquots of 0.5 M acetic anhydride (prepared by dilution of pure acetic anhydride into 1,4-dioxane) were added to each of the six fractions. After acetylation, proteins were transferred to 100 mM citrate buffer (pH 7.4) using a centrifugal filtration device (5 kDa cutoff, Corning® Spin-X® UF, Corning, NY, USA). For this transfer, proteins were diluted ~ 20 fold into citrate buffer and concentrated. This concentration-dilution was repeated ~ 5 times and the final pH of the solution was measured to be pH 7.4. The six aliquots of progressively acetylated protein (Figure 1) were combined to obtain a 600 μ M Mb charge ladder in a 100 mM citrate buffer, which was stored at -80 °C in 50 μ L aliquots.

Hydrogen/Deuterium exchange measured by LC-ESI-MS:

In order to initiate H/D exchange, two 50 μ L samples of the Mb charge ladder were removed from the freezer, thawed and centrifugally concentrated at $3500 \times g$ for ~ 4 minutes using a centrifugal filtration device (5 kDa cutoff). The final concentration of Mb was 1.2 mM using UV-Vis spectroscopy ($\lambda_{\text{max}} = 280 \text{ nm}$, $\epsilon = 13,940 \text{ M}^{-1} \cdot \text{cm}^{-1}$). A 45 μ L aliquot of this Mb-Ac solution was added to 405 μ L of 50 mM Tris-DCI (pH 7.4) in 99.9

% D₂O (Cambridge Isotope Laboratories, Inc., Tewksbury, MA, USA). At the desired time point of the H/D exchange reaction (i.e., 5, 10, 15, 25, 35, 45, 60, 70, and 80 min) three aliquots (10 μL each) were flash frozen in liquid nitrogen (to quench H/D exchange) and stored at -80 °C for < 6 hours until mass spectrometric analysis.

Protein solutions that were frozen at various time points were removed from the freezer and instantly thawed, followed by the addition of 190 μL of ice-chilled 0.3 % formic acid to the 10 μL protein solution (i.e., a 1:20 dilution). The samples were then immediately injected into the LC-ESI-MS. We used a Waters Synapt ESI-HDMS (Waters Inc., Manchester, UK) to measure H/D exchange. The ESI-MS capillary voltage was 3.5 kV and the source temperature was 120 °C. At the end of the H/D exchange experiment, we also generated perdeuterated charge ladders (to quantify back-exchange) by heating 40 μL of Mb-Ac/D₂O solutions in a Peltier device (Mastercycler® pro, Eppendorf, Hauppauge, NY, USA) at 70 °C for 10 minutes. Each sample was then equilibrated to room temperature (23 °C), from which a 20 μL aliquot of the denatured sample was injected into the ESI-MS after adding 380 μL (i.e., a 1:20 dilution) of ice-chilled 0.3 % formic acid solution.

The front of the mass spectrometer was equipped with a Rheodyne® valve that was submerged in ice, with a front syringe injection port. A 1 cm protein desalting column (Michrom BioResources, Inc., Auburn, CA, USA) was placed between the valve and the MS to trap the Mb-Ac and to permit the desalting of protein solutions prior to MS. After trapping the Mb-Ac, the column was rapidly washed with 1.5 mL of ice-chilled 0.3 % formic acid solution (in less than 10 seconds) in order to remove any salt or buffer residuals.

The Mb-Ac proteins were eluted from the HPLC column with the following mixture: 60 % acetonitrile/40 % of 0.3 % formic acid solution in water. The flow rate of the HPLC system was 400 $\mu\text{L}/\text{min}$. The resulting mass spectra were deconvoluted using the ProMass feature within XcaliburTM (Novatia LLC., Newtown, PA, USA). The entire process of thawing solutions, desalting, and MS analysis required approximately 5 min and could be reproduced at a variability of ± 1 min.

Adjustment of pH of Mb Solutions upon the Addition of Hofmeister Cations:

In order to counteract the drift of pH upon the addition of cations to D₂O solutions, 50 mM Tris-DCl was incorporated into all of the D₂O/Hofmeister solutions made, allowing for more accurate readings from the pH electrode. The pD of each deuterated salt solution was verified to be at pD 7.8 before H/D exchange. The values of pD reported in this chapter for salt solutions are values of pH_{read} (reported by the pH meter) with a correction of 0.4 units added to the measured value.

Results and Discussion

Myoglobin Retains Its Heme Group upon Acetylation:

The thermogram of unacetylated and acetylated Mb (Figure 6.2E) exhibited a $T_m = 80$ °C (for Mb-Ac(0)) and $T_m = 68$ °C for (Mb-Ac(~16)), which confirmed that myoglobin was in its holo state (the T_m of unacetylated apo-Mb = 63 °C³²¹). The 12 °C reduction in T_m of holo-Mb that occurred upon acetylation does not suggest that acetylation dissociated the heme group.

These magnitudes of destabilization have been observed for other non-heme proteins.⁸⁶ Moreover, Mb retained its holo-state upon acetylation as measured by the peak at $\lambda_{\max} = 408$ nm in UV-Vis spectra (Figure 8.37).

Supporting Figures

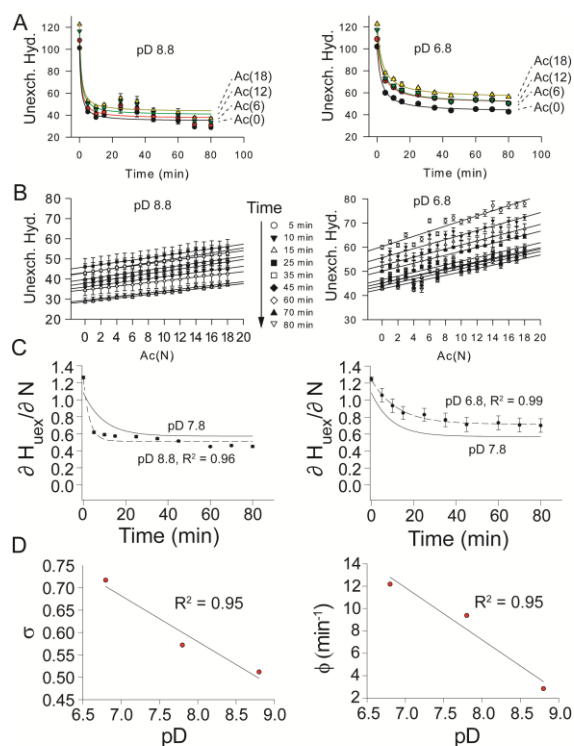


Figure 8.36 Amide H/D exchange of Mb-Lys-Ac(N) charge ladder measured at different pH with mass spectrometry (left column = pD 8.8; right column = pD 6.8). **(A)** Plots of H/D exchange as a function of time (0 M Hofmeister salt); pD = 7.8. Error bars are the standard deviation of three separate measurements. **(B)** Plots of the number of unexchanged hydrogens in each rung of the Mb charge ladder at each time point (5 min to 80 min in D₂O) versus the acetylation number, i.e., a plot of $\partial H_{\text{uex}}/\partial N$ for all 19 rungs. Error bars are the same standard deviation shown in part (A). **(C)** Plots of $\partial H_{\text{uex}}/\partial N$ (the slope of each line in part (A)) as a function of time. Error bars are the standard errors associated with the linear fit of $\partial H_{\text{uex}}/\partial N$ points from part (B). The longitudinal plot of $\partial H_{\text{uex}}/\partial N$ at pD 7.8 is shown as a solid black line in both panels as reference. **(D)** Plots of “penetration” constant (σ) and “shielding” decay constant (ϕ) as a function of pD.

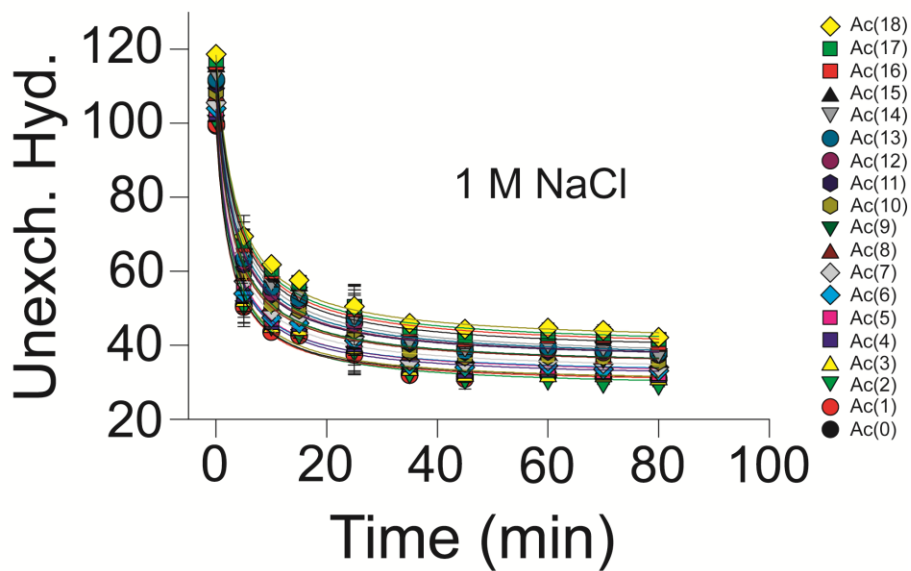
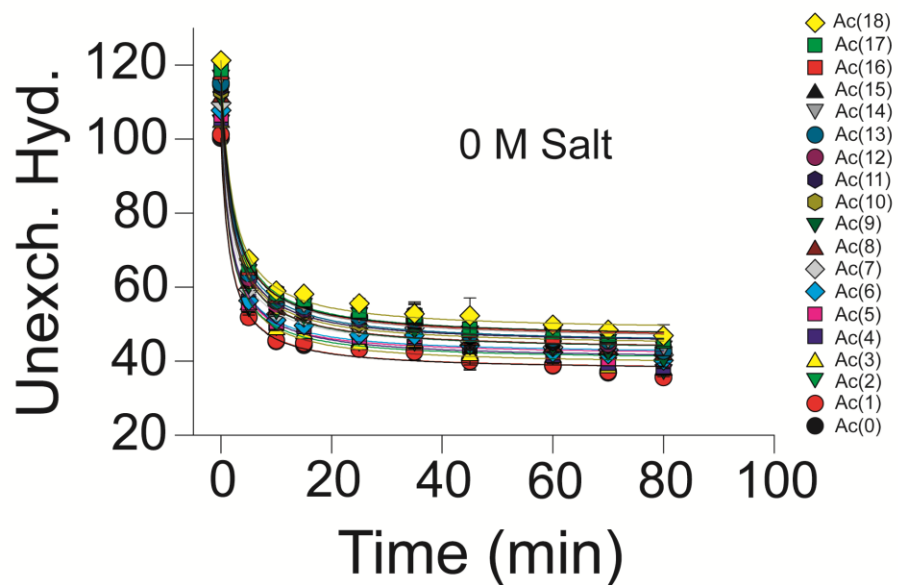


Figure 8.37 Amide H/D exchange for all 19 rungs of the Mb charge ladder in the (A) absence and (B) presence of 1 M NaCl; pD = 7.8.

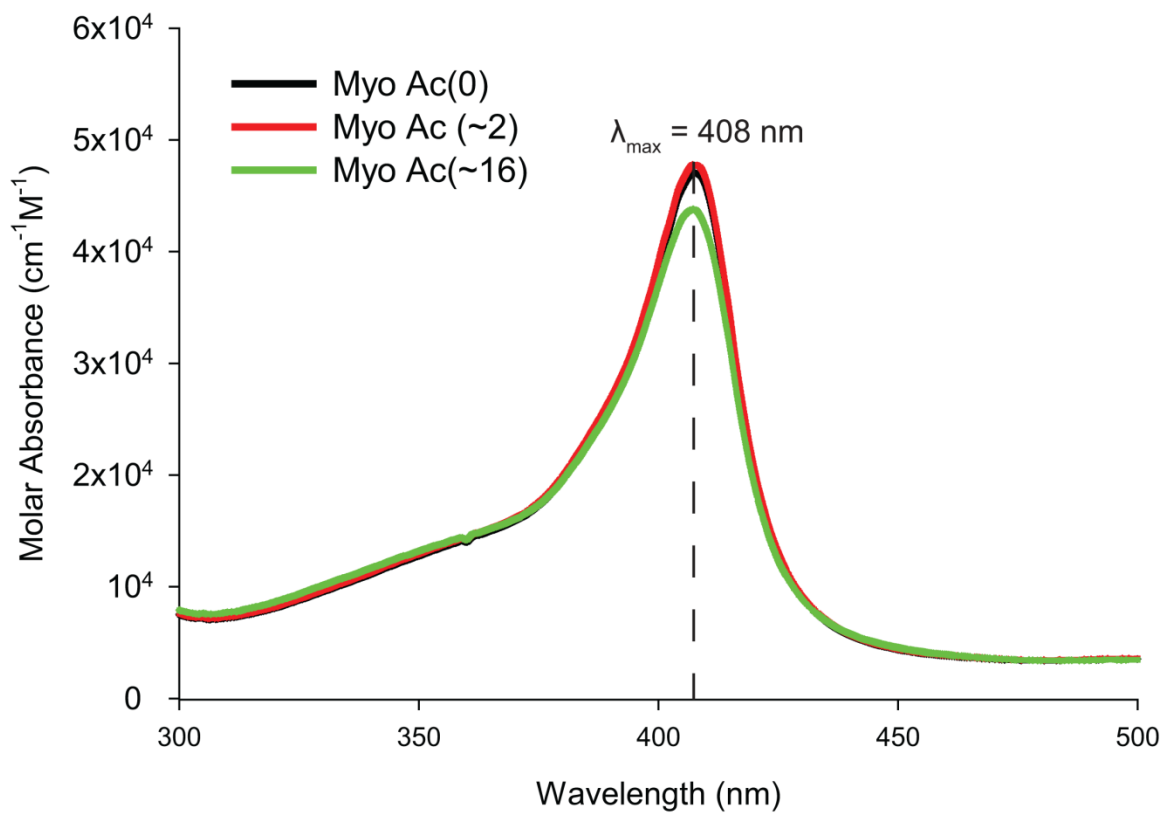


Figure 8.38 UV-Vis spectra of Mb-Ac(0) and Mb-Ac(~16). The peak at $\lambda_{\text{max}} = 408$ nm confirmed the presence of the prosthetic heme group in Mb, and that acetylation does not cause the heme group to dissociate from Mb.

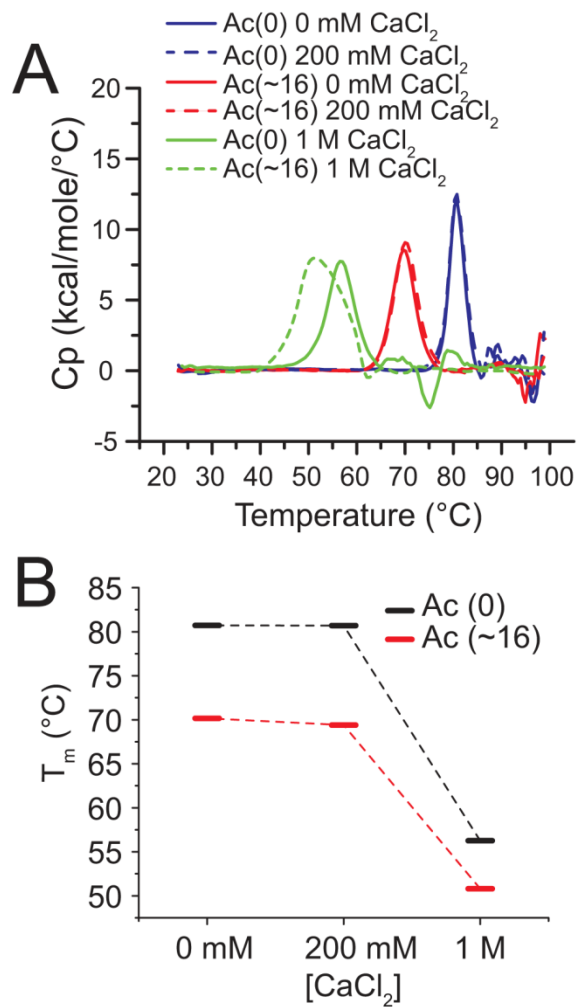


Figure 8.39 (A) Differential scanning calorimetry of unacetylated and acetylated (i.e., Ac(~16)) Mb in the presence of 0 M, 200 mM, and 1 M CaCl_2 . (B) Plot of T_m values of unacetylated and acetylated Mb as a function of CaCl_2 concentration.

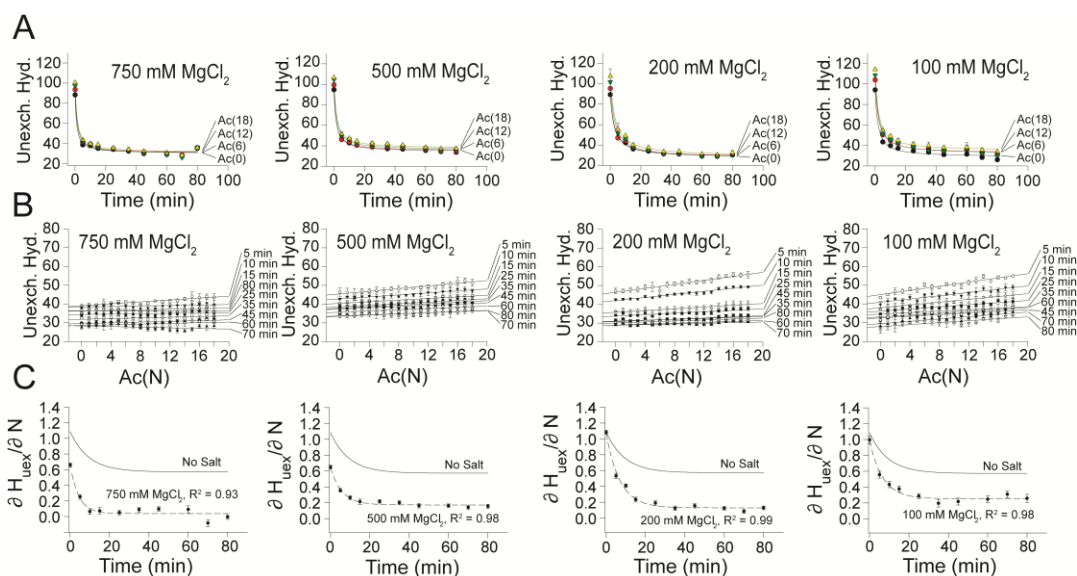


Figure 8.40 (A) Amide H/D exchange of Mb-Lys-Ac(N) charge ladder at diminishing concentrations of MgCl₂. Error bars represent standard deviation from three separate measurements. (B) Partial derivatives of plots in part (A); error bars represent the standard deviation of three separate runs. (C) Plots of partial derivative as a function of time; in each panel, solid line represents partial derivative of Mb-Lys-Ac(N) charge ladder in 0 mM Mg²⁺ shown for reference. Error bars are the standard errors associated with the linear fit of $\partial H_{\text{uex}}/\partial N$ points from panel (B).

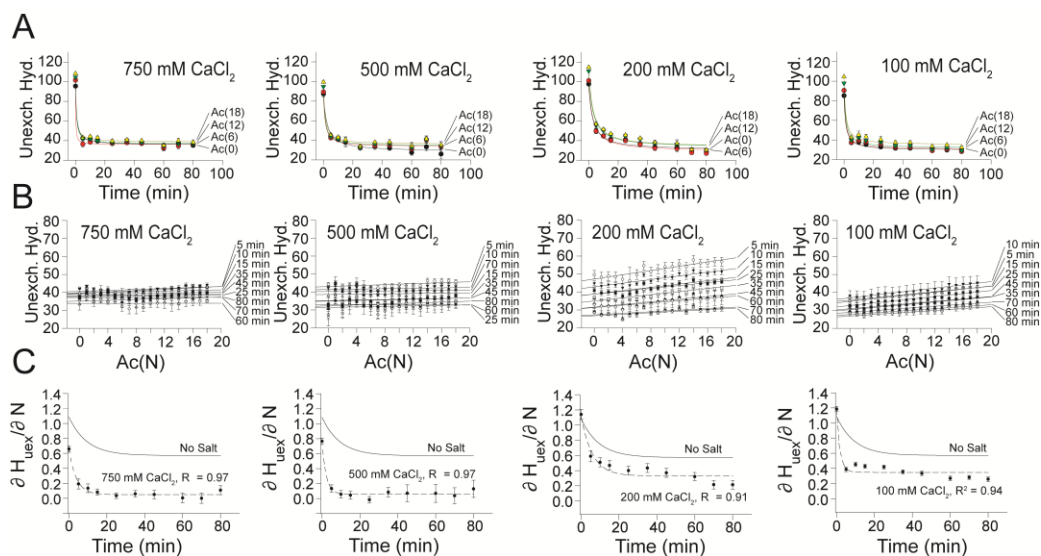


Figure 8.41 (A) Amide H/D exchange of Mb-Lys-Ac(N) charge ladder at diminishing concentrations of Ca^{2+} . Error bars represent standard deviation from three separate measurements. (B) Partial derivatives of plots in part (A); error bars represent the standard deviation of three separate runs. (C) Plots of partial derivative as a function of time; solid line in each panel represents partial derivative of Mb-Lys-Ac(N) charge ladder in 0 mM Ca^{2+} shown as reference. Error bars represent standard error from the linear fit in part (B).

REFERENCES

1. Skovronsky, D. M., Lee, V. M., Trojanowski, J. Q. (2006) Neurodegenerative diseases: new concepts of pathogenesis and their therapeutic implications. *Annu Rev Pathol. 1*, 151-170.
2. Ramanan, V. K., Saykin, A. J. (2013) Pathways to neurodegeneration: mechanistic insights from GWAS in Alzheimer's disease, Parkinson's disease, and related disorders. *Am J Neurodegener Dis. 2*, 145-175.
3. Wada, K., *Neurodegenerative disorders as systemic diseases*. p viii, 304 pages.
4. Selkoe, D. J., Hardy, J. (2016) The amyloid hypothesis of Alzheimer's disease at 25 years. *Embo Mol. Med. 8*, 595-608.
5. FINDER, V. H., GLOCKSHUBER, R. (2007) Amyloid- β aggregation. *Neurodegener Dis. 4*, 13-27.
6. Taylor, J. P., Brown, R. H., Cleveland, D. W. (2016) Decoding ALS: from genes to mechanism. *Nature. 539*, 197-206.
7. Rosen, D. R. (1993) Mutations in Cu/Zn superoxide dismutase gene are associated with familial amyotrophic lateral sclerosis. *Nature. 362*, 59-62.
8. Giraldez-Perez, R., Antolin-Vallespin, M., Munoz, M., Sanchez-Capelo, A. (2014) Models of α -synuclein aggregation in Parkinson's disease. *Acta Neuropathol Commun. 2*, 176.
9. Knowles, T. P. J., Waudby, C. A., Devlin, G. L., Cohen, S. I. A., Aguzzi, A., Vendruscolo, M., Terentjev, E. M., Welland, M. E., Dobson, C. M. (2009) An analytical solution to the kinetics of breakable filament assembly. *Science. 326*, 1533-1537.
10. Knowles, T. P., Vendruscolo, M., Dobson, C. M. (2014) The amyloid state and its association with protein misfolding diseases. *Nat Rev Mol Cell Biol. 15*, 384-396.
11. Nelson, R., Sawaya, M. R., Balbirnie, M., Madsen, A. O., Riek, C., Grothe, R., Eisenberg, D. (2005) Structure of the cross- β spine of amyloid-like fibrils. *Nature. 435*, 773-778.
12. Sipe, J. D., Cohen, A. S. (2000) Review: history of the amyloid fibril. *J Struct Biol. 130*, 88-98.

13. Sawaya, M. R. et al. (2007) Atomic structures of amyloid cross- β spines reveal varied steric zippers. *Nature*. 447, 453-457.
14. Eisenberg, D., Jucker, M. (2012) The amyloid state of proteins in human diseases. *Cell*. 148, 1188-1203.
15. Sangwan, S., Zhao, A., Adams, K. L., Jayson, C. K., Sawaya, M. R., Guenther, E. L., Pan, A. C., Ngo, J., Moore, D. M., Soriaga, A. B., Do, T. D., Goldschmidt, L., Nelson, R., Bowers, M. T., Koehler, C. M., Shaw, D. E., Novitch, B. G., Eisenberg, D. S. (2017) Atomic structure of a toxic, oligomeric segment of SOD1 linked to amyotrophic lateral sclerosis (ALS). *Proc Natl Acad Sci U S A*. 114, 8770-8775.
16. Ivanova, M. I., Sievers, S. A., Guenther, E. L., Johnson, L. M., Winkler, D. D., Galaleldeen, A., Sawaya, M. R., Hart, P. J., Eisenberg, D. S. (2014) Aggregation-triggering segments of SOD1 fibril formation support a common pathway for familial and sporadic ALS. *Proc Natl Acad Sci U S A*. 111, 197-201.
17. Fink, A. L. (1998) Protein aggregation: folding aggregates, inclusion bodies and amyloid. *Fold Des*. 3, R9-23.
18. Kerman, A., Liu, H. N., Croul, S., Bilbao, J., Rogaeva, E., Zinman, L., Robertson, J., Chakrabarty, A. (2010) Amyotrophic lateral sclerosis is a non-amyloid disease in which extensive misfolding of SOD1 is unique to the familial form. *Acta Neuropathol*. 119, 335-344.
19. Yoshimura, Y., Lin, Y., Yagi, H., Lee, Y. H., Kitayama, H., Sakurai, K., So, M., Ogi, H., Naiki, H., Goto, Y. (2012) Distinguishing crystal-like amyloid fibrils and glass-like amorphous aggregates from their kinetics of formation. *Proc Natl Acad Sci U S A*. 109, 14446-14451.
20. Pigino, G., Morfini, G., Atagi, Y., Deshpande, A., Yu, C., Jungbauer, L., LaDu, M., Busciglio, J., Brady, S. (2009) Disruption of fast axonal transport is a pathogenic mechanism for intraneuronal amyloid beta. *Proc Natl Acad Sci U S A*. 106, 5907-5912.
21. Bucciantini, M. et al. (2012) Toxic effects of amyloid fibrils on cell membranes: the importance of ganglioside GM1. *FASEB J*. 26, 818-831.
22. Espargaro, A., Busquets, M. A., Estelrich, J., Sabate, R. (2016) Key points concerning amyloid infectivity and prion-like neuronal invasion. *Front Mol Neurosci*. 9, 29.
23. Brundin, P., Melki, R., Kopito, R. (2010) Prion-like transmission of protein aggregates in neurodegenerative diseases. *Nat Rev Mol Cell Biol*. 11, 301-307.

24. Laganowsky, A., Liu, C., Sawaya, M. R., Whitelegge, J. P., Park, J., Zhao, M., Pensalfini, A., Soriaga, A. B., Landau, M., Teng, P. K., Cascio, D., Glabe, C., Eisenberg, D. (2012) Atomic view of a toxic amyloid small oligomer. *Science*. 335, 1228-1231.
25. Jiang, L., Liu, C., Leibly, D., Landau, M., Zhao, M., Hughes, M. P., Eisenberg, D. S. (2013) Structure-based discovery of fiber-binding compounds that reduce the cytotoxicity of amyloid beta. *Elife*. 2, e00857.
26. Shaw, B. F., Valentine, J. S. (2007) How do ALS-associated mutations in superoxide dismutase 1 promote aggregation of the protein? *Trends Biochem Sci*. 32, 78-85.
27. Rakhit, R., Chakrabartty, A. (2006) Structure, folding, and misfolding of Cu,Zn superoxide dismutase in amyotrophic lateral sclerosis. *Biochim Biophys Acta*. 1762, 1025-1037.
28. Forman, H. J., Fridovich, I. (1973) On the stability of bovine superoxide dismutase. The effects of metals. *J Biol Chem*. 248, 2645-2649.
29. Abel, O., Shatunov, A., Jones, A. R., Andersen, P. M., Powell, J. F., Al-Chalabi, A. (2013) Development of a smartphone App for a genetics website: the amyotrophic lateral sclerosis online genetics database (ALSoD). *JMIR Mhealth Uhealth*. 1, e18.
30. Rodriguez, J. A., Shaw, B. F., Durazo, A., Sohn, S. H., Doucette, P. A., Nersissian, A. M., Faull, K. F., Eggers, D. K., Tiwari, A., Hayward, L. J., Valentine, J. S. (2005) Destabilization of apoprotein is insufficient to explain Cu,Zn-superoxide dismutase-linked ALS pathogenesis. *Proc Natl Acad Sci U S A*. 102, 10516-10521.
31. Shaw, B. F., Moustakas, D. T., Whitelegge, J. P., Faull, K. F. (2010) Taking charge of proteins from neurodegeneration to industrial biotechnology. *Adv Protein Chem Struct Biol*. 79, 127-164.
32. Bunton-Stasyshyn, R. K., Saccon, R. A., Fratta, P., Fisher, E. M. (2015) SOD1 function and its implications for amyotrophic lateral sclerosis pathology: new and renascent themes. *Neuroscientist*. 21, 519-529.
33. Saccon, R. A., Bunton-Stasyshyn, R. K. A., Fisher, E. M. C., Fratta, P. (2013) Is SOD1 loss of function involved in amyotrophic lateral sclerosis? *Brain*. 136, 2342-2358.
34. Reaume, A. G. et al. (1996) Motor neurons in Cu/Zn superoxide dismutase-deficient mice develop normally but exhibit enhanced cell death after axonal injury. *Nat Genet*. 13, 43-47.

35. Lindberg, M. J., Tibell, L., Oliveberg, M. (2002) Common denominator of Cu/Zn superoxide dismutase mutants associated with amyotrophic lateral sclerosis: decreased stability of the apo state. *Proc Natl Acad Sci U S A.* 99, 16607-16612.
36. Chiti, F., Stefani, M., Taddei, N., Ramponi, G., Dobson, C. M. (2003) Rationalization of the effects of mutations on peptide and protein aggregation rates. *Nature.* 424, 805-808.
37. Jahn, T. R., Radford, S. E. (2008) Folding versus aggregation: polypeptide conformations on competing pathways. *Arch Biochem Biophys.* 469, 100-117.
38. Thompson, D. B., Cronican, J. J., Liu, D. R. (2012) Engineering and identifying supercharged proteins for macromolecule delivery into mammalian cells. *Methods Enzymol.* 503, 293-319.
39. Osborne, T. B. (1902) The basic character of the protien molecule and the reactions of edestin with definite quantities of acids and alkalies. *J Am Chem Soc.* 24, 39-78.
40. Felder, C. E., Prilusky, J., Silman, I., Sussman, J. L. (2007) A server and database for dipole moments of proteins. *Nucleic Acids Res.* 35, W512-521.
41. Shi, Y., Abdolvahabi, A., Shaw, B. F. (2014) Protein charge ladders reveal that the net charge of ALS-linked superoxide dismutase can be different in sign and magnitude from predicted values. *Protein Sci.* 23, 1417-1433.
42. McNaughton, B. R., Cronican, J. J., Thompson, D. B., Liu, D. R. (2009) Mammalian cell penetration, siRNA transfection, and DNA transfection by supercharged proteins. *Proc Natl Acad Sci U S A.* 106, 6111-6116.
43. Lee, S., Kim, H. J. (2015) Prion-like mechanism in amyotrophic lateral sclerosis: are protein aggregates the key? *Exp Neurobiol.* 24, 1-7.
44. Munch, C., O'Brien, J., Bertolotti, A. (2011) Prion-like propagation of mutant superoxide dismutase-1 misfolding in neuronal cells. *Proc Natl Acad Sci U S A.* 108, 3548-3553.
45. Abdolvahabi, A., Shi, Y., Rhodes, N. R., Cook, N. P., Marti, A. A., Shaw, B. F. (2015) Arresting amyloid with Coulomb's law: acetylation of ALS-linked SOD1 by aspirin impedes aggregation. *Biophys J.* 108, 1199-1212.
46. Roberts, D., Keeling, R., Tracka, M., van der Walle, C. F., Uddin, S., Warwicker, J., Curtis, R. (2014) The role of electrostatics in protein-protein interactions of a monoclonal antibody. *Mol Pharm.* 11, 2475-2489.

47. Gitlin, I., Carbeck, J. D., Whitesides, G. M. (2006) Why are proteins charged? Networks of charge-charge interactions in proteins measured by charge ladders and capillary electrophoresis. *Angewandte Chemie*. 45, 3022-3060.
48. Lessene, G., Czabotar, P. E., Sleebs, B. E., Zobel, K., Lowes, K. N., Adams, J. M., Baell, J. B., Colman, P. M., Deshayes, K., Fairbrother, W. J., Flygare, J. A., Gibbons, P., Kersten, W. J., Kulasegaram, S., Moss, R. M., Parisot, J. P., Smith, B. J., Street, I. P., Yang, H., Huang, D. C., Watson, K. G. (2013) Structure-guided design of a selective BCL-X(L) inhibitor. *Nature Chem Biol*. 9, 390-397.
49. Lee, S., Zheng, X., Krishnamoorthy, J., Savelieff, M. G., Park, H. M., Brender, J. R., Kim, J. H., Derrick, J. S., Kochi, A., Lee, H. J., Kim, C., Ramamoorthy, A., Bowers, M. T., Lim, M. H. (2014) Rational design of a structural framework with potential use to develop chemical reagents that target and modulate multiple facets of Alzheimer's disease. *J Am Chem Soc*. 136, 299-310.
50. Shahian, T., Lee, G. M., Lazic, A., Arnold, L. A., Velusamy, P., Roels, C. M., Guy, R. K., Craik, C. S. (2009) Inhibition of a viral enzyme by a small-molecule dimer disruptor. *Nature Chem Biol*. 5, 640-646.
51. Sreedharan, J., Brown, R. H., Jr. (2013) Amyotrophic lateral sclerosis: problems and prospects. *Ann Neurol*. 74, 309-316.
52. Grisolia, S., Santos, I., Mendelson, J. (1968) Inactivation of enzymes by aspirin and salicylate. *Nature*. 219, 1252.
53. Alfonso, L., Ai, G., Spitale, R. C., Bhat, G. J. (2014) Molecular targets of aspirin and cancer prevention. *Br J Cancer*. 111, 61-67.
54. Bateman, L. A., Zaro, B. W., Miller, S. M., Pratt, M. R. (2013) An alkyne-aspirin chemical reporter for the detection of aspirin-dependent protein modification in living cells. *J Am Chem Soc*. 135, 14568-14573.
55. Barneoud, P., Curet, O. (1999) Beneficial effects of lysine acetylsalicylate, a soluble salt of aspirin, on motor performance in a transgenic model of amyotrophic lateral sclerosis. *Exp Neurol*. 155, 243-251.
56. Choudhary, C., Weinert, B. T., Nishida, Y., Verdin, E., Mann, M. (2014) The growing landscape of lysine acetylation links metabolism and cell signalling. *Nat Rev Mol Cell Biol*. 15, 536-550.
57. Chiti, F., Dobson, C. M. (2009) Amyloid formation by globular proteins under native conditions. *Nat Chem Biol*. 5, 15-22.
58. Lawrence, M. S., Phillips, K. J., Liu, D. R. (2007) Supercharging proteins can impart unusual resilience. *J Am Chem Soc*. 129, 10110-10112.

59. Csonka, F. A., Murphy, J. C., Jones, D. B. (1926) The iso-electric points of various proteins. *J Am Chem Soc.* 48, 763-768.
60. Shaw, B. F., Schneider, G. F., Bilgicer, B., Kaufman, G. K., Neveu, J. M., Lane, W. S., Whitelegge, J. P., Whitesides, G. M. (2008) Lysine acetylation can generate highly charged enzymes with increased resistance toward irreversible inactivation. *Protein sci.* 17, 1446-1455.
61. Sandelin, E., Nordlund, A., Andersen, P. M., Marklund, S. S., Oliveberg, M. (2007) Amyotrophic lateral sclerosis-associated copper/zinc superoxide dismutase mutations preferentially reduce the repulsive charge of the proteins. *J Biol Chem.* 282, 21230-21236.
62. Shi, Y., Mowery, R. A., Shaw, B. F. (2013) Effect of metal loading and subcellular pH on net charge of superoxide dismutase-1. *J Mol Biol.* 425, 4388-4404.
63. Della Valle, M. C., Sleat, D. E., Zheng, H., Moore, D. F., Jadot, M., Lobel, P. (2011) Classification of subcellular location by comparative proteomic analysis of native and density-shifted lysosomes. *Mol Cell Proteomics.* 10, M110 006403.
64. Shi, Y., Rhodes, N. R., Abdolvahabi, A., Kohn, T., Cook, N. P., Marti, A. A., Shaw, B. F. (2013) Deamidation of asparagine to aspartate destabilizes Cu, Zn superoxide dismutase, accelerates fibrillization, and mirrors ALS-linked mutations. *J Am Chem Soc.* 135, 15897-15908.
65. Pepys, M. B. (2006) Amyloidosis. *Annu Rev Med.* 57, 223-241.
66. Maji, S. K., Schubert, D., Rivier, C., Lee, S., Rivier, J. E., Riek, R. (2008) Amyloid as a depot for the formulation of long-acting drugs. *PLoS Biol.* 6, e17.
67. Shi, Y., et al. (2012) Abnormal SDS-PAGE migration of cytosolic proteins can identify domains and mechanisms that control surfactant binding. *Protein sci.* 21, 1197-1209.
68. Chattopadhyay, M., Durazo, A., Sohn, S. H., Strong, C. D., Gralla, E. B., Whitelegge, J. P., Valentine, J. S. (2008) Initiation and elongation in fibrillation of ALS-linked superoxide dismutase. *Proc Natl Acad Sci U S A.* 105, 18663-18668.
69. Shammas, S. L. et al. (2011) Perturbation of the stability of amyloid fibrils through alteration of electrostatic interactions. *Biophys J.* 100, 2783-2791.
70. Erickson, H. P. (2009) Size and shape of protein molecules at the nanometer level determined by sedimentation, gel filtration, and electron microscopy. *Biol Proced Online.* 11, 32-51.

71. Shaw, B. F., Durazo, A., Nersissian, A. M., Whitelegge, J. P., Faull, K. F., Valentine, J. S. (2006) Local unfolding in a destabilized, pathogenic variant of superoxide dismutase 1 observed with H/D exchange and mass spectrometry. *J Biol Chem.* 281, 18167-18176.
72. LeVine, H., 3rd (1999) Quantification of β -sheet amyloid fibril structures with thioflavin T. *Methods Enzymol.* 309, 274-284.
73. Vali, G. (2008) Repeatability and randomness in heterogeneous freezing nucleation. *Atmos. Chem. Phys.* 8, 5017-5031.
74. Prindle, A., Hasty, J. (2010) Biochemistry. Stochastic emergence of groupthink. *Science.* 328, 987-988.
75. Xue, W. F., Homans, S. W., Radford, S. E. (2008) Systematic analysis of nucleation-dependent polymerization reveals new insights into the mechanism of amyloid self-assembly. *Proc Natl Acad Sci U S A.* 105, 8926-8931.
76. Fodera, V., Librizzi, F., Groenning, M., van de Weert, M., Leone, M. (2008) Secondary nucleation and accessible surface in insulin amyloid fibril formation. *J Phys Chem B.* 112, 3853-3858.
77. Morris, R. J., Eden, K., Yarwood, R., Jourdain, L., Allen, R. J., Macphee, C. E. (2013) Mechanistic and environmental control of the prevalence and lifetime of amyloid oligomers. *Nat Commun.* 4, 1891.
78. Hortschansky, P., Schroeckh, V., Christopeit, T., Zandomenighi, G., Fandrich, M. (2005) The aggregation kinetics of Alzheimer's β -amyloid peptide is controlled by stochastic nucleation. *Protein sci.* 14, 1753-1759.
79. Ghag, G., Ghosh, P., Mauro, A., Rangachari, V., Vaidya, A. (2013) Stability analysis of 4-species A aggregation model: A novel approach to obtaining physically meaningful rate constants. *Appl Math Comput.* 224, 205-215.
80. Hellstrand, E., Boland, B., Walsh, D. M., Linse, S. (2010) Amyloid β -protein aggregation produces highly reproducible kinetic data and occurs by a two-phase process. *ACS Chem Neurosci.* 1, 13-18.
81. Oxtoby, D. W. (1993) Nonclassical nucleation theory: an exactly soluble model. *Physica Scripta.* 1993, 65.
82. Oxtoby, D. W. (1998) Nucleation of First-Order Phase Transitions. *Acc Chem Res.* 31, 91-97.
83. Rotunno, M. S., Bosco, D. A. (2013) An emerging role for misfolded wild-type SOD1 in sporadic ALS pathogenesis. *Front Cell Neurosci.* 7, 253.

84. Buell, A. K., Hung, P., Salvatella, X., Welland, M. E., Dobson, C. M., Knowles, T. P. (2013) Electrostatic effects in filamentous protein aggregation. *Biophys J.* *104*, 1116-1126.
85. Chan, P. K., Chattopadhyay, M., Sharma, S., Souda, P., Gralla, E. B., Borchelt, D. R., Whitelegge, J. P., Valentine, J. S. (2013) Structural similarity of wild-type and ALS-mutant superoxide dismutase-1 fibrils using limited proteolysis and atomic force microscopy. *Proc Natl Acad Sci U S A.* *110*, 10934-10939.
86. Shaw, B. F., Arthanari, H., Narovlyansky, M., Durazo, A., Frueh, D. P., Pollastri, M. P., Lee, A., Bilgicer, B., Gygi, S. P., Wagner, G., Whitesides, G. M. (2010) Neutralizing positive charges at the surface of a protein lowers its rate of amide hydrogen exchange without altering its structure or increasing its thermostability. *J Am Chem Soc.* *132*, 17411-17425.
87. Abdolvahabi, A., Gober, J. L., Mowery, R. A., Shi, Y., Shaw, B. F. (2014) Metal-ion-specific screening of charge effects in protein amide H/D exchange and the hofmeister series. *Anal Chem.* *86*, 10303-10310.
88. Nikolai Lorenzen, E. E. W., and Daniel E. Otzen, Inhibition of amyloid formation by small molecules. In *Amyloid Fibrils and Prefibrillar Aggregates: Molecular and Biological Properties*, Otzen, D. E., Ed. Wiley-VCH Verlag & Co. KGaA: Weinheim, 2013; pp 350-356.
89. Morel, B., Varela, L., Conejero-Lara, F. (2010) The thermodynamic stability of amyloid fibrils studied by differential scanning calorimetry. *J Phys Chem B.* *114*, 4010-4019.
90. Gitlin, I., Gudiksen, K. L., Whitesides, G. M. (2006) Effects of surface charge on denaturation of bovine carbonic anhydrase. *Chembiochem.* *7*, 1241-1250.
91. Shaw, B. F., Schneider, G. F., Arthanari, H., Narovlyansky, M., Moustakas, D., Durazo, A., Wagner, G., Whitesides, G. M. (2011) Complexes of native ubiquitin and dodecyl sulfate illustrate the nature of hydrophobic and electrostatic interactions in the binding of proteins and surfactants. *J Am Chem Soc.* *133*, 17681-17695.
92. Seefeldt, M. B., Kim, Y. S., Tolley, K. P., Seely, J., Carpenter, J. F., Randolph, T. W. (2005) High-pressure studies of aggregation of recombinant human interleukin-1 receptor antagonist: thermodynamics, kinetics, and application to accelerated formulation studies. *Protein sci.* *14*, 2258-2266.
93. Rodriguez, J. A., Valentine, J. S., Eggers, D. K., Roe, J. A., Tiwari, A., Brown, R. H., Jr., Hayward, L. J. (2002) Familial amyotrophic lateral sclerosis-associated mutations decrease the thermal stability of distinctly metallated species of human copper/zinc superoxide dismutase. *J Biol Chem.* *277*, 15932-15937.

94. Banci, L., Bertini, I., Durazo, A., Girotto, S., Gralla, E. B., Martinelli, M., Valentine, J. S., Vieru, M., Whitelegge, J. P. (2007) Metal-free superoxide dismutase forms soluble oligomers under physiological conditions: a possible general mechanism for familial ALS. *Proc Natl Acad Sci U S A.* *104*, 11263-11267.
95. Nijholt, D. A., De Kimpe, L., Elfrink, H. L., Hoozemans, J. J., Scheper, W. (2011) Removing protein aggregates: the role of proteolysis in neurodegeneration. *Curr Med Chem.* *18*, 2459-2476.
96. Cooper, G. M., Hausman, R. E., *The cell : a molecular approach.* 6th ed.; Sinauer Associates: Sunderland, MA, 2013; pp.
97. Grad, L. I., Yerbury, J. J., Turner, B. J., Guest, W. C., Pokrishevsky, E., O'Neill, M. A., Yanai, A., Silverman, J. M., Zeineddine, R., Corcoran, L., Kumita, J. R., Luheshi, L. M., Yousefi, M., Coleman, B. M., Hill, A. F., Plotkin, S. S., Mackenzie, I. R., Cashman, N. R. (2014) Intercellular propagated misfolding of wild-type Cu/Zn superoxide dismutase occurs via exosome-dependent and -independent mechanisms. *Proc Natl Acad Sci U S A.* *111*, 3620-3625.
98. Abdolvahabi, A., Shi, Y., Chuprin, A., Rasouli, S., Shaw, B. F. (2016) Stochastic formation of fibrillar and amorphous superoxide dismutase oligomers linked to amyotrophic lateral sclerosis. *ACS Chem Neurosci.* *7*, 799-810.
99. Ayers, J. I., Fromholt, S. E., O'Neal, V. M., Diamond, J. H., Borchelt, D. R. (2015) Prion-like propagation of mutant SOD1 misfolding and motor neuron disease spread along neuroanatomical pathways. *Acta Neuropathol.* *131*, 103-114.
100. Lang, L., Zetterstrom, P., Brannstrom, T., Marklund, S. L., Danielsson, J., Oliveberg, M. (2015) SOD1 aggregation in ALS mice shows simplistic test tube behavior. *Proc Natl Acad Sci U S A.* *112*, 9878-9883.
101. Lang, L., Kurnik, M., Danielsson, J., Oliveberg, M. (2012) Fibrillation precursor of superoxide dismutase 1 revealed by gradual tuning of the protein-folding equilibrium. *Proc Natl Acad Sci U S A.* *109*, 17868-17873.
102. Cao, Z., Ferrone, F. A. (1997) Homogeneous nucleation in sickle hemoglobin: stochastic measurements with a parallel method. *Biophys J.* *72*, 343-352.
103. Hofrichter, J. (1986) Kinetics of sickle hemoglobin polymerization. III. Nucleation rates determined from stochastic fluctuations in polymerization progress curves. *J Mol Biol.* *189*, 553-571.
104. Szavits-Nossan, J., Eden, K., Morris, R. J., MacPhee, C. E., Evans, M. R., Allen, R. J. (2014) Inherent variability in the kinetics of autocatalytic protein self-assembly. *Phys Rev Lett.* *113*, 098101.

105. Querido, E., Gallardo, F., Beaudoin, M., Menard, C., Chartrand, P. (2011) Stochastic and reversible aggregation of mRNA with expanded CUG-triplet repeats. *J Cell Sci.* 124, 1703-1714.
106. Elowitz, M. B., Levine, A. J., Siggia, E. D., Swain, P. S. (2002) Stochastic gene expression in a single cell. *Science.* 297, 1183-1186.
107. Gregor, T., Fujimoto, K., Masaki, N., Sawai, S. (2010) The onset of collective behavior in social amoebae. *Science.* 328, 1021-1025.
108. Giehm, L., Otzen, D. E. (2010) Strategies to increase the reproducibility of protein fibrillization in plate reader assays. *Anal Biochem.* 400, 270-281.
109. Furukawa, Y., Kaneko, K., Yamanaka, K., Nukina, N. (2010) Mutation-dependent polymorphism of Cu,Zn-superoxide dismutase aggregates in the familial form of amyotrophic lateral sclerosis. *J Biol Chem.* 285, 22221-22231.
110. Vassall, K. A., Stubbs, H. R., Primmer, H. A., Tong, M. S., Sullivan, S. M., Sobering, R., Srinivasan, S., Briere, L.-A. K., Dunn, S. D., Colón, W., Meiering, E. M. (2011) Decreased stability and increased formation of soluble aggregates by immature superoxide dismutase do not account for disease severity in ALS. *Proc Natl Acad Sci U S A.* 108, 2210-2215.
111. Pratt, A. J., Shin, D. S., Merz, G. E., Rambo, R. P., Lancaster, W. A., Dyer, K. N., Borbat, P. P., Poole, F. L., 2nd, Adams, M. W., Freed, J. H., Crane, B. R., Tainer, J. A., Getzoff, E. D. (2014) Aggregation propensities of superoxide dismutase G93 hotspot mutants mirror ALS clinical phenotypes. *Proc Natl Acad Sci U S A.* 111, E4568-4576.
112. Bergh, J., Zetterstrom, P., Andersen, P. M., Brannstrom, T., Graffmo, K. S., Jonsson, P. A., Lang, L., Danielsson, J., Oliveberg, M., Marklund, S. L. (2015) Structural and kinetic analysis of protein-aggregate strains *in vivo* using binary epitope mapping. *Proc Natl Acad Sci U S A.* 112, 4489-4494.
113. Crisp, M. J., Mawuenyega, K. G., Patterson, B. W., Reddy, N. C., Chott, R., Self, W. K., Weihl, C. C., Jockel-Balsarotti, J., Varadhachary, A. S., Bucelli, R. C., Yarasheski, K. E., Bateman, R. J., Miller, T. M. (2015) *In vivo* kinetic approach reveals slow SOD1 turnover in the CNS. *J Clin Invest.* 125, 2772-2780.
114. Wang, J. et al. (2003) Copper-binding-site-null SOD1 causes ALS in transgenic mice: aggregates of non-native SOD1 delineate a common feature. *Hum Mol Genet.* 12, 2753-2764.
115. Wang, J., Xu, G., Borchelt, D. R. (2002) High molecular weight complexes of mutant superoxide dismutase 1: age-dependent and tissue-specific accumulation. *Neurobiol Dis.* 9, 139-148.

116. Tiwari, A., Hayward, L. J. (2003) Familial amyotrophic lateral sclerosis mutants of copper/zinc superoxide dismutase are susceptible to disulfide reduction. *J Biol Chem.* 278, 5984-5992.
117. Doucette, P. A., Whitson, L. J., Cao, X., Schirf, V., Demeler, B., Valentine, J. S., Hansen, J. C., Hart, P. J. (2004) Dissociation of human copper-zinc superoxide dismutase dimers using chaotrope and reductant. Insights into the molecular basis for dimer stability. *J Biol Chem.* 279, 54558-54566.
118. Leal, S. S., Cristovao, J. S., Biesemeier, A., Cardoso, I., Gomes, C. M. (2015) Aberrant zinc binding to immature conformers of metal-free copper-zinc superoxide dismutase triggers amorphous aggregation. *Metallomics.* 7, 333-346.
119. Ferreira, A. S., da Silva, M. A., Cressoni, J. C. (2003) Stochastic modeling approach to the incubation time of prionic diseases. *Phys Rev Lett.* 90, 198101.
120. Colby, D. W., Cassady, J. P., Lin, G. C., Ingram, V. M., Wittrup, K. D. (2006) Stochastic kinetics of intracellular huntingtin aggregate formation. *Nat Chem Biol.* 2, 319-323.
121. Zhu, M., Souillac, P. O., Ionescu-Zanetti, C., Carter, S. A., Fink, A. L. (2002) Surface-catalyzed amyloid fibril formation. *J Biol Chem.* 277, 50914-50922.
122. Vacha, R., Linse, S., Lund, M. (2014) Surface effects on aggregation kinetics of amyloidogenic peptides. *J Am Chem Soc.* 136, 11776-11782.
123. Fandrich, M. (2007) Absolute correlation between lag time and growth rate in the spontaneous formation of several amyloid-like aggregates and fibrils. *J Mol Biol.* 365, 1266-1270.
124. Wright, G. S., et al. (2013) Ligand binding and aggregation of pathogenic SOD1. *Nat Commun.* 4, 1758.
125. Younan, N. D., Viles, J. H. (2015) A comparison of three fluorophores for the detection of amyloid fibers and prefibrillar oligomeric assemblies. ThT (Thioflavin T); ANS (1-Anilinonaphthalene-8-sulfonic Acid); and bisANS (4,4'-Dianilino-1,1'-binaphthyl-5,5'-disulfonic Acid). *Biochemistry.* 54, 4297-4306.
126. Hawe, A., Sutter, M., Jiskoot, W. (2008) Extrinsic fluorescent dyes as tools for protein characterization. *Pharm Res.* 25, 1487-1499.
127. Ghosh, D., Singh, P. K., Sahay, S., Jha, N. N., Jacob, R. S., Sen, S., Kumar, A., Riek, R., Maji, S. K. (2015) Structure based aggregation studies reveal the presence of helix-rich intermediate during α -Synuclein aggregation. *Sci Rep.* 5, 9228.

128. Limpert, E., Stahel, W. A., Abbt, M. (2001) Log-normal distributions across the sciences: keys and clues: on the charms of statistics, and how mechanical models resembling gambling machines offer a link to a handy way to characterize log-normal distributions, which can provide deeper insight into variability and probability—normal or log-normal: that is the question. *BioScience*. 51, 341-352.
129. Clarke, G., Collins, R. A., Leavitt, B. R., Andrews, D. F., Hayden, M. R., Lumsden, C. J., McInnes, R. R. (2000) A one-hit model of cell death in inherited neuronal degenerations. *Nature*. 406, 195-199.
130. Clarke, G., Lumsden, C. J. (2005) Heterogeneous cellular environments modulate one-hit neuronal death kinetics. *Brain Res Bull*. 65, 59-67.
131. Knudson, A. G., Jr. (1971) Mutation and cancer: statistical study of retinoblastoma. *Proc Natl Acad Sci U S A*. 68, 820-823.
132. Abdolvahabi, A., Shi, Y., Rasouli, S., Croom, C. M., Aliyan, A., Marti, A. A., Shaw, B. F. (2017) Kaplan-Meier meets chemical kinetics: intrinsic rate of SOD1 amyloidogenesis decreased by subset of ALS mutations and cannot fully explain age of disease onset. *ACS Chem Neurosci*. 8, 1378-1389.
133. Renton, A. E., Chio, A., Traynor, B. J. (2014) State of play in amyotrophic lateral sclerosis genetics. *Nat Neurosci*. 17, 17-23.
134. Chattopadhyay, M., Nwadiibia, E., Strong, C. D., Gralla, E. B., Valentine, J. S., Whitelegge, J. P. (2015) The disulfide bond, but not zinc or dimerization, controls initiation and seeded growth in amyotrophic lateral sclerosis-linked Cu, Zn superoxide dismutase (SOD1) fibrillation. *J Biol Chem*. 290, 30624-30636.
135. Merlini, G., Wechalekar, A. D., Palladini, G. (2013) Systemic light chain amyloidosis: an update for treating physicians. *Blood*. 121, 5124-5130.
136. Wang, Q., Johnson, J. L., Agar, N. Y., Agar, J. N. (2008) Protein aggregation and protein instability govern familial amyotrophic lateral sclerosis patient survival. *PLoS Biol*. 6, e170.
137. Li, H. F., Wu, Z. Y. (2016) Genotype-phenotype correlations of amyotrophic lateral sclerosis. *Transl Neurodegener*. 5, 3.
138. Millecamps, S. et al. (2010) SOD1, ANG, VAPB, TARDBP, and FUS mutations in familial amyotrophic lateral sclerosis: genotype-phenotype correlations. *J Med Genet*. 47, 554-560.
139. Yamashita, S., Ando, Y. (2015) Genotype-phenotype relationship in hereditary amyotrophic lateral sclerosis. *Transl Neurodegener*. 4, 13.

140. Kepp, K. P. (2015) Genotype-property patient-phenotype relations suggest that proteome exhaustion can cause amyotrophic lateral sclerosis. *PLoS One*. 10, e0118649.
141. Lu, J. T., Campeau, P. M., Lee, B. H. (2014) Genotype-phenotype correlation--promiscuity in the era of next-generation sequencing. *N Engl J Med*. 371, 593-596.
142. Kroos, M., Hoogeveen-Westerveld, M., van der Ploeg, A., Reuser, A. J. (2012) The genotype-phenotype correlation in Pompe disease. *Am J Med Genet C Semin Med Genet*. 160C, 59-68.
143. Mason, P. J., Bautista, J. M., Gilsanz, F. (2007) G6PD deficiency: the genotype-phenotype association. *Blood Rev*. 21, 267-283.
144. Campioni, S., Carret, G., Jordens, S., Nicoud, L., Mezzenga, R., Riek, R. (2014) The presence of an air-water interface affects formation and elongation of α -synuclein fibrils. *J Am Chem Soc*. 136, 2866-2875.
145. Sear, R. P. (2014) Quantitative studies of crystal nucleation at constant supersaturation: experimental data and models. *Crystengcomm*. 16, 6506-6522.
146. Maggioni, G. M., Mazzotti, M. (2015) Modelling the stochastic behaviour of primary nucleation. *Faraday Discuss*. 179, 359-382.
147. Ayers, J. I., Fromholt, S., Koch, M., DeBosier, A., McMahon, B., Xu, G., Borchelt, D. R. (2014) Experimental transmissibility of mutant SOD1 motor neuron disease. *Acta Neuropathol*. 128, 791-803.
148. Rich, J. T., Neely, J. G., Paniello, R. C., Voelker, C. C., Nussenbaum, B., Wang, E. W. (2010) A practical guide to understanding Kaplan-Meier curves. *Otolaryngol Head Neck Surg*. 143, 331-336.
149. Goel, M. K., Khanna, P., Kishore, J. (2010) Understanding survival analysis: Kaplan-Meier estimate. *Int J Ayurveda Res*. 1, 274-278.
150. Cardona, A. E., Pioro, E. P., Sasse, M. E., Kostenko, V., Cardona, S. M., Dijkstra, I. M., Huang, D., Kidd, G., Dombrowski, S., Dutta, R., Lee, J. C., Cook, D. N., Jung, S., Lira, S. A., Littman, D. R., Ransohoff, R. M. (2006) Control of microglial neurotoxicity by the fractalkine receptor. *Nat Neurosci*. 9, 917-924.
151. Puttapparthi, K., Gitomer, W. L., Krishnan, U., Son, M., Rajendran, B., Elliott, J. L. (2002) Disease progression in a transgenic model of familial amyotrophic lateral sclerosis is dependent on both neuronal and non-neuronal zinc binding proteins. *J Neurosci*. 22, 8790-8796.

152. Aalen, O. O., Borgan, Ø., Gjessing, S., *Survival and event history analysis : a process point of view*. Springer: New York, NY, 2008; p xviii, 539 p.
153. Bystrom, R., Andersen, P. M., Grobner, G., Oliveberg, M. (2010) SOD1 mutations targeting surface hydrogen bonds promote amyotrophic lateral sclerosis without reducing apo-state stability. *J Biol Chem.* 285, 19544-19552.
154. Kitahama, Y., Egashira, M., Suzuki, T., Tanabe, I., Ozaki, Y. (2014) Sensitive marker bands for the detection of spin states of heme in surface-enhanced resonance Raman scattering spectra of metmyoglobin. *Analyst.* 139, 6421-6425.
155. Oztug Durer, Z. A., Cohlberg, J. A., Dinh, P., Padua, S., Ehrenclou, K., Downes, S., Tan, J. K., Nakano, Y., Bowman, C. J., Hoskins, J. L., Kwon, C., Mason, A. Z., Rodriguez, J. A., Doucette, P. A., Shaw, B. F., Valentine, J. S. (2009) Loss of metal ions, disulfide reduction and mutations related to familial ALS promote formation of amyloid-like aggregates from superoxide dismutase. *PLoS One.* 4, e5004.
156. Prudencio, M., Lelie, H., Brown, H. H., Whitelegge, J. P., Valentine, J. S., Borchelt, D. R. (2012) A novel variant of human superoxide dismutase 1 harboring amyotrophic lateral sclerosis-associated and experimental mutations in metal-binding residues and free cysteines lacks toxicity *in vivo*. *J Neurochem.* 121, 475-485.
157. Lelie, H. L., Liba, A., Bourassa, M. W., Chattopadhyay, M., Chan, P. K., Gralla, E. B., Miller, L. M., Borchelt, D. R., Valentine, J. S., Whitelegge, J. P. (2011) Copper and zinc metallation status of copper-zinc superoxide dismutase from amyotrophic lateral sclerosis transgenic mice. *J Biol Chem.* 286, 2795-2806.
158. Lushchak, V. I. (2012) Glutathione homeostasis and functions: potential targets for medical interventions. *J Amino Acids.* 2012, 736837.
159. Getz, E. B., Xiao, M., Chakrabarty, T., Cooke, R., Selvin, P. R. (1999) A comparison between the sulfhydryl reductants tris(2-carboxyethyl)phosphine and dithiothreitol for use in protein biochemistry. *Anal Biochem.* 273, 73-80.
160. McAlary, L., Aquilina, J. A., Yerbury, J. J. (2016) Susceptibility of Mutant SOD1 to Form a Destabilized Monomer Predicts Cellular Aggregation and Toxicity but Not In vitro Aggregation Propensity. *Fronti Neurosci.* 10, 499.
161. Ratovitski, T. et al. (1999) Variation in the biochemical/biophysical properties of mutant superoxide dismutase 1 enzymes and the rate of disease progression in familial amyotrophic lateral sclerosis kindreds. *Hum Mol Genet.* 8, 1451-1460.
162. Noskov, B. A. et al. (2010) Bovine serum albumin unfolding at the air/water interface as studied by dilational surface rheology. *Langmuir.* 26, 17225-17231.

163. Niwayama, R., Nagao, H., Kitajima, T. S., Hufnagel, L., Shinohara, K., Higuchi, T., Ishikawa, T., Kimura, A. (2016) Bayesian inference of forces causing cytoplasmic streaming in *Caenorhabditis elegans* embryos and mouse oocytes. *PLoS One*. *11*, e0159917.
164. Borchelt, D. R., Wong, P. C., Becher, M. W., Pardo, C. A., Lee, M. K., Xu, Z. S., Thinakaran, G., Jenkins, N. A., Copeland, N. G., Sisodia, S. S., Cleveland, D. W., Price, D. L., Hoffman, P. N. (1998) Axonal transport of mutant superoxide dismutase 1 and focal axonal abnormalities in the proximal axons of transgenic mice. *Neurobiol Dis*. *5*, 27-35.
165. Williamson, T. L., Cleveland, D. W. (1999) Slowing of axonal transport is a very early event in the toxicity of ALS-linked SOD1 mutants to motor neurons. *Nat Neurosci*. *2*, 50-56.
166. Smith, D. H., Meaney, D. F. (2000) Axonal damage in traumatic brain injury. *Neuroscientist*. *6*, 483-495.
167. Seals, R. M., Hansen, J., Gredal, O., Weisskopf, M. G. (2016) Physical trauma and amyotrophic lateral sclerosis: A population-based study using Danish national registries. *Am J Epidemiol*. *183*, 294-301.
168. Prudencio, M., Hart, P. J., Borchelt, D. R., Andersen, P. M. (2009) Variation in aggregation propensities among ALS-associated variants of SOD1: correlation to human disease. *Hum Mol Genet*. *18*, 3217-3226.
169. Jonsson, P. A., Graffmo, K. S., Brannstrom, T., Nilsson, P., Andersen, P. M., Marklund, S. L. (2006) Motor neuron disease in mice expressing the wild type-like D90A mutant superoxide dismutase-1. *J Neuropathol Exp Neurol*. *65*, 1126-1136.
170. Galvagnion, C., Buell, A. K., Meisl, G., Michaels, T. C., Vendruscolo, M., Knowles, T. P., Dobson, C. M. (2015) Lipid vesicles trigger α -synuclein aggregation by stimulating primary nucleation. *Nat Chem Biol*. *11*, 229-234.
171. Burke, K. A., Yates, E. A., Legleiter, J. (2013) Biophysical insights into how surfaces, including lipid membranes, modulate protein aggregation related to neurodegeneration. *Front Neurol*. *4*, 17.
172. Groenning, M. (2010) Binding mode of Thioflavin T and other molecular probes in the context of amyloid fibrils-current status. *J Chem Biol*. *3*, 1-18.
173. Tomiyama, T., Nagata, T., Shimada, H., Teraoka, R., Fukushima, A., Kanemitsu, H., Takuma, H., Kuwano, R., Imagawa, M., Ataka, S., Wada, Y., Yoshioka, E., Nishizaki, T., Watanabe, Y., Mori, H. (2008) A new amyloid β variant favoring oligomerization in Alzheimer's-type dementia. *Ann Neurol*. *63*, 377-387.

174. Hubin, E., Deroo, S., Schierle, G. K., Kaminski, C., Serpell, L., Subramaniam, V., van Nuland, N., Broersen, K., Raussens, V., Sarroukh, R. (2015) Two distinct beta-sheet structures in Italian-mutant amyloid- β fibrils: a potential link to different clinical phenotypes. *Cell Mol Life Sci.* 72, 4899-4913.
175. Cloe, A. L., Orgel, J. P., Sachleben, J. R., Tycko, R., Meredith, S. C. (2011) The Japanese mutant A β (Δ E22-A β (1-39)) forms fibrils instantaneously, with low-thioflavin T fluorescence: seeding of wild-type A β (1-40) into atypical fibrils by Δ E22-A β (1-39). *Biochemistry.* 50, 2026-2039.
176. Jonsson, P. A., Graffmo, K. S., Andersen, P. M., Brannstrom, T., Lindberg, M., Oliveberg, M., Marklund, S. L. (2006) Disulphide-reduced superoxide dismutase-1 in CNS of transgenic amyotrophic lateral sclerosis models. *Brain.* 129, 451-464.
177. Kirby, J., Menzies, F. M., Cookson, M. R., Bushby, K., Shaw, P. J. (2002) Differential gene expression in a cell culture model of SOD1-related familial motor neurone disease. *Hum Mol Genet.* 11, 2061-2075.
178. Tiwari, A., Xu, Z., Hayward, L. J. (2005) Aberrantly increased hydrophobicity shared by mutants of Cu,Zn-superoxide dismutase in familial amyotrophic lateral sclerosis. *J Biol Chem.* 280, 29771-29779.
179. Flagmeier, P., et al. (2016) Mutations associated with familial Parkinson's disease alter the initiation and amplification steps of α -synuclein aggregation. *Proc Natl Acad Sci U S A.* 113, 10328-10333.
180. Galvagnion, C., Brown, J. W. P., Ouberai, M. M., Flagmeier, P., Vendruscolo, M., Buell, A. K., Sparr, E., Dobson, C. M. (2016) Chemical properties of lipids strongly affect the kinetics of the membrane-induced aggregation of α -synuclein. *Proc Natl Acad Sci U S A.* 113, 7065-7070.
181. Pasinelli, P., Brown, R. H. (2006) Molecular biology of amyotrophic lateral sclerosis: insights from genetics. *Nat Rev Neurosci.* 7, 710-723.
182. Deng, H. X. et al. (2006) Conversion to the amyotrophic lateral sclerosis phenotype is associated with intermolecular linked insoluble aggregates of SOD1 in mitochondria. *Proc Natl Acad Sci U S A.* 103, 7142-7147.
183. Gurney, M. E. et al. (1994) Motor neuron degeneration in mice that express a human Cu,Zn superoxide dismutase mutation. *Science.* 264, 1772-1775.
184. Shi, Y., Acerson, M. J., Abdolvahabi, A., Mowery, R. A., Shaw, B. F. (2016) Gibbs energy of superoxide dismutase heterodimerization accounts for variable survival in amyotrophic lateral sclerosis. *J Am Chem Soc.* 138, 5351-5362.

185. Abdolvahabi, A., Shi, Y., Rasouli, S., Croom, C. M., Chuprin, A., Shaw, B. F. (2017) How do gyrating beads accelerate amyloid fibrillization? *Biophys J.* *112*, 250-264.
186. Saar, K. L., Yates, E. V., Muller, T., Saunier, S., Dobson, C. M., Knowles, T. P. (2016) Automated ex situ assays of amyloid formation on a microfluidic platform. *Biophys J.* *110*, 555-560.
187. Arosio, P., Michaels, T. C., Linse, S., Mansson, C., Emanuelsson, C., Presto, J., Johansson, J., Vendruscolo, M., Dobson, C. M., Knowles, T. P. (2016) Kinetic analysis reveals the diversity of microscopic mechanisms through which molecular chaperones suppress amyloid formation. *Nat Commun.* *7*, 10948.
188. Ayers, J. I., McMahon, B., Gill, S., Lelie, H. L., Fromholt, S., Brown, H., Valentine, J. S., Whitelegge, J. P., Borchelt, D. R. (2016) Relationship between mutant SOD1 maturation and inclusion formation in cell models. *J Neurochem.* *140*, 140-150.
189. Ankarcrona, M., Winblad, B., Monteiro, C., Fearn, C., Powers, E. T., Johansson, J., Westermarck, G. T., Presto, J., Ericzon, B. G., Kelly, J. W. (2016) Current and future treatment of amyloid diseases. *J Intern Med.* *280*, 177-202.
190. Cho, Y., Baranczak, A., Helmke, S., Teruya, S., Horn, E. M., Maurer, M. S., Kelly, J. W. (2015) Personalized medicine approach for optimizing the dose of tafamidis to potentially ameliorate wild-type transthyretin amyloidosis (cardiomyopathy). *Amyloid.* *22*, 175-180.
191. Young, L. M. et al. (2015) Screening and classifying small-molecule inhibitors of amyloid formation using ion mobility spectrometry-mass spectrometry. *Nat Chem.* *7*, 73-81.
192. Anzai, I., Toichi, K., Tokuda, E., Mukaiyama, A., Akiyama, S., Furukawa, Y. (2016) Screening of drugs inhibiting *in vitro* oligomerization of Cu/Zn-superoxide dismutase with a mutation causing amyotrophic lateral sclerosis. *Front Mol Biosci.* *3*, 40.
193. Pronchik, J., He, X., Giurleo, J. T., Talaga, D. S. (2010) *In vitro* formation of amyloid from α -synuclein is dominated by reactions at hydrophobic interfaces. *J Am Chem Soc.* *132*, 9797-9803.
194. Giacomelli, C. E., Norde, W. (2003) Influence of hydrophobic Teflon particles on the structure of amyloid β -peptide. *Biomacromolecules.* *4*, 1719-1726.
195. Buell, A. K., et al. (2014) Solution conditions determine the relative importance of nucleation and growth processes in α -synuclein aggregation. *Proc Natl Acad Sci U S A.* *111*, 7671-7676.

196. Cohlberg, J. A., Li, J., Uversky, V. N., Fink, A. L. (2002) Heparin and other glycosaminoglycans stimulate the formation of amyloid fibrils from α -synuclein *in vitro*. *Biochemistry*. *41*, 1502-1511.
197. Uversky, V. N., Li, J., Fink, A. L. (2001) Evidence for a partially folded intermediate in α -synuclein fibril formation. *J Biol Chem*. *276*, 10737-10744.
198. Wiesbauer, J., Prassl, R., Nidetzky, B. (2013) Renewal of the air-water interface as a critical system parameter of protein stability: aggregation of the human growth hormone and its prevention by surface-active compounds. *Langmuir*. *29*, 15240-15250.
199. Di Stasio, E., De Cristofaro, R. (2010) The effect of shear stress on protein conformation: Physical forces operating on biochemical systems: The case of von Willebrand factor. *Biophys Chem*. *153*, 1-8.
200. Schneider, S. W., Nuschele, S., Wixforth, A., Gorzelanny, C., Alexander-Katz, A., Netz, R. R., Schneider, M. F. (2007) Shear-induced unfolding triggers adhesion of von Willebrand factor fibers. *Proc Natl Acad Sci U S A*. *104*, 7899-7903.
201. Xue, W. F., Hellewell, A. L., Gosal, W. S., Homans, S. W., Hewitt, E. W., Radford, S. E. (2009) Fibril fragmentation enhances amyloid cytotoxicity. *J Biol Chem*. *284*, 34272-34282.
202. Nicoud, L., Lazzari, S., Balderas Barragan, D., Morbidelli, M. (2015) Fragmentation of amyloid fibrils occurs in preferential positions depending on the environmental conditions. *J Phys Chem B*. *119*, 4644-4652.
203. Harwood, L. M., Moody, C. J., *Experimental organic chemistry : principles and practice*. Blackwell Scientific Publications: Oxford England ; Boston, 1990; p xii, 778 p.
204. Sluzky, V., Tamada, J. A., Klivanov, A. M., Langer, R. (1991) Kinetics of insulin aggregation in aqueous solutions upon agitation in the presence of hydrophobic surfaces. *Proc Natl Acad Sci U S A*. *88*, 9377-9381.
205. Jorgensen, L., Bennedsen, P., Hoffmann, S. V., Krogh, R. L., Pinholt, C., Groenning, M., Hostrup, S., Bukrinsky, J. T. (2011) Adsorption of insulin with varying self-association profiles to a solid Teflon surface--influence on protein structure, fibrillation tendency and thermal stability. *Eur J Pharm Sci*. *42*, 509-516.
206. Banga, A. K., *Therapeutic peptides and proteins : formulation, processing, and delivery systems*. 2nd ed.; CRC/Taylor & Francis: Boca Raton, FL, 2006; p 354 p.

207. Gray, J. J. (2004) The interaction of proteins with solid surfaces. *Curr Opin Struct Biol.* 14, 110-115.
208. Whitehouse, D. J., *Surfaces and their measurement*. Kogan Page Science: London, 2004; p xi, 395 p.
209. Ferri, F. A., Malegori, G., Enachescu, M., Veis, M., Behary, N., Das, P. K., De Oliveira, R. R. L., Horng, T. L., Bellitto, V. J., Gupta, V., *Measurement of the nanoscale roughness by atomic force microscopy: basic principles and applications*. INTECH Open Access Publisher: 2012.
210. Biancalana, M., Koide, S. (2010) Molecular mechanism of thioflavin-T binding to amyloid fibrils. *Biochim Biophys Acta.* 1804, 1405-1412.
211. Bagnall, R. D., Annis, J. A., Sherliker, S. J. (1980) Adsorption of plasma proteins on hydrophobic surfaces. IV. Contact angle studies on implanted polymers. *J Biomed Mater Res.* 14, 1-10.
212. Mittal, K. L., *Polymer surface modification: relevance to adhesion*. Taylor & Francis: 2000.
213. Slepicka, P., Kasalkova, N. S., Stranska, E., Bacakova, L., Svorcik, V. (2013) Surface characterization of plasma treated polymers for applications as biocompatible carriers. *Express Polymer Letters.* 7, 535-545.
214. Hilgenberg, S. P. et al. (2008) Evaluation of surface physical properties of acrylic resins for provisional prosthesis. *Mat Res.* 11, 257-260.
215. Zhang, Y., Wang, R., Yi, S. L., Setiawan, L., Hu, X., Fane, A. G. (2011) Novel chemical surface modification to enhance hydrophobicity of polyamide-imide (PAI) hollow fiber membranes. *J Membr Sci.* 380, 241-250.
216. Goswami, S., Klaus, S., Benziger, J. (2008) Wetting and absorption of water drops on Nafion films. *Langmuir.* 24, 8627-8633.
217. Tong, W. L. et al. (2015) Coupled effects of hydrophobic layer and vibration on thermal efficiency of two-phase closed thermosyphons. *Rsc Advances.* 5, 10332-10340.
218. Smith, M. S., Taft, S. B., Moulton, J. (2014) Contact angle measurements for advanced thermal management technologies *Front Heat Mass Trans.* 5, 1-9.
219. Amaral, M. et al. (2002) Wettability and surface charge of Si₃N₄-bioglass composites in contact with simulated physiological liquids. *Biomaterials.* 23, 4123-4129.

220. Santos, F. d. P., Campos, E. d., Costa, M., Melo, F. C. L., Honda, R. Y., Mota, R. P. (2003) Superficial modifications in TiO₂ and Al₂O₃ ceramics. *Mat Res.* 6, 353-357.
221. Pacha-Olivenza, M. A., Gallardo-Moreno, A. M., Mendez-Vilas, A., Bruque, J. M., Gonzalez-Carrasco, J. L., Gonzalez-Martin, M. L. (2008) Effect of UV irradiation on the surface Gibbs energy of Ti₆Al₄V and thermally oxidized Ti₆Al₄V. *J Colloid Interface Sci.* 320, 117-124.
222. Hedberg, Y., Karlsson, M. E., Blomberg, E., Wallinder, I. O., Hedberg, J. (2014) Correlation between surface physicochemical properties and the release of iron from stainless steel AISI 304 in biological media. *Colloids and Surfaces B-Biointerfaces.* 122, 216-222.
223. Tanaka, M., Collins, S. R., Toyama, B. H., Weissman, J. S. (2006) The physical basis of how prion conformations determine strain phenotypes. *Nature.* 442, 585-589.
224. Hanaor, D. A. H., Gan, Y. X., Einav, I. (2015) Contact mechanics of fractal surfaces by spline assisted discretisation. *Int J Solids Struct.* 59, 121-131.
225. Johnson, K. L., *Contact mechanics.* Cambridge University Press: Cambridge Cambridgeshire ; New York, 1985; p xi, 452 p.
226. Shin, Y. J., Su, C. C., Shen, Y. H. (2006) Dispersion of aqueous nano-sized alumina suspensions using cationic polyelectrolyte. *Mater Res Bulletin.* 41, 1964-1971.
227. Cohen, S. I. et al. (2013) Proliferation of amyloid-β42 aggregates occurs through a secondary nucleation mechanism. *Proc Natl Acad Sci U S A.* 110, 9758-9763.
228. Chiti, F., Bucciantini, M., Capanni, C., Taddei, N., Dobson, C. M., Stefani, M. (2001) Solution conditions can promote formation of either amyloid protofilaments or mature fibrils from the HypF N-terminal domain. *Protein Sci.* 10, 2541-2547.
229. Chiti, F., Webster, P., Taddei, N., Clark, A., Stefani, M., Ramponi, G., Dobson, C. M. (1999) Designing conditions for in vitro formation of amyloid protofilaments and fibrils. *Proc Natl Acad Sci U S A.* 96, 3590-3594.
230. Cao, A., Hu, D., Lai, L. (2004) Formation of amyloid fibrils from fully reduced hen egg white lysozyme. *Protein Sci.* 13, 319-324.
231. Jha, A., Narayan, S., Udgaonkar, J. B., Krishnamoorthy, G. (2012) Solvent-induced tuning of internal structure in a protein amyloid protofibril. *Biophys J.* 103, 797-806.

232. Rezaei-Ghaleh, N., Ebrahim-Habibi, A., Moosavi-Movahedi, A. A., Nemat-Gorgani, M. (2007) Role of electrostatic interactions in 2,2,2-trifluoroethanol-induced structural changes and aggregation of α -chymotrypsin. *Arch Biochem Biophys.* 457, 160-169.
233. Culik, R. M., Abaskharon, R. M., Pazos, I. M., Gai, F. (2014) Experimental validation of the role of trifluoroethanol as a nanocrowder. *J Phys Chem B.* 118, 11455-11461.
234. Dunstan, D. E., Hamilton-Brown, P., Asimakis, P., Ducker, W., Bertolini, J. (2009) Shear flow promotes amyloid- β fibrilization. *Protein Eng Des Sel.* 22, 741-746.
235. Varongchayakul, N., Johnson, S., Quabili, T., Cappello, J., Ghandehari, H., Solares Sde, J., Hwang, W., Seog, J. (2013) Direct observation of amyloid nucleation under nanomechanical stretching. *ACS Nano.* 7, 7734-7743.
236. Xu, Z., Paparcone, R., Buehler, M. J. (2010) Alzheimer's A β (1-40) amyloid fibrils feature size-dependent mechanical properties. *Biophys J.* 98, 2053-2062.
237. Hachiya, N. S., Kozuka, Y., Kaneko, K. (2008) Mechanical stress and formation of protein aggregates in neurodegenerative disorders. *Med Hypotheses.* 70, 1034-1037.
238. Stein, T. D., Alvarez, V. E., McKee, A. C. (2014) Chronic traumatic encephalopathy: a spectrum of neuropathological changes following repetitive brain trauma in athletes and military personnel. *Alzheimers Res Ther.* 6, 4.
239. Hu, W. et al. (2013) Stepwise protein folding at near amino acid resolution by hydrogen exchange and mass spectrometry. *Proc Natl Acad Sci U S A.* 110, 7684-7689.
240. Walters, B. T. et al. (2013) Folding of a large protein at high structural resolution. *Proc Natl Acad Sci U S A.* 110, 18898-18903.
241. Anderson, J. S., Hernandez, G., Lemaster, D. M. (2008) A billion-fold range in acidity for the solvent-exposed amides of *Pyrococcus furiosus* rubredoxin. *Biochemistry.* 47, 6178-6188.
242. Skinner, J. J., Lim, W. K., Bedard, S., Black, B. E., Englander, S. W. (2012) Protein dynamics viewed by hydrogen exchange. *Protein sci.* 21, 996-1005.
243. Radkiewicz, J. L., Zipse, H., Clarke, S., Houk, K. N. (2001) Neighboring side chain effects on asparaginyl and aspartyl degradation: an ab initio study of the relationship between peptide conformation and backbone NH acidity. *J Am Chem Soc.* 123, 3499-3506.

244. Jungwirth, P., Winter, B. (2008) Ions at aqueous interfaces: from water surface to hydrated proteins. *Annu Rev Phys Chem.* 59, 343-366.
245. Li, L., Li, C., Zhang, Z., Alexov, E. (2013) On the dielectric "constant" of proteins: smooth dielectric function for macromolecular modeling and its implementation in DelPhi. *J Chem Theory Comput.* 9, 2126-2136.
246. Matthew, J. B., Richards, F. M. (1983) The pH dependence of hydrogen exchange in proteins. *J Biol Chem.* 258, 3039-3044.
247. Dempsey, C. E. (1986) pH dependence of hydrogen exchange from backbone peptide amides in apamin. *Biochemistry.* 25, 3904-3911.
248. Christoffersen, M., Bolvig, S., Tuchsén, E. (1996) Salt effects on the amide hydrogen exchange of bovine pancreatic trypsin inhibitor. *Biochemistry.* 35, 2309-2315.
249. Kim, P. S., Baldwin, R. L. (1982) Influence of charge on the rate of amide proton exchange. *Biochemistry.* 21, 1-5.
250. Di Russo, N. V., Estrin, D. A., Marti, M. A., Roitberg, A. E. (2012) pH-dependent conformational changes in proteins and their effect on experimental $pK_{(a)}$ s: the case of nitrophorin 4. *PLoS Comput Biol.* 8, e1002761.
251. Jungwirth, P., Cremer, P. S. (2014) Beyond Hofmeister. *Nat Chem.* 6, 261-263.
252. Krezel, A., Bal, W. (2004) A formula for correlating pK_a values determined in D_2O and H_2O . *J Inorg Biochem.* 98, 161-166.
253. Maity, H., Lim, W. K., Rumbley, J. N., Englander, S. W. (2003) Protein hydrogen exchange mechanism: local fluctuations. *Protein sci.* 12, 153-160.
254. Shaw, B. F., Schneider, G. F., Whitesides, G. M. (2012) Effect of surfactant hydrophobicity on the pathway for unfolding of ubiquitin. *J Am Chem Soc.* 134, 18739-18745.
255. Nagaraj, R. H. et al. (2012) Acetylation of αA -crystallin in the human lens: effects on structure and chaperone function. *Biochim Biophys Acta.* 1822, 120-129.
256. Bai, Y. W. et al. (1993) Primary structure effects on peptide group hydrogen-exchange. *Proteins: Struct Funct Genet.* 17, 75-86.
257. Caravella, J. A. et al. (1999) Long-range electrostatic contributions to protein-ligand binding estimated using protein charge ladders, affinity capillary electrophoresis, and continuum electrostatic theory. *J Am Chem Soc.* 121, 4340-4347.

258. Heyda, J., Vincent, J. C., Tobias, D. J., Dzubiella, J., Jungwirth, P. (2010) Ion specificity at the peptide bond: molecular dynamics simulations of N-methylacetamide in aqueous salt solutions. *J Phys Chem B*. 114, 1213-1220.
259. Algaer, E. A., van der Vegt, N. F. (2011) Hofmeister ion interactions with model amide compounds. *J Phys Chem B*. 115, 13781-13787.
260. Okur, H. I., Kherb, J., Cremer, P. S. (2013) Cations bind only weakly to amides in aqueous solutions. *J Am Chem Soc*. 135, 5062-5067.
261. Hunter, C. L., Maurus, R., Mauk, M. R., Lee, H., Raven, E. L., Tong, H., Nguyen, N., Smith, M., Brayer, G. D., Mauk, A. G. (2003) Introduction and characterization of a functionally linked metal ion binding site at the exposed heme edge of myoglobin. *Proc Natl Acad Sci U S A*. 100, 3647-3652.
262. Nihonyanagi, S., Yamaguchi, S., Tahara, T. (2014) Counterion effect on interfacial water at charged interfaces and its relevance to the Hofmeister series. *J Am Chem Soc*. 136, 6155-6158.
263. Collins, K. D. (1997) Charge density-dependent strength of hydration and biological structure. *Biophys J*. 72, 65-76.
264. Abdolvahabi, A. et al. (2013) Colorimetric and longitudinal analysis of leukocoria in recreational photographs of children with retinoblastoma. *PLoS One*. 8, e76677.
265. Dimaras, H., Kimani, K., Dimba, E. A., Gronsdahl, P., White, A., Chan, H. S., Gallie, B. L. (2012) Retinoblastoma. *Lancet*. 379, 1436-1446.
266. Zhang, J. et al. (2012) A novel retinoblastoma therapy from genomic and epigenetic analyses. *Nature*. 481, 329-334.
267. Houston, S. K., Murray, T. G., Wolfe, S. Q., Fernandes, C. E. (2011) Current update on retinoblastoma. *Int Ophthalm Clinics*. 51, 77-91.
268. Kivela, T. (2009) The epidemiological challenge of the most frequent eye cancer: retinoblastoma, an issue of birth and death. *Br J Ophthalmol*. 93, 1129-1131.
269. Kiss, S., Leiderman, Y. I., Mukai, S. (2008) Diagnosis, classification, and treatment of retinoblastoma. *Int Ophthalm Clinics*. 48, 135-147.
270. Shrestha, A., Adhikari, R. C., Saiju, R. (2010) Retinoblastoma in a 37 years old man in Nepal: a case report. *Kathmandu University medical journal*. 8, 247-250.
271. Broaddus, E., Topham, A., Singh, A. D. (2009) Incidence of retinoblastoma in the USA: 1975-2004. *Br J Ophthalmol*. 93, 21-23.

272. Broaddus, E., Topham, A., Singh, A. D. (2009) Survival with retinoblastoma in the USA: 1975-2004. *Br J Ophthalmol.* 93, 24-27.
273. Seregard, S., Lundell, G., Svedberg, H., Kivela, T. (2004) Incidence of retinoblastoma from 1958 to 1998 in Northern Europe: advantages of birth cohort analysis. *Ophthalmology.* 111, 1228-1232.
274. Swaminathan, R., Rama, R., Shanta, V. (2008) Childhood cancers in Chennai, India, 1990-2001: incidence and survival. *Int J Cancer.* 122, 2607-2611.
275. Wessels, G., Hesselning, P. B. (1996) Outcome of children treated for cancer in the Republic of Namibia. *Med Pediatr Oncol.* 27, 160-164.
276. Bowman, R. J., Mafwiri, M., Luthert, P., Luande, J., Wood, M. (2008) Outcome of retinoblastoma in east Africa. *Pediatr Blood Cancer.* 50, 160-162.
277. Leander, C., Fu, L. C., Pena, A., Howard, S. C., Rodriguez-Galindo, C., Wilimas, J. A., Ribeiro, R. C., Haik, B. (2007) Impact of an education program on late diagnosis of retinoblastoma in Honduras. *Pediatr Blood Cancer.* 49, 817-819.
278. Wilson, M. W., Qaddoumi, I., Billups, C., Haik, B. G., Rodriguez-Galindo, C. (2011) A clinicopathological correlation of 67 eyes primarily enucleated for advanced intraocular retinoblastoma. *Br J Ophthalmol.* 95, 553-558.
279. Canturk, S., Qaddoumi, I., Khetan, V., Ma, Z., Furmanchuk, A., Antoneli, C. B., Sultan, I., Kebudi, R., Sharma, T., Rodriguez-Galindo, C., Abramson, D. H., Chantada, G. L. (2010) Survival of retinoblastoma in less-developed countries impact of socioeconomic and health-related indicators. *Br J Ophthalmol.* 94, 1432-1436.
280. Rodriguez-Galindo, C. et al. (2008) Retinoblastoma: one world, one vision. *Pediatrics.* 122, e763-770.
281. Epelman, S. (2012) Preserving vision in retinoblastoma through early detection and intervention. *Curr Oncol Rep.* 14, 213-219.
282. Narang, S., Mashayekhi, A., Rudich, D., Shields, C. L. (2012) Predictors of long-term visual outcome after chemoreduction for management of intraocular retinoblastoma. *Clin Exp Ophthalmol.* 40, 736-742.
283. Ventura, G., Cozzi, G. (2012) Red reflex examination for retinoblastoma. *Lancet.* 380, 803; author reply 803-804.
284. Li, J., Coats, D. K., Fung, D., Smith, E. O., Paysse, E. (2010) The detection of simulated retinoblastoma by using red-reflex testing. *Pediatrics.* 126, e202-207.

285. Abramson, D. H., Beaverson, K., Sangani, P., Vora, R. A., Lee, T. C., Hochberg, H. M., Kirsztrot, J., Ranjithan, M. (2003) Screening for retinoblastoma: presenting signs as prognosticators of patient and ocular survival. *Pediatrics*. 112, 1248-1255.
286. Maki, J. L., Marr, B. P., Abramson, D. H. (2009) Diagnosis of retinoblastoma: how good are referring physicians? *Ophthalmic Genet*. 30, 199-205.
287. Haider, S., Qureshi, W., Ali, A. (2008) Leukocoria in children. *J Pediatr Ophthalmol Strabismus*. 45, 179-180.
288. Rubin, M. P., Mukai, S. (2008) Coats' disease. *Int Ophthalmol Clinics* 48, 149-158.
289. Lim, Z., Rubab, S., Chan, Y. H., Levin, A. V. (2010) Pediatric cataract: the Toronto experience-etiology. *Am J Ophthalmol*. 149, 887-892.
290. Shoji, K., Ito, N., Ito, Y., Inoue, N., Adachi, S., Fujimaru, T., Nakamura, T., Nishina, S., Azuma, N., Saitoh, A. (2010) Is a 6-week course of ganciclovir therapy effective for chorioretinitis in infants with congenital cytomegalovirus infection? *J Pediatr*. 157, 331-333.
291. Kumar, A., Jethani, J., Shetty, S., Vijayalakshmi, P. (2010) Bilateral persistent fetal vasculature: a study of 11 cases. *J AAPOS*. 14, 345-348.
292. Haik, B. G., Saint Louis, L., Smith, M. E., Ellsworth, R. M., Abramson, D. H., Cahill, P., Deck, M., Coleman, D. J. (1985) Magnetic resonance imaging in the evaluation of leukocoria. *Ophthalmology*. 92, 1143-1152.
293. Smirniotopoulos, J. G., Bargallo, N., Mafee, M. F. (1994) Differential diagnosis of leukokoria: radiologic-pathologic correlation. *Radiographics*. 14, 1059-1079; quiz 1081-1052.
294. Phan, I. T., Stout, T. (2010) Retinoblastoma presenting as strabismus and leukocoria. *J Pediatr*. 157, 858.
295. Smith, A. R. (1978) Color gamut transform pairs. *SIGGRAPH Comput. Graph*. 12, 12-19.
296. Marshall, J., Gole, G. A. (2003) Unilateral leukocoria in off axis flash photographs of normal eyes. *Am J Ophthalmol*. 135, 709-711.
297. Russell, H. C., Agarwal, P. K., Somner, J. E., Bowman, R. J., Dutton, G. N. (2010) Off-axis digital flash photography: a common cause of artefact leukocoria in children. *J Pediatr Ophthalmol Strabismus*. 1-3.

298. Cha, S. B., Shields, C., Shields, J. A. (1993) The parents of a 9-month-old black girl discovered a yellow pupil in her right eye. Retinoblastoma. *J Ophthalmic Nurs Technol.* 12, 182, 189.
299. Sussman, D. A., Escalona-Benz, E., Benz, M. S., Hayden, B. C., Feuer, W., Cicciarelli, N., Toledano, S., Markoe, A., Murray, T. G. (2003) Comparison of retinoblastoma reduction for chemotherapy vs external beam radiotherapy. *Arch Ophthalmol.* 121, 979-984.
300. Ollivier, F. J., Samuelson, D. A., Brooks, D. E., Lewis, P. A., Kallberg, M. E., Komaromy, A. M. (2004) Comparative morphology of the tapetum lucidum (among selected species). *Vet Ophthalmol.* 7, 11-22.
301. *Retinoblastoma.* Springer 2010.
302. Yorek, M. A., Figard, P. H., Kaduce, T. L., Spector, A. A. (1985) A comparison of lipid metabolism in two human retinoblastoma cell lines. *Invest Ophthalmol Vis Sci.* 26, 1148-1154.
303. Hyman, B. T., Spector, A. A. (1981) Accumulation of *n*-3 polyunsaturated fatty acids cultured human Y79 retinoblastoma cells. *J Neurochem.* 37, 60-69.
304. Goustard-Langelier, B., Alessandri, J. M., Raguenez, G., Durand, G., Courtois, Y. (2000) Phospholipid incorporation and metabolic conversion of *n*-3 polyunsaturated fatty acids in the Y79 retinoblastoma cell line. *J Neurosci Res.* 60, 678-685.
305. Yorek, M. A., Bohnker, R. R., Dudley, D. T., Spector, A. A. (1984) Comparative utilization of *n*-3 polyunsaturated fatty acids by cultured human Y-79 retinoblastoma cells. *Biochim Biophys Acta.* 795, 277-285.
306. Hyman, B. T., Spector, A. A. (1982) Choline uptake in cultured human Y79 retinoblastoma cells: effect of polyunsaturated fatty acid compositional modifications. *J Neurochem.* 38, 650-656.
307. Makky, A., Michel, J. P., Ballut, S., Kasselouri, A., Maillard, P., Rosilio, V. (2010) Effect of cholesterol and sugar on the penetration of glycodendrimeric phenylporphyrins into biomimetic models of retinoblastoma cells membranes. *Langmuir.* 26, 11145-11156.
308. Gombos, D. S., et al. (2000) Cholesterosis following chemoreduction for advanced retinoblastoma. *Arch Ophthalmol.* 118, 440-441.
309. Murphy, D., Bishop, H., Edgar, A. (2012) Leukocoria and retinoblastoma--pitfalls of the digital age? *Lancet.* 379, 2465.

310. Luna-Fineman, S., Barnoya, M., Bonilla, M., Fu, L., Baez, F., Rodriguez-Galindo, C. (2012) Retinoblastoma in central America: report from the central American association of pediatric hematology oncology (AHOPCA). *Pediatr Blood Cancer*. 58, 545-550.
311. (2006) Explosive growth continues for India's mobile-phone market. *Microwaves & Rf*. 45, 22-22.
312. (2010) Dotty but dashing. *The Economist*. Apr. 8th,
313. Wang, S., Zhao, X., Khimji, I., Akbas, R., Qiu, W., Edwards, D., Cramer, D. W., Ye, B., Demirci, U. (2011) Integration of cell phone imaging with microchip ELISA to detect ovarian cancer HE4 biomarker in urine at the point-of-care. *Lab Chip*. 11, 3411-3418.
314. Zhu, H., Yaglidere, O., Su, T. W., Tseng, D., Ozcan, A. (2011) Cost-effective and compact wide-field fluorescent imaging on a cell-phone. *Lab Chip*. 11, 315-322.
315. Rodriguez-Galindo, C. (2011) The basics of retinoblastoma: back to school. *Pediatr Blood Cancer*. 57, 1093-1094.
316. Smith, A. Smartphone Ownership-2013 Update 2013.
317. Poulaki, V., Mukai, S. (2009) Retinoblastoma: genetics and pathology. *Int Ophthalmol Clinics*. 49, 155-164.
318. Kokot, Z., Burda, K. (1998) Simultaneous determination of salicylic acid and acetylsalicylic acid in aspirin delayed-release tablet formulations by second-derivative UV spectrophotometry. *J Pharm Biomed Anal*. 18, 871-875.
319. Anderson, J. R., Chemiavskaya, O., Gitlin, I., Engel, G. S., Yuditsky, L., Whitesides, G. M. (2002) Analysis by capillary electrophoresis of the kinetics of charge ladder formation for bovine carbonic anhydrase. *Anal Chem*. 74, 1870-1878.
320. Furukawa, Y., O'Halloran, T. V. (2005) Amyotrophic lateral sclerosis mutations have the greatest destabilizing effect on the apo- and reduced form of SOD1, leading to unfolding and oxidative aggregation. *J Biol Chem*. 280, 17266-17274.
321. Nelson, D. L. *Lehninger Principles of Biochemistry*. W.H. Freeman: New York, 2008.